COMPUTATIONAL MODELING OF TURBULENT SPRAY COMBUSTION

COMPUTATIONAL MODELING OF TURBULENT SPRAY COMBUSTION

Proefschrift

ter verkrijging van de graad van doctor
aan de Technische Universiteit Delft,
op gezag van de Rector Magnificus prof. ir. K. C. A. M. Luyben,
voorzitter van het College voor Promoties,
in het openbaar te verdedigen op dinsdag, 17 mei, 2016 om 12:30 uur

door

Likun MA

Master of Science
National University of Defense Technology, China
geboren te Gansu, China

Dit proefschrift is goedgekeurd door de:

Prof. dr. D.J.E.M. Roekaerts

Samenstelling promotiecommissie:

Rector Magnificus,	voorzitter
Prof. dr. D.J.E.M. Roekaerts,	Technische Universiteit Delft
Onafhankelijke leden:	
Prof. dr. W.P. Jones,	Imperial College London
Prof. dr. ir. B. Merci,	Universiteit Gent
Dr. J.B.W. Kok,	Universiteit Twente
Prof. dr. L.P.H. de Goey,	Technische Universiteit Eindhoven
Dr. A. Gangoli Rao,	Technische Universiteit Delft
Prof. dr. ir. R.A.W.M. Henkes,	Technische Universiteit Delft
Prof. dr. ir. B.J. Boersma,	Technische Universiteit Delft, reservelid

The author of this thesis was financially supported by the China Scholar Council (CSC). This research was sponsored by Netherlands Organization for Scientific Research (NWO) for the use of supercomputer facilities.

Keywords: Spray Combustion, Numerical simulation, OpenFOAM, Flamelet Generated Manifolds, MILD combustion

Printed by: Gildeprint

ISBN 978-94-6233-281-2

An electronic version of this dissertation is available at
http://repository.tudelft.nl/.

To my parents, my wife and my daughter...

SUMMARY

The objective of the research presented in this thesis is development and validation of predictive models or modeling approaches of liquid fuel combustion (spray combustion) in hot-diluted environments, known as flameless combustion or MILD combustion. The goal is to combine good physical insight, appropriate numerical methods and good software development in the context of the general framework of Computational Fluid Dynamics (CFD). For model validation to be possible, availability of relevant, accurate and complete experimental datasets is important. For this study the database of Delft Spray-in-Hot-Coflow(DSHC) flames has been employed.

Using different combinations of model components and approaches, the modeling has been developed and tested at three levels of complexity and accuracy. Depending on the chosen combination of turbulence and combustion models, the modeling methods used in this thesis are the following: 1) Reynolds Averaged Navier-Stokes (RANS) approach for turbulence modeling with Steady Flamelet Model (SFM) approach for combustion; 2) Transported Probability Density Function (TPDF) approach for turbulence modeling with Flamelet Generated Manifolds (FGM) for combustion; 3) Largy Eddy Simulation (LES) for turbulence with FGM for combustion. The CFD codes that are used for these methods are respectively the commercial software ANSYS Fluent® (version 15.0), the in-house code "PDFD" and the open source software OpenFOAM®.

The first stage of the research aimed at exploring the characteristics of the target flames, and gaining understanding of the relevance of each model component in order to clarify the directions of further model improvements. Existing standard models (RANS/SFM) within the commercial software were employed for this purpose. The main outcome of this stage of the study is that the SFM fails in predicting the lifted-off phenomena of the DSHC flames, and it is concluded that a more sophisticated Turbulence-Chemistry Interaction (TCI) model is required.

In the second stage of the study, advancements on both turbulence and combustion models have been made, respectively with TPDF and FGM. TPDF was used because it offers a more detailed description of statistical properties and FGM because it offers the possibility to include finite rate chemical effects in the frame of TPDF at affordable cost. In this stage of the study the focus was on simulations of the dilute spray region. Ignoring the dense region close to the atomizer, the simulation starts from a certain distance downstream, preferably a region where experimental data are available or good insight in local conditions is available by other means. Because of the careful specification of the boundary conditions of spray as well as gas phase, the flow and combustion development downstream were correctly reproduced by this approach, including the lift-off height. Next, based on this platform, parametric studies on many important aspects have been carried out, for example, the influence of the droplet initial temperature, a comparison between different model variants on evaporation etc. Good agreement with experimental data was achieved and useful information on model performance was ob-

tained. However, also limitations of the modeling approach were identified. The most important one is that the use of an adiabatic approach disregarding the energy consumed in the evaporation of liquid (adiabatic FGM table) over-predicts the gas phase temperature in the region of intense droplets evaporation.

In the third stage of this study we used Large Eddy Simulation of turbulence in combination with non-adiabatic FGM for evaporation and combustion. The subgrid scale fluctuations of the FGM scalars were modeled using assumed-shape PDFs. The CFD platform for doing so is the open source CFD package — OpenFOAM®. Since the desired FGM model is not available in the public released version of OpenFOAM®, the first step in this third stage was development and validation of a new implementation of FGM. A well-documented gaseous lifted flame in hot-diluted coflow was used as test case. In this study, it was found that the auto-ignition process is highly sensitive to the model constants that are used to evaluate the variances of mixture fraction and progress variable. Dynamic procedures have been developed for the determination of these constants in the context of LES. Using the developed dynamic models significant improvement of the prediction of the flame lift-off height has been achieved. The second step of LES/FGM method development was the extension of the implemented FGM method to spray combustion. Two major model developments were completed in this step — the Condition Droplet Injection Model (CDIM) and the non-adiabatic FGM method. The CDIM was proposed to take into account the influence of flash-boiling atomization of the DSHC flames. The comparison of CIDM with a conventional droplet injection model showed superior performance of the CDIM in modeling of the DSHC flames. Furthermore, with the addition of enthalpy deficit as an extra dimension of the FGM table, the prediction of the gas phase temperature was significantly improved. The third step of modeling stage three was to apply the developed LES/FGM method to a wide range of test cases including the hot and cold coflow cases to test the range of applicability of models, and to some virtual (i.e. not yet studied experimentally) cases in order to gain deeper insight on the involved phenomena. The simulations showed that the developed LES/FGM method is able to correctly capture major features of spray flames under different coflow conditions, for example the flame width and flame lift-off height. Independent parameter study of the coflow temperature and oxygen concentration clarified the effects of these two important factors, and suggested better operation conditions to achieve a strict MILD spray combustion condition. Simulation and comparison of the hot coflow (H_{II}) and cold coflow (A_{II}) cases revealed very interesting mechanisms that determine different flame structures and their transition in spray combustion. The “single” and “double” flame structures of these two cases have been successfully reproduced. Detailed analysis showed that the actual flame topologies have been over-simplified by their conventional names (single/double flame) used in literature, which are mainly based on the experimental observation. It was found that the appearance of multi-flame or multiple reaction regions in spray combustion are resulting from the disparity of time scales of the processes involved. And it was further demonstrated that by matching important time scales, similar flame structure can be achieved under considerably different operating conditions.

In summary, three different levels of modeling approaches for spray combustion have been developed and tested. These approaches can be employed in different ap-

plications based on the consideration of the required accuracy and computational affordability. The RANS/SFM is the cheapest one in terms of computation cost, but the interpretation of the results should take into account that a number of important aspects such as lift-off height are not well predicted. The LES/FGM method provides most accurate results compared to other two, but is also most computationally demanding. The method using the last approach offers the most promises for a better understanding of the MILD spray combustion and design of clean and efficient combustion technology.

SAMENVATTING

Het onderzoek in dit proefschrift heeft als doel de ontwikkeling en de validatie van voorspellende modellen voor de verbranding van vloeibare brandstoffen in de vorm van een spray en in de condities van 'vlamloze verbranding' (flameless combustion, MILD combustion). Het doel is goed fysisch inzicht, gepaste numerieke methoden en goede software ontwikkeling te combineren in de context van numerieke stromingsleer (Computational Fluid Dynamics (CFD)). Om model validatie mogelijk te maken is beschikbaarheid van relevante, accurate en volledige experimentele datasets belangrijk. Voor deze studie is de database van 'Delft-Spray-in-Hot-Coflow (DSHC)' vlammen gebruikt.

Gebruik makend van verschillende combinaties van deelmodellen en wijze van aanpak, werden modellen ontwikkeld en getest op drie niveaus van complexiteit en nauwkeurigheid. Al naar gelang de combinatie van turbulentie en verbrandingsmodellen, zijn de modelleringsmethoden gebruikt in dit proefschrift de volgende: 1) Reynolds gemiddelde Navier Stokes (RANS) voor turbulentie met Stationair Flamelet model (SFM) voor verbranding; 2) Transportvergelijking voor Waarschijnlijkheidsdichtheidsfunctie (TPDF) voor turbulentiemodelering met Flamelet Gegenereerd Manifold (FGM) voor verbranding; 3) Largy Eddy Simulatie (LES) voor turbulentie met FGM voor verbranding. De CFD codes die gebruikt worden voor deze methoden zijn, respektievelijk, de commerciële software ANSYS Fluent® (version 15.0), de in-huis code "PDFDën de open source code OpenFOAM®.

Het eerste stadium van het onderzoek had tot doel de exploratie van de karakteristieken van de te onderzoeken vlammen en begripsvorming over de relevantie van elke modelcomponent om zo de richting voor verdere modelverbeteringen te verhelderen. Voor dit doel werden de bestaande standaard modellen (RANS/SFM) in de commerciële software gebruikt. Het voornaamste resultaat na dit stadium was de conclusie dat SFM niet in staat is te voorspellen dat de DSHC vlam los komt van de brander (lift-off) en dat daarom een meer gesofisticeerd model voor turbulentie-chemie-interactie (TCI) nodig is.

In het tweede stadium werden meer geavanceerde modellen gebruikt voor turbulentie en voor verbranding, respectievelijk TPDF en FGM. TPDF werd gebruikt omdat het een meer gedetailleerde beschrijving geeft van statistische eigenschappen en FGM omdat het de mogelijkheid biedt eindig snelle chemie effecten mee te nemen in TPDF tegen een aanvaardbare kost. In dit stadium was de focus op de simulatie van het gebied waarin de spray verdund (dilute) is. Hierbij wordt het gebied met hoge vloeistofdichtheid niet beschreven en start de simulatie op een zekere afstand stroomafwaarts van de verstuiver. Na zorgvuldige specificatie van de randvoorwaarden van zowel spray als gasfase werd met deze modellen de ontwikkeling van zowel de stroming als de verbranding als functie van de afstand van de injector correct gereproduceerd. Deze aanpak diende als platform voor parameterstudies van vele belangrijke aspecten, bijvoorbeeld de invloed van de initiële druppeltemperatuur, een vergelijking van verschillende modelvarianten

voor verdamping enz. Goede overeenstemming werd bereikt met experimentele data en het leverde nuttige informatie op over de prestaties van de modellen. Maar ook werden er beperkingen van de modellen geïdentificeerd. De meest belangrijke is het feit dat het verwaarlozen van de energie die nodig is om de vloeistof te verdampen adiabatische FGM tabel) er toe leidt dat de temperatuur van de gasfase te hoog voorspeld in het gebied met intense verdamping van druppels.

In het derde stadium van deze studie gebruikten we Large Eddy Simulatie van turbulentie met een niet-adiabatisch FGM voor de verdamping en verbranding. De fluctuations van de FGM scalars op de sub-grid schaal werden gemodelleerd met een aangenomen-PDF methode. Het CFD platform om dit te doen is het open source CFD pakket — OpenFOAM®. Omdat het gewenste FGM model niet beschikbaar is in the publiek beschikbare versie van OpenFOAM®, is de eerste stap in dit derde stadium van deze studie was de implementatie en validatie van dat FGM model. Een goed-gedocumenteerde gasvlam in een hete verdunde omgevingsstroming (coflow) die loskomt van de brander werd als testgeval gebruikt. In deze studie werd gevonden dat het proces van zelfontbranding (auto-ignition) hoogst gevoelig is voor de waarde van model constanten in de modelvergelijkingen die gebruikt worden om de variantie van de mengselfractie en de voortgangsvariabele te berekenen. Dynamische procedures werden ontwikkeld om deze constanten te bepalen in de context van LES. Door de ontwikkeling van dynamische modellen werden significante verbeteringen bereikt in de voorspelling van de lift-off hoogte. De tweede stap op het gebied van LES/FGM methode ontwikkeling was de uitbreiding van de geïmplementeerde FGM methode naar spray verbranding. Twee grote ontwikkelingen werden voltooid in deze stap: een Conditioneel Druppel Injectie Model (CDIM) en een niet-adiabatische FGM method. Het CDIM werd ingevoerd om de invloed in rekening te brengen van de verstuiving met flash-verdamping die optreedt bij de DSHC vlammen. De vergelijking met een conventioneel druppel injectiemodel toonde aan dat CDIM betere voorspellingen geeft van de eigenschappen van de DSHC vlammen. Verder, met de toevoeging van enthalpietekort als extra dimensie van de FGM tabel, werd de voorspelling van de gasfase temperatuur significant beter. De derde stap van het derde stadium van modelontwikkeling was de toepassing van de ontwikkelde LES/FGM methode op een breed bereik aan testgevallen, met zowel hete als koude coflow, om het toepassingsgebied van de modellen te testen, en op enkele virtuele (d.w.z. nog niet experimenteel bestudeerde) gevallen, om dieper inzicht te verkrijgen in alle verschijnselen die een rol spelen. De simulaties toonden aan dat de ontwikkelde LES/FGM methode in staat is om belangrijke eigenschappen van spray vlammen onder verschillende coflow condities, bijvoorbeeld de vlambreedte en de vlam lift-off hoogte. In een parameterstudie werd de invloed van coflow temperatuur en coflow zuurstofconcentratie onafhankelijk van elkaar onderzocht. Zo werden de effecten van deze twee belangrijke factoren verklaard, en konden vervolgens suggesties worden gedaan voor betere instellingen om een de condities voor MILD verbranding te realiseren. Simulatie en onderlinge vergelijking van de gevallen met hete coflow (H_{II}) en koude coflow (A_{II}) bracht zeer interessante mechanismes aan het licht die de verschillende vlamstructuren en de overgangen ertussen bepalen in spray verbranding. De structuren met een 'enkele' en een 'dubbele' vlamstructuur respectievelijk voorkomend bij deze twee gevallen werden met succes gereproduceerd. Gedetailleerde analyse toonde aan dat de voorspelde vlamtopologie meer

complex is dan de voornamelijk op visuele observatie gebaseerde conventionele benamingen (enkele vlam / dubbele vlam) aangeven.

Het voorkomen van gevallen met meerdere vlamzones of reactiezones werd verklaard als gevolg van de relatieve waarde van de verschillende relevante tijdschalen van de betrokken processen (convectie, verdamping, chemische reactie). En verder werd er aangetoond dat door belangrijke tijdschalen met elkaar overeen te laten komen, een gelijke vlamstructuur kan gerealiseerd worden onder aanmerkelijk verschillende werkingscondities.

Samengevat, drie niveaus van modellering voor spray verbranding werden ontwikkeld en gevalideerd. Deze drie verschillende formuleringen kunnen gebruikt worden in verschillende toepassingen afhankelijk van de vereiste nauwkeurigheid en de toegelaten rekentijd. De RANS/SFM methode is het goedkoopst wat betreft rekentijd, maar de interpretatie van de resultaten moet er mee rekening houden dat een aantal belangrijke aspecten zoal lift-off hoogte goed voorspeld wordt. De LES/FGM methode levert de meest nauwkeurige voorspellingen in vergelijking met de andere twee methoden, maar is ook meest veeleisend wat rekenkracht betreft. Deze methode is het meest veelbelovend voor een beter begrip van MILD spray verbranding en ontwerp van schone en zuinige verbrandingstechnologie.

CONTENTS

NOMENCLATURE

LIST OF SYMBOLS

B_M	Spalding mass transfer number
C	Scaled progress variable
C_D	Droplet diameter
C_p	Specific heat under constant pressure
D	Diffusivity
L_v	Latent heat of evaporation
N_p	Number of droplets represented by each parcel
P	Probability density function
R	Gas constant
R_{ij}	Reynolds or sub-grid stresses
R_u	universal gas constant
S	Source term
S_{ij}	Strain rate tensor
$V_{k,j}$	J-component of diffusion velocity of species k
W	Molecular weight
X_i	Mole fraction of species i
Y_c	Unscaled progress variable
Y_i	Mass fraction of species i
Z	Mixture fraction
$\mathcal{Z}$	Axial coordinate
D_p	Droplet diameter
Nu	Nusselt number
Pr	Prandtl number
Re	Reynolds number
Sc	Schmidt number
Sh	Sherwood number
χ	Scalar dissipation rate
$\dot{\omega}_k$	Reaction source term of species k
$\dot{m}_l$	Liquid mass flow rate
$\mathbf{g}$	Gravitational force
$\mathbf{q}$	Heat flux vector
$\dot{m}_\mathrm{p}$	Droplet evaporation rate
ρ	Density
$\widetilde{Z''^2}$	Variance of mixture fraction
ζ_Z	Scaled variance of mixture fraction
a	Strain rate
h	Enthalpy
h_s	Sensible enthalpy
k	Turbulent kinetic energy
m_p	Droplet mass
p	Pressure
r or R	Radial coordinate
u or U	Velocity

GREEK SYMBOLS

α_p	Droplet velocity scale parameter
ϵ	Dissipation rate of turbulent kinetic energy
η_h	Scaled enthalpy loss
λ	Thermal conductivity
μ	Dynamic viscosity
τ_{ij}	Viscous stress tensor
τ_p	Droplet relaxation time
θ	Droplet trajectory angle

SUSCRIPTS

L	Properties of large droplets
S	Properties of small droplets
cntr	Properties at droplet center
m	Droplet film properties
g	Gas phase properties
surf	Properties at droplet surface
vap	Properties of fuel vapor
cf	Coflow properties
e	evaporation
l	Properties of liquid fuel
max	Maximum
min	Minimum
p	droplet
$seen$	Droplet seen properties
sgs	Sub-Grid Scale
t	turbulent

SUPERSCRIPTS

D	Deviatoric part of a tensor

ABBREVIATIONS

CDF	Cumulative Distribution Function
CDIM	Conditional Droplet Injection Model
DNS	Direct Numerical Simulation
FGM	Flamelet Generated Manifolds
IEM	Interaction by Exchange with the Mean

LES	Large Eddy Simulation
MILD	Moderate or Intense Low-oxygen Dilution
PDF	Probability Density Function
RANS	Reynolds-Averaged Navier Stokes
rms	root mean square
RR	Reaction Regions
SFM	Steady Flamelet Model
SGS	Sub-Grid Scale
TCI	Turbulence-Chemistry Interaction

1

INTRODUCTION

1

1.1. ENERGY AND ENVIRONMENTAL ISSUES

Research and use of renewable energies is booming, and they are expected to take the place of fossil fuels in the future in order to finally achieve a sustainable development. However, these renewable energies have their own limitations, for example the strong time and place dependency of wind and solar energy and the safety issues for nuclear energy. They alone are insufficient to meet global energy requirement in the foreseeable future. As shown in Fig. 1.1, in the next few decades, in spite of the rapid growth of renewable energies, the fossil fuels — oil, gas and coal — will remain the main sources for global energy supply.

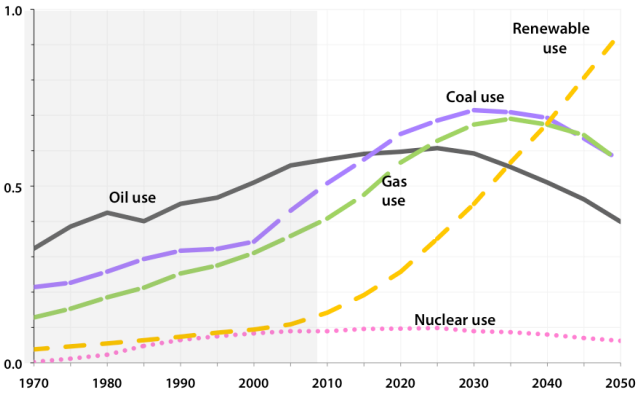

Figure 1.1: Forecast of global energy consumption, Scales: Energy uses (0–7 billion tonnes of oil equivalent per year) [1].

The fossil fuels are predominantly consumed by combustion. Combustion has been broadly applied in all kinds of energy supplying systems, because it is easy to use and can generate high power intensity. However, the wide use of combustion system comes with a price, that is the significant impact on the environment.

The side effects of combustion on environment are mainly due to the emission of greenhouse gases (GHG), mainly carbon dioxide (CO_2), and pollutants, for example nitrogen oxides (NOx). The global warming, caused by increase of GHG, is a serious threat not only to the long term sustainable development but also to the daily life or even survival, especially for some island countries and low altitude regions. Research has shown that the global average temperature has increased by $0.8°C$ in the past decades, and two thirds of the warming has occurred since 1975 [2]. Considering the vast amount of heat that is needed to warm all the oceans, atmosphere, and land, this change is significant.

Actions have been taken to restrict and minimize theses influences. Very recently, 195 countries have reached the first ever global agreement on climate change — 'the Paris Agreement'. One of the biggest achievement of this agreement is that all members agreed on "holding the increase in the global average temperature to well below $2°C$ above pre-industrial levels and to pursue efforts to limit the temperature increase to $1.5°C$ above pre-industrial levels" . Also in this agreement, it is agreed to reach global peaking of GHG emissions as soon as possible, and to balance all anthropogenic emis-

sions after 2050. To meet all these goals, innovations on combustion technologies are urgently required.

1.2. MOTIVATION AND OBJECTIVES

Many clean combustion technologies have been developed in the past few decades (see [3] and references therein), in this thesis we focus on one of them — the Moderate or Intense Low-oxygen Dilution (MILD) combustion, and in particular, its application to spray combustion.

MILD combustion is a combustion technology that was firstly developed in Japan in 1990 [4]. The essential features of this technology are the elevated reactant temperature and small temperature increment in the combustion process. The promising performance of MILD combustion is including high thermal efficiency, significant reduction of CO and NOx emission, nearly uniform radiative thermal field, low combustion noise, easy flame stabilization, etc. [3, 5].

A definition of MILD combustion is given by Cavaliere and de Joannon in [5] as: "A combustion process is named MILD when the inlet temperature of the reactant mixture is higher than mixture self-ignition temperature whereas the maximum allowable temperature increase with respect to inlet temperature during combustion is lower than mixture self-ignition temperature (in Kelvin)". When MILD combustion occurs, no visible flame is present, especially if gaseous fuel or light oils are used, and the light received mainly comes from hot furnace walls. Therefore it is also named "flameless combustion" or "flameless oxidation" (FLOX). High temperature air combustion (HiTAC) also refers to similar technology.

As shown in Fig. 1.2, the temperature and O_2 concentration of the reactants are two important parameters to determine whether or not the system operates in MILD condition. It has been shown that the formation of the thermal NOx is strongly related to the presence of N_2 and O_2 in high temperature region. Therefore most NOx-reducing technologies are based on the ideas of limiting the peak temperature, shortening the residence time in high temperature areas and reducing oxygen availability in these areas [3]. In MILD combustion, the dilution of reactants lowers the flame peak temperature and avoids the presence of high concentration of O_2. Therefore considerable reduction in the NOx emissions can be achieved when the MILD combustion is established [3, 6]. Furthermore, the dilution leads to relatively slow reactions and a distributed reaction zone. The temperature distribution is nearly uniform in MILD combustion furnace, this can be beneficial for many processes. The inlet temperature for MILD combustion is higher than the auto-ignition temperature, so no special flame stabilization is needed.

MILD combustion is predominantly realized by the dilution of reactants with recirculated flue gas [7]. MILD combustion furnaces are normally designed in such a way that the supply of air and fuel is separated so that the fuel or air or both can already mix with recirculated exhaust gas before they mix with each other and react.

MILD combustion has been intensively studied both experimentally and numerically since 2000, but these studies mainly focused on gaseous fuels [7, 9–11]. Liquid fuel combustion or spray combustion is widely utilized in engines and industrial burners, so innovative technologies in spray combustion is of great practical interest. However, in spite of its importance, the research on MILD spray combustion is still in its infant stage

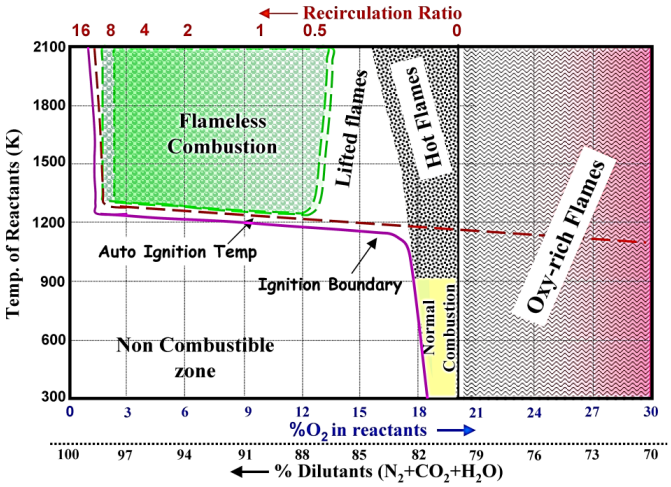

Figure 1.2: Combustion regimes in diluted combustion [8].

[12–14].

Weber et al. [12] performed in-furnace experimental studies of MILD combustion for various fuels, including light and heavy oils, and demonstrated the feasibility of spray MILD combustion. Derudi and Rota [13] investigated MILD combustion of liquid hydrocarbons using a dual-nozzle laboratory-scale burner. They found that compared to gaseous fuels, the MILD combustion region in the $T_{avg} - K_V$ space enlarges when liquid hydrocarbons are used, where T_{avg} and K_V are respectively the chamber temperature and dilution ratio. Recently, experimental study of prevaporized liquid fuel (ethanol, acetone and n-heptane) MILD combustion has been carried out by Ye et al [14] under elevated pressure. It was found that the CO emission is always low under MILD condition regardless of the pressure, however, the range of equivalence ratio, within which both the emissions of NOx and CO are low, narrows under elevated pressure. Delft Spray-in-Hot-Coflow flames have also been developed to study the MILD spray combustion, and significant differences between conventional and MILD spray combustion have been observed [15–17].

The encouraging experimental observations of applying MILD technology to spray combustion actually call for further research in order to gain understanding in greater detail. Numerical simulation is an ideal tool to do so due to the facts that it is normally cheaper than experiments, and more information is available from the simulation results.

Modeling of spray combustion is very difficult, not only because it is a twophase problem but also due to the presence of many strongly coupled phenomena, including liquid atomization, droplet dispersion, evaporation, turbulent field, combustion and radiation [18, 19]. The main challenge is to find a best compromise between the computational efficiency, achieved through simplification of mathematical models of each process, and the need for detailed description of relevant processes. Given the difficulties, it is clear that different levels of modeling approaches are needed in order to meet

different requirements.

New difficulties arise when it comes to the MILD spray combustion. The presence of hot-diluted gas significantly affects the liquid atomization and evaporation as observed in the DSHC experiment [16]. Models that can take into account these influences are required. The combustion model that can effectively and accurately accounts for the turbulence-chemistry interaction in MILD spray combustion is still to be developed. And the questions of whether the models that were originally developed for conventional spray combustion are still applicable in the MILD condition or not, and which model components have more significant influence on the predication, are to be answered. To the author's knowledge, numerical studies on the MILD spray combustion have not yet been reported in the literature.

The objectives of this study are, first, to develop and validate predictive modeling approaches for spray combustions in MILD condition, and second, to use these approaches to pursue a deeper insight on this new technologies in spray combustion.

1.3. COMPUTATIONAL PLATFORM

For a successful simulation of spray combustion it is crucial to have a well established computational platform where all necessary model components can be integrated efficiently. A typical modern Computational Fluid Dynamic (CFD) software consists of millions of lines of code, and enormous amount of knowledge and effort are required to build such a code. Since the main focus of this project is on the physical modeling of spray combustion rather than the developing of CFD code from scratch, several existing CFD codes have been employed in the current study, and secondary developments have been conducted on top of these codes. The codes that have been used in the research of this thesis include the commercial CFD code ANSYS Fluent®, the in-house code "PDFD" and the open source CFD package OpenFOAM®.

ANSYS Fluent® is a commercial CFD software owned by ANSYS, Inc. It has been widely used in academic research and industrial applications for simulating many fluid related problems. As a commercial software, it is stable and user friendly. Most required models are available, so it can be readily used for a certain purpose. In this project, ANSYS Fluent® will be used at the initial stage in order to gain some understandings on the significance of each model components. However, limitations of using commercial software for research is also obvious. The most important one being the lack of transparency. The practical implementation of the models is not accessible to the users, and this limits the credibility of the simulation results in some cases. Furthermore, the implementation of new models is relatively difficult. For model development, adding and testing new models is frequently required, but this is not straightforward to be done in commercial software. Use of ANSYS Fluent® will be presented in Chapter 4.

Many research groups have their own in-house code. In most cases, these codes focus on certain applications or methods rather than useful for general purposes. Main advantages of these codes are the full accessibility and transparency, and relatively straightforward possibility to change and implement new models. However, if such a code is not well designed and maintained at a high level, version control can be a big issue for the long term development. Careful verifications and validations (V&V) are required in order to establish confidence on the results obtained with these codes. In this thesis, the

in-house code “PDFD" will also be used for the modeling of spray combustion, details will be presented in Chapter 5.

Another type of CFD code, that is increasingly attracting attention, is the open source code. This type of codes were mostly developed as in-house or commercial code initially, and then opened to the public, such as OpenFOAM® [20]. The open source codes have most advantages of the in-house codes, namely the accessibility and transparency. But also have some features of the commercial code, for example, many models are already available and have been validated, and can be used for a wide range of applications. Some of these codes perform comparably or even better than their commercial counterpart in terms of accuracy and advancement. The development and maintenance of these code are largely driven by the active user community. However, open source codes are normally insufficiently documented, reading and understanding of source code is obligatory in this situation. This makes the learning curves of these codes very steep. Stability and accuracy of these codes are not guaranteed, patience and careful V&V are demanded for the use of these codes. OpenFOAM® has been chosen to carry out part of the simulation works in this thesis, use of OpenFOAM will be presented in Chapters 6 to 9.

1.4. VALIDATION DATABASE

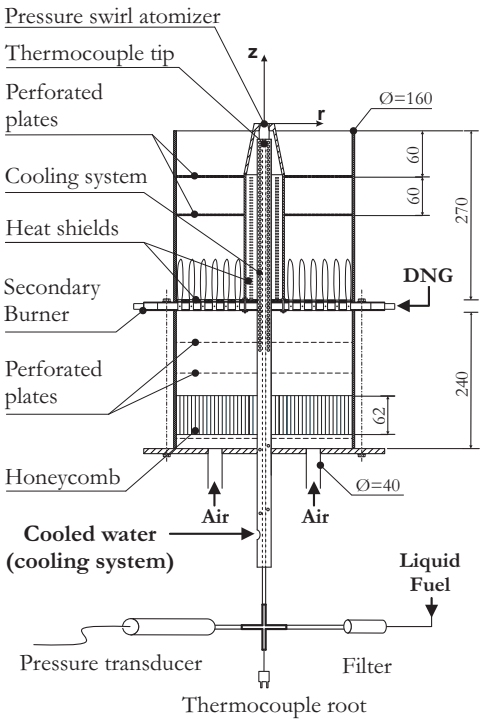

Figure 1.3: Schematic of the DSHC burner [16].

In this thesis, we have chosen the Delft Spray-in-Hot-Coflow (DSHC) flames as validation database for numerical simulation. Details of this databases will be given below.

The DSHC burner has been designed to study the fundamental aspects of MILD combustion of light oils [15]. The following criteria have been followed during the design of the DSHC burner in order to simplify the latter numerical studies: (1) The spray and coflow configuration is axisymmetric and a 2D RANS modeling is possible. (2) The burner design allows many experimental techniques to be applicable, providing sufficient information for model validation. (3) The coflow diameter and velocity should be large enough to isolate the jet flames from the laboratory air for the maximum downstream distance. This enables the simplification of the three-stream problem (fuel, coflow and air), which is difficult to model with some existing models, to two-stream problem (fuel and coflow). (4) Stable and uniform coflow, further simplifying the inlet boundary conditions for simulation. (5) Burner setup able to provide a range of coflow conditions (e.g. coflow temperature, stoichiometry and velocity). (6) Use of kinetically simple liquid fuels that have well-documented physical properties. All these features make the DSHC database very suitable for model development and validation.

A schematic of the DSHC burner is shown in Fig. 1.3. The liquid fuel is injected into the hot-diluted coflow by a pressure-swirl atomizer (type: Delavan WDA 0.5 GPH). This atomizer has a 0.21 mm exit orifice and generates a hollow cone spray with 60° spray angle. The hot-diluted coflow is generated by a secondary burner matrix to emulate the diluted air by recirculated combustion products in a large scale MILD combustion furnace. This secondary burner operates on premixed air and Dutch Natural Gas (DNG). The air/DNG ratio and the radiative heat loss through the burner wall together determine the temperature and O_2 level in the coflow. By varying the air/DNG ratio, different coflow temperatures and O_2 concentrations can be achieved. However, this burner configuration also has a limitation that the coflow temperature and O_2 concentration can not be changed independently, increase of one is accompanied with decrease of the other. Further discussion on this issue, and numerical parameter study on coflow temperature and O_2 concentration will be presented in Chapter 8. The flames with hot-diluted coflow ideally work in the “MILD" mode, further discussion on this will also be given in Chapter 8. For comparison, if the secondary burner is switched off, room temperature air is then supplied as coflow, the DSHC burner works in “Conventional" mode.

Comprehensive laser diagnostic measurements, including Laser Doppler Anemometry (LDA), Phase Doppler Anemometry (PDA) and Coherent Anti-Stokes Raman Scattering (CARS) have been conducted. Gas phase velocity components, temperature and O_2 volume fraction have been measured along the radial direction at coflow exit ($\mathcal{Z}$ = 0 mm). This information provides reliable inlet boundary conditions for a simulation that starts from $\mathcal{Z}$ = 0 mm, for example those that will be presented in Chapters 7 to 9. Gas phase and droplets properties have been measured along the radial direction at several axial locations. An example of available experimental data is given in Table 1.1. Information shown here is for the case A_{II}, the specific measurement locations can be different in other cases.

Many different cases exist in the DSHC database, they differ from each other in coflow conditions or fuel type (ethanol or acetone). In the course of this thesis, we focus on the ethanol cases, those both in conventional mode (case A_{II}) and MILD mode (cases H_I

1

Table 1.1: Example of available information in the DSHC database (case A_{II}), ✓denotes experimental data is available.

$\mathcal{Z} = [mm]$	0	8	10	12	15	20	30	35	40	45	50	60
					Gas phase properties							
Velocity	✓[a]	✓	✓	✓	✓	✓	✓	✓	✓	✓		
Temperature	✓				✓	✓	✓		✓		✓	✓
X_{O_2}	✓											
					Droplet properties							
Velocity		✓	✓	✓	✓	✓	✓	✓	✓	✓		
Diameter		✓	✓	✓	✓	✓	✓	✓	✓	✓		
Mass flux		✓	✓	✓	✓	✓	✓	✓	✓	✓		
Number concentration		✓	✓	✓	✓	✓	✓	✓	✓	✓		
High speed visualization	✓[b]											

[a]Measured by LDA, gas phase velocity at other locations was measured with PDA using small droplets as tracer.
[b]For atomization process near the atomizer exit.

Table 1.2: Boundary conditions for different cases in the DSHC database.

Case	$\overline{T}_{cf}$ $[K]$	$\overline{X}_{O_2,cf}$ [%]	$\overline{X}_{N_2,cf}$ [%]	$\overline{X}_{H_2O,cf}$ [%]	$\overline{X}_{CO_2,cf}$ [%]	$\bar{U}_{cf}$ $[m/s]$	$\bar{I}_{cf}$ [%]	$\dot{m}_{liq}$ $[kg/hr]$
A_{II}	300	21	79	0	0	0.25	2.5	1.7
H_I	1600	6.89	74.26	12.51	6.34	3.5	3.0	1.36
H_{II}	1400	8.71	74.81	10.94	5.54	2.5	2.0	1.46
H_{III}	1350	9.30	75.02	10.41	5.27	2.0	2.5	1.48

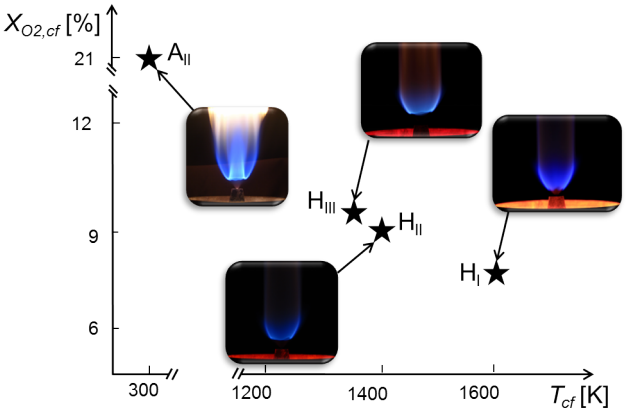

Figure 1.4: Cases in the DSHC database, indicated in $T_{cf} - X_{O_2,cf}$ space.

to H_{III}). The representative boundary conditions are given in Table 1.2. Subscript "cf" refers to the property of coflow, and the last column is the mass flow rate of the liquid fuel at the injector. I is the flow turbulent intensity. One may notice that the coflow temperature and O_2 mole fraction shown in Table 1.2 are slightly different from those reported in [16] and [17]. This is because that the whole profile including the boundary layer was considered for the averaging in [16] and [17], while a representative condition at the plateau of the coflow profile is used in this study. For further details about the DSHC burner and the database, the readers are referred to [15–17].

Figure 1.4 shows the position of the aforementioned four cases in the $T_{cf} - X_{O_2,cf}$ space, and the flame pictures of each case. It is observed that the appearance of the conventional and MILD spray combustion are very different, different MILD cases also show different features. Accurate prediction and understanding of underlying physics of these flames will be pursued throughout this thesis.

1.5. OUTLINE OF THE THESIS

With the focus of development and validation of predictive modeling approaches for spray combustion, especially those under MILD combustion conditions, this thesis is structured as following in four parts: introduction, theory, applications and conclusions.

The current chapter, Chapter 1, introduces some background information of this research, clarifies the motivation and objectives, and draws an overall picture of the studies that are conducted in this thesis, including the software used and the validation database.

The second part, including Chapters 2 and 3, explains the theories that are involved in the modeling of turbulent spray combustion, for both gas phase and the spray. All the modeling approaches that will be used later on are presented in these two chapters. The purpose is to put all model components and possibilities in a complete framework, which can hopefully help understanding of the subsequent content in this thesis.

The third part, containing Chapters 4 to 9, is the application of the theories to model of the chosen target flames, and is also the main body of this thesis. The content of these chapters follows the following storyline: first, the development and test of different modeling approaches based on a single test case. Second, the application of the established best combination of models to a wide range of test cases in order the check its ability on trend capturing. And third, to apply this validated modeling approach to other new cases in order to gain deeper insight on the involved processes.

Chapter 4 reports the initial modeling attempts on the DSHC flame with commercial software ANSYS Fluent®. Within this study, existing models have been employed in their standard form. This study helps on the initial accumulation of knowledge on the numerical simulation of the target flame.

Based on the knowledge gained and shortcomings identified in the study of Chapter 4, a next step was taken to improve the predictive power of the numerical models in Chapter 5. This includes, on one hand, the replacement of simple models with more sophisticated candidates, for example, use of Flamelet Generated Manifolds (FGM) model instead of Steady Flamelet Model (SFM), and use of transported PDF/Reynolds Stresses model instead of presumed PDF/$k-\epsilon$ model, etc. And on the other hand, the use of different computational platforms — in-house code "PDFD". It is worth to mention that in

this chapter we perform a dilute spray simulation, in which the dense region is ignored. Significant improvements in the simulation results have been achieved by these measures. However, some limitations have again been identified. For example, the use of adiabatic FGM table over-predicts the gas phase temperature. And the 2D steady simulation prevents the possibility of studying the flame ignition and stabilization. A logic next step is to perform Large Eddy Simulation (LES) to study these dynamic processes.

The open source Code OpenFOAM® has been chosen to be the platform for further model development. Due to the absence of the desired combustion model — FGM — in the original OpenFOAM® release, the study in Chapter 6 has been dedicated to the implementation and validation of FGM model into OpenFOAM®, and its use for LES studies. As a first step validation, a lifted gaseous flame, which shares many common features with the DSHC flames has been studied in this chapter. In order to obtain a better and more generally applicable prediction, some dynamic procedures have been developed to determine model constants that have to be prescribed otherwise. These dynamic procedures were shown to have strong influence on the results.

After the model has been implemented and validated, it was then applied to the chosen spray combustion test case in Chapter 7. In this chapter, we perform LES for the test case, incorporating also the dense region. A new droplet injection model, and a new non-adiabatic FGM lookup procedure have been developed and validated. Many different options for several model components have been compared, for example, different methods for FGM table generation. Based on these efforts, satisfactory results were obtained.

Chapter 8 and 9 are further applications of the modeling approach developed in Chapter 7. Chapter 8 checks whether this approach can be applied to other hot coflow cases or not. And the answer was positive both qualitatively and quantitatively. Chapter 9 further extends the application also to the cold coflow case (A_{II}). Again, satisfactory results were obtained, and the mechanism of the different flame structures was unveiled.

In the last part, Chapter 10, the main conclusions and findings of this study are summarized, suggestions and recommendations have been made for future studies.

REFERENCES

[1] J. Randers, *2052: A global forecast for the next forty years* (Chelsea Green Publishing, 2012).

[2] J. Hansen, R. Ruedy, R. Sato, and K. Lo, *Global surface temperature change,* Reviews of Geophsics **48**, 1 (2010).

[3] J. A. Wünning and J. G. Wünning, *Flameless oxidation to reduce thermal no-formation,* Progress in Energy and Combustion Science **23**, 81 (1997).

[4] I. Nakamachi, K. Yasuzawa, T. Miyahara, and T. Nagata, *Apparatus or method for carrying out combustion in a furnace,* (1990), US Patent 4,945,841.

[5] A. Cavaliere and M. de Joannon, *Mild Combustion,* Progress in Energy and Combustion Science **30**, 329 (2004).

[6] A. Sepman, S. Abtahizadeh, A. Mokhov, J. van Oijen, H. Levinsky, and L. de Goey, *Numerical and experimental studies of the NO formation in laminar coflow diffusion flames on their transition to MILD combustion regime,* Combustion and Flame **160**, 1364 (2013).

[7] P. Li, J. Mi, B. B. Dally, F. Wang, L. Wang, Z. Liu, S. Chen, and C. Zheng, *Progress and recent trend in MILD combustion,* Science China Technological Sciences **54**, 255 (2011).

[8] A. G. Rao and Y. Levy, *A new combustion methodology for low emission gas turbine engines,* in *8th HiTAC conference* (2010).

[9] F. Christo and B. Dally, *Modeling turbulent reacting jets issuing into a hot and diluted coflow,* Combustion and Flame **142**, 117 (2005).

[10] E.-S. Cho, B. Danon, W. de Jong, and D. Roekaerts, *Behavior of a 300kWth regenerative multi-burner flameless oxidation furnace,* Applied Energy **88**, 4952 (2011).

[11] M. Sánchez, F. Cadavid, and A. Amell, *Experimental evaluation of a 20kW oxygen enhanced self-regenerative burner operated in flameless combustion mode,* Applied Energy **111**, 240 (2013).

[12] R. Weber, J. P. Smart, and W. V. Kamp, *On the (MILD) combustion of gaseous, liquid, and solid fuels in high temperature preheated air,* Proceedings of the Combustion Institute **30**, 2623 (2005).

[13] M. Derudi and R. Rota, *Experimental study of the mild combustion of liquid hydrocarbons,* Proceedings of the Combustion Institute **33**, 3325 (2011).

[14] J. Ye, P. R. Medwell, E. Varea, S. Kruse, B. B. Dally, and H. G. Pitsch, *An experimental study on MILD combustion of prevaporised liquid fuels,* Applied Energy **151**, 93 (2015).

[15] H. Correia Rodrigues, *Spray combustion in moderate and intense low-oxygen conditions - An experimental study*, Ph.D. thesis, Delft University of Technology (2015).

[16] H. Correia Rodrigues, M. J. Tummers, E. H. van Veen, and D. Roekaerts, *Spray flame structure in conventional and hot-diluted combustion regime,* Combustion and Flame **162**, 759 (2015).

[17] H. Correia Rodrigues, M. Tummers, E. van Veen, and D. Roekaerts, *Effects of coflow temperature and composition on ethanol spray flames in hot-diluted coflow,* International Journal of Heat and Fluid Flow **51**, 309 (2015).

[18] E. Gutheil, *Issues in Computational Studies of Turbulent Spray Combustion,* in *Experiments and Numerical Simulations of Diluted Spray Turbulent Combustion*, edited by B. Merci, D. Roekaerts, and A. Sadiki (Springer, 2011) pp. 1–39.

[19] P. Jenny, D. Roekaerts, and N. Beishuizen, *Modeling of turbulent dilute spray combustion,* Progress in Energy and Combustion Science **38**, 846 (2012).

[20] OpenFOAM, *OpenFOAM: The open source CFD Toolbox,* (2015).

I

THEORY

2

THEORY: GAS PHASE

In this chapter, the gas phase theories and models that will be used in this thesis are explained.

2.1. GOVERNING EQUATIONS

The theory in this chapter partially follows Refs. [1–3]. The Einstein summation convention is used throughout this thesis. Repeated indices imply summation, for example, $\tau_{ij}u_i = \tau_{1j}u_1 + \tau_{2j}u_2 + \tau_{3j}u_3$.

Under the continuum hypothesis, the governing equations of dispersed two-phase flow can be derived by considering mass, momentum and energy balance over a infinitesimal volume.

Mass conservation or continuity equation:

$$\frac{\partial \rho}{\partial t} + \frac{\partial \rho u_j}{x_j} = S^e_\rho, \tag{2.1}$$

Momentum conservation equations:

$$\frac{\partial \rho u_i}{\partial t} + \frac{\partial \left(\rho u_i u_j\right)}{\partial x_j} = -\frac{\partial p}{\partial x_i} + \frac{\partial \tau_{ij}}{\partial x_j} + S_{M,i} + S^e_{u_i}, \tag{2.2}$$

Species conservation equation:

$$\frac{\partial \rho Y_k}{\partial t} + \frac{\partial \left(\rho Y_k u_j\right)}{\partial x_j} = \frac{\partial}{\partial x_j}\left(-\rho V_{k,j} Y_k\right) + \dot{\omega}_k + S^e_{Y_k} \quad k = 1, ..., N, \tag{2.3}$$

Enthalpy (sensible + chemical):

$$\frac{\partial \rho h}{\partial t} + \frac{\partial \left(\rho h u_j\right)}{\partial x_j} = \frac{Dp}{Dt} - \frac{\partial q_j}{\partial x_j} + \tau_{ij}\frac{\partial u_i}{\partial x_j} + S_H + S^e_H. \tag{2.4}$$

The S terms in each equations represent the non-combustion caused source term, for example body force or radiation. The superscript “e" denotes the source term due to droplet evaporation.

For Newtonian fluid flow, the viscous stress component τ_{ij} can be related to strain rate as:

$$\tau_{ij} = 2\mu S_{ij} - \frac{2}{3}\mu\delta_{ij}S_{kk} = 2\mu\left(S_{ij} - \frac{1}{3}\delta_{ij}S_{kk}\right) = 2\mu S^D_{ij}, \tag{2.5}$$

where

$$S_{ij} = \frac{1}{2}\left(\frac{\partial u_i}{\partial x_j} + \frac{\partial u_j}{\partial x_i}\right), \tag{2.6}$$

is the strain rate tensor, and μ is the molecular viscosity. $S^D_{ij} = \left(S_{ij} - \frac{1}{3}\delta_{ij}S_{kk}\right)$ is the deviatoric part of the strain rate tensor.

The molecular diffusion term $V_{k,j}Y_k$ can be approximated either by Fick's law or Hirschfelder and Curtiss approximation [3]. If mixture contains only two species ($N = 2$), or if all binary diffusion between two species are equal ($D_{ij} = D$), Fick's law can be used to compute the molecular diffusion:

$$V_{k,j}Y_k = -D\frac{\partial Y_k}{\partial x_j}. \tag{2.7}$$

If more detailed description of transport is required, Hirschfelder and Curtiss approximation is commonly used, where $D_{k,i}$ is the binary diffusion coefficient of species k into i.

$$V_{k,j}Y_k = -D_k \frac{\partial Y_k}{\partial x_j} \quad \text{with} \quad D_k = \frac{1-Y_k}{\sum_{i\neq k} X_i / D_{k,i}}. \tag{2.8}$$

Fourier's law of heat conduction relates the heat flux to the local temperature gradient:

$$q_j = -\lambda \frac{\partial T}{\partial x_j}, \tag{2.9}$$

where λ is the thermal conductivity.

Relationships between the thermodynamic variables can be obtained through the assumption of thermodynamic equilibrium. Equation of state relates other variables to two state variables. For example, if ρ and T are used as state variables:

$$p = p(\rho, T). \tag{2.10}$$

For ideal gas:

$$p = \rho R T \quad , \tag{2.11}$$

where $R = R_u/W$ is the gas constant, and $R_u = 8.314\ J/(K \cdot mol)$ the universal gas constant.

Direct solving of the discretized governing equations using high order accuracy numerical schemes is referred to as Direct Numerical Simulation (DNS). Since all the scales are directly resolved in DNS, its results provide valuable insight into the physical processes and can be used to develop and validate new approximate models. However, due to the fact that the spatial and temporal scales involved in practical combustion devices span a very wide range, and enormous computational resources are required to resolve all these scales, DNS is still limited to academic research. For industrial application, the Reynolds-Averaged Navier Stokes (RANS) simulation, in which all the behaviors of turbulence are emulated with certain models, has for long been the workhorse. In between these two extremes lies the Large Eddy Simulation (LES). In LES, the large, energy containing scales are resolved, and the small scales are modeled. The research in this thesis focuses on RANS and LES.

2.2. REYNOLDS AVERAGED NAVIER-STOKES EQUATIONS

2.2.1. REYNOLDS AND FAVRE AVERAGE

Any variables in the turbulent field can be decomposed in an average component and a fluctuating component. The time or Reynolds average reads:

$$\phi = \overline{\phi} + \phi', \tag{2.12}$$

$$\overline{\phi} = \frac{1}{\Delta t}\int_0^{\Delta t} \phi(t)\, dt. \tag{2.13}$$

For variable density flow, e.g. combustion, density-weighted or Favre average is preferred:

$$\phi = \tilde{\phi} + \phi'', \tag{2.14}$$

$$\tilde{\phi} = \frac{\int_0^{\Delta t} \rho(t)\phi(t)\,dt}{\int_0^{\Delta t} \rho(t)\,dt} = \frac{\overline{\rho\Phi}}{\bar{\rho}}. \tag{2.15}$$

Variance and root mean square (r.m.s.) can be defined as follows:

$$\overline{\phi'^2} = \frac{1}{\Delta t}\int_0^{\Delta t} \left(\phi'(t)\right)^2 dt \quad \text{or} \quad \widetilde{\phi''^2} = \frac{\overline{\rho\phi''^2}}{\bar{\rho}}, \tag{2.16}$$

$$\phi_{rms,R} = \sqrt{\overline{\phi'^2}} = \left(\frac{1}{\Delta t}\int_0^{\Delta t} \left(\phi'(t)\right)^2 dt\right)^{\frac{1}{2}} \quad \text{or} \quad \phi_{rms,F} = \sqrt{\widetilde{\phi''^2}}. \tag{2.17}$$

From now on, the Favre averaged variance, $\widetilde{\phi''^2}$, and rms, $\phi_{rms,F}$ will be used unless explicitly indicated otherwise.

Note that the averaging operation, by definition, is an integration. Therefore, the order of time averaging and summation, further integration and/or differential can be swapped or commuted, the so-called commutative property. Applying Reynolds averaging Eq. (2.13) to Eqs. (2.1) to (2.4), and make use of Favre averaging, Eq. (2.15), the RANS equations can be derived:

$$\frac{\partial\bar{\rho}}{\partial t} + \frac{\partial\bar{\rho}\tilde{u}_i}{\partial x_i} = \bar{S}_\rho, \tag{2.18}$$

$$\frac{\partial\bar{\rho}\tilde{u}_i}{\partial t} + \frac{\partial\left(\bar{\rho}\tilde{u}_i\tilde{u}_j\right)}{\partial x_j} = -\frac{\partial\bar{p}}{\partial x_i} + \frac{\partial}{\partial x_j}\left(\bar{\tau}_{ij} - \bar{\rho}\widetilde{u_i''u_j''}\right) + \bar{S}_{u_i}, \tag{2.19}$$

$$\frac{\partial\bar{\rho}\tilde{Y}_k}{\partial t} + \frac{\partial\left(\bar{\rho}\tilde{Y}_k\tilde{u}_j\right)}{\partial x_j} = \frac{\partial}{\partial x_j}\left(-\overline{V_{k,j}Y_k} - \bar{\rho}\widetilde{u_j''Y_k''}\right) + \overline{\dot{\omega}_k} + \bar{S}^e_{Y_k} \quad k = 1, N, \tag{2.20}$$

$$\frac{\partial\bar{\rho}\tilde{h}}{\partial t} + \frac{\partial\left(\bar{\rho}\tilde{h}\tilde{u}_j\right)}{\partial x_j} = \frac{D\bar{p}}{Dt} - \frac{\partial}{\partial x_j}\left(\bar{q}_j + \bar{\rho}\widetilde{u_j''h''}\right) + \overline{\tau_{ij}\frac{\partial u_i}{\partial x_j}} + \bar{S}_H + \bar{S}^e_H. \tag{2.21}$$

In the averaged enthalpy equation, the viscous heating source term, $\Phi = \overline{\tau_{ij}\frac{\partial u_i}{\partial x_j}}$, is much smaller than the heat released by combustion and therefore can be neglected. Then the remaining unclosed in the RANS equations are:

- **Reynolds stresses**: $R_{ij} = \bar{\rho}\widetilde{u_i''u_j''}$,
- **Turbulent fluxes**, $\bar{\rho}\widetilde{u_j''Y_k''}$, and $\bar{\rho}\widetilde{u_j''h''}$,
- **Averaged reaction source term**: $\overline{\dot{\omega}_k}$.

In order to solve the averaged governing equations, Eqs. (2.18) to (2.21), these terms have to be evaluated, models that are used to close R_{ij} and $\overline{\dot{\omega}_k}$ are referred to as turbulence and combustion models, respectively.

2.2.2. THE TURBULENT (EDDY) VISCOSITY HYPOTHESIS

The Reynolds stresses R_{ij} are normally modeled using the turbulent (eddy) viscosity hypothesis:

$$\overline{\rho u_i'' u_j''} = \bar{\rho}\widetilde{u_i'' u_j''} \equiv -\mu_t\left(\frac{\partial \tilde{u}_i}{\partial x_j} + \frac{\partial \tilde{u}_j}{\partial x_i} - \frac{2}{3}\frac{\partial \tilde{u}_k}{\partial x_k}\delta_{ij}\right) + \frac{2}{3}\bar{\rho}k\delta_{ij} = -2\mu_t \tilde{S}_{ij}^D + \frac{2}{3}\bar{\rho}k\delta_{ij}, \quad (2.22)$$

where μ_t is the turbulent (dynamic) viscosity, which still needs to be closed with further models. And the turbulent kinetic energy k (per unit mass) is defined as:

$$k = \frac{1}{2}\sum_{i=1}^{3}\widetilde{u_{(i)}'' u_{(i)}''}, \quad (2.23)$$

parenthesis around the index denote that the Einstein convention is not used here.

The second term of Eq. (2.22) ensures that the formula gives the correct result for the normal Reynolds stresses ($\rho\widetilde{u_{(i)}'' u_{(i)}''}$). If this term is omitted, the sum of normal stresses $\bar{\rho}\sum_{i=1}^{3}\widetilde{u_{(i)}'' u_{(i)}''} = 0$. However, it should be $\bar{\rho}\sum_{i=1}^{3}\widetilde{u_{(i)}'' u_{(i)}''} = 2\bar{\rho}k$, according to Eq. (2.23). An equal third is allocated to each normal stress component to ensure their sum always has its physically correct value. This implies an isotropic assumption for the normal Reynolds stress [2].

2.2.3. TURBULENCE MODELS - CLOSURE OF μ_t

Based on the dimensional analysis, the turbulent (kinematic) viscosity ν_t has dimension of m^2/s. It can therefore be expressed as a product of turbulent velocity scale v_t (m/s) and a turbulent length scale l_t (m). A common expression of μ_t reads:

$$\mu_t = \bar{\rho}\nu_t = C\bar{\rho}v_t l_t, \quad (2.24)$$

where C is a dimensionless constant. Models that are used to calculate (specify) the turbulent velocity scale v_t and turbulent length scale l_t together with the corresponding constant C are called eddy viscosity turbulence models. Based on the extra transport equations that have to be solved in order to determine the aforementioned properties, turbulence models are classified as zero, one or two equations models, as summarized in Table 2.1.

The zero equation mixing length model tries to find a representative single value of turbulent velocity and length scales for the whole problem of interest. Thus is expected to perform well only in very special and simple situations. On the other hand, one or two equation models are proposed to calculate the turbulent velocity and length scales from properties that are obtained from extra transport equation(s). In this category of models, the $k-\epsilon$ model is used in our study. So only the $k-\epsilon$ model will be discussed in detail.

Table 2.1: Eddy viscosity turbulence models

No. of extra transport equations	Model name
Zero	Mixing length model
One	Spalart-Allmaras model
Two	$k-\epsilon$ model
	$k-\omega$ model

THE $k-\epsilon$ MODEL

In the standard $k-\epsilon$ model [4], the turbulent velocity scale v_t and length scale l_t respectively can be expressed by the turbulent kinetic energy, k, and its dissipation rate, ϵ, as follows:

$$v_t = k^{1/2} \quad \text{and} \quad l_t = \frac{k^{3/2}}{\epsilon}. \tag{2.25}$$

The eddy viscosity can be specified as:

$$\mu_t = C\rho v_t l_t = \rho C_\mu \frac{k^2}{\epsilon}, \tag{2.26}$$

where C_μ is a dimensionless constant.

The k and ϵ are respectively calculated by their transport equations, which are obtained based on the best understanding of the relevant processes causing changes to these variables.

$$\frac{\partial(\rho k)}{\partial t} + \frac{\partial}{\partial x_j}(\rho k \tilde{u}_j) = \frac{\partial}{\partial x_j}\left[\left(\mu + \frac{\mu_t}{\sigma_k}\right)\frac{\partial k}{\partial x_j}\right] + 2\mu_t S_{ij}\cdot S_{ij} - \rho\epsilon + S_k^e, \tag{2.27}$$

$$\frac{\partial(\rho\epsilon)}{\partial t} + \frac{\partial}{\partial x_j}(\rho\epsilon \tilde{u}_j) = \frac{\partial}{\partial x_j}\left(\frac{\mu_t}{\sigma_\epsilon}\frac{\partial\epsilon}{\partial x_j}\right) + C_{1\epsilon}\frac{\epsilon}{k}2\mu_t S_{ij}\cdot S_{ij} - C_{2\epsilon}\rho\frac{\epsilon^2}{k} + S_\epsilon^e, \tag{2.28}$$

where S_k^e and S_ϵ^e are the source term due to the presence of spray droplets, the so called two-way coupling.

The equations contain five adjustable constants: C_μ, σ_k, σ_ϵ, $C_{1\epsilon}$ and $C_{2\epsilon}$, having the following default values [4]:

$$C_\mu = 0.09, \quad \sigma_k = 1.00, \quad \sigma_\epsilon = 1.30, \quad C_{1\epsilon} = 1.44, \quad C_{2\epsilon} = 1.92. \tag{2.29}$$

The Reynolds stresses can be computed using the Boussinesq relationship:

$$-\tilde{\rho}\widetilde{u_i'' u_j''} = -2\mu_t \tilde{S}_{ij}^D + \frac{2}{3}\tilde{\rho}k\delta_{ij}. \tag{2.30}$$

2.2.4. REYNOLDS STRESS TRANSPORT MODELS

The turbulence models based on the turbulent viscosity hypothesis imply that the normal Reynolds stresses are isotropic. This assumption fails in many complex flows, for example, flows with strong swirl, where it leads to inaccurate predictions. In **Reynolds**

stress equation models (also known in the literature as second-order or second-moment closure models) transport equations for the Reynolds stresses themselves are derived and solved [5, 6]. Taking into account symmetry, $R_{ij} = R_{ji}$, that means six transport equations for each Reynolds stress component, R_{ij}, and one for for the rate of dissipation of turbulent knetic energy ϵ. In total, seven addition transport equations. Therefore the RSM is computationally more expensive than the two equation models.

REYNOLDS STRESSES TRANSPORT EQUATIONS

To simplify the notation, $R_{ij} = \widetilde{u_i'' u_j''}$ (without $\bar{\rho}$) will be used in the transport equations of Reynolds stresses.

$$\frac{\partial}{\partial t}\left(\bar{\rho} R_{ij}\right) + \frac{\partial}{\partial x_k}\left(\bar{\rho} R_{ij} \tilde{u}_k\right) = D_{T,ij} + D_{L,ij} + P_{ij} + \Pi_{ij} + \epsilon_{ij} + T_{ij}, \tag{2.31}$$

with convection term C_{ij}:

$$C_{ij} = \frac{\partial}{\partial x_k}\left(\bar{\rho} R_{ij} \tilde{u}_k\right), \tag{2.32}$$

the turbulent diffusion term:

$$D_{T,ij} = -\frac{\partial}{\partial x_k}\left[\bar{\rho}\widetilde{u_i'' u_j'' u_k''} + \overline{p'\left(\delta_{kj} u_i'' + \delta_{ik} u_j''\right)}\right], \tag{2.33}$$

the molecular diffusion term:

$$D_{L,ij} = \frac{\partial}{\partial x_k}\left[\mu \frac{\partial}{\partial x_k} R_{ij}\right], \tag{2.34}$$

the production term P_{ij}:

$$P_{ij} = -\left(\bar{\rho} R_{ik} \frac{\partial \tilde{u}_j}{\partial x_k} + \bar{\rho} R_{jk} \frac{\partial \tilde{u}_i}{\partial x_k}\right), \tag{2.35}$$

the pressure strain term (correlation between fluctuating pressure and fluctuating strain):

$$\Pi_{ij} = \overline{p'\left(\frac{\partial u_i''}{\partial x_j} + \frac{\partial u_j''}{\partial x_i}\right)}, \tag{2.36}$$

the dissipation term ϵ_{ij}:

$$\epsilon_{ij} = -2\mu \overline{\frac{\partial u_i''}{\partial x_k} \frac{\partial u_j''}{\partial x_k}}, \tag{2.37}$$

the production by system rotation term:

$$M_{ij} = -2\bar{\rho}\Omega_k\left(R_{jm}\epsilon_{ikm} + R_{im}\epsilon_{jkm}\right), \tag{2.38}$$

where Ω_k is the system rotation rate (angular velocity), and ϵ_{ijk} is the third rank alternating symbol or the Levi-Civita symbol.

Within these terms, the C_{ij}, $D_{L,ij}$, P_{ij} and M_{ij} are closed. However, $D_{T,ij}$, Π_{ij} and ϵ_{ij} need to be modeled to close the Reynolds stresses transport equations.

CLOSURE STRATEGY

The turbulent diffusion term $D_{T,ij}$ can be modeled by the generalized gradient-diffusion model of Daly and Harlow [7]:

$$D_{T,ij} = C_s \frac{\partial}{\partial x_k}\left(\bar{\rho}\frac{kR_{k,l}}{\epsilon}\frac{\partial R_{ij}}{\partial_{x_l}}\right). \tag{2.39}$$

However, this equation can result in numerical instabilities, so it has been simplified to [8]:

$$D_{T,ij} = \frac{\partial}{\partial x_k}\left(\frac{\mu_t}{\sigma_k}\frac{\partial R_{ij}}{\partial x_k}\right). \tag{2.40}$$

The turbulent viscosity, μ_t, is computed by Eq. (2.26).

The Dissipation term, ϵ_{ij}, is modeled as

$$\epsilon_{ij} = -\frac{2}{3}\delta_{ij}\left(\bar{\rho}\epsilon + Y_M\right), \tag{2.41}$$

where $Y_M = 2\rho\epsilon M_t^2$ is a an additional "dilatation dissipation" term. The turbulent Mach number in this term is defined as

$$M_t = \sqrt{k/a^2}, \tag{2.42}$$

where $a = \sqrt{\gamma RT}$ is the speed of sound. The ϵ is computed with the transport equation similar to that in the standard $k-\epsilon$ model Eq. (2.28).

Modeling of pressure-strain correlation, Π_{ij}, is an important part in the RSM. There have been many models developed for the closure of this term, such as the Rotta's model, the isotropization of production model (IPM), the Launder, Reece and Rodi model (LRR), the Shih-Lumley (SL) model and the Speziale, Sarkar and Gatski model (SSG), see [6] for more details about these models. A general form of modeled Π_{ij} can be rewritten as following [9]:

$$\Pi^*_{ij} = \epsilon \sum_{n=1}^{8} A^{(n)} T^n_{ij},, \tag{2.43}$$

where $A^{(n)}$ are scalar coefficients and $T^{(n)}_{ij}$ are the nondimensional, symmetric, deviatoric tensors. They are related to the anisotropy tensor,

$$b_{ij} \equiv \frac{\widetilde{u_i u_j}}{u_l u_l} - \frac{1}{3}\delta_{ij},, \tag{2.44}$$

the normalized strain rate,

$$S_{ij} \equiv \frac{1}{2}\frac{k}{\epsilon}\left(\frac{\partial \tilde{u}_i}{\partial x_j} + \frac{\partial \tilde{u}_j}{\partial x_i}\right), \tag{2.45}$$

and the rotation tensors,

$$W_{ij} \equiv \frac{1}{2}\frac{k}{\epsilon}\left(\frac{\partial \tilde{u}_i}{\partial x_j} - \frac{\partial \tilde{u}_j}{\partial x_i}\right). \tag{2.46}$$

Certain correspondence between modeling of the pressure-strain correlation and the Langevin model in PDF method exists, more details of pressure-strain correlation modeling will be given in section 2.6.2.

2.3. LARGE EDDY SIMULATION

In turbulence flows, the larger eddies are dictated by the geometry, and are more anisotropic. On the other hand, the smaller eddies are nearly anisotropic and have a near universal behavior. The different behavior of large and small eddies prevent the development of general-purpose RANS based models, in which all the turbulent scales must be described by a single turbulence model. In LES, the problem dependent large eddies are directly resolved with time-dependent solution. On the other hand, the universal behavior of smaller eddies is hopefully easier to be modeled.

A spatial filtering is operated on the time-dependent flow equations. The information on the turbulent structure larger than the filter width is resolved. The information of the smaller structures is not resolved by these "filtered equations" and remaining to be modeled. The models to describe the effects of unresolved smaller eddies on the resolved larger eddies are called sub-grid scale (SGS) models.

2.3.1. FILTER FUNCTION

In LES, the separation of large and small turbulence structure is carried out by means of a **filter function** $F\left(\mathbf{x},\mathbf{x}^{'},\Delta\right)$ as follows:

$$\bar{\phi}(\mathbf{x},t) \equiv \int_{-\infty}^{\infty}\int_{-\infty}^{\infty}\int_{-\infty}^{\infty} \phi\left(\mathbf{x}^{'},\mathbf{t}\right) F\left(\mathbf{x},\mathbf{x}^{'},\Delta\right) dx_1^{'} dx_2^{'} dx_3^{'}, \tag{2.47}$$

where $\bar{\phi}(\mathbf{x},t)$ is filtered function, $\phi(\mathbf{x},t)$ the original (unfiltered) function and Δ the filter width or cut-off width.

For variable density flow, a mass-weighted Favre filtering is introduced:

$$\tilde{\phi}(\mathbf{x},t) \equiv \frac{\overline{\rho\phi(\mathbf{x},t)}}{\bar{\rho}}. \tag{2.48}$$

The commonly used filtering functions are:

- Top-hat or box filter:

$$F\left(\mathbf{x},\mathbf{x}^{'},\Delta\right) = \begin{cases} 1/\Delta^3 & |\mathbf{x}-\mathbf{x}^{'}| \le \Delta/2 \\ 0 & |\mathbf{x}-\mathbf{x}^{'}| \ge \Delta/2. \end{cases} \tag{2.49a}$$

- Gaussian filter:

$$F\left(\mathbf{x},\mathbf{x}^{'},\Delta\right) = \left(\frac{\gamma}{\pi\Delta^2}\right)^{3/2} exp\left(-\gamma\frac{|\mathbf{x}-\mathbf{x}^{'}|^2}{\Delta^2}\right), \tag{2.49b}$$

typical value for parameter $\gamma = 6$.

- Spectral cutoff:

$$F\left(\mathbf{x},\mathbf{x}^{'},\Delta\right) = \prod_{i=1}^{3} \frac{sin\left[(x_i - x_i^{'})/\Delta\right]}{(x_i - x_i^{'})}. \tag{2.49c}$$

The box filter is used in finite volume implementations of LES. In CFD simulations with finite volume method (FVM), e.g. OpenFOAM, the most common choice of the filter width is the cube root of the grid cell volume, e.g. for a hexahedral grid,

$$\Delta = \sqrt[3]{\Delta x \Delta y \Delta z}. \tag{2.50}$$

If the cube root cut-off width is used, the aspect ratio of the computational grid should not be too large, otherwise the cut-off width is mainly determined by the max of Δx, Δy and Δz, therefore it causes waste of the grid resolution in other directions.

2.3.2. FILTERED NAVIER-STOKES EQUATIONS

Applying the filtering operation (2.47) to Eqs. (2.1) to (2.4), the filtered Navier-Stokes equations are as following (same filtering function is used through out the computational domain, i.e. assuming F is independent of position $\mathbf{x}$):

$$\frac{\partial \bar{\rho}}{\partial t} + \frac{\partial \bar{\rho}\tilde{u}_i}{\partial x_i} = \bar{S}_\rho, \tag{2.51}$$

$$\frac{\partial \bar{\rho}\tilde{u}_i}{\partial t} + \frac{\partial \left(\bar{\rho}\tilde{u}_i\tilde{u}_j\right)}{\partial x_j} = -\frac{\partial \bar{p}}{\partial x_i} + \frac{\partial}{\partial x_j}\left(\bar{\tau}_{ij} - \bar{\rho}\widetilde{u_i'' u_j''}\right) + \bar{S}_{u_i}, \tag{2.52}$$

$$\frac{\partial \bar{\rho}\tilde{Y}_k}{\partial t} + \frac{\partial \left(\bar{\rho}\tilde{Y}_k\tilde{u}_j\right)}{\partial x_j} = \frac{\partial}{\partial x_j}\left(-\overline{V_{k,j}Y_k} - \bar{\rho}\widetilde{u_j'' Y_k''}\right) + \overline{\dot{\omega}_k} + \bar{S}^e_{Y_k} \quad k = 1, N, \tag{2.53}$$

$$\frac{\partial \bar{\rho}\tilde{h}}{\partial t} + \frac{\partial \left(\bar{\rho}\tilde{h}\tilde{u}_j\right)}{\partial x_j} = \frac{D\bar{p}}{Dt} - \frac{\partial}{\partial x_j}\left(\bar{q}_j + \bar{\rho}\widetilde{u_j'' h''}\right) + \overline{\tau_{ij}\frac{\partial u_i}{\partial x_j}} + \bar{S}_H + \bar{S}^e_H. \tag{2.54}$$

These equations have the same form as the RANS equations (Eqs. (2.18) to (2.21)). However, the notations of $\bar{*}$ and $\tilde{*}$ are different. They stand for time or ensemble average in RANS, and spatial average at the SGS scale in LES. In this set of equations, the SGS stresses, $\bar{\rho}\widetilde{u_i'' u_j''}$, the SGS scalar fluxes, $\bar{\rho}\widetilde{u_j'' Y_k''}$, $\bar{\rho}\widetilde{u_j'' h''}$, and the filtered source terms, $\overline{\dot{\omega}_k}$, are unclosed and need to be modeled.

2.3.3. CLOSURE OF SGS STRESSES

Similar to the closure of Reynolds stresses in RANS, the SGS stresses in LES can be modeled based on a turbulent viscosity hypothesis:

$$R_{ij} = \bar{\rho}\left(\widetilde{u_i u_j} - \tilde{u}_i\tilde{u}_j\right) = -2\mu_{sgs}\tilde{S}^D_{ij} + \frac{2}{3}\bar{\rho}k\delta_{ij}, \tag{2.55}$$

where μ_{SGS} is the SGS viscosity. k is the SGS kinetic energy defined by

$$\bar{\rho}k = \frac{1}{2}R_{kk} = \frac{1}{2}\bar{\rho}\left(\widetilde{u_k u_k} - \tilde{u}_k\tilde{u}_k\right). \tag{2.56}$$

The SGS viscosity μ_{sgs} and SGS kinetic energy k have to be modeled. Yoshizawa's formula is often used for modeling of the SGS kinetic energy [10]:

$$R_{kk} = 2\bar{\rho}k = C_I 2\bar{\rho}\Delta^2|\tilde{S}|^2, \tag{2.57}$$

where C_I is the model constant, $|\tilde{S}| = \left(2\tilde{S}_{ij}\tilde{S}_{ij}\right)^{1/2}$ is the magnitude of the strain rate tensor.

Erlebacher et al [11] pointed out that for turbulent Mach numbers $M_t < 0.4$ this term is negligible. This term can also be incorporated into a modified pressure $P = p + \frac{2}{3}k$. This leads to the a modified equation of state, which takes the form [12]:

$$P = \bar{\rho}R\tilde{v} + \frac{3\gamma - 5}{6}\tau_{kk}, \tag{2.58}$$

where $v = \bar{T} - \frac{1}{2C_v\bar{\rho}}\tau_{kk}$ is the modified temperature, γ is the specific heat ratio. This expression shows that with typical gas properties ($\gamma = 1.4$, $c_v = 718 J/Kg{\cdot}K$, $\rho = 1.25 Kg/m^3$ for air at room temperature) the second term is indeed negligible , unless τ_{kk} is very large. This means that the SGS stress trace can be incorporated in the pressure with no modification to the equation of state [13], this approach is adopted in the current study.

SMAGORINSKY MODEL

The Smagorinsky SGS model assumes that the kinematic SGS viscosity ν_{SGS} (m^2/s) can be described in terms of one length (Δ) and one velocity ($\Delta|\tilde{S}|$) scale. Thus, the SGS viscosity is evaluated as follows:

$$\mu_{SGS} = \bar{\rho}\left(C_S\Delta\right)^2|\tilde{S}| = \bar{\rho}\left(C_S\Delta\right)^2\left|\sqrt{2\tilde{S}_{ij}\tilde{S}_{ij}}\right|. \tag{2.59}$$

The model constant C_S is case dependent, ranging from $C_S \approx 0.1$ for strongly anisotropic turbulence [2] to $C_S \approx 0.2$ homogeneous isotropic flow [3].

DYNAMIC SMAGORINSKY MODEL

The main drawback of the Smagorinsky model is that there is no single value of model constant C_s that is universally applicable to a wide range of flows. Germano et al [14] proposed a procedure to dynamically calculate the model constant based on an algebraic identity between the subgrid-scale stresses arising from filtering at two different filter sizes. The basic idea in this model is to apply same SGS stress model at two different scales, and thus to adjust the constant to agree with known information from the resolved field. A test filter G, with filter width $\widehat{\Delta}$ larger than the LES filter (size $\bar{\Delta}$) is introduced.

To simplify the derivation, here we consider the incompressible flow without extra source term. The filtered momentum equation can be rewritten as:

$$\frac{\partial\rho\bar{u}_i}{\partial t} + \frac{\partial\left(\rho\overline{u_iu_j}\right)}{\partial x_j} = -\frac{\partial\bar{p}}{\partial x_i} + \frac{\partial\bar{\tau}_{ji}}{\partial j}. \tag{2.60}$$

Applying the test filter ($\hat{*}$) to the filtered momentum equation, (2.60).

$$\frac{\partial\rho\hat{\bar{u}}_i}{\partial t} + \frac{\partial\left(\rho\hat{\bar{u}}_i\hat{\bar{u}}_j\right)}{\partial x_j} = -\frac{\partial\hat{\bar{p}}}{\partial x_i} + \frac{\partial}{\partial j}\left(\hat{\bar{\sigma}}_{ji} - T_{ij}\right), \tag{2.61}$$

where $T_{ij} = \rho\left(\widehat{\overline{u_iu_j}} - \hat{\bar{u}}_i\hat{\bar{u}}_j\right)$ is the SGS stress at test level. Eq. (2.60) can be rearranged with the SGS stress $\tau_{ij} = \rho\left(\overline{u_iu_j} - \bar{u}_i\bar{u}_j\right)$ as:

$$\frac{\partial\rho\bar{u}_i}{\partial t} + \frac{\partial\left(\rho\bar{u}_i\bar{u}_j\right)}{\partial x_j} = -\frac{\partial\bar{p}}{\partial x_i} + \frac{\partial}{\partial j}\left(\bar{\sigma}_{ji} - \tau_{ij}\right). \tag{2.62}$$

Applying the test filter to Eq. (2.62),

$$\frac{\partial \rho \hat{\bar{u}}_i}{\partial t} + \frac{\partial \left(\rho \hat{\bar{u}}_i \hat{\bar{u}}_j\right)}{\partial x_j} = -\frac{\partial \hat{\bar{p}}}{\partial x_i} + \frac{\partial}{\partial j}\left(\hat{\bar{\sigma}}_{ji} - \hat{\tau}_{ij} - L_{ij}\right), \tag{2.63}$$

where $L_{ij} = \rho\left(\widehat{\bar{u}_i \bar{u}_j} - \hat{\bar{u}}_i \hat{\bar{u}}_j\right)$ is resolved turbulent stress, and can be directly calculated from the resolved velocity field.

Comparing Eq. (2.61) and Eq. (2.63), one obtains the Germano identity:

$$L_{ij} = T_{ij} - \hat{\tau}_{ij}. \tag{2.64}$$

The SGS stress τ_{ij} and SGS stress at test level T_{ij} can both be modeled by Smagorinsky model:

$$R_{ij} - \frac{1}{3}\tau_{kk}\delta_{ij} = -2\rho\left(C_S\overline{\Delta}\right)^2 |\bar{S}|\bar{S}_{ij} = C\alpha_{ij}. \tag{2.65}$$

$$T_{ij} - \frac{1}{3}T_{kk}\delta_{ij} = -2\rho\left(C_S\widehat{\Delta}\right)^2 |\hat{\bar{S}}|\hat{\bar{S}}_{ij} = C\beta_{ij}, \tag{2.66}$$

where $C = C_s^2$ is the constant to be determined, $\alpha_{ij} = -2\rho\overline{\Delta}^2|\bar{S}|\bar{S}_{ij}$ and $\beta_{ij} = -2\rho\widehat{\Delta}^2|\hat{\bar{S}}|\hat{\bar{S}}_{ij}$.

Then the Germano identity is rewritten as:

$$L_{ij} - \frac{1}{3}L_{kk}\delta_{ij} = C\left(\beta_{ij} - \hat{\alpha}_{ij}\right). \tag{2.67}$$

The model constant can, in principle, be determined from the Eq. (2.67).

The dynamic Smagorinsky model has been extended to compressible by Moin et al [15] and Martin et al [13]. In compressible flow, the resolved turbulent stresses are $L_{ij} = \left(\widehat{\overline{\rho u_i \rho u_j}/\bar{\rho}}\right) - \widehat{\overline{\rho u_i}}\,\widehat{\overline{\rho u_j}}/\hat{\bar{\rho}}$, and the subtest stresses are $T_{ij} = \hat{\bar{\rho}}\widetilde{u_i u_j} - \hat{\bar{\rho}}\breve{\tilde{u}}_i\breve{\tilde{u}}_j$ (where $\breve{\tilde{f}} = \widehat{\overline{\rho f}}/\hat{\bar{\rho}}$).

Germano identity for compressible flow has the same form with the incompressible version Eq. (2.67),

$$L_{ij} - \frac{1}{3}L_{kk}\delta_{ij} = CM_{ij}, \tag{2.68}$$

where $M_{ij} = \beta_{ij} - \hat{\alpha}_{ij}$, $\alpha_{ij} = -2\overline{\Delta}^2\bar{\rho}|\tilde{S}_{ij}|\tilde{S}^D_{ij}$ and $\beta_{ij} = -2\widehat{\Delta}^2\hat{\bar{\rho}}|\breve{\tilde{S}}|\breve{\tilde{S}}^D_{ij}$.

Eq. (2.68) is over-determined, because it represents five independent equations for one unknown. The least squares method proposed by Lilly [16] is commonly used to minimize the error. Define Q to be the square of error in Eq. (2.68), i.e.

$$Q = \left(L_{ij} - \frac{1}{3}L_{kk}\delta_{ij} - CM\right). \tag{2.69}$$

Setting $\partial Q/\partial C = 0$, C is evaluated as

$$C = C_s^2 = \frac{\left\langle L^*_{ij}M_{ij}\right\rangle}{\langle M_{kl}M_{kl}\rangle}, \tag{2.70}$$

where $L^*_{ij} = L_{ij} - \frac{1}{3}L_{kk}\delta_{ij}$.

In the original formulation, C is not determined locally but averaged in homogeneous directions or along streamlines following a Lagrangian procedure [3]. In the present study the angle brackets in Eq.(2.70) represents local average over computational volume [13] due to the absence of homogeneous direction in spray jet flames. It is well known that Eq. (2.70) may produce a negative C value, which means negative SGS viscosity. This is interpreted, in some papers, as back-scattering (energy transfer from small scale eddies to large scale eddies). However, the model constant C is bounded to be non-negative in the present study, meaning $\mu_{SGS} \geq 0$.

2.4. TURBULENT/SGS SCALAR FLUXES

In both RANS and LES, the species and energy equations are closed in similar ways. The turbulent species flux or the unresolved species flux, $\bar{\rho}\widetilde{Y_k'' u_j''}$, $\bar{\rho}\left(\widetilde{Y_k u_j} - \tilde{Y}_k \tilde{u}_j\right)$, and the turbulent enthalpy or the unresolved enthalpy flux, $\bar{\rho}\widetilde{h_s'' u_j''}$, $\bar{\rho}\left(\widetilde{h u_j} - \tilde{h}\tilde{u}_j\right)$ are often described using gradient diffusion assumption.

$$\bar{\rho}\widetilde{Y_k'' u_j''} = -\frac{\mu_t}{Sc_t}\frac{\partial \tilde{Y}_k}{\partial x_i} \quad \text{or} \quad \bar{\rho}\left(\widetilde{Y_k u_j} - \tilde{Y}_k \tilde{u}_j\right) = -\frac{\mu_{sgs}}{Sc_{SGS}}\frac{\partial \tilde{Y}_k}{\partial x_i}, \tag{2.71}$$

$$\bar{\rho}\widetilde{h'' u_j''} = -\frac{\mu_t}{Pr_t}\frac{\partial \tilde{h}}{\partial x_i} \quad \text{or} \quad \bar{\rho}\left(\widetilde{h u_j} - \tilde{h}\tilde{u}_j\right) = -\frac{\mu_{sgs}}{Pr_{SGS}}\frac{\partial \tilde{h}}{\partial x_i}, \tag{2.72}$$

where Sc_t, Sc_{SGS}, Pr_t and Pr_{SGS} are the turbulent/SGS Schmidt and Prandtl number, and are normally set as constant around unity. For simplicity, the term turbulent will be used from now on to refer to turbulent properties in RANS and SGS properties in LES.

2.5. CLOSURE OF SPECIES AND ENERGY EQUATIONS

The remaining untreated term is the mean or filtered reaction source term in the species and enthalpy equations. Models that are aimed at closing these terms are called combustion model or turbulent-chemistry interaction (TCI) models if the influence of turbulence on the mean (filtered) reaction source is directly incorporated. Combustion predominantly happens at small scales that are numerically not resolved, even in LES. Therefore the modeling of combustion in the context of LES is not easier than in RANS. In fact, most LES combustion models are directly adopted form RANS models. Over decades of development, many combustion or TCI models been proposed and widely tested [17–19].

2.5.1. CHEMICAL REACTION

A detailed chemical mechanism usually contains a large number of elementary reactions. An elementary reaction is one that occurs on a molecular level exactly in the way which is described by the reaction equation [1]

If the equation of an elementary reaction r is given by

$$\sum_{s=1}^{S} \nu_{rs}^{(e)} A_s \xrightarrow{k_r} \sum_{s=1}^{S} \nu_{rs}^{(p)} A_s, \tag{2.73}$$

then the formation rate of species i in reaction r is given by the rate law

$$\left(\frac{\partial C_i}{\partial t}\right)_r = k_r \left(\nu_{r,i}^{(p)} - \nu_{r,i}^{(e)}\right) \prod_{s=1}^{S} C_s^{\nu_{r,s}^{(e)}}. \tag{2.74}$$

where the $\nu_{r,i}^{(e)}$ and $\nu_{r,i}^{(p)}$ are the stoichiometric coefficients of reactants and products, C_s denotes the concentration of s species. k_f and k_b are the forward and backward rate constants. For a mechanism composed of R elementary reactions of S species, the rate of formation of a species i is given by summation over the rate equations of all elementary reactions:

$$\frac{\partial C_i}{\partial t} = \sum_{r=1}^{R} k_r \left(\nu_{r,i}^{(p)} - \nu_{r,i}^{(e)}\right) \prod_{s=1}^{S} C_s^{\nu_{r,s}^{(e)}} \quad \text{with} \quad i = 1, ..., S. \tag{2.75}$$

The rate constant k_r strongly depends on the temperature, and is given by the Arrhenius law:

$$k_r = AT^b exp(-\frac{E_a}{RT}). \tag{2.76}$$

where A and b are constants, and E_a is the activation energy.

In the CFD code, Eq. (2.75) is usually written in the form of mass fraction Y_i, which is directly available in the simulation. The reaction rate in terms of mass fraction reads:

$$w_i = \frac{\partial C_i}{\partial t} = \sum_{r=1}^{R} k_r \left(\nu_{r,i}^{(p)} - \nu_{r,i}^{(e)}\right) \prod_{s=1}^{S} \left(\frac{\rho Y_s}{M_s}\right)^{\nu_{r,s}^{(e)}} \quad \text{with} \quad i = 1, ..., S. \tag{2.77}$$

The reaction source terms in Eq. (2.3), which is the mass of species i produced per unit volume and unit time, is obtained as:

$$\dot{\omega}_i = W_i w_i = W_i \sum_{r=1}^{R} k_r \left(\nu_{r,i}^{(p)} - \nu_{r,i}^{(e)}\right) \prod_{s=1}^{S} \left(\frac{\rho Y_s}{M_s}\right)^{\nu_{r,s}^{(e)}} \quad \text{with} \quad i = 1, ..., S. \tag{2.78}$$

Evaluating of the reaction source for each species with Eq. (2.78) results in a set of Ordinary Differential Equations (ODEs).

2.5.2. TURBULENCE-CHEMISTRY INTERACTION

According to whether or not the ODEs from chemical reactions are solved during the CFD, combustion models can be categorized into two groups. In the first group, the species transport equations are solved during the simulation, their source term comes from the solution of chemical reaction ODEs. The Eddy breakup (EBU) model, the Eddy breakup concept (EDC) model and the partially stirred reactor (PaSR) model belongs to the first group. The second group decouples the chemical reaction calculation from the flow field calculation based on certain assumptions on the local flame structure. The species fields are often updated in a lookup manner using a pre-computed database, for example, the steady laminar flamelet (SLF) model, the Flamelet Generated Manifolds (FGM) model. The second group is referred to as tabulated chemistry method, which will be the main TCI model in this thesis.

2.5.3. FLAMELET AND FGM MODEL

Detailed mechanisms of practical fuels normally involve large amount of species and reactions. Furthermore, reactions of different species span a wide range of time scales, leading to a very stiff set of ODEs. These together makes the direct solving of detailed chemical reactions computationally very expensive. For most applications, chemistry reduction is required. As summarized in [20], there are four levels of chemical kinetics modeling: 1) detailed mechanism; 2) Skeletion Mechanism; 3) Manifolds methods; and 4) global mechanism. The last three levels belongs to chemistry methods. Description and comparison of these methods can be found in [20].

The flamelet model [21] and Flamelet Generated Manifold [22] can be categrized as the manifolds methods or tabulated chemistry methods. Flamelet model is the most widely used and important tabulated chemistry. It assumes that all chemical reactions are faster than the smallest turbulent time scale, i.e. the Kolmogorov time scale. This can be expressed as Damköhler number $Da >> 1$. Therefore the chemical reactions happen on a thin layer (flame front), for which only the changes perpendicular to the flame front is important, other two dimensions (parallel to the flame front) are negligible. Thus, the flame structure is reduced to one dimension — flamelet. For non-premixed combustion, the remaining one dimension can be characterized with a new variable — mixture fraction Z. $Z = 0$ denotes the oxidizer side and $Z = 1$ means the fuel side. By coordinate transformation, the governing equations for species and energy can be transfered to mixture fraction space:

$$\rho \frac{\partial \Phi_k}{\partial \tau} = \rho \frac{\chi}{2} \frac{\partial^2 \Phi_k}{\partial Z^2} + \dot{\omega}_k, \tag{2.79}$$

$$\chi = 2D \left(\frac{\partial Z}{\partial x_i} \right)^2. \tag{2.80}$$

where scalar Φ_k represent species or temperature, $\dot{\omega}_k$ the corresponding source term.

From Eq. (2.79) we can infer that in this situation, the species and temperature are only functions of time, τ, mixture fraction, Z, and scalar dissipation rate, χ. In order to solve Eq. (2.79), knowledge of χ is required. A model function $\chi(\chi)$ was derived by Peters [21]. Its value at stoichiometric condition, χ_{st}, is normally used to characterize each flamelet. Furthermore, if the unsteady term is eliminated, solution of the system reduces to a two dimensional function:

$$\Phi = \Phi(Z, \chi_{st}). \tag{2.81}$$

Based on this, to simulate any flame, one only needs to find the value of Z and χ_{st}, then the values of species concentration and temperature can be retrieved from relation (2.81) — table lookup. This avoids solving a large set of scalar transport equations and the chemical reactions, therefore can greatly reduce the computational cost.

The dependence of in Eq. (2.81) can be directly obtained by solving the flamelet equations in mixture fraction space, but can also first solve a simple laminar flame, e.g. counterflow configuration, in physical space, and then convert the properties to the mixture fraction space, see Fig. 2.1.

In RANS or LES simulation, not only the mean or filtered values $\tilde{Z}$ and $\tilde{\chi}_{st}$ have to be considered, but also the turbulent or SGS unresolved fluctuations. This is done by

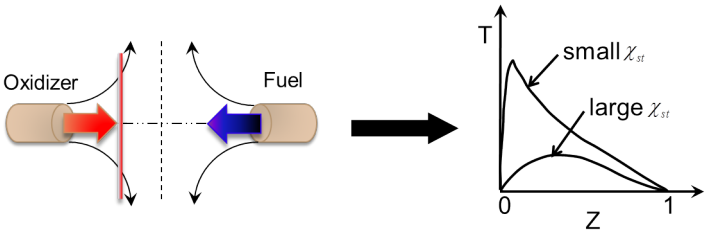

Figure 2.1: Counter flow laminar flame (left) and flamelet library (right).

introducing the joint Probability Density Function (PDF) of the controlling parameters — Z and χ_{st}. The Favre-averaged/filtered scalars are calculated as:

$$\tilde{\phi} = \int_0^1 \int_0^\infty \phi(Z,\chi_{st})\tilde{P}(Z,\chi_{st})dZd\chi_{st}, \tag{2.82}$$

and mean density as:

$$\frac{1}{\tilde{\rho}} = \int_0^1 \int_0^\infty \frac{1}{\rho}\tilde{P}(Z,\chi_{st})dZd\chi_{st}, \tag{2.83}$$

where $\tilde{P}(Z,\chi_{st})$ is the joint PDF of mixture fraction and stoichiometric scalar dissipation rate,

$$\tilde{P}(Z,\chi_{st}) = \tilde{P}(Z)\tilde{P}(\chi_{st} \mid Z). \tag{2.84}$$

$\tilde{P}$ denotes the "Favre-probability-density functions", namely using the Favre-averaged statistics rather than conventional time averages. If Z and χ_{st} are assumed statistically independent, then Eq. (2.84) reduces to:

$$\tilde{P}(Z,\chi_{st}) = \tilde{P}(Z)\,\tilde{P}\left(\chi_{st}\right), \tag{2.85}$$

where

$$\tilde{P}(Z) = \int_0^\infty \tilde{P}(Z,\chi_{st})d\chi_{st} \quad \text{and} \quad \tilde{P}(\chi_{st}) = \int_0^1 \tilde{P}(Z,\chi_{st})dZ, \tag{2.86}$$

are the marginal PDFs of Z and χ_{st}. $\tilde{P}(Z)$ and $\tilde{P}\left(\chi_{st}\right)$ can be obtained either by transported PDF or presumed PDF method. This is the so-called steady flamelet model, and will be used in Chapter 4.

Flamelet Generated Manifolds (FGM) method is conceptually very similar to steady flamelet model in the sense that it assume that local condition can be obtained from pre-calculated laminar flames. But the difference is that in FGM it is not only the scalar composition that is retrieved from a flamelet, but also chemical source term for a selected set of progress variables. Instead of solving all the species and energy transport equation during simulation, the chemical process in turbulent combustion is assumed to happen in a lower dimensional manifold. This means that there are only a few variables can change independently in the whole composition space. Very often, the mixture fraction Z, which represents the extent of mixture between "fuel" and "oxidizer", and

progress variable C, which denotes the progress of chemical reaction from pure mixing ($C = 0$) to fully burnt ($C = 1$), are chosen as independent variables in FGM method. The dimension of the FGM lookup table can be extended to incorporate more physics when required, for example, adding enthalpy h to account for the heat loss/gain [21], adding scalar dissipation rate χ to consider the influence of strain [23] and adding pressure p to take into account the effect of pressure variation [24].

2.6. PROBABILITY DENSITY FUNCTION METHOD

In this thesis we distinguish the transported PDF method, in which the (joint) PDFs are obtained from modeled transport equations, and presumed PDF, in which the pdf is assumed to have a particular shape that is parametrized (usually) by its first and second moments. In this section we briefly explain the transported PDF method. The content in this section partially follows Refs [18, 25–27].

2.6.1. PROBABILITY DENSITY FUNCTION (PDF)

The cumulative distribution function (CDF) of a single composition variable, e.g. a species mass fraction, at position $\mathbf{x}$ and time t can be defined as:

$$F_\phi\left(\psi;\mathbf{x},t\right) \equiv Prob\left\{\phi\left(\mathbf{x},t\right) < \psi\right\}, \tag{2.87}$$

where ψ is the sample-space variable of ϕ. The one-point, one-time Eulerian Probability Density Function (PDF) of ϕ is

$$f_\phi\left(\psi;\mathbf{x},t\right) \equiv \frac{\partial}{\partial\psi} F_\phi\left(\psi,\mathbf{x},t\right). \tag{2.88}$$

The joint pdf of multi-composition $\Phi\left(\mathbf{x},t\right)$ where $\Phi = \left\{\phi_1,\phi_2,...,\phi_i\right\}$ can be defined as

$$F_\Phi\left(\Psi;\mathbf{x},t\right) \equiv Prob\left\{\phi_1\left(\mathbf{x},t\right) < \psi_1, \phi_2\left(\mathbf{x},t\right) < \psi_2, ..., \phi_i\left(\mathbf{x},t\right) < \psi_i\right\}, \tag{2.89}$$

and

$$f_\Phi\left(\Psi;\mathbf{x},t\right) \equiv \frac{\partial}{\partial\Psi} F_\Phi\left(\Psi;\mathbf{x},t\right), \tag{2.90}$$

where $\Psi = \left\{\psi_1,\psi_2,...,\psi_i\right\}$ is the sample-space variables of ϕ.

We introduce the sample-space velocity variables $\mathbf{V} = \{V_1, V_2, V_3\}$ and denote the joint PDF of velocity by $f_\mathbf{u}\left(\mathbf{V};\mathbf{x},t\right)$. Finally, the joint velocity-composition pdf is denoted as $f_{\mathbf{u},\phi}\left(\mathbf{V},\Psi;\mathbf{x},t\right)$. For variable density flow, it is convenient to consider the joint velocity-scalar mass density function (MDF) defined as $F_{\mathbf{u},\Phi} = \rho\left(\Phi\right) f_{\mathbf{u},\Phi}\left(\mathbf{V},\Psi;\mathbf{x},t\right)$. The transport

equation for the MDF can be derived from the conservation equations [25]:

$$\begin{aligned}\frac{\partial F}{\partial t}+\frac{\partial V_j F}{\partial x_j}=&-\frac{\partial}{\partial V_j}\left[\frac{1}{\rho(\psi)}\left(-\frac{\langle p\rangle}{\partial x_j}-\frac{\partial\langle T_{ij}\rangle}{\partial x_i}\right)F\right]\\&+\frac{\partial}{\partial V_j}\left[\frac{1}{\rho(\psi)}\langle-\frac{\partial p^{'}}{\partial x_j}-\frac{\partial T_{ij}}{\partial x_i}|\mathbf{U}=\mathbf{V},\Phi=\Psi\rangle F\right]\\&+\frac{\partial}{\partial\Psi_\alpha}\left[\left(-\frac{1}{\rho(\psi)}\frac{\partial\langle J_i^\alpha\rangle}{\partial x_i}+S_\alpha(\Psi)\right)F\right]\\&+\frac{\partial}{\partial\Psi_\alpha}\left[\frac{1}{\rho(\psi)}\langle-\frac{\partial J_i^{\alpha'}}{\partial x_i}|\mathbf{U}=\mathbf{V},\Phi=\Psi\rangle F\right],\end{aligned}\tag{2.91}$$

where $\langle\rangle$ denotes average, and notation $\langle A|B\rangle$ denotes the conditional expectation value of A upon condition B.

In this equation, the first two terms on the RHS describe the evolution in velocity space and the last two terms describe the evolution in composition space. The first term and the first part of the third term on the RHS can be expressed with mean velocity and scalar fields, therefore are closed. The reaction source term, S_α can be evaluated with scalar variables Φ without further model assumptions, thus is also closed. The fact that convection and finite-rate nonlinear reaction rate can be handled without modeling assumptions is actually the greatest advantage of the PDF method. The second and fourth terms on the RHS describes the mean effects of the fluctuating pressure, the fluctuating viscous stress tensor as well as the molecular diffusion or micro-mixing process, and remain to be modeled.

2.6.2. LAGRANGIAN PDF METHODS

The joint velocity-scalar PDF in principle can be obtained by directly solving the modeled MDF transport equation Eq. (2.91). However, the high-dimensional nature of this equation ($2d+n$ dimensions with d the spatial dimension and n the number of species) prevents its practical usage of solving this equation with conventional differential techniques. Alternatively, the Monte Carlo method provides a computationally more effective approach to obtain the high-dimensional joint PDF [25]. In the Monte Carlo method, the $2d+n$ dimensional mass density function is represented by a large number of notational fluid particles. The statistical error tends to zero with $N^{-1/2}$, with N the number of Monte Carlo particles [26]. These particles evolve according to certain models such that the evolution of the statistics of the particle ensemble corresponds to the modeled PDF evolution. The properties of computational particles contain include the position, $\mathbf{x}^*$, velocity, $\mathbf{U}^*$, and composition, ϕ^*.

The notational fluid particles evolve according to stochastic differential equations (SDEs):

$$d\mathbf{x}^*=\mathbf{U}^*(t)\,dt,\tag{2.92}$$

$$dU_i^*=-K_i^u dt+b_{ij}^u dW_{ij},\tag{2.93}$$

$$d\Phi_\alpha^*=-K_\alpha^\phi dt+b_{\alpha\beta}^\phi dW_\beta.\tag{2.94}$$

The evolution of velocity and scalars is realized both by a deterministic change, denoted by the drift vectors $\mathbf{K}^u$ and $\mathbf{K}^\phi$, and a stochastic change, denoted by term containing the increment of the Wiener process dW. The increment in the Wiener process $dW(t)$ is a Gaussian random variable with mean zero, and variance dt, and with increment at different times statistically independent of each other.

LANGEVIN MODEL

The particle velocity evolution is often modeled with Langevin model. Pope and Haworth proposed the Generalized Langevin model (GLM) with the following form [28, 29]:

$$d\mathbf{U}^* = \left(-\frac{1}{\rho}\frac{\partial \bar{p}}{\partial x_i} - \frac{\partial \tilde{\tau}_{ij}}{\partial x_i}\right) dt + G_{ij}\left(U_j^* - \tilde{U}_j\right) dt + (C_0\epsilon)^{1/2}\, dW_i, \tag{2.95}$$

where the drift coefficient tensor G_{ij} reads [9]:

$$G_{ij} = \frac{\epsilon}{k}\left(\alpha_1\delta_{ij} + \alpha_2 b_{ij} + \alpha_3 b_{ij}^2\right) + H_{ijkl}\frac{\partial \tilde{U}_k}{\partial x_l}, \tag{2.96}$$

with

$$\begin{aligned} H_{ijkl} = {} & \beta_1\delta_{ij}\delta_{kl} + \beta_2\delta_{ik}\delta_{jl} + \beta_3\delta_{il}\delta_{jk} \\ & + \gamma_1\delta_{ij}b_{kl} + \gamma_2\delta_{ik}b_{jl} + \gamma_3\delta_{il}b_{jk} + \gamma_4 b_{ij}\delta_{kl} + \gamma_5 b_{ik}\delta_{jl} + \gamma_6 b_{il}\delta_{jk}. \end{aligned} \tag{2.97}$$

The choice of coefficients α_i, β_i and γ_i together with coefficient C_0 defines the specific form of GLM [9, 30].

The Monte Carlo (MC) PDF method can be combined with standard Finite Volume (FV) approach [31, 32], in which the mean velocity, pressure, turbulent kinetic energy (Reynolds stresses) and its dissipation rate can be obtained and supplied to the MC part. Care should be take for the choice of turbulent model in the FV part in such a combined hybrid method. Because the Langevin model describes the evolution of the full joint velocity PDF, it also provides information for the higher moments of velocity, including the Reynolds stresses. The GLM (Eq. (2.95)) implies a pressure-strain correlation model (Eq. (2.43)) in the RSM that takes the following form:

$$\Pi_{ij}^* = \left(\frac{2}{3} + C_0\right)\epsilon\delta_{ij} + G_{il}\widetilde{u_l'' u_j''} + G_{jl}\widetilde{u_l'' u_i''}. \tag{2.98}$$

Thus for a certain choice of G_{ij}, there is a corresponding Reynolds stress equation of the form Eq. (2.31) which is realizable. For the correspondence and consistency between RSM and Langevin model, readers are referred to [5, 9, 27, 30].

MICRO-MIXING MODEL

Combustion can only take place if the fuel and oxidizer are mixed at the molecular level. For the one time - one point PDF, information on length and time scales is missing, therefore unclosed terms appear in its exact equation and an extra model is required to account for the micro-mixing process. Actually, the micro-mixing model is one of the most important and also probably most challenging model components in the context of transported PDF.

Conditions that a “good" micro-mixing model should satisfy are as following [27, 33, 34]:

1. **Constant scalar mean** The mean properties must not be affected by the mixing process, this is a strictly required property of mixing model.

2. **Scalar variance decay** The joint velocity-scalar PDF does not provide information on the decay rate, the mixing model should model correctly the scalar dissipation rate.

3. **Boundedness of scalar values** During mixing, scalars should stay within their physical bounds, for example mixture fraction between 0 and 1. This property simply means that unphysical scalar values like negative species mass fraction should not occur.

4. **Linearity and independence** The linearity property of the scalar micro-mixing arises from the fact that transport equations are linear in the scalar values. The micro-mixing of one scalar should be independent of the distribution of other scalars [35].

5. **Relaxation to Gaussian** With mixing, the PDF of a single inert scalar in homogeneous turbulence should eventually relax to a Gaussian distribution.

6. **Localness in scalar space** The mixing of fluid particles in a physical volume of fluid, where scalar fields are continuous, is also local in scalar space.

Besides above mentioned ones, there are also other criteria exits for the evaluation of a micro-mixing model, e.g. flow and reaction conditions dependence [34].

The most widely used micro-mixing model is the Interaction by Exchange with the Mean (IEM) model (also known as Linear Mean Square Estimation (LMSE) model [36]) because of its simplicity. This model is also used in the study of this thesis. The IEM model satisfy first four conditions, namely it conserves the scalar mean and provides correct variance decay rate, scalars are bounded and has linearity and independence.

In the IEM model, the decay of scalar variance is modeled by a deterministic relaxation of all scalar values to the local mean:

$$d\phi^*_\alpha = -\frac{1}{2}\omega_\phi \left(\phi^*_\phi - \tilde{\phi}_\alpha\right) dt, \tag{2.99}$$

where C_ϕ is a model constant with standard value 2. The decay rate is modeled with $\omega_\phi = C_\phi \omega = C_\phi \epsilon / k$.

Many other micro-mixing models have been proposed and tested, for example, the Coalescence and Dispersion (CD) model [37], the Mapping Closure (MC) model [38], the Euclidean minimum spanning tree (EMST) [39], the Multiple mapping conditioning (MMC) model [40], and the Parameterized scalar profile (PSP) model [41], etc. For the review and comparison of these models, we refer to [33, 34, 42] and references therein.

2.6.3. PDF METHOD FOR MULTI-PHASE FLOW

The Lagrangian PDF method is relatively straightforward to be extended to dispersed twophase or multiphase flows. Over the past decades, there have been many studies on the applying of transported PDF method to multiphase flow.

Zhu et al. [43] studied the PDF transport equations for two-phase reactive flows and sprays in 2000. A general framework for the turbulent polydispersed two-phase flows in the context of transported PDF method was developed by Minier and Peirano [44] in 2001. In this work, the mathematic description of the joint PDF for the fluid and for the discrete particles was derived.

Liu et al. [45] proposed a new joint PDF method for modeling turbulent spray evaporating and combustion. In this method, the droplet velocity, temperature, diameter, and droplet-seen gas velocity and compositions are considered as stochastic variables of the dispersed phase. The Langevin model for seen gas velocity is used to close the droplet dispersion model. And this transported PDF method was combined with the second-order moment (SOM) model of gas turbulence. This joint PDF method was shown be able to give good prediction on droplet properties even in the recirculation zone, where the droplet concentration is low, while the stochastic particle trajectory (SPT) method show poor performance in this situation.

Naud [32] systematically studied a joint PDF method for spray combustion. It comprises a joint velocit-composition PDF for the gas phase and a joint velocity, diameter, temperature, seen gas velocity and composition PDF for the dispersed phase. Due to the high dimensionality, the joint PDF is obtained with Monte Carlo particle method. Besides the Lagrangian description, the gas phase is also solved using a Eulerian method for the mean properties. Therefore it is an Eulerian-Lagrangian-Lagrangian approach. For simplicity, this approach is referred to as Lagrangian-Lagrangian approach hereafter. Beishuizen [46] invested the particle-turbulence interaction of turbulent spray combustion in the framework of Lagrangian-Lagrangian approach.

Ge and Gutheil [47] combined the transported PDF method with spray flamelet model, and proposed a joint mixture fraction-enthalpy PDF method for the simulation of spray flames. Latter on, Ge et al. [48] also used the joint ga-phase velocity-mixture fraction PDF method to model turbulent evaporating spray flows.

Recent applications of transported PDF method on spray combustion including Bhattacharjee and Haworth [49], Pei et al. [50, 51] and others. Heye et al. [52] applied the LES/probability density function approach in the simulation of a pilot-stabilized spray flame. Large discrepancies, especially on gas phase temperature, were observed when compared to experimental data, and this was attributed to the inaccurate inflow boundary conditions. Latter on, similar approach was used to study a series of methanol spray flames in order to investigate the influence of the spray/combustion interactions on auto-ignition, and good agreement with experimental data was obtained [53]. Very recently, Irannejad et al. [54] simulated a high speed evaporating and combusting n-haptane sprays using the LES/filtered mass density function method. Jones and coworkers [55, 56] worked on applying the stochastic field method, which is an Eulerian PDF approach, for spray combustion.

Readers are referred to [57] for a recent comprehensive review on the application of Lagrangian PDF method to two-phase reactive flows.

In this thesis, we apply the Lagrangian-Lagrangian approach developed by Naud [32], and combine it with the FGM method to simulation the DSHC flame. Fig. 2.2 illustrates the Lagrangian-Lagrangian representation of the two-phase PDFs in the simulation. Details of this study will by given in Chapter 5.

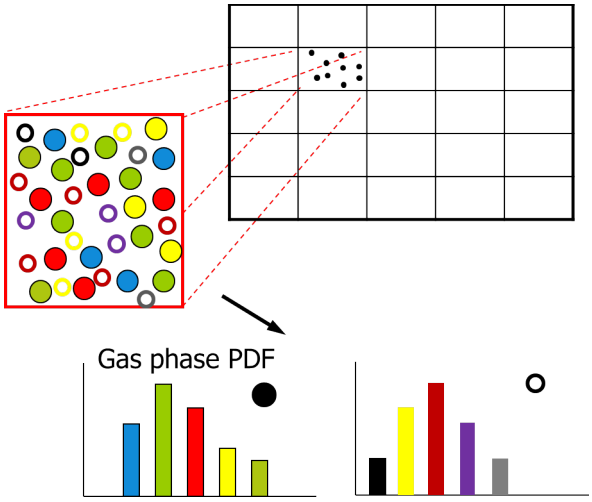

Figure 2.2: Illustration of PDF method applied to modeling spray combustion [32].

REFERENCES

[1] J. Warnatz, U. Maas, and R. Dibble, *Combustion (4th ediction)* (Springer, 2006).

[2] H. Versteeg and W. Malalasekera, *An Introduction to Computational Fluid Dynamics (Second Edition)* (Pearson Eduction, 2007).

[3] T. Poinsot and D. Veynante, *Theoretical and Numerical combustion (Third Edition)* (Aquaprint, 2012).

[4] B. E. Launder and D. B. Spalding, *The numerical computation of turbulent flows,* Computer Methods in Applied Mechanics and Engineering **3**, 269 (1974).

[5] S. B. Pope, *Turbulent Flows* (Cambridge University, 2000).

[6] K. Hanjalić and B. Launder, *Modeling turbulence in engineering and the environment — Second-moment routes to closure* (Cambridge University, 2011).

[7] B. J. Daly, *Transport Equations in Turbulence,* Physics of Fluids **13**, 2634 (1970).

[8] ANSYS, *Fluent 15.0 Theory Guide,* (2014).

[9] S. B. Pope, *On the relationship between stochastic Lagrangian models of turbulence and second-moment closures,* Physics of Fluids **6**, 973 (1994).

[10] A. Yoshizawa, *Statistical theory for compressible turbulent shear flows, with the application to subgrid modeling,* Physics of Fluids **29**, 2152 (1986).

[11] G. Erlebacher, M. Y. Hussaini, C. G. Speziale, and T. A. Zang, *Toward the large-eddy simulation of compressible turbulent flows,* Journal of Fluid Mechanics **238**, 155 (1992).

[12] M. Lesieur, O. Metais, and P. Comte, *Large-Eddy Simulation of Turbulence* (Cambridge University Press, 2005).

[13] M. P. Mart, U. Piomelli, and G. V. Candler, *Subgrid-Scale Models for Compressible Large-Eddy Simulations,* Theoretical and Computational Fluid Dynnamics **13**, 361 (2000).

[14] M. Germano, U. Piomelli, P. Moin, and W. H. Cabot, *A dynamic subgrid-scale eddy viscosity model,* Physics of Fluids A: Fluid Dynamics **3**, 1760 (1991).

[15] P. Moin, K. Squires, W. Cabot, and S. Lee, *A dynamic subgrid-scale model for compressible turbulence and scalar transport,* Physics of Fluids A: Fluid Dynamics **3**, 2746 (1991).

[16] D. K. Lilly, *A proposed modification of the Germano subgrid-scale closure method,* Physics of Fluids A: Fluid Dynamics **4**, 633 (1992).

[17] R. Bilger, S. Pope, K. Bray, and J. Driscoll, *Paradigms in turbulent combustion research,* Proceedings of the Combustion Institute **30**, 21 (2005).

[18] D. Haworth, *Progress in probability density function methods for turbulent reacting flows,* Progress in Energy and Combustion Science **36**, 168 (2010).

[19] S. B. Pope, *Small scales, many species and the manifold challenges of turbulent combustion,* Proceedings of the Combustion Institute **34**, 1 (2013).

[20] U. Maas, *Combustion chemistry,* in *Best practice guidelines for computational fluid dynamics of turbulent combustion*, edited by L. Vervisch and D. Roekaerts (ERCOFTAC, 2015) pp. 39–75.

[21] N. Peters, *Laminar diffusion flamelet models in non-premixed turbulent combustion,* Progress in Energy and Combustion Science **10**, 319 (1984).

[22] J. A. van Oijen and L. P. H. de Goey, *Modelling of premixed laminar flames using flamelet-generated manifolds,* Combustion Science and Technology **161**, 113 (2000).

[23] M. Ihme and Y. C. See, *Prediction of autoignition in a lifted methane/air flame using an unsteady flamelet/progress variable model,* Combustion and Flame **157**, 1850 (2010).

[24] C. Bekdemir, *Tabulated Chemical Kinetics for Efficient and Detailed Simulations of Diesel Engine Combustion*, Ph.D. thesis, Eindhoven University of Technology (2012).

[25] S. B. Pope, *PDF methods for turbulent reactive flows,* Progress in Energy and Combustion Science **11**, 119 (1985).

[26] S. B. Pope, *Lagrangian methods for turbuletn flow,* Annual Review of Fluid Mechanics **26**, 23 (1994).

[27] D. Roekaerts, *Probability density function (pdf) methods,* in *Lecture notes of JMBC Course on Combustion*, edited by J. van Oijen (2013) pp. 157–168.

[28] S. Pope, *A Lagrangian two-time probability density function equation for inhomogeneous turbulent flows,* Physics of Fluids **26**, 3448 (1983).

[29] D. C. Haworth and S. B. Pope, *A generalized Langevin model for turbulent flows,* Physics of Fluids **29**, 387 (1986).

[30] B. Naud, B. Merci, and D. Roekaerts, *Generalised Langevin Model in correspondence with a chosen standard scalar-flux second-Moment closure,* Flow, Turbulence and Combustion **85**, 363 (2010).

[31] S. M. Correa and S. B. Pope, *Comparison of a Monte Carlo PDF/finite-volume mean flow model with bluff-body Raman data,* Proceedings of the Combustion Institute **24**, 279 (1992).

[32] B. Naud, *PDF modeling of turbulent sprays and flames using a particle stochastic approach*, Ph.D. thesis, Delft University of Technology (2003).

[33] L. Wang and R. O. Fox, *Comparison of micromixing models for CFD simulation of nanoparticle formation,* AIChE Journal **50**, 2217 (2004).

[34] C. Celis and L. F. Figueira da Silva, *Lagrangian Mixing Models for Turbulent Combustion: Review and Prospects,* Flow, Turbulence and Combustion **94**, 643 (2015).

[35] H. A. Wouters, P. A. Nooren, T. W. J. Peeters, and D. Roekaerts, *Eects of micro-mixing in gas-phase turbulent jets,* International Journal of Heat and Fluid Flow **19**, 201 (1998).

[36] C. Dopazo and E. E. O'Brien, *An approach to the autoignltlon of a turbulent mixture,* Acta Astronautic **1**, 1239 (1974).

[37] R. L. Curl, *Dispersed phase mixing: I. Theory and effects in simple reactors,* AIChE Journal **9**, 175 (1963).

[38] S. B. Pope, *Mapping Closures for Turbulent Mixing and Reaction,* Theoretical and Computational Fluid Dynnamics **2**, 255 (1991).

[39] S. Subramaniam and S. B. Pope, *A mixing model for turbulent reactive flows based on euclidean minimum spanning trees,* Combustion and Flame **115**, 487 (1998).

[40] a. Y. Klimenko and S. B. Pope, *The modeling of turbulent reactive flows based on multiple mapping conditioning,* Physics of Fluids **15**, 1907 (2003).

[41] D. W. Meyer and P. Jenny, *A mixing model for turbulent flows based on parameterized scalar profiles,* Physics of Fluids **18**, 035105 (2006).

[42] D. W. Meyer and P. Jenny, *Micromixing models for turbulent flows,* Journal of Computational Physics **228**, 1275 (2009).

[43] M. Zhu, K. Bray, O. Rumberg, and B. Rogg, *PDF Transport Equations for Two-Phase Reactive Flows and Sprays,* Combustion and Flame **122**, 327 (2000).

[44] J.-P. Minier and E. Peirano, *The pdf approach to turbulent polydispersed two-phase flows,* Physics Report **352**, 1 (2001).

[45] Z. Liu, C. Zheng, and L. Zhou, *A joint PDF model for turbulent spray evaporation/combustion,* Proceedings of the Combustion Institute **29**, 561 (2002).

[46] N. A. Beishuizen, *PDF modelling and particle-turbulence interaction of turbulent spray flames,* Ph.D. thesis, Delft University of Technology (2008).

[47] H.-W. Ge and E. Gutheil, *Simulation of a turbulent spray flame using coupled PDF gas phase and spray flamelet modeling,* Combustion and Flame **153**, 173 (2008).

[48] H.-W. Ge, Y. Hu, and E. Gutheil, *Joint gas-phase velocity-scalar PDF modeling for turbulent evaporating spray flows,* Combustion Science and Technology **184**, 1664 (2012).

[49] S. Bhattacharjee and D. C. Haworth, *Simulations of transient n-heptane and n-dodecane spray flames under engine-relevant conditions using a transported PDF method,* Combustion and Flame **160**, 2083 (2013).

[50] Y. Pei, E. R. Hawkes, and S. Kook, *A comprehensive study of effects of mixing and chemical kinetic models on predictions of n-heptane jet ignitions with the PDF method,* Flow, Turbulence and Combustion **91**, 249 (2013).

[51] Y. Pei, E. R. Hawkes, and S. Kook, *Transported probability density function modelling of the vapour phase of an n-heptane jet at diesel engine conditions,* Proceedings of the Combustion Institute **34**, 3039 (2013).

[52] C. Heye, V. Raman, and A. R. Masri, *LES/probability density function approach for the simulation of an ethanol spray flame,* Proceedings of the Combustion Institute **34**, 1633 (2013).

[53] C. Heye, V. Raman, and A. R. Masri, *Influence of spray/combustion interactions on auto-ignition of methanol spray flames,* Proceedings of the Combustion Institute **35**, 1639 (2015).

[54] A. Irannejad, A. Banaeizadeh, and F. Jaberi, *Large eddy simulation of turbulent spray combustion,* Combustion and Flame **162**, 431 (2015).

[55] W. Jones, A. Marquis, and K. Vogiatzaki, *Large-eddy simulation of spray combustion in a gas turbine combustor,* Combustion and Flame **161**, 222 (2014).

[56] W. Jones, A. Marquis, and D. Noh, *LES of a methanol spray flame with a stochastic sub-grid model,* Proceedings of the Combustion Institute **35**, 1685 (2015).

[57] J.-P. Minier, *On Lagrangian stochastic methods for turbulent polydisperse two-phase reactive flows,* Progress in Energy and Combustion Science **50**, 1 (2015).

3

THEORY: SPRAY MODELS

In this chapter, the spray related model components that will be used in this thesis are explained.

Part of this chapter has been published in:
D. Roekaerts, L. Ma, “Spray combustion", Book chapter In: lecture note of International Combustion Institute Winter School, 2016, Editor: J.A. van Oijen.

3.1. INTRODUCTION

Spray combustion refers to the combustion process in which the fuel and/or oxidizer are supplied in liquid form. It is widely used in many industrial and transportation systems, for example, furnaces, internal combustion engines, liquid rocket engines, etc.. To achieve a cleaner and more efficient spray combustion process, deep understanding and accurate prediction of the phenomena involved is essential, and has been the key goal for research of spray combustion.

Spray combustion involves many phenomena and processes; the strong coupling between them makes its modeling very difficult [1]. Based on the volume fraction of the liquid phase, the dense and dilute regions are distinguished in spray combustion systems. Fig. 3.1 illustrates the key processes in dilute region of spray combustion and the interactions between them. For the gas phase, the turbulence, dispersion, micro-mixing and combustion have to be considered. And for the liquid phase, the atomization, dispersion and evaporation require to be modeled. The two phases are closely coupled through momentum, heat and mass transfer.

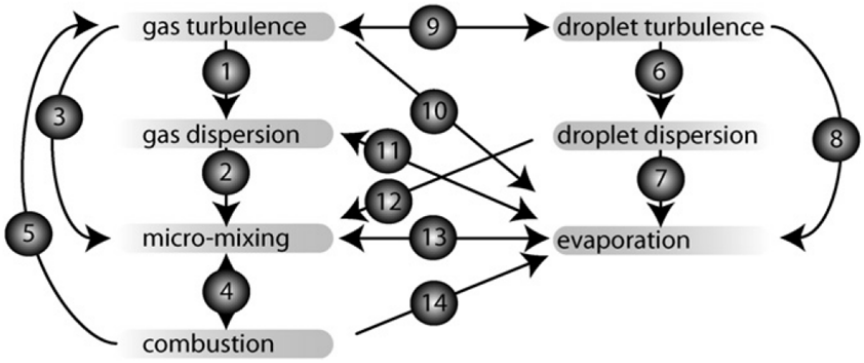

Figure 3.1: Phenomena and their interaction in dilute spray combustion [1].

In general, three approaches exist to handle the two-phase flow field: Eulerian-Eulerian (E-E), Eulerian-Lagrangian (E-L) and Lagrangian-Lagrangian (L-L) approaches. In the E-E approach, also referred to as two-fluid method [2], transport equations for continuum properties associated with both phases are solved. The terms in the transport equations are weighted by the volume fraction of each phase. In the contrast, both phases are tracked in a Lagrangian manner in the L-L approach. The L-L approach is normally used in the context of transported PDF method [3]. The E-L approach is mostly widely used in spray combustion modeling. In this method, transport equations are solved for the gas phase, while the dispersed phase is accounted for with the Lagrangian method.

The main advantage of the E-E method is that large volume fraction of the second phase can be handled, and the phase interface can be captured and reconstructed. This makes the E-E method particularly suited for dense flows, i.e. flow field at the vicinity of the injector exit. However, for a polydispersed phase, this approach may be computationally expensive. In the majority of spray simulations, the E-L method is adopted. Because the Lagrangian approach allows to deal straightforwardly and accurately with

many complex phenomena such as collision, coalescence, heat and mass transfer and so on, whereas these can be very difficult to handle in an Eulerian approach [4]. In this chapter we focus on the E-L method, but models for atomization using the E-E method will also be mentioned for completeness.

For a fully resolved multi-phase flow simulation, the conditions at the phase interface have to be considered in addition to the governing equations of each phase [1]. This requires enormous computational resources, and is far from feasible for a practical spray combustion system. It is a common practice, especially in the E-L approach, that droplets are treated as a point source of momentum, heat and mass — "point source" assumption. This assumption is even applied in many DNS of spray combustion [5, 6]. The point source assumption is employed in all the discussions in this chapter unless explicitly pointed out otherwise.

For simplicity, in the following discussion, we assume that only the fuel is in liquid state, and it is injected into the gaseous oxidizer, which is indeed the case for most applications. From the injection of liquid fuel till the fuel vapor is produced, the liquid phase undergoes several processes. First of all, depending on the atomizer and operational condition, the liquid flow disintegrates, for example due to the instability induced by the aerodynamic forces on the interface. This process is called atomization. The formed droplets move around, their position and velocity change with time, this is called dispersion. The processes of heat and mass transfer between the two phases is called evaporation (condensation is possible in general, but can be ignored in hot environment). Models for these three processes will be discussed in this section.

In the remaining of this chapter, the major model components for both gas and liquid phases will be briefly reviewed, with the goal of drawing an overall picture in terms of the possibilities and limitations of the state of the art models.

3.2. ATOMIZATION MODEL

The atomization of liquid fuel is indispensable in practical spray combustion system in order to create large liquid surface-to-volume ratio which facilitates fast evaporation. The whole atomization process can be broadly classified into primary breakup and secondary breakup. The primary breakup is the process that liquid jet or sheet disintegrates into irregular-shaped ligaments or large droplets. A review on the modeling of primary atomization is given by Gorokhobski and Herrmann [7]. The secondary breakup refers to the process of the further disintegration of these large droplets and ligaments into even smaller fragments.

According to Jenny et al. [1], the two-phase flow field can be divided into three regimes based on the volume fraction occupied by the dispersed phase. The region that has a dispersed phase volume fraction above 10^{-3} is referred to as the dense regime. In the dilute regime, the dispersed phase volume fraction is in the range between 10^{-6} and 10^{-3}. When the dispersed phase volume fraction is less than 10^{-6}, it is called very dilute regime. The majority of spray combustion simulation only considers the dilute region for simplicity. However, in practical applications, the dense region is unavoidable, and is more challenging.

Disintegration of a liquid jet may be caused by many factors, for instance, the turbulence in the liquid jet, cavitation in the nozzle and the interfacial forces between the liq-

uid jet and the surrounding medium [8]. Owing to the rich physics involved and strong configuration and operation condition dependence, the mechanism of atomization is still far from been fully understood.

It is very difficult to experimentally measure all necessary spray properties, especially near the dense region. Kourmatzis et al. [9] conducted experiment of spray jet flame with substantial liquid-liquid interaction at the exit plane. Techniques based on novel image processing and calibration revealed the existence of three different liquid fragment shapes: ligaments, droplets and large, irregular objects. An review of recent advances in the diagnostics of dense sprays was given by [10].

DNS is a very attractive tool to create understanding of this complicated process. For a DNS of the spray atomization, there are some new difficulties compared to the DNS of single phase flow. The first one, being the lack of information on the smallest scale. Due to presence of evaporation, the droplet size continuously regresses until zero, and there will be certainly some part remaining unresolved in the simulation. Unfortunately, it was found in [11], that a coarse mesh may result in an unrealistic pinch-off leading to formation of artificial droplets. Some assumptions have been made to control the size of droplets. For example, in the DNS of atomization by Lebas et al. [12], the surface tension is set three times larger than that in reality, secondary breakup and evaporation are excluded. The second difficulty on the DNS of atomization is the accurate reconstruction of the liquid/gas interface. The most common strategies for two phase flow calculation are the volume of fluid (VOF) method, level set method, and the front tracking method. The level set method is capable of accurately capture the interface, but suffers from mass conservation issues, therefore it is sometimes coupled with VOF method in DNS studies [11–13]. Although difficult, these limited DNS studies of primary atomization process and the further analysis of the datasets still provide valuable insight on this complicated process, and hopefully implying new model development.

Practical simulations of spray combustion still rely on models that have good balance between accuracy and computational efficiency. In the following we briefly discuss some atomization models with this in mind.

3.2.1. LISA MODEL

The LISA (Linearized Instability Sheet Atomization) model was designed for modeling primary breakup of pressure-swirl atomizers [14], sometimes also referred to as simplex atomizer. Fig. 3.2 shows the atomization process of pressure-swirl atomizer. The centrifugal motion of the liquid within the injector chamber creates an air core surrounded by a liquid sheet. Disintegration of this liquid sheet occurs due to the growth of waves on the interface caused by the aerodynamic forces acting on the sheet. Fragments of liquid will break off once the waves reach a critical amplitude. Capillary forces then cause the unstable ligaments to break into droplets.

The LISA model contains description of two subprocesses during the atomization: the formation of liquid sheet, and its breakup into ligaments and eventually to droplets. The initial sheet thickness h_0 is related to the measured effective mass flow rate $\dot{m}_{eff}$ and axial component of the sheet velocity u by conservation of mass:

$$\dot{m}_{eff} = \pi \rho_1 u h_0 \left(d_{inj} - h_0\right). \tag{3.1}$$

Figure 3.2: Snapshot of atomization by pressure-swirl atomizer [15] (left), and Sketch of liquid sheet breakup.

where d_{inj} is the exit diameter of the injector orifice, ρ_1 the liquid density.

Breakup of the liquid sheet is affected by the surrounding gas, liquid viscosity, and surface tension. The mechanism of the liquid sheet breakup is believed to dependent on the wavelength of the unstable interfacial wave [14]. For waves that are long compared with the sheet thickness, ligaments are assumed to form from the sheet breakup process once the unstable waves reach a critical amplitude. If it is assumed that the ligaments are formed from tears in the sheet twice per wavelength, the resulting diameter is given by:

$$d_L = \sqrt{\frac{8h_b}{K_s}}, \tag{3.2}$$

where K_s is the wave number corresponding to the maximum wave growth rate which is determined, in practice, by numerically maximizing the analytical wave growth rate derived in [14]. h_b is the sheet thickness at point of breakup.

For waves that are short compared with the sheet thickness, it is assumed that the ligaments are formed from tears in the sheet once per wavelength:

$$d_L = \sqrt{\frac{16h_b}{K_s}}, \tag{3.3}$$

In either the long-wave or the short-wave case, the breakup from ligaments to droplets is assumed to be caused by capillary instability. If it is assumed that breakup occurs when the amplitude of the unstable waves is equal to the radius of a ligament, one droplet will be formed per wavelength. A mass balance then gives:

$$d_D = 1.88 d_L (1 + 3Oh)^{1/6} \tag{3.4}$$

for droplet size d_D, where $Oh = \mu_l / \left(\rho_l \sigma d_L\right)^{1/2}$ is the Ohnesorge number, μ_l is the liquid viscosity, and σ the surface tension. The actual droplet size is chosen from a Rosin-Rammler distribution with the size predicted from Eq. (3.4) as the mean diameter.

The LISA model is available in many CFD code, e.g. ANSYS Fluent, OpenFOAM, etc., and it can be applied to both LES and RANS simulations. Some difference in implementation can appears, e.g. in ANSYS Fluent, the ligament diameter in the short wave mode is implemented differently from Eq. (3.3), and is assumed to be linearly proportional to the wavelength that breaks up the sheet,

$$d_L = \frac{2\pi C_L}{K_s}, \tag{3.5}$$

where C_L is the ligament constant [16].

3.2.2. ELSA MODEL

The ELSA (Eulerian-Lagrangian Spray Atomization) model was designed originally to describe atomization of a liquid jet with high Weber and Reynolds values [17]. In the ELSA model, the two phase flow is studied as a single phase flow composed of two species, liquid and gas, with different density. Transport equations for liquid/gas interface density and liquid volume fraction have to be solved. The characteristic droplet diameter can be derived from these two properties. DNS of primary atomization by Lebas et al. [12] and Duret et al. [13] have been used to verify assumptions and model constants in the ELSA model. This method was mainly applied in RANS studies [12], but later on has been extended also to LES [18].

The ELSA model can by used for both primary and secondary breakup. But closures of the surface density production and destruction are required. The influence of turbulence, droplet collision and coalescence on the interface density have been reported in many studies [12, 13], and the model for the “equilibrium" interface density turns out to be crucial. The problem that has been less addressed is the incorporation of vaporization into the interface density equation. And it is not straightforward to see how the classic evaporation models which are mainly developed for spherical droplets can be properly coupled with the ELSA model [19]. To solve this problem, some attempts to combine the Eulerian approach for dense region and Lagrangian approach for dilute region have been made [20].

3.2.3. LES-FDF MODEL

The ELSA model discussed above only provides cell level information on the interface density and volume fraction, with which only the mean size, e.g. Sauter Mean Diameter (SMD), can be retrieved. However, since large and small droplets behave considerably different, the droplets size distribution in each cell is of importance. This distribution can be calculated using a stochastic method based on the solution of a joint volume fraction-interface density sub-grid Probability Density Function (PDF) or Filtered Density Function (FDF) [21]. The method permits to obtain instantaneous sub-grid characteristic size distributions. It can be used for both primary and secondary breakup. This model is only applicable in the context of LES.

3.2.4. MODELS SPECIFIC FOR SECONDARY BREAKUP

The Taylor analogy breakup (TAB) model is based on an analogy between an oscillating-distorting droplet and a spring mass system. The aerodynamic force, the surface tension and the liquid viscosity are respectively related to the external force, the restoring force and the damping of the spring mass system. When the droplet oscillations grow to a critical value the “parent” droplet will break up into a number of smaller “children” droplets. The dimensionless oscillation can be expressed as a function of time, drag force, surface tension, droplet size and other liquid/gas phase properties [16]. And it is calculated for each droplet at each time step; if it exceeds a certain value, then breakup happens. For this model, the size distribution of the children droplets has to be prescribed a priori[22].

The Kelvin-Helmholtz (KH) model considers the liquid-gas interface instability due to the growth of Kelvin-Helmholtz waves caused by aerodynamic forces. Droplet size is calculated based on the wavelength of the unstable waves on the liquid surface. This

model is able to describe a liquid core near the nozzle exit.

The blob model assumes that large droplets or "blobs" with a characteristic size equal to the injector nozzle diameter are directly injected from the nozzle. Small droplets at downstream are produced by breakup up of the big blob. The atomization is modeled by a stochastic model in which the characteristic radius of droplets is assumed to be a time-dependent stochastic variable with a given initial distribution. The breakup of parent droplet into children droplets is treated as the temporal and spatial evolution of the distribution function according to a certain differential equation. Gorokhovski and coworkers [23, 24], Jones and coworkers [25, 26] all contributed to the development along this line, but different methods have been used for the determination of the size of children droplets.

3.3. DISPERSION MODEL

The effect of gas phase on the transport of discrete liquid phase droplets is called dispersion [27]. In the E-L framework, the evolution of droplet position and velocity is often described based on the following assumptions: 1), spherical droplet; 2), liquid density much larger than surrounding gas; 3), droplet internal vortical flow is neglected. Then dominant for droplets are the drag and gravitational forces, and therefore the particle momentum equation, also known as BBO (Basset-Boussinesq-Ossen) [28], is greatly simplified. The droplet motion can be described as:

$$\frac{d\mathbf{X}}{dt} = \mathbf{U}_p, \tag{3.6}$$

$$\frac{d\mathbf{U}_p}{dt} = \frac{\mathbf{U}_{seen} - \mathbf{U}_p}{\tau_\mathrm{p}} + \mathbf{g}, \tag{3.7}$$

where $\mathbf{U}_p$ is the droplet velocity vector, and $\mathbf{U}_{seen}$ is the gas phase velocity "seen" by the droplets. τ_p is the droplet relaxation time for Stokes flow:

$$\tau_\mathrm{p} = \frac{\tau_p^{St}}{C_D}, \quad \tau_p^{St} = \frac{\rho_{liq} D_p^2}{18\mu_\mathrm{m}}. \tag{3.8}$$

The deviation from Stokes drag (C_D) in most cases is given by the Schiller-Naumann correlation:

$$C_D = \begin{cases} 1 + 0.15 Re_p^{0.687}, & Re_p \le 1000 \\ 0.44 Re_p / 24, & Re_p > 1000 \end{cases} \tag{3.9}$$

some other empirical corrections are also reported in literature [29]. The droplet Reynolds number $\mathrm{Re_p}$ is defined as:

$$\mathrm{Re_p} = \frac{\rho_\mathrm{g} |\mathbf{U}_\mathrm{seen} - \mathbf{U}_\mathrm{p}| D_\mathrm{p}}{\mu_\mathrm{m}}, \tag{3.10}$$

D_p is the droplet diameter, ρ_g the gas phase density and μ_m the gas phase viscosity evaluated at the film (subscript "m") condition (see Eq. (3.28)).

Sazhin et al. [30] have suggested a modification of C_D for the evaporating spray:

$$C_{D,evp} = \frac{C_D}{(1+B_M)^\alpha}, \quad \alpha = \begin{cases} 1, & B_M < 0.78 \\ 0.75, & B_M \ge 0.78 \end{cases} \tag{3.11}$$

where B_M is the Spalding mass transfer number, definition of which is given by Eq. 3.15.

In order to calculate droplet drag force, the seen gas phase velocity, $\mathbf{U}_{seen}$, has to be provided. It can be decomposed as follows:

$$\mathbf{U}_{seen} = \tilde{\mathbf{U}}\left(\mathbf{x}_p, t\right) + \mathbf{u}''_{\mathbf{seen}} \tag{3.12}$$

where $\tilde{\mathbf{U}}$ is the mean continuous phase velocity, given by solving the Favre-averaged or filtered Navier-Stokes equation. The process of determining the fluctuating component, $\mathbf{u}''_{\mathbf{seen}}$, is called dispersion modeling [27].

Two main groups of dispersion models are the Continuous Random Work (CRW) model and the Langevin model. The droplet seen velocity fluctuation $\mathbf{u}''_{\mathbf{seen}}$ is related to the gas phase Reynolds stresses obtained from a turbulence model, e.g. Reynolds Stress Model (RSM), or transported PDF method in these models. For the details of these two models, please refer to [27, 31] and references therein.

3.4. EVAPORATION MODEL

Models that describe the heat and mass transfer between liquid and gas phase are called evaporation model. Evaporation is a very complicated process, to simplify the discussion, the following assumptions are made for the evaporation models that will be discussed below: 1), single component spherical droplet; 2), atmospheric pressure; 3), radiative heat transfer is neglected. A complete single droplet evaporation model includes four parts: Liquid Phase Model (LPM), Droplet Surface Properties (DSP) model, gas side Heat and Mass Transfer (HMT) model and “Seen" Gas Properties (SGP) model, see Fig. 3.3.

3.4.1. LIQUID PHASE MODEL (LPM)

Liquid fuels are normally injected at a relative low temperature. Combustion in the gas phase creates a hot environment for the droplets, which raise their temperature through convective heat transfer at the droplet surface. Droplet heating models can be subdivided into following cases with increasing complexity [32]:

1. constant droplet temperature;
2. uniform but time-evolving droplet temperature model (infinite conductivity model) [29];
3. finite conductivity model, but ignoring recirculation inside droplets (conduction limit model) [33];
4. models taking into account both finite conductivity and internal recirculation by introducing a correction factor to the liquid thermal conductivity (effective conductivity models) [34];
5. models describing the recirculation inside droplets in terms of vortex dynamics (vortex models);
6. models based on the full solution of the Navier-Stokes equation [32].

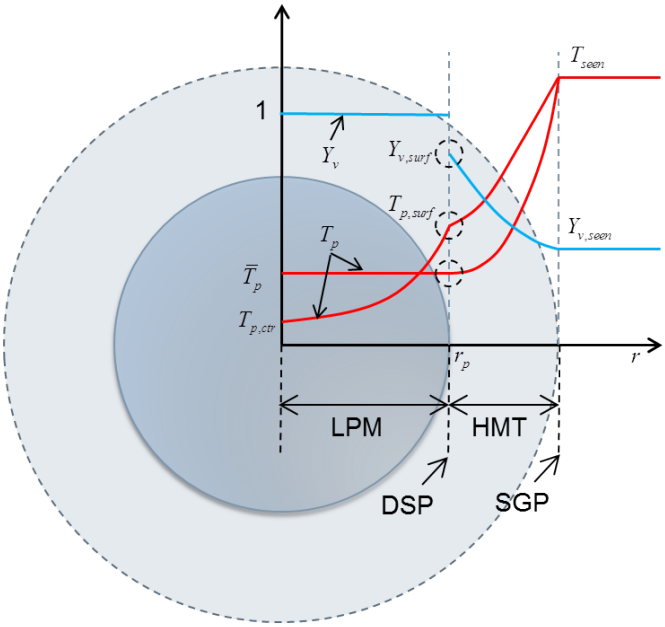

Figure 3.3: Illustration of evaporation modeling.

The infinite conductivity model is the most widely used one due to its computational efficiency and easy to implement. The temperature evolution described by this model is given in Eq. (3.13).

$$\frac{dT_\mathrm{p}}{dt} = \frac{\pi D_\mathrm{p} \lambda_\mathrm{m} \mathrm{Nu}}{m_\mathrm{p} C_{p,\mathrm{liq}}} \left(T_\mathrm{seen} - T_\mathrm{p}\right) + \frac{1}{C_{p,\mathrm{liq}}} \frac{L_v\left(T_\mathrm{p}\right)}{m_\mathrm{p}} \dot{m}_\mathrm{p}. \tag{3.13}$$

where T_p is the droplet temperature, λ_m is the gas phase thermal conductivity (see Eq. (3.28)), Nu the Nusselt number, $C_{p,\mathrm{liq}}$ the liquid phase heat capacity, L_v the latent heat of evaporation, and m_p the droplet mass.

Alternative to Eq. (3.13), finite droplet conductivity can be accounted for with more sophisticated models for droplet internal temperature profile. Sazhin et al [33] proposed a finite conductivity model, in which the temperature distribution inside the droplet is assumed to be a parabola. This model is named “parabolic temperature profile model". Besides the mean droplet temperature, the droplet surface temperature is also obtained during the calculation. And from these information, the temperature distribution inside the droplets can be obtained.

3.4.2. DROPLET SURFACE PROPERTIES (DSP) MODEL

The mass transfer rate is given as:

$$\frac{dm_p}{dt} = \pi D_p Sh \mathscr{D}_\mathrm{vap} \rho_g ln\left(1 + B_M\right). \tag{3.14}$$

B_M is the Spalding mass transfer number and is calculated as following:

$$B_M = \frac{Y_{v,surf} - Y_{v,seen}}{1 - Y_{v,seen}} \tag{3.15}$$

The vapor mass fraction at the droplet surface, $Y_{v,surf}$, is required in order to evaluate the B_M. The surface fuel mass fraction is normally obtained from Raoult's Law, which assumes that the mole fraction at the droplet surface is equal to the ratio of the partial pressure of fuel vapor to the total pressure of the gas. Various correlations exist to evaluate the partial pressure of fuel vapor at droplet surface. If it is assumed that the equilibrium between gas and droplet surface has been reached at each time step, the mole fraction of fuel vapor $X_{v,surf}$ at the droplet surface can be calculated from the Clausius-Clapeyron equation:

$$X^{eq}_{v,surf} = \exp\left[\frac{L_v(T_{\text{surf}})}{R_u/W_v}\left(\frac{1}{T_{\text{boil}}} - \frac{1}{T_{\text{surf}}}\right)\right], \tag{3.16}$$

and then

$$Y_{v,surf} = \frac{X^{eq}_{v,surf}}{X^{eq}_{v,surf} + \left(1 - X^{eq}_{v,surf}\right) W_{seen}/W_v}. \tag{3.17}$$

This is the so-called equilibrium model, R_u is the universal gas constant, W the molecular weight, subscript "v" refers to fuel vapor properties, and T_{boil} is the liquid boiling temperature.

Instead of Eq. (3.16), the non-equilibrium effect can be considered by using Lamgmuir-Knudsen law:

$$X^{neq}_{v,surf} = X^{eq}_{v,surf} - \left(\frac{L_K}{D_{\text{p}}/2}\right)\beta, \tag{3.18}$$

where L_K is the Knudsen layer thickness:

$$L_K = \frac{\mu_{\text{m}}\sqrt{2\pi T_{\text{p}} R_u/W_v}}{\alpha_e \text{Sc}_{\text{m}} \text{Pr}_{\text{m}}}. \tag{3.19}$$

$\alpha_e = 1$ is the molecular accommodation coefficient [29]. The non-dimensional evaporation parameter β is:

$$\beta = -\left(\frac{3\text{Pr}_{\text{m}}\tau^{St}_{\text{p}}}{2}\right)\frac{\dot{m}_{\text{p}}}{m_{\text{p}}}, \tag{3.20}$$

where Pr_{m} and Sc_{m} are the Prandtl and Schmidt number, respectively. Replacing the $X^{eq}_{v,surf}$ in Eq. (3.17) with $X^{neq}_{v,surf}$, one obtains the non-equilibrium evaporation model. Non-equilibrium effects were shown to be significant when the initial droplet diameter is less than 50 μm and are enhanced with increasing slip velocity [29].

3.4.3. GAS SIDE HEAT AND MASS TRANSFER (HMT) MODEL

In practical applications, the droplets are always exposed to a convective environment, the enhancements of heat and mass transfer by the convective flow are normally incorporated by introducing the Nusselt number, Nu, and Sherwood number, Sh (in Eqs. (3.13)

and (3.14)). For flow around a solid sphere, they can be evaluated by the well known Ranz-Marshall correlation:

$$\mathrm{Sh} = 2 + 0.552\mathrm{Re}_\mathrm{p}^{1/2}\mathrm{Sc}_\mathrm{m}^{1/3} \quad \text{and} \quad \mathrm{Nu} = 2 + 0.552\mathrm{Re}_\mathrm{p}^{1/2}\mathrm{Pr}_\mathrm{m}^{1/3}, \tag{3.21}$$

Gas phase Prandtl number and Schmidt number are given by

$$\mathrm{Pr}_\mathrm{m} = \frac{\mu_\mathrm{m} C_{p,\mathrm{m}}}{\lambda_m} \quad \text{and} \quad \mathrm{Sc}_\mathrm{m} = \frac{\mu_\mathrm{m}}{\rho_g D_m}. \tag{3.22}$$

where D_m is the diffusivity evaluated at film properties (see Eq. (3.28)).

Abramzon and Sirignano [34] proposed the following corrections for Nu and Sh in order to take into account the effects of Stefan flow (outward flow) on the surface of evaporating droplets:

$$\mathrm{Sh}^* = 2 + \frac{\mathrm{Sh} - 2}{F_M}, \quad \text{and} \quad \mathrm{Nu}^* = 2 + \frac{\mathrm{Nu} - 2}{F_T}. \tag{3.23}$$

$$F_M = (1 + B_M)^{0.7} \frac{\ln(1 + B_M)}{B_M}, \quad \text{and} \quad F_T = (1 + B_T)^{0.7} \frac{\ln(1 + B_T)}{B_T}. \tag{3.24}$$

$$B_T = (1 + B_M)^{\phi} - 1, \quad \text{with} \quad \phi = \frac{C_{p,\mathrm{vap}}}{C_{p,\mathrm{m}}} \frac{\mathrm{Sh}^*}{\mathrm{Nu}^*} \frac{\mathrm{Pr}_\mathrm{m}}{\mathrm{Sc}_\mathrm{m}}. \tag{3.25}$$

B_T is the Spalding mass and heat transfer numbers. In the Abramzon-Sirignano model Nu and Sh in Eqs. (3.13) and (3.14) are replaced with Nu^* and Sh^*. This model is generally recommended for modeling droplet evaporation.

Alternatively, Bird's correction [35] can be applied for Nu to account for the reduction of heat transfer due to evaporation:

$$\mathrm{Nu}' = \mathrm{Nu} \frac{\beta}{e^{\beta} - 1}, \tag{3.26}$$

β is given in Eq. (3.20). This correction is the analytic expression of the quasi-steady solution of the gas field equations coupled to the droplet surface boundary conditions. And compared to Abramzon and Sirignano model it does not require an iterative solution, therefore is slightly computationally cheaper than the latter. To apply correction (3.26), the Nu in Eq. (3.13) should be replaced by Nu'.

Only Bird's correction is implemented in the public release of OpenFOAM®. A comparison of the performance between the Abramzon and Sirignano model and Bird's correction will be given in Chapter 7.

3.4.4. "SEEN" GAS PROPERTIES (SGP) MODEL

Similar to the situation in the dispersion model where the seen gas velocity is required, the temperature and composition of seen gas are required in order to close the evaporation model. For most applications, these seen properties are evaluated using the mean values in RANS simulations [36] or filtered quantities in LES [37, 38], neglecting the influence of turbulent fluctuations. Transported PDF methods potentially allow for more refined modeling of the seen composition and temperature. Jones and co-workers [39]

developed a stochastic Markov model to account for the effect of the SGS fluctuations of gas-phase reactive scalars on droplet dispersion and evaporation in LES. Naud and De Meester [40, 41] proposed to sample the “seen" gas temperature and composition from a given gas-phase stochastic particle present in the same computational cell. The gas-phase particle is chosen to be the one with enthalpy the closest to the enthalpy of the saturated mixture.

As shown in Fig. 3.3, gas phase conditions change quickly from droplet surface properties to seen gas phase properties within a thin film surrounding the droplets. A decision has to be made on at which condition the gas phase properties (indicated by subscript ‘m’) used in the evaporation and dispersion model should be evaluated. Weighted averages of droplet surface properties and “seen" gas properties are normally used:

$$T_{\mathrm{m}} = (1-\alpha)\, T_{\mathrm{surf}} + \alpha T_{\mathrm{seen}} \quad \text{and} \quad \mathbf{Y}_{\mathrm{m}} = (1-\alpha)\, \mathbf{Y}_{\mathrm{surf}} + \alpha \mathbf{Y}_{\mathrm{seen}}. \tag{3.27}$$

Typically $\alpha = 1/3$ is widely accepted for spray combustion simulation. It is the well known “1/3 rule" [42]. However, many other possibilities exist, for example $\alpha = 1$ means to directly use the “seen" gas properties, $\alpha = 1/2$ has also been used in some model variants [29]. A comparative study on the role of the “1/3 rule" showed that it does not only has a strong influence on the evaporation process but also influences the droplet dispersion behavior. Using $\alpha = 1$ leads to too fast decay of droplet velocity [3], while $\alpha = 1/3$ gives very good results. Application of the averaging rule means the evaluation of gas phase properties as following:

$$\begin{aligned} \mu_{\mathrm{m}} &= \mu(T_{\mathrm{m}}, \mathbf{Y}_{\mathrm{m}}), \quad \lambda_m = \lambda(T_{\mathrm{m}}, \mathbf{Y}_{\mathrm{m}}), \\ D_m &= D(T_{\mathrm{m}}, \mathbf{Y}_{\mathrm{m}}), \quad C_{p,\mathrm{m}} = C_p(T_{\mathrm{m}}, \mathbf{Y}_{\mathrm{m}}). \end{aligned} \tag{3.28}$$

3.5. TURBULENT TWO-WAY COUPLING

The turbulence model here refers to the models that are used to close the Reynolds stresses in the RANS equations or the sub-grid stresses in the filtered N-S equations. The influence of the dispersed phase on gas phase flow is accounted for by the so-called “two-way coupling". It is represented in the form of terms in the RANS or the LES filtered equations for momentum, mass and energy. For more information on the turbulent two-way coupling modeling, please refer to [1] and [43]. Two way coupling also occurs on the droplet scale, Shinjo and Umemura [44, 45] numerically studied the early flame kernel development around the droplet with in a realistic dense spray DNS. They found that in the dense spray, the droplet wake vorticity enhances the mixing and suggested that the point source assumption, which assumes that the droplet scale is much smaller than the turbulent eddy scale, needs to be modified with diffusion enhancement model.

3.6. COMBUSTION MODELS FOR SPRAY FLAME

The compromise between precise representation of the flame characteristics and reducing computation cost is the main concern for the modelers to develop a new combustion model. The flamelet model, proposed by Peters [46], enables employing detail chemical mechanism without significant increase of the computational cost, thus has been widely used in the simulation of gaseous fuel combustion. Different variants of

flamelet model have been reported in literature, such as the steady-flamelet model [46], unsteady-flamelet model [47], flamelet/progress-variable approach [48], and Flamelet Generated Manifolds (FGM) [49]. These models are referred to as flamelet-based models.

Application of flamelet model in the simulation of spray combustion was firstly introduced by Hollmann and Gutheil [50] through the modification of the conservation equations of both the mixture fraction and its scalar dissipation rate to account for spray processes. But soon it became clear that the direct use of the gaseous flamelet-based model on spray combustion may not be sufficiently accurate. To understand the characteristics of the spray flame, many studies have been done on the laminar spray counterflow flame [51–55].

In the case of a spray flame, the mixture fraction is no longer a conserved scalar because of the droplet evaporation providing local fuel source [53]. Values of gas temperature, mass fractions of chemical species in the spray flame are significantly different from values in a gaseous diffusion flame. In particular, the temperature in the spray flame can be much higher than that in the gaseous diffusion flame. This is believed to be due to a lower scalar dissipation rate and the coexistence of premixed and diffusion combustion in the spray flame [53]. Droplet evaporation modifies the reaction zone in the mixture fraction space: the inclusion of the evaporation source term may shift the reaction zone or create a dual reaction zone structure[56]. Unlike the gaseous flame, the scalars (i.e. species mass fraction and gas phase temperature) are not uniquely dependent on the mixture fraction and scalar dissipation rate or progress variable[1, 52, 55]. The presence of the droplet evaporation plays an essential role making the spray flame characteristics different from its gaseous counterpart. Droplet evaporation not only introduces mass and heat transfer between two phase which goes beyond classical flamelet-like models, but also alters the gas phase reaction rate[55]. The pronounced differences between spray flames and gaseous flames suggest that the application of a lookup table that is based on a flamelet equation associated with a gaseous diffusion flame to the spray flames can lead to significant errors [53].

Many improvements have been suggested in literature to improve the capability of the flmelet-based models on the prediction of spray flames.

Hollmann and Gutheil [57] proposed a spray flamelet model. The spray flamelet library is built by calculating the spray counterflow flame, i.e., replacing the gaseous fuel inlet in the gaseous counterflow configuration with the fuel droplets carried by gas (normally air). This strategy explicitly includes most of the spray flame characteristics into the flamelet library, however, it requires a very high-dimensional library as all physical spray parameters have to be included to characterize the spray flamelet: the initial droplet diameter, the initial spray velocity and the equivalence ration, etc.. Therefore it also requires a high-dimensional PDF in the turbulent spray combustion simulation.

Baba and Kurose [53] suggested a modified flamelet/progress variable (FPV) approach, in which total enthalpy rather than product mass fraction is chosen as the progress variable in the Flamelet/ Progress variable model to take into account the heat and mass transfer between two phases. However, even the DNS with the modified flamelet/progress variable approach tends to underestimate the gaseous temperature in the central region of the spray jet flame.

Franzelli et al. [54] developed a Partially Pre-mixed Flamelet method (2PFT), parametrized by the progress variable Yc, the mixture fraction z, and the scalar dissipation rate χ^*, identifying the combustion regime. And compared the new method with the Pre-mixed Flamelet (PFT) method and Diffusion Flamelet (DFT) method. Results showed that the 2PFT tabulation method better describes the flame structure compared to the classical techniques based on single archetypal flamelets and is more adequate for counterflow spray flames. It has also been demonstrated that the chemical structure of laminar spray flames could be modeled by a tabulated multi-regime flamelet combustion regime based on gaseous flamelets.

Luo et al. [56] derived new flamelet equations for spray combustions, directly taking into account the influences of the evaporation:

$$\rho\frac{\partial Y_i}{\partial \tau}-\rho\frac{\chi}{2}\frac{\partial^2 Y_i}{\partial Z^2}=\dot{\omega}_i+\dot{S}_m\left(Z-1\right)\frac{\partial Y_i}{\partial Z}+\left(\delta_{i,i_f}-Y_i\right)\dot{S}_m, \tag{3.29}$$

$$\rho\frac{\partial T}{\partial \tau}-\rho\frac{\chi}{2}\frac{\partial^2 T}{\partial Z^2}=\frac{1}{C_p}\left(\dot{\omega}_T+\dot{S}_T\right)+\dot{S}_m\left(Z-1\right)\frac{\partial T}{\partial Z}-T\dot{S}_m, \tag{3.30}$$

where Y_i is the mass fraction of ith species, T the gas phase temperature, $\dot{S}_m$ and $\dot{S}_T$ are respectively the mass and heat transfer due to evaporation, δ_{i,i_f} is the Dirac delta function, and i_f denotes the fuel. The last two terms in the spray Eqs. (3.29) and (3.30) respectively describe the effects of mixing of the evaporated vapor and the direct effect of mass transfer.

Olguin and Gutheil [55] analyzed the influence of the evaporation of liquid fuel on the flamelet structures by means of numerical simulations of an axisymmetric laminar mono-disperse ethanol/air counterflow spray flame. The results showed that the distribution of the spray evaporation rate plays a key role in the characterization of the spray flame structure. The derived spray flamelet equations are identical to that of Luo[56]. They proposed to introduce the droplet evaporation rate as an additional controlling parameter in order to better characterize the spray flame. However, there are certain practical issues for this method. For example, the evaporation rate strongly depends on many parameters, and it is difficult to be estimated before the real simulation is down. Therefore to built a lookup table that covers all possible evaporation rate can be challenging.

Very recently, Franzelli et al. [58] proposed a generalized definition of mixture fraction for the two phase mixing in spray combustion. And have derived new spray flamelet formulations in this new defined mixture fraction space.

Other models that have been applied to model spray combustion including: Conditional Moment Closure (CMC) [59, 60], Probability Density Function (PDF) or Filtered Density Function (FDF) [36, 61], two phase turbulent combustion model (FSM) [62] and second-order moment (SOM) turbulent combustion model [63].

REFERENCES

[1] P. Jenny, D. Roekaerts, and N. Beishuizen, *Modeling of turbulent dilute spray combustion,* Progress in Energy and Combustion Science **38**, 846 (2012).

[2] S. Balachandar and J. K. Eaton, *Turbulent Dispersed Multiphase Flow,* Annual Review of Fluid Mechanics **42**, 111 (2010).

[3] L. Ma, B. Naud, and D. Roekaerts, *Transported PDF Modeling of Ethanol Spray in Hot-Diluted Coflow Flame,* Flow, Turbulence and Combustion , DOI:10.1007/s10494 (2015).

[4] D. Rochaya, *Numerical Simulation of Spray Combustion using Bio-mass Derived Liquid Fuels*, Ph.D. thesis, Cranfield University (2007).

[5] K. Luo, H. Pitsch, M. Pai, and O. Desjardins, *Direct numerical simulations and analysis of three-dimensional n-heptane spray flames in a model swirl combustor,* Proceedings of the Combustion Institute **33**, 2143 (2011).

[6] A. Fujita, H. Watanabe, R. Kurose, and S. Komori, *Two-dimensional direct numerical simulation of spray flames - Part 1: Effects of equivalence ratio, fuel droplet size and radiation, and validity of flamelet model,* Fuel **104**, 515 (2013).

[7] M. Gorokhovski and M. Herrmann, *Modeling Primary Atomization,* Annual Review of Fluid Mechanics **40**, 343 (2008).

[8] M. Birouk and I. Gokalp, *Current status of droplet evaporation in turbulent flows,* Progress in Energy and Combustion Science **32**, 408 (2006).

[9] A. Kourmatzis, P. X. Pham, and A. R. Masri, *Characterization of atomization and combustion in moderately dense turbulent spray flames,* Combustion and Flame **162**, 978 (2015).

[10] M. Linne, *Imaging in the optically dense regions of a spray: A review of developing techniques,* Progress in Energy and Combustion Science **39**, 403 (2013).

[11] J. Shinjo and A. Umemura, *Detailed simulation of primary atomization mechanisms in Diesel jet sprays (isolated identification of liquid jet tip effects),* Proceedings of the Combustion Institute **33**, 2089 (2011).

[12] R. Lebas, T. Menard, P. Beau, A. Berlemont, and F. Demoulin, *Numerical simulation of primary break-up and atomization: DNS and modelling study,* International Journal of Multiphase Flow **35**, 247 (2009).

[13] B. Duret, J. Reveillon, T. Menard, and F. Demoulin, *Improving primary atomization modeling through DNS of two-phase flows,* International Journal of Multiphase Flow **55**, 130 (2013).

[14] P. Senecal, D. Schmidt, I. Nouar, C. Rutland, R. Reitz, and M. Corradini, *Modeling high-speed viscous liquid sheet atomization,* International Journal of Multiphase Flow **25**, 1073 (1999).

[15] H. Correia Rodrigues, M. J. Tummers, E. H. van Veen, and D. Roekaerts, *Spray flame structure in conventional and hot-diluted combustion regime,* Combustion and Flame **162**, 759 (2015).

[16] ANSYS, *Fluent 15.0 Theory Guide,* (2014).

[17] A. Vallet and R. Borghi, *Modélisation Szhin de l'atomisation d'un jet liquide,* Computational fluid mechanics **327**, 1015 (1999).

[18] J. Chesnel, J. Reveillon, T. Menard, and F.-X. Demoulin, *Large eddy simulation of liquid jet atomization,* Atomization and Sprays **21**, 711– (2011).

[19] D. Lakehal, M. Meier, and M. Fulgosi, *Interface tracking towards the direct simulation of heat and mass transfer in multiphase flows,* International Journal of Heat and Fluid Flow **23**, 242 (2002).

[20] M. Herrmann, *A parallel Eulerian interface tracking/Lagrangian point particle multi-scale coupling procedure,* Journal of Computational Physics **229**, 745 (2010).

[21] S. Navarro-Martinez, *Large eddy simulation of spray atomization with a probability density function method,* International Journal of Multiphase Flow **63**, 11 (2014).

[22] N. Patel and S. Menon, *Simulation of spray-turbulence-flame interactions in a lean direct injection combustor,* Combustion and Flame **153**, 228 (2008).

[23] M. A. Gorokhovski and V. L. Saveliev, *Analyses of Kolmogorov's model of breakup and its application into Lagrangian computation of liquid sprays under air-blast atomization,* Physics of Fluids **15**, 184 (2003).

[24] S. Apte, M. Gorokhovski, and P. Moin, *LES of atomizing spray with stochastic modeling of secondary breakup,* International Journal of Multiphase Flow **29**, 1503 (2003).

[25] W. P. Jones and C. Lettieri, *Large eddy simulation of spray atomization with stochastic modeling of breakup,* Physics of Fluids **22**, 115106 (2010).

[26] W. Jones, C. Lettieri, A. Marquis, and S. Navarro-Martinez, *Large Eddy Simulation of the two-phase flow in an experimental swirl-stabilized burner,* International Journal of Heat and Fluid Flow **38**, 145 (2012).

[27] E. Amani and M. Nobari, *Systematic tuning of dispersion models for simulation of evaporating sprays,* International Journal of Multiphase Flow **48**, 11 (2013).

[28] J. S. Shirolkar, C. F. M. Coimbra, and M. Q. Mcquay, *Flundamental aspects of modeling turbulent particle dispersion in dilute flows,* Progress in Energy and Combustion Science **22**, 363 (1996).

[29] R. S. Miller, K. Harstad, and J. Bellan, *Evaluation of equilibrium and non-equilibrium evaporation models for many-droplet gas-liquid flow simulations,* International Journal of Multiphase Flow **24**, 1025 (1998).

[30] S. S. Sazhin, W. A. Abdelghaffar, E. M. Sazhina, and M. R. Heikal, *Models for droplet transient heating: Effects on droplet evaporation, ignition, and break-up,* International Journal of Thermal Sciences **44**, 610 (2005).

[31] B. Naud, *Particle dispersion modelling based on the Generalised Langevin Model for the seen velocity,* in *Turbulence, Heat and Mass Transfer 7* (2012).

[32] S. S. Sazhin, *Advanced models of fuel droplet heating and evaporation,* Progress in Energy and Combustion Science **32**, 162 (2006).

[33] S. S. Sazhin, T. Kristyadi, W. Abdelghaffar, and M. Heikal, *Models for fuel droplet heating and evaporation: Comparative analysis,* Fuel **85**, 1613 (2006).

[34] B. Abramzon and W. Sirignano, *Droplet vaporization model for spray combustion calculations,* International Journal of Heat and Mass Transfer **32**, 1605 (1989).

[35] R. Bird, W. Stewart, and W. Lightfoot, *Transport Phenomena* (Wiley, US, 1960).

[36] S. Bhattacharjee and D. C. Haworth, *Simulations of transient n-heptane and n-dodecane spray flames under engine-relevant conditions using a transported PDF method,* Combustion and Flame **160**, 2083 (2013).

[37] S. De and S. H. Kim, *Large eddy simulation of dilute reacting sprays: Droplet evaporation and scalar mixing,* Combustion and Flame **160**, 2048 (2013).

[38] M. Chrigui, A. R. Masri, A. Sadiki, and J. Janicka, *Large Eddy Simulation of a polydisperse ethanol wpray flame,* Flow, Turbulence and Combustion **90**, 813 (2013).

[39] W. Jones, A. Marquis, and K. Vogiatzaki, *Large-eddy simulation of spray combustion in a gas turbine combustor,* Combustion and Flame **161**, 222 (2014).

[40] R. de Meester, *Analysis of scalar mixing in hybrid RANS-PDF calculations of turbulent gas and spray flames*, Ph.D. thesis, University Ghent (2012).

[41] R. de Meester, B. Naud, U. Maas, and B. Merci, *Transported scalar PDF calculations of a swirling bluff body flame SM1 with a reaction diffusion manifold,* Combustion and Flame **159**, 2415 (2012).

[42] G. Faeth, *Evaporation and combustion of sprays,* Progress in Energy and Combustion Science **9**, 1 (1983).

[43] N. A. Beishuizen, *PDF modelling and particle-turbulence interaction of turbulent spray flames*, Ph.D. thesis, Delft University of Technology (2008).

[44] J. Shinjo and A. Umemura, *Droplet/turbulence interaction and early flame kernel development in an autoigniting realistic dense spray,* Proceedings of the Combustion Institute **34**, 1553 (2013).

[45] J. Shinjo, J. Xia, and A. Umemura, *Droplet/ligament modulation of local small-scale turbulence and scalar mixing in a dense fuel spray,* Proceedings of the Combustion Institute (2014), 10.1016/j.proci.2014.06.088.

[46] N. Peters, *Laminar diffusion flamelet models in non-premixed turbulent combustion,* Progress in Energy and Combustion Science **10**, 319 (1984).

[47] H. Pitsch and H. Steiner, *Scalar mixing and dissipation rate in large-eddy simulations of non-premixed turbulent combustion,* Proceedings of the Combustion Institute **28**, 41 (2000).

[48] C. D. Pierce and P. Moin, *Progress-variable approach for large-eddy simulation of non-premixed turbulent combustion,* Journal of Fluid Mechanics **504**, 73 (2004).

[49] J. A. van Oijen and L. P. H. de Goey, *Modelling of premixed laminar flames using flamelet-generated manifolds,* Combustion Science and Technology **161**, 113 (2000).

[50] C. Hollmann and E. Gutheil, *Modeling of turbulent spray flames including detailed chemistry,* in *26 th Symposium (International) on Combustion* (1996) pp. 1731–1738.

[51] E. Gutheil and W. Sirignano, *Counterflow spray combustion modeling with detailed transport and detailed chemistry,* Combustion and Flame **113**, 92 (1998).

[52] H. Watanabe, R. Kurose, S. Hwang, and F. Akamatsu, *Characteristics of flamelets in spray flames formed in a laminar counterflow,* Combustion and Flame **148**, 234 (2007).

[53] Y. Baba and R. Kurose, *Analysis and flamelet modelling for spray combustion,* Journal of Fluid Mechanics **612**, 45 (2008).

[54] B. Franzelli, B. Fiorina, and N. Darabiha, *A tabulated chemistry method for spray combustion,* Proceedings of the Combustion Institute **34**, 1659 (2013).

[55] H. Olguin and E. Gutheil, *Influence of evaporation on spray flamelet structures,* Combustion and Flame **161**, 987 (2014).

[56] K. Luo, J. Fan, and K. Cen, *New spray flamelet equations considering evaporation effects in the mixture fraction space,* Fuel **103**, 1154 (2013).

[57] C. Hollmann and E. Gutheil, *Flamelet-modeling of turbulent spray diffusion flames based on a laminar spray flame library,* Combustion Science and Technology **135**, 175 (1998).

[58] B. Franzelli, A. Vié, and M. Ihme, *On the generalisation of the mixture fraction to a monotonic mixing-describing variable for the flamelet formulation of spray flames,* Combustion Theory and Modelling **7830**, 1 (2015).

[59] S. Ukai, A. Kronenburg, and O. Stein, *LES-CMC of a dilute acetone spray flame,* Proceedings of the Combustion Institute **34**, 1643 (2013).

[60] S. Ukai, A. Kronenburg, and O. Stein, *Large eddy simulation of dilute acetone spray flames using CMC coupled with tabulated chemistry,* Proceedings of the Combustion Institute **35**, 1667 (2015).

[61] W. Jones, A. Marquis, and D. Noh, *LES of a methanol spray flame with a stochastic sub-grid model,* Proceedings of the Combustion Institute **35**, 1685 (2015).

[62] F. Wang, B. Hu, and Y. Huang, *A two-phase turbulent combustion model and its validation for spray flames,* Fuel **113**, 280 (2013).

[63] K. Luo, Y. Bai, J. Yang, H. Wang, L. Zhou, and J. Fan, *A-priori validation of a second-order moment combustion model via DNS database,* International Journal of Heat and Mass Transfer **86**, 415 (2015).

II

APPLICATIONS

4

STUDY OF DSHC FLAME USING STEADY FLAMELET MODEL

This chapter reports the first attempt of modeling DSHC flame using ANSYS Fluent®. The steady laminar flamelet model with a detailed chemical mechanism is employed. The turbulent two-phase flow field is predicted by the standard k-ϵ turbulence model taking into account the turbulence two-way coupling. The Linearized Instability Sheet Atomization (LISA) model is used to simulate the injection and atomization processes of the liquid fuel. The calculated droplet velocities at different downstream elevations for different droplet size classes show good agreement with the measured results. Predicted gas phase velocities also display reasonably good agreement. The main failure of the present model is its inability to predict the lifted-off phenomenon of this flame.

Content in this chapter has been published in the following paper:
L. Ma, S. Zhu, M. J. Tummers, T. H. van der Meer and D. Roekaerts, "Numerical Investigation of Ethanol Spray-in-Hot-Coflow Flame using Steady Flamelet Model", In Proceedings of Eighth Mediterranean Combustion Symposium (2013), pp. 1-12.

4.1. INTRODUCTION

Spray combustion is widely utilized in various engineering applications, such as industrial furnaces and propulsion systems. Due to the increasing demand on both the performance of these combustion devices and pollutant emission control, a deep insight into the processes and phenomena involved in spray combustion is essential.

Flameless combustion also known as mild combustion is attracting wide scientific interests due to its potential of high efficiency and low NOx emission. A lot of attention has been paid to the investigation of flameless combustion of gaseous fuel by means of both experiment and numerical simulation [2–4]. Liquid fuel, which contributes to a large proportion of the global energy supply, however, is rarely studied in the mode of flameless combustion [5]. The Delft Spray-in-Hot-Coflow (DSHC) burner was designed to study the flameless oxidation of light oils [6]. A numerical study of DSHC is presented in this paper. Modeling of turbulent spray combustion is particularly challenging because many physical and chemical processes including turbulence, atomization, evaporation, combustion and radiative heat transfer are involved and interact with each other. A set of models, hence has to be carefully chosen to accurately predict the aforementioned processes. In this study, a Eulerian-Lagrangian RANS approach is adopted for the two phase flow. The exchanges of mass, momentum and heat between two phases are described by extra source terms appearing in the governing equations for both phases. The Linearized Instability Sheet Atomization (LISA) model [7] is used to simulate the interaction processes between the droplets and the continuous phase. The standard $k-\epsilon$ model taking into account turbulence two-way coupling is used to predict the turbulent flow field. Radiative heat transfer is predicted by the Discrete Ordinates (DO) radiation model with the weighted-sum-of-gray-gases model (WSGGM).

Turbulence-chemistry interaction is described using the non-premixed Steady Flamelet Model (SFM). The chemical mechanism used in flamelet generation is the detailed ethanol high temperature oxidation mechanism of Marinov [8] consisting of 57 species and 383 reactions. The application of the classical flamelet model to spray combustion was first made by Hollmann and Gutheil [9] to simulate a methanol/air diffusion flame and extended by them to a formulation using spray flamelets [10]. Later many applications and improvements of this concept followed [11–13]. In the present investigation the standard gaseous flamelet model is used as implemented in the CFD code ANSYS Fluent®. An overview of advantages and disadvantages of this and other modeling possibilities is given in [14].

The purpose of this paper is to investigate the applicability of the above-mentioned models in the modeling of spray combustion under hot coflow condition. The calculated results are compared with the DSHC experimental data for this reason. The experimental setup, relevant models, the simulation results as well as the discussions on the ability and limitations of the present models are discussed sequentially hereafter.

4.2. MODELING APPROACH

4.2.1. CALCULATION DOMAIN AND BOUNDARY CONDITIONS

Due to the axisymmetric structure of the experimental setup, a 2D calculation with one half of the burner longitudinal cross-section was conducted. Different calculation do-

mains with different grid resolutions have been made to demonstrate the grid independence of the results. The calculation domain and the boundary conditions are shown in Fig. 4.1. Due to the restriction of the present modeling approach, only one mixture frac-

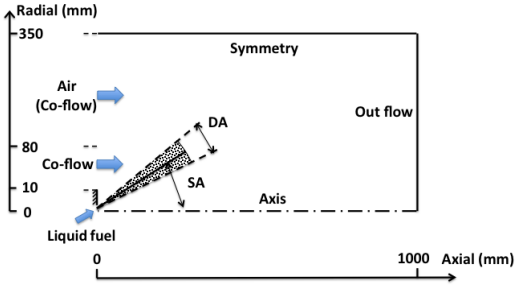

Figure 4.1: Schematic of calculation domain (SA: Spray Angle, DA: Dispersion Angle).

tion and hence two different types of streams, can be applied. This means the entrainment of the ambient air into the coflow cannot be taken into account. This is acceptable in the sense that the influence of the ambient air in the near injector region, where this study focuses on, is minor as observed in our comparative analysis. In the simulation, the ambient air is then replaced with the coflow composition but with ambient temperature. Regarding to the grid resolution, the Eulerian-Lagrangian approach used in this study raises the restriction that the discrete phase volume fraction should not exceed 10%-12%. A direct consequence of this constraint is that the computation cell should not be too small, especially in the dense region near the nozzle exit. Further refinement may even result in a convergence problem because of low number of parcels per cell. On the other hand, due to the presence of the high temperature coflow in the vicinity of the nozzle and the volatile nature of ethanol, fast evaporation is expected in this region. Fine grid is required to capture the mixing between the fuel vapor and the hot coflow and the motion of the droplets. Therefore, a compromise should be made on the grid resolution. A finest resolution of 0.2 mm near the nozzle has finally been employed and this gives a maximum discrete phase volume fraction less than 3% in the near nozzle region. Velocity

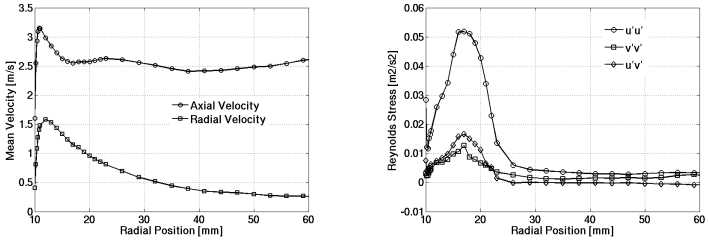

Figure 4.2: Velocity and turbulence boundary condition of co-flow. Left: mean axial and radial velocity, right: Reynolds stress components.

inlet boundary conditions are employed for both coflow and ambient air. Measured velocity and Reynolds stress profiles as shown in Fig. 4.2 are incorporated. Temperature

Table 4.1: Coflow and spray boundary conditions.

Coflow temperature and composition (mole fraction)				
Temperature (K)	O_2	CO_2	H_2O	N_2
1316.5	8.70 %	5.55 %	10.95 %	74.80 %
Spray inlet conditions				
Fuel Temperature (K)	Fuel flow rate (kg/s)		Injection pressure (bar)	Spray angle
301.15	1.46		7	70°

measurement has not yet been conducted for DSHC. Therefore, an assumed enthalpy loss together with measured oxygen concentration is used to calculate the equilibrium temperature and composition of the coflow by in-house code "FLAME". Table 4.1 gives the calculated co-flow temperature and species mole fractions.

As for the spray boundary condition, the method proposed in [15] is employed to estimate the injector exit diameter and the spray angle from the measured droplet concentration distributions. The measured droplet concentration is displayed in Fig. 4.3 . The positions where the droplet concentration has the peak value are treated as the center of the spray trajectory at that axial location. The trajectory is estimated according to these center positions. As shown in Fig. 4.4, the simulated trajectory with a spray angle of 70°and injector exit diameter of 0.21 mm seems giving a better fit with the measured trajectory. However, because the measurement starts at relatively high axial location, the trajectory already has been influenced by the coflow. The spray angle of 70° and injector exit diameter of 0.9 mm are used in the present study. And this results in a very good agreement of the droplets velocities with the experimental data as shown in the results and discussion section. The spray inlet conditions are also listed in Table 4.1.

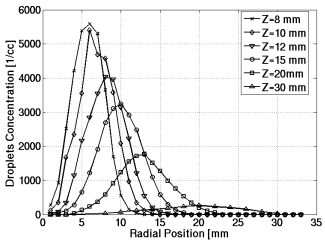

Figure 4.3: Droplet concentration at different axial locations ($\mathcal{Z}$ represents the axial position).

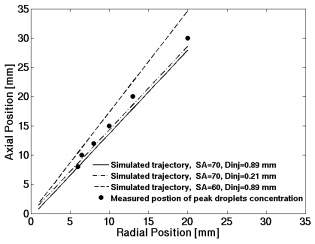

Figure 4.4: Estimation of the spray trajectory (SA: spray angle, D_{inj}: diameter of injector exit).

4.2.2. SPRAY MODEL

In spray combustion studies, most often the focus is on the modeling of the dilute spray combustion [14, 16] due to the complexity of the processes of injection and atomization. And the droplet distributions from experiment at a certain axial location, where the atomization has already finished and only a minor part of the evaporation has occurred, are often taken as boundary conditions. However, because of the hot coflow in DSHC, significant evaporation has already occurred before the first measured axial lo-

cation ($\mathcal{Z} = 8\ mm$), and the vapor concentration is difficult to measure. This yields a serious problem for application of dilute spray combustion modeling approach in this flame.

Alternatively, The Linearized Instability Sheet Atomization (LISA) model is employed to simulate the transition of the ethanol from internal injector flow to fully developed spray by pressure-swirl atomizer in the DSHC burner. It assumes that the growth of the Kelvin-Helmholtz waves on the sheet eventually break the liquid into ligaments. And then the ligaments break up into droplets due to varicose instability. The evolution of the spray is determined by drag, collision, coalescence, and secondary breakup. The LISA model consists of two stages: film formation and sheet breakup and atomization.

For the first stage, the centrifugal motion of the liquid within the injector creates a liquid film. The film thickness, t, is related to the mass flow rate by:

$$\dot{m}_{eff} = \pi \rho u t \left(d_{inj} - t\right), \tag{4.1}$$

where d_{inj} is the injector exit diameter, $\dot{m}_{eff}$ is the effective mass flow rate, u is the axial velocity at the injector exit.

The sheet breakup is based on the growth of sinusoidal waves. For waves that are long compared with the sheet thickness, ligaments are assumed to form once the unstable waves reach critical amplitude. If the surface disturbance has reached a value of η_b at a breakup time τ, the sheet breaks up and ligaments will be formed at a length given by:

$$L_b = U_\tau = \frac{U}{\Omega} \ln\left(\frac{\eta_b}{\eta_0}\right), \tag{4.2}$$

where Ω is the maximum growth rate, and $\ln\left(\eta_b/\eta_0\right)$ is an empirical sheet constant. The diameter of the ligaments formed at the point of breakup can be obtained from a mass balance:

$$d_L = \sqrt{\frac{8h}{K_s}}, \tag{4.3}$$

where K_s is the wave number corresponding to the maximum growth rate, Ω. For short waves, the ligament diameter is assumed to be linearly proportional to the wavelength that breaks up the sheet, as following:

$$d_L = \frac{2\pi C_L}{K_s}, \tag{4.4}$$

where C_L, the ligament constant, is equal to 0.5 by default.

In either the long-wave or the short-wave case, the breakup from ligaments to droplets is assumed to behave according to Weber's analysis for capillary instability. The most probable diameter for droplet diameter distribution, d_0, is determined form:

$$d_0 = 1.88 d_L \left(1 + 3Oh\right)^{1/6}. \tag{4.5}$$

Where Oh is the Ohnesorge number, which is a combination of the Reynolds number and the Weber number. The droplet diameter distribution is then determined in addition with a spread parameter and a dispersion angle.

The acceleration of the particle is predicted in the following manner:

$$\frac{du_{p,j}}{dt} = \frac{18\mu}{\rho_P D_p^2}\frac{C_D \mathrm{Re_p}}{24}\left(U_i - u_{p,i}\right) + \frac{g_i\left(\rho_p - \rho\right)}{\rho_p}, \tag{4.6}$$

where u_p is the droplet velocity, U the gas phase velocity, mu the molecular fluid viscosity, ρ_p the droplet density, rho the gas phase density, D_p the droplet diameter, $\mathrm{Re_p}$ the relative Reynolds number and C_D the drag coefficient. The first term in the right hand side represents the drag force per unit particle mass, and the second term is the gravity acceleration.

The droplet dispersion due to turbulence is treated through a stochastic tracking method with U_i sampled from an assumed velocity distribution. For the coupling between droplets and the gas phase, the momentum, heat and mass exchanges are updated while the droplets pass through the control volume. The momentum, heat and mass transfer between two phases are calculated in the following manner respectively:

$$F = \sum \dot{m}\frac{18\mu}{\rho_P D_p^2}\frac{C_D \mathrm{Re_p}}{24}\left(U - u_p\right)\Delta t, \tag{4.7}$$

$$Q = \left[\frac{\dot{m}_p}{m_{p,0}} C_p \Delta T_p + frac\Delta m_p m_{p,0}\left(-h_{fg} + \int_{T_{ref}}^{T} C_{p,i}\, dT\right)\right] m_{p,0}, \tag{4.8}$$

$$M = \Delta m_p. \tag{4.9}$$

Droplets can damp or produce turbulence. The influence of the presence of droplets on the gas phase turbulence is taken into account using the formulation described in [17] and [18]. The evaporation model employed in this study is based on the infinite droplet conductivity assumption, in which the temperature of the droplet is uniform but time varying. The evaporation rate of the droplet is assumed to be governed by gradient diffusion, with the flux of droplet vapor into the gas phase related to the difference in vapor concentration at the droplet surface and the bulk gas:

$$N_i = k_c\left(C_{i,s} - C_{i,\infty}\right), \tag{4.10}$$

where N_i is the molar flux of vapor, $C_{i,s}$ is the vapor concentration at the droplet surface, $C_{i,\infty}$ is the vapor concentration in the bulk gas and k_C is the mass transfer coefficient.

The concentration of the vapor at the droplet surface is evaluated by assuming that the partial pressure of vapor at the interface is equal to the saturated vapor pressure, P_{sat}, at the droplet temperature, T_p:

$$C_{s,i} = \frac{P_{sat}\left(T_p\right)}{RT_p}, \tag{4.11}$$

where R is the universal gas constant.

4.2.3. TURBULENCE-CHEMISTRY INTERACTION MODEL

The flamelet concept views the turbulent flame as an ensemble of thin, laminar, locally one-dimensional flamelet structures embedded within the turbulent flow field. In flamelet models, in general, the conservation equations of mass, momentum and mixture fraction Z as a conserved scalar are solved in the flow field, and temperature and chemical species mass fractions at each position are identified by referring to the flamelet library. The flamelet library is obtained by solving a one-dimensional flamelet equation in the Z space:

$$\rho\frac{\partial Y_i}{\partial t}=\frac{1}{2}\rho\chi\frac{\partial^2 Y_i}{\partial Z^2}+S_i, \tag{4.12}$$

$$\rho\frac{\partial T}{\partial t}=\frac{1}{2}\rho\chi\frac{\partial^2 T}{\partial Z^2}-\frac{1}{C_p}\sum_i H_i S_i+\frac{1}{2C_p}\rho\chi\left[\frac{\partial C_p}{\partial Z}+\frac{1}{C_p}\sum_i\frac{\partial Y_i}{\partial Z}\right]\frac{\partial T}{\partial Z}, \tag{4.13}$$

where $\chi\,(=2D_Z\Delta Z\cdot\Delta Z)$ is the scalar dissipation rate, here S_Z is the diffusion coefficient of Z. The strained flamelet library used in this study is calculated by solving the flamelet equations with different scalar dissipation rate varying form 0.01 s^{-1} till the quenching value by the step of 1.0 s^{-1}. The quenching scalar dissipation rate in the present study is 56 s^{-1}. Several flamelets with different χ_{st} as well as the mixing line are shown in Fig. 4.5. The main limitation of the SFM used in this study is that the extinguished flamelets are excluded from the flamelet library. Non-physical results will be obtained when exceeds the quenching value, as will be further discussed in the following section.

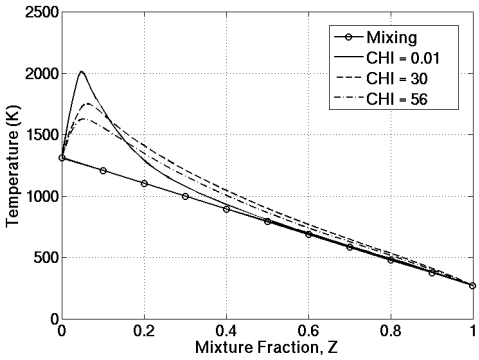

Figure 4.5: Schematic of flamelet tables with different scalar dissipation rate.

The Favre-averaged values of quantities in the turbulent flame are then obtained through the use of Favre-averaged probability density function, $\tilde{f}\left(Z,\chi_{st}\right)$:

$$\tilde{\Phi}=\int_0^\infty\int_0^1\Phi\left(Z,\chi_{st}\right)\tilde{f}\left(Z,\chi_{st}\right)dZd\chi_{st}, \tag{4.14}$$

where χ_{st} is the stoichiometric scalar dissipation, is calculated by the turbulent kinetic energy, k, turbulent dissipation rate, ϵ, and variance of mixture fraction, $\widetilde{Z''^2}$, by:

$$\tilde{\chi}_{st}=\frac{C_\chi\widetilde{Z''^2}}{k}. \tag{4.15}$$

Here C_χ is a constant with default value of 2.0. Z and χ_{st} are assumed to be statistically independent, so the joint PDF can be simplified as $\tilde{f}(Z)\,\tilde{f}(\chi_{st})$. Mixture fraction is assumed to follow the β-function PDF, and scalar dissipation fluctuations are ignored so that the PDF of χ_{st} is delta function.

In order to take into account the influence of non-adiabatic effects due to the droplet evaporation and radiative heat transfer, an additional parameter, enthalpy, is required. However, the modeling of steady flamelets over a range of enthalpies is a difficult issue. Hence, for simplicity, heat loss or gain to the system is assumed to have a negligible effect on the species mass fractions. So the adiabatic species mass fractions are still used, and the temperature is adjusted according to the mean enthalpy gain or loss, $\tilde{H}$. To avoid the PDF convolutions at run-time, the integrations in Eq. (4.14) are preprocessed and stored in look-up tables.

4.3. RESULTS AND DISCUSSIONS

The predicted droplet sauter mean diameter (SMD) show good agreement with the experimental data at various axial positions, as shown in Fig. 4.6. The range of the droplet size and the trend of the SMD distribution are well predicted. However, the radial distribution of the droplets are not accurately predicted, too small droplets are found at the inner edge while too large droplets are found at the outer edge of the spray. This indicates that the random walk model employed in this study does not describe well the dispersion of droplet, further improvement is still required in future studies.

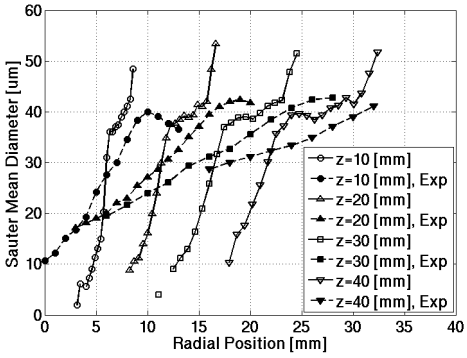

Figure 4.6: Droplet Sauter Mean Diameter.

Figure 4.7 shows the mean droplet axial velocity of different droplet sizes at various elevations. Good agreement is observed for all droplets classes, especially at high axial locations. This is partly due to the good estimation of the injector exit diameter and the spray parameters. As is expected, large droplets have higher velocity. Because they have higher inertia, thus are less easily influenced by the relative low velocity gas phase.

The trend of the droplet radial velocity is also well predicted, as shown in Fig. 4.8. However, an overall overprediction is observed and the outer branch where the droplet radial velocity decreases is not correctly predicted in the simulation. Large deviations can be observed at low elevations for small droplets. This is a consequence of an early

ignition in the simulation. The SFM employed in this study still requires further development in order to accurately predict the ignition and extinction [19]. Therefore, instead of a lift-off flame as observed in the experiment, the combustion starts almost immediately downstream the injector exit in the simulation. Fig. 4.9 shows the contour of predicted OH mole fraction. High concentration of OH is found near the injector. The combustion at the near injector region leads to an expansion of the gas, which in turn pushes the droplets outwards. The small droplets are more likely to be influenced by this expansion. The gas phase velocity shown in Fig. 4.10 and Fig. 4.11 also demonstrates this expansion.

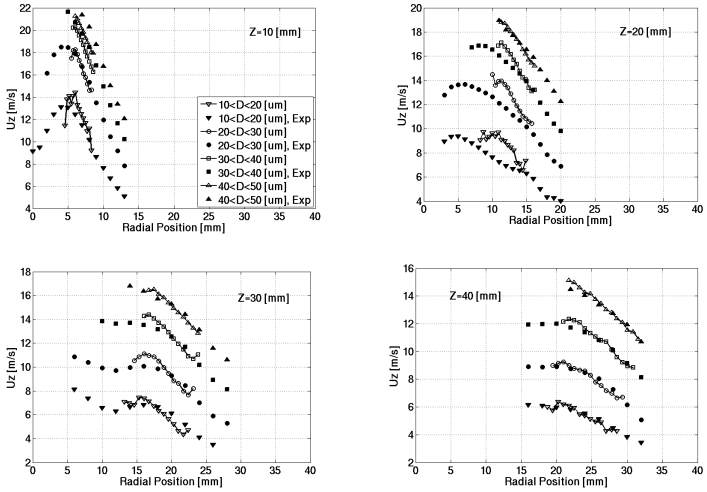

Figure 4.7: Predicted mean droplets axial velocity at different elevations.

Comparison between predicted and measured gas phase axial and radial velocities is shown in Fig. 4.10 and Fig. 4.11 respectively. Note that the gas phase velocity in the experiment is represented by small droplets (D 6 m) velocity. This is due to the difficulty in measuring the gas phase velocity, and the small droplets are supposed to follow the gas phase motion. However, the fact that the measured gas phase velocity at $\mathcal{Z} = 10\ mm$ resemble well with the small droplets velocity distributions in Fig. 4.7 and Fig. 4.8, and have a significant deviation with the predicted gas phase velocity shows that this may not be the case in the near injector region. The predicted gas phase velocity in the further downstream region agrees reasonably well with the available experimental data.

Despite the agreement of the droplets and gas phase velocity distributions we observed, limitations of the present modeling approach are also non-negligible. As already mentioned above, the present simulation can hardly predict the flame lift-off. A possible reason is that the extinguished flamelets are not included in the present steady laminar flamelet model. Therefore, non-physical results may be obtained in the region where the strain rate or scalar dissipation rate exceeds the quenching value. An evidence for this is the fact that the applied steady laminar flamelet model predicts a temperature peak in the region where the strain rate is greater than the critical value and extinction is ex-

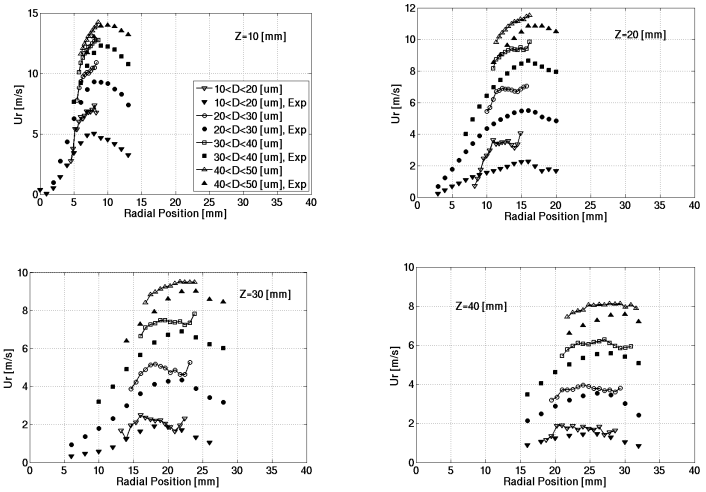

Figure 4.8: Predicted mean droplets radial velocity at different elevations.

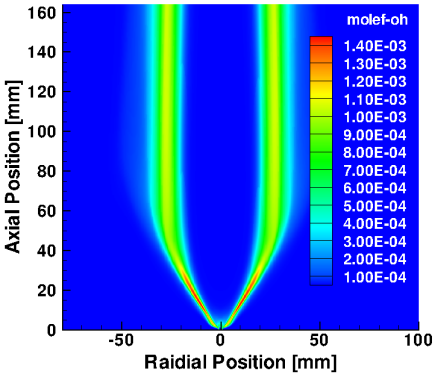

Figure 4.9: Predicted OH distribution.

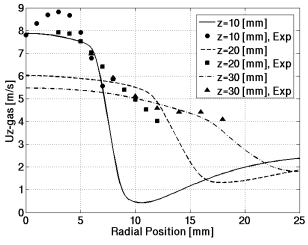

Figure 4.10: Gas phase axial velocity at different elevations.

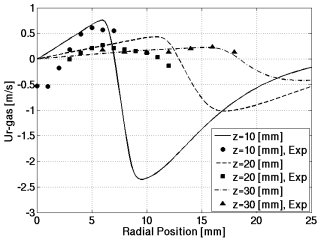

Figure 4.11: Gas phase radial velocity at different elevations.

pected [13]. The unsteady flamelet model available in Fluent has also been tested, but no obvious improvement has been achieved.

For the DSHC, because of the presence of the high temperature co-flow, the droplets have a high evaporation rate near the injector. Also very high strain rate is expected in this region due to the high velocity of the droplets, and this is expected to suppress chemical reaction. However, in the simulation, the combustion has already started in this region, and temperature in this region is relatively high. This in turn accelerates the evaporation of the droplets, and aggravates the drawback of the present model. The evaporation model employed in this study assumes infinite droplet conductivity, and also this is believed to lead to an overprediction of the evaporation rate. The lack of measured temperature data also limits the validation of numerical results. Comparing with the conventional spray combustion, in order to accurately predict the flameless spray combustion, more efforts should be made on precise evaporation model and accurate consideration of auto-ignition and local extinction.

Possible improvements for the present model are to take progress variable as another independent parameter in the lookup table to properly predict the ignition process as in the FGM model [20], and to use droplets as well as carrier gas instead of fuel vapor for the fuel side in the generation of the flamelet library, which is done in the spray flamelet model [21]. Taking into account the variance of scalar dissipation rate, i.e. use more sophisticated PDF instead of delta function for the , may also help to improve the ability of the present model for correct prediction of the high strain region.

4.4. CONCLUSIONS

In this study, an ethanol spray in hot coflow flame, DSHC, was numerically investigated and validated by comparing with the experimental results. An Eulerian-Langrangian RANS approach and the steady laminar flamelet model with detailed chemical mechanism of Marinov were employed. Except at the inner and outer radial boundaries of the spray, good agreements of droplet SMD were obtained. Droplet velocities at various elevations resemble the experimental data well for all the droplet size classes. Gas phase velocities were also validated by available measured results, and a reasonable good match was found. In addition, drawbacks and limitations of the present modelling approach were discussed. Due to the exclusion of the extinguished flamelet, the flamelet model employed in this study has been demonstrated to have a poor ability to predict correct results in the high strain region. The presence of the high temperature coflow in the near injector region in DSHC aggravates this drawback. More efforts on precise evaporation model and accurate treatment of auto-ignition and extinction processes have to be made to correctly predict the flameless spray combustion. Possible improvements have been suggested and will be investigated in future studies.

REFERENCES

[1] L. Ma, S. Zhu, M. J. Tummers, T. H. van der Meer, and D. Roekaerts, *Numerical investigation of ethanol spray-in-hot-coflow flame using steady flamelet model,* in *Proceedings of Eighth Mediterranean Combustion Symposium* (2013) pp. 1–12.

[2] A. Cavaliere and M. de Joannon, *Mild Combustion,* Progress in Energy and Combustion Science **30**, 329 (2004).

[3] P. Li, J. Mi, B. B. Dally, F. Wang, L. Wang, Z. Liu, S. Chen, and C. Zheng, *Progress and recent trend in MILD combustion,* Science China Technological Sciences **54**, 255 (2011).

[4] G. Sarras, M. K. Stoellinger, and D. J. E. M. Roekaerts, *Transported PDF simulations of the Delft-jet-in-hot-coflow burner based on 3D FGM tabulated chemistry,* in *7th Internal Symposium on Turbulence, Heat and Mass transfer* (2012) pp. 1–10.

[5] R. Weber, J. P. Smart, and W. V. Kamp, *On the (MILD) combustion of gaseous, liquid, and solid fuels in high temperature preheated air,* Proceedings of the Combustion Institute **30**, 2623 (2005).

[6] H. Rodrigues, M. J. Tummers, and D. J. E. M. Roekaerts, *Experiments on turbulent ethanol spray flames in EEC conditions,* in *International Conference on Liquid Atomization and Spray Systems* (Heidelberg, Germany, 2012) pp. 1–6.

[7] P. Senecal, D. Schmidt, I. Nouar, C. Rutland, R. Reitz, and M. Corradini, *Modeling high-speed viscous liquid sheet atomization,* International Journal of Multiphase Flow **25**, 1073 (1999).

[8] N. M. Marinov, *A Detailed Chemical Kinetic Model for High Temperature Ethanol Oxidation,* International Journal of Chemical Kinetics **31**, 183 (1998).

[9] C. Hollmann and E. Gutheil, *Modeling of turbulent spray flames including detailed chemistry,* in *26 th Symposium (International) on Combustion* (1996) pp. 1731–1738.

[10] C. Hollmann and E. Gutheil, *Flamelet-modeling of turbulent spray diffusion flames based on a laminar spray flame library,* Combustion Science and Technology **135**, 175 (1998).

[11] H. Watanabe, R. Kurose, S. Hwang, and F. Akamatsu, *Characteristics of flamelets in spray flames formed in a laminar counterflow,* Combustion and Flame **148**, 234 (2007).

[12] Y. Baba and R. Kurose, *Analysis and flamelet modelling for spray combustion,* Journal of Fluid Mechanics **612**, 45 (2008).

[13] D. Rochaya, *Numerical Simulation of Spray Combustion using Bio-mass Derived Liquid Fuels*, Ph.D. thesis, Cranfield University (2007).

[14] P. Jenny, D. Roekaerts, and N. Beishuizen, *Modeling of turbulent dilute spray combustion,* Progress in Energy and Combustion Science **38**, 846 (2012).

[15] S. Zhu, D. Roekaerts, and T. van der Meer, *Numerical simulation of a turbulent methanol spray flame using the Euler-Lagrange method and the steady laminar flamelet model,* in *7th Mediterranean Combustion Symposium* (Sardinia, Italy, 2011) pp. 1–12.

[16] E. Gutheil, *Issues in Computational Studies of Turbulent Spray Combustion,* in *Experiments and Numerical Simulations of Diluted Spray Turbulent Combustion*, edited by B. Merci, D. Roekaerts, and A. Sadiki (Springer, 2011) pp. 1–39.

[17] A. A. Amsden, P. J. O'Rourke, and T. D. Butler, *KIVA-2: A computer program for chemically reactive flows with sprays*, Tech. Rep. LA-11560-MS,UC-96 (1989).

[18] G. M. Faeth, *KIVA-2: A computer program for chemically reactive flows with sprays*, Tech. Rep. 1986-136 (AIAA, 1986).

[19] S. Piffaretti, *Flame age model: A transient laminar flamelet approach for turbulent diffusion flames*, Ph.D. thesis, ETH (2007).

[20] C. Bekdemir, *Tabulated Chemical Kinetics for Efficient and Detailed Simulations of Diesel Engine Combustion*, Ph.D. thesis, Eindhoven University of Technology (2012).

[21] E. Gutheil and W. Sirignano, *Counterflow spray combustion modeling with detailed transport and detailed chemistry,* Combustion and Flame **113**, 92 (1998).

5

STUDY OF DSHC FLAME WITH TRANSPORTED PDF METHOD

This chapter presents a numerical study of the H_{II} case of the DSHC database using dilute a spray combustion modeling approach. A "Lagrangian-Lagrangian" approach, where both the joint velocity-scalar Probability Density Function (PDF) for the continuous phase and the joint PDF of droplet properties are modeled and solved, is adopted. The evolution of the gas phase composition is described by a Flamelet Generated Manifold (FGM) and the interaction by exchange with the mean (IEM) micro-mixing model. Effects of finite conductivity on droplet heating and evaporation are accounted for. The inlet boundary conditions starting in the dilute spray region are obtained from the available experimental data together with the results of a calculation presented in Chapter 4. The current modeling approach is capable of accurately predicting main properties, including mean velocity, droplet mean diameter and number density. The gas temperature is under-predicted in the region where the enthalpy loss due to droplet evaporation is important. The experimental and modeled temperature PDFs are compared, highlighting the capabilities and limitations of the proposed model.

Content in this chapter has been published in the following paper:
L. Ma, B. Naud, and D. Roekaerts, Transported PDF Modeling of Ethanol Spray in Hot-diluted Coflow Flame, Flow, Turbulent and Combustion, 96 (2): 469-502, 2016.

5.1. INTRODUCTION

Spray combustion is widely utilized in various engineering applications, such as industrial furnaces and propulsion systems. To achieve higher efficiency while minimizing the pollutant emission, novel combustion technologies are demanded. Among others, the MILD (Moderate or Intense Low-oxygen Dilution) combustion is demonstrated to be a promising technology [1, 2]. By dilution of the reactants with the recirculated reaction products, the flame peak temperature is substantially reduced, resulting in a low production of NOx. Delft Spray-in-Hot-Coflow (DSHC) burner has been used to study fundamental aspects of MILD oxidation of bio-derived liquid fuels [3]. A first numerical study of an ethanol flame from DSHC database with the transported PDF method is reported in this paper.

Modeling of turbulent spray combustion is particularly challenging, because many physical and chemical processes including turbulence, atomization, evaporation, combustion and radiative heat transfer are involved and interact with each other [4]. These phenomena and processes have to be modeled in a proper way in the sense that the main physical characteristics have to be accounted for, but with a reasonable computational cost. For simplicity, many spray combustion studies have been carried out in the regime of dilute spray [5, 6], and this approach is also deployed in this study.

The transported probability density function (PDF) method [7] has proven to be a powerful closure method for modeling turbulent reactive flow [8, 9]. PDF method has been applied to spray combustion since the 1990s, and is still an active research area. Naud et al. [10–13] developed a hybrid finite-volume/transported PDF method, and systematically studied the modeling issues in the context of Lagrangian-Lagrangian approach. Beishuizen [14] studied the particle-turbulence interaction of turbulent spray flames. Ge and Gutheil [15] proposed a joint mixture fraction-enthalpy PDF method for modeling turbulent spray combustion, and recently developed a joint velocity-mixture fraction PDF model [16]. Bhattacharjee and Haworth [17] compared well-stirred reactor (WSR) model with PDF method for n-heptane and n-dodecane spray flames under engine conditions, concluding that the PDF method performs better due to the fact that the turbulent fluctuations have been taken into account. Pei et al. [18, 19] simulated diesel engine combustion using composition PDF coupled with Reynolds-averaged k-ϵ model. Recently, attention has been paid to the FDF (filtered density function) method in conjunction with Large Eddy Simulation. Heye et al. [6] modeled the Sydney ethanol spray flame with a LES/FDF approach. Jones et al. [20] modeled a gas turbine combustor using LES with sub-grid probability density function to account for the sub-grid turbulence-chemistry interaction. Despite the contribution of these works, the micro-mixing model, small scale droplet models, as well as the combustion models for the application of PDF methods to spray combustion are still open issues.

The most outstanding advantage of transported PDF methods is that the mean reaction source term appears as a closed term. However, the direct use of detailed chemistry is computationally very expensive. Proper chemistry reduction is required for affordable yet accurate models. This is normally accomplished by either using reduced chemical mechanisms, or employing tabulated chemistry methods. In this study the Flamelet Generated Manifold model [21] is used, which falls in the second group of chemistry reduction methods. In the FGM model, the scalars, such as temperature, species mass

fractions, density or progress variable source term, are stored in a lookup table as a function of a few independent variables — usually the mixture fraction and a progress variable. The scalars are then retrieved from the pre-built lookup table during turbulent combustion simulation according to the value of the modeled independent variables. The influence of turbulence fluctuations on the mean properties is accounted for through the joint PDF of the independent variables. For many applications, the shape of the PDFs of independent variables are simply assumed before simulation. For instance, mixture fraction is often presumed as a β-function with shape parameters determined by its mean and variance values. However, many studies [4, 22] already pointed out that due to the presence of droplet evaporation, the β shape PDF is no longer valid for mixture fraction in spray combustion. For the PDF of progress variable, even more ambiguities exist, both β-function and δ-function have been reported in the literatures [5, 23], and further studies are required. Alternatively, in this study, the transport equation of the joint PDF of gas phase properties is directly modeled and solved, such that the turbulence-chemistry interaction is considered in a more precise manner.

The application of the classical flamelet model to spray combustion was first made by Hollmann and Gutheil [24, 25] to simulate a methanol/air diffusion flame and extended by them to a formulation using spray flamelets [15, 26]. However, the high dimensionality of the spray flamelets makes them difficult to tabulate and use. A novel two dimensional spray flamelet, using mixture fraction and droplet evaporation rate as independent variables, was recently proposed by Olguin and Gutheil [27]. However, the shape of the PDF for droplet evaporation rate is still an open issue for the application of this model with presumed PDF methods. Chrigui et al. [5, 28] applied a FGM model to Large Eddy Simulation of ethanol spray combustion, using presumed β-PDF for mixture fraction and δ-function for progress variable. To the authors' knowledge, application of FGM model for spray combustion in the context of transported PDF has not yet been reported.

The purpose of this paper is twofold: on the one hand, to validate the transported PDF modeling approach with FGM for spray combustion; and on the other, to increase the understanding of MILD spray combustion. This paper is structured as follows: some background information for the current study is firstly given in this section, followed by mathematical modeling approaches for continuous and dispersed phase respectively in Sections 5.2 and 5.3. The experimental configuration and numerical setup of the target flame are presented in Section 5.4. The results are discussed in Section 5.5, focussing on: the role of the "1/3" rule; the influence of the droplet initial temperature and of the evaporation model; the comparison with experimental data; the flame structure; and the temperature PDF. Major conclusions and future study are then emphasized in Section 5.6.

5.2. MODEL FOR THE CONTINUOUS PHASE

5.2.1. TRANSPORTED PDF HYBRID FINITE VOLUME / PARTICLE METHOD

The in-house RANS / transported PDF code "PDFD", which has already been successfully used in gaseous flames, evaporating sprays and coal combustion [10, 14, 23, 29], is used in this study (where RANS refers here and in the following to averaged Navier-

Stokes equations in the sense of Favre averages). The continuous phase is described by the joint velocity-scalar PDF, where the scalars considered are the FGM independent variables: mixture fraction Z and progress variable Y_c. As detailed in the next section, the dispersed phase is described by the joint PDF of droplet position, velocity, temperature, diameter, and the gaseous properties "seen" by the droplets. To cope with the high-dimensionality, the joint PDFs are solved by Monte Carlo particle methods. In contrast with the Eulerian-Lagrangian approach, both the gas phase and the dispersed phase evolution are defined by Lagrangian equations, and we are therefore considering a "Lagrangian-Lagrangian" approach.

To overcome the bias error due to the limited number of computational particles in the Monte Carlo (MC) method, the continuous phase mean velocities and Reynolds stresses are calculated using a Finite-Volume (FV) method, in which the Favre-averaged Navier Stokes equations are solved [12]. Similar approaches were also used by Ge et al. [16], Bhattacharjee et al. [17] and Anand et al. [30]. Note that in our case, special attention is paid to the consistency between the particle velocity evolution and the Reynolds-stress and scalar-flux second moment closures used in the RANS model [11, 13]. Fig. 5.1

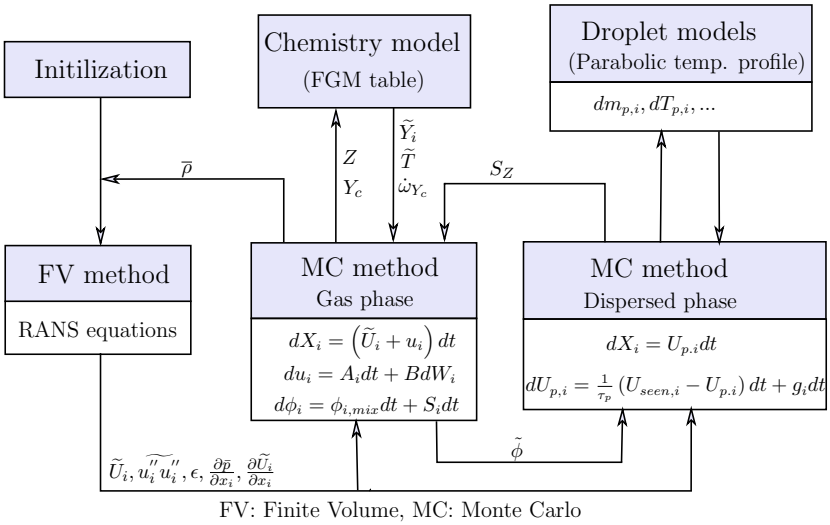

Figure 5.1: Sketch of the hybrid Finite Volume/Monte Carlo modeling approach

illustrates the computational algorithm. The FV submodel provides the mean velocity and its gradient, mean pressure gradient, Reynolds stresses and mean turbulent dissipation rate to the MC part.

The fluctuating velocity increment of the gas phase particles is determined by the generalized Langevin model (GLM) — more specifically, by the variable C_0 formulation of the GLM presented in [13] — in correspondence with the LRR-IPM Reynolds-stress model used for the modeling of the pressure strain correlation in the FV part. The evolution of the gas phase composition is described by the FGM and the interaction by ex-

change with the mean (IEM) micro-mixing model:

$$dZ = \theta_{\text{mix}}(Z)dt + S_Z dt \quad \text{and} \quad dY_c = \theta_{\text{mix}}(Y_c)dt + \dot{\omega}^{\text{FGM}}_{Y_c}(Z, Y_c)dt, \tag{5.1}$$

where the mixture fraction Z is not a conserved scalar in spray combustion and its source term S_Z corresponds to the mass coming from droplet evaporation. On the other hand, by definition of the progress variable Y_c, as we will see in Eq. (5.3), its source term does not include effects of the evaporated fuel and $\dot{\omega}^{\text{FGM}}_{Y_c}$ corresponds to the chemical reaction source term, shown in Fig. 5.3, retrieved from the FGM lookup table as a function of the independent variables. The IEM mixing model reads:

$$\theta_{\text{mix}}(\phi) = -\frac{1}{2}\omega_\phi \left(\phi - \widetilde{\phi}\right) dt, \tag{5.2}$$

where $\omega_\phi = C_\phi \epsilon / k$ is the modeled scalar variance decay frequency, with C_ϕ the mixing model constant, set to $C_\phi = 2$. The mean turbulent kinetic energy (k) and turbulent dissipation rate (ϵ) are provided by the FV part.

The two-way coupling source terms due to the drag force appearing in the momentum and Reynolds stress equations [14] are not included here since these effects proved to be small for the dilute spray considered. However, we do include the mean mass source terms in the mean continuity and momentum equations.

5.2.2. COMBUSTION MODEL

In flamelet-based models, the multi-dimensional turbulent flame is considered as a set of 1D flamelets. The 1D flamelets are characterized by different controlling parameters to describe the local variations of the real flame. For the FGM model, the controlling parameters are mixture fraction Z and a progress variable Y_c. Different methods exist for the construction of the 2D FGM lookup table [31]. A commonly used one is to first calculate different steady flamelet equations with scalar dissipation rate increasing from a very small value to the extinguished value. These steady flamelets are then mapped in (Z, Y_c)-space together with the unsteady extinguishing flamelet solution [28]. Another approach is to solve the unsteady process of a 1D diffusion flame in physical space from pure mixing until the steady flame is established. The flamelet solution at different time is then transformed into (Z, Y_c)-space. Compared to the “extinguishing" FGM generated by the first method, the second method generates an “auto-igniting" FGM table, which is therefore more suitable to describe the auto-ignition process of the DSHC flame. Note that so-called unsteady flamelet / progress variable approaches have also been proposed where both ideas are combined. In that case, igniting and extinguishing flamelets are resolved for different scalar dissipation rates, as for instance presented recently in [32, 33]. However, such approaches require one additional control parameter, and a 3D lookup table needs to be considered in (Z, χ, Y_c)-space, with χ the scalar dissipation rate. Auto-ignition lookup tables can also be constructed by solving Perfectly Stirred Reactors (PSR) [34] or combining with premixed flamelets [35].

The 2D auto-igniting FGM table used in this study is generated with the CHEM1D code developed at the Eindhoven University of Technology [36]. The conterflow diffusion flame is solved in physical space at unity Lewis number where the boundary conditions are specified such that the specified strain rate is 100s^{-1} and the fuel corresponds

to pure C_2H_5OH vapor at its boiling temperature T_{boil} = 351K. Compared to PSR, this configuration takes into account the diffusion during ignition, therefore it is physically more representative of the reality. The chosen strain rate of $100s^{-1}$ (corresponding to a rather low stoichiometric scalar dissipation rate of $1.85s^{-1}$) is consistent with the observation made in [32], for a lifted methane/air flame with similar coflow conditions as the current case, that ignition happens in relatively low scalar dissipation rate regions. The detailed ethanol high temperature oxidation mechanism containing 57 species and 383 reactions by Marinov [37] is employed. The ignition process is illustrated by the temperature profiles in mixture fraction space with increasing time, as shown in Fig. 5.2. The progress variable in this study is defined as a weighted sum of species mass fractions as follows:

$$Y_c = \frac{Y_{H_2O}}{W_{H_2O}} + \frac{Y_{CO_2}}{W_{CO_2}} + \frac{Y_{H_2}}{W_{H_2}}, \tag{5.3}$$

where W_k refers to the molecular weight of species k. The progress variable source term $\dot{\omega}_c^{FGM}(Z, Y_c)$ is shown in Fig. 5.3 in mixture fraction and normalized progress variable space. In principle, droplet evaporation influences the gas phase flamelet structure by

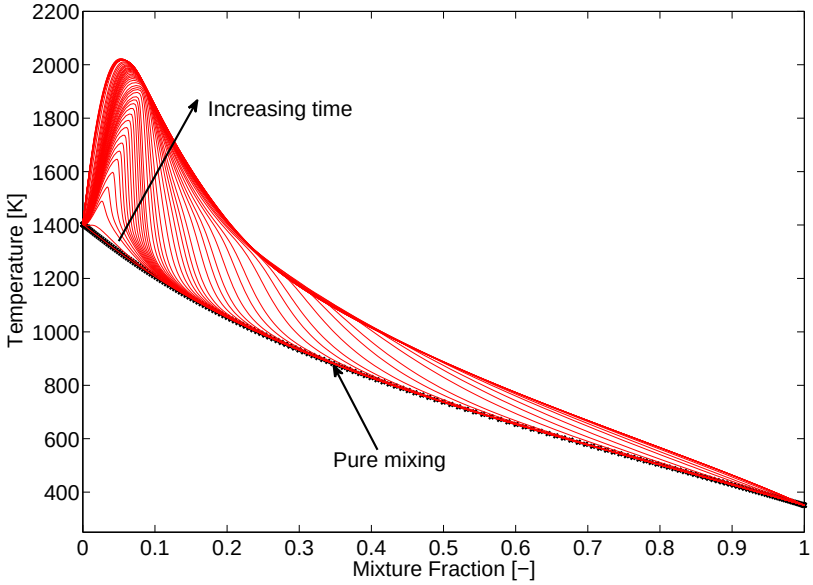

Figure 5.2: Temperature versus mixture fraction in auto-ignitiong FGM

consuming energy and adding fuel vapor. As explained in Section 5.2.1, the vaporized fuel is accounted for by the source term for mixture fraction. Many different approaches have been proposed to take into account the enthalpy loss effect of droplet evaporation. For example, spray flamelets [25], using total enthalpy as progress variable [38], partially premixed flamelet method [39] or generating FGM table by solving new spray flamelets equations as derived in [40] and [27]. In this study, as a first step of the model validation,

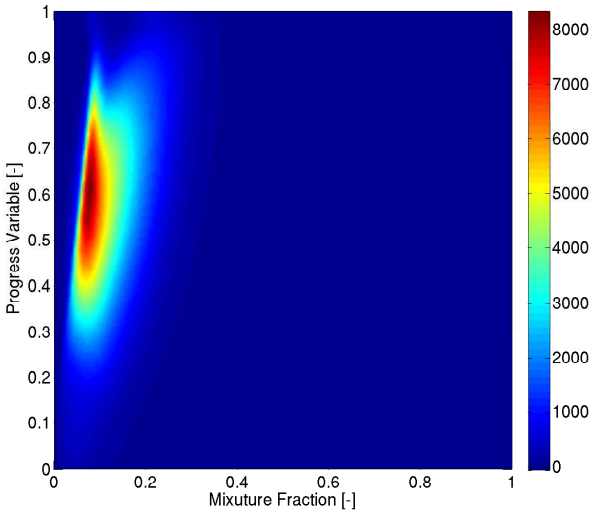

Figure 5.3: Progress variable source term in mixture fraction and normalized progress variable space

an adiabatic gaseous FGM table generated by using pure fuel vapor as fuel stream is employed, and enthalpy loss is not included in this 2D FGM table. The influence of this scheme on the results will be further discussed in Section 5.5.

5.3. MODEL FOR THE DISPERSED PHASE AND PHASE INTERACTIONS

Accurate prediction of the droplet dispersion and evaporation in turbulent flows are of crucial importance since they are considered rate limiting processes in modeling dilute spray combustion [4]. In the proposed Lagrangian modeling of the dispersed phase PDF, the evolution of the properties of the stochastic particles representing posible realizations of the turbulent spray is chosen to follow Lagrangian models for single droplets [10]. The dispersed phase stochastic particles will be denoted “parcels” in the following.

5.3.1. DROPLET MOTION

For practical spray combustion, the droplet drag force and the gravitational force are dominant compared to other forces, for instance the buoyancy force and Basset force. Therefore the particle momentum equation, also known as BBO (Basset-Boussinesq-Ossen) [41], is greatly simplified:

$$\frac{dU_{\mathrm{p},i}}{dt} = \frac{U_{\mathrm{seen},i} - U_{\mathrm{p},i}}{\tau_{\mathrm{p}}} + g_i. \tag{5.4}$$

The droplet relaxation time τ_p is determined by:

$$\tau_p = \frac{4}{3}\frac{\rho_p}{\rho_g}\frac{D_p}{C_D|\mathbf{U}_{seen} - \mathbf{U}_p|}, \tag{5.5}$$

where ρ_p and ρ_g respectively refer to the liquid droplet and gas-phase densities, and D_p is the droplet diameter. The drag coefficient C_D is given by the Schiller-Naumann semi-empirical correlation:

$$C_D = \begin{cases} \frac{24}{Re_p}\left(1 + 0.15Re_p^{0.687}\right), & \text{if } Re_p \leq 1000 \\ 0.44, & \text{if } Re_p > 1000 \end{cases}, \tag{5.6}$$

with the particle Reynolds number:

$$Re_p = \frac{\rho_g|\mathbf{U}_{seen} - \mathbf{U}_p|D_p}{\mu_g}. \tag{5.7}$$

In the above equations and in the following, the subscript "seen" refers to the properties seen by the droplets (the undisturbed fluid flow properties at the position of the droplet center, which modelling is detailed in Section 5.3.6). The subscripts "p" and "g" respectively refer to droplet and gas-phase properties.

5.3.2. PARABOLIC TEMPERATURE PROFILE

For droplet heating and evaporation processes, a variety of models with different levels of complexity exist [42–46]. Among them a widely used one is the "infinite conductivity model", in which the temperature distribution inside the droplet is assumed uniform. However the finite conductivity effects become important when the droplet heating process is fast as is the case in the hot-diluted coflow condition of this study. Fully resolving the heat conduction problem inside the droplets greatly increases the computational cost. By checking droplet temperature distribution, $T_p(r,t)$, one observes that, except at the very beginning of heating, the shape of the curve $T_p(r)$ looks close to a parabola [46]. Hence, the finite rate heat conduction process is taken into account by assuming that the temperature profile between the droplet surface and its center is a parabola [47]:

$$T_p(r,t) = T_{cntr}(t) + [T_{surf}(t) - T_{cntr}(t)]\left(\frac{r}{R_p}\right)^2, \tag{5.8}$$

where T_{cntr} is the temperature at the droplet center (at $r = 0$) and T_{surf} is the droplet surface temperature (at $r = R_p$, with R_p the droplet radius). If we generalize the derivation of [47] for evaporating droplets as done in [48], we can consider the volume averaged droplet temperature $\overline{T}_p$, defined as:

$$\overline{T}_p(t) = \frac{1}{\frac{4}{3}\pi R_p^3}\int_0^{R_p} 4\pi r^2 T_p(r,t)\,dr = \frac{2T_{cntr}(t) + 3T_{surf}(t)}{5}. \tag{5.9}$$

After considering the boundary condition at the droplet surface as in [47], its time evolution then reads:

$$\frac{d\overline{T}_p}{dt} = \frac{1}{1+0.2\zeta}\left[\frac{6\mathrm{Nu}\lambda_m}{\rho_{liq}C_{p,liq}D_p^2}\left(T_\infty - \overline{T}_p\right) + \left(\frac{dT}{dt}\right)_{evap}\right] \quad \text{with} \quad \zeta = \frac{\mathrm{Nu}}{2}\frac{\lambda_m}{\lambda_{liq}}, \tag{5.10}$$

where Nu is the Nusselt number, given in (5.16), and where C_p refers to the specific heat capacity and λ to the thermal conductivity. The subscript "liq" refers to liquid properties, while the subscript "m" refers to the gas-phase properties close to the droplet surface (considered in Section 5.3.5). The temperature T_∞, far away from the droplet surface, is interpreted here as the seen temperature T_{seen}. The surface temperature is obtained as:

$$T_{\text{surf}} = \frac{1}{1+0.2\zeta}\left[\left(\overline{T}_{\text{p}} + 0.2\zeta T_\infty\right) + 0.1\left(\frac{dT}{dt}\right)_{\text{evap}} \frac{\rho_{\text{liq}} D_{\text{p}}^2 C_{p,\text{liq}}}{6\lambda_{\text{liq}}}\right]. \tag{5.11}$$

Note that the temperature at the center of the droplet can be obtained from Eq. (5.9) as: $T_{\text{cntr}} = \left(5\overline{T}_{\text{p}} - 3T_{\text{surf}}\right)/2$.

5.3.3. ABRAMZON AND SIRIGNANO EVAPORATION MODEL

In the above equations, we introduced the notation for the temperature evolution due to evaporation such that:

$$m_p C_{p,\text{liq}} \left(\frac{dT}{dt}\right)_{\text{evap}} = -\dot{m}_{\text{p}} L_v\left(T_{\text{surf}}\right), \tag{5.12}$$

where $\dot{m}_{\text{p}}$ is the evaporation rate and $L_v\left(T_{\text{surf}}\right)$ is the latent heat of vaporization at droplet surface temperature T_{surf}.

Abramzon and Sirignano [44] proposed modified Nusselt and Sherwood numbers, Nu^*, Sh^*, deduced from "film theory", to account for the boundary layer thickening effect by the Stefan flow. They express the evaporation rate based on mass diffusion of vapor or based on heat transfer as:

$$\dot{m}_{\text{p}} = \pi \rho_{\text{m}} \mathscr{D}_{\text{vap}} D_{\text{p}} \text{Sh}^* \ln\left(1+B_M\right) \quad \text{or} \quad \dot{m}_{\text{p}} = \pi \frac{\lambda_{\text{m}}}{C_{p,\text{vap}}} D_{\text{p}} \text{Nu}^* \ln\left(1+B_T\right), \tag{5.13}$$

where ρ_{m} and λ_{m} are the average density and thermal conductivity of the film gas mixture (i.e. at temperature T_{m} and composition $\mathbf{Y}_{\text{m}}$, as explained in Section 5.3.5), $\mathscr{D}_{\text{vap}}$ is the binary diffusion coefficient of pure vapor in the film gas mixture and $C_{p,\text{vap}}$ is the specific heat of pure vapor at temperature T_{m}. The modified Sherwood and Nusselt numbers read:

$$\text{Sh}^* = 2 + \frac{\text{Sh}-2}{F_M} \quad \text{and} \quad \text{Nu}^* = 2 + \frac{\text{Nu}-2}{F_T}, \tag{5.14}$$

with the correction factors, representing the relative change of the boundary layer thickness due to the Stefan flow, approximated as:

$$F_M = (1+B_M)^{0.7} \frac{\ln(1+B_M)}{B_M} \quad \text{and} \quad F_T = (1+B_T)^{0.7} \frac{\ln(1+B_T)}{B_T}. \tag{5.15}$$

B_M and B_T are the Spalding mass and heat transfer numbers. Sh and Nu are the Sherwood number and Nusselt number for flow around a solid sphere, and can be evaluated by the well known Ranz and Marshall correlation:

$$\text{Sh} = 2 + 0.552 \text{Re}_{\text{p}}^{1/2} \text{Sc}_{\text{m}}^{1/3} \quad \text{and} \quad \text{Nu} = 2 + 0.552 \text{Re}_{\text{p}}^{1/2} \text{Pr}_{\text{m}}^{1/3}, \tag{5.16}$$

where $\mathrm{Sc_m}$ and $\mathrm{Pr_m}$ are the Schmidt and Prandtl number respectively:

$$\mathrm{Sc_m} = \frac{\mu_\mathrm{m}}{\rho_\mathrm{m}\mathscr{D}_\mathrm{vap}} \quad \text{and} \quad \mathrm{Pr_m} = \frac{\mu_\mathrm{m} C_{p,\mathrm{m}}}{\lambda_\mathrm{m}}. \tag{5.17}$$

In the Abramzon and Sirignano model, the evaporation rate is obtained using the second expression in Eq. (5.13), based on heat transfer. Using the equality with the first expression based on mass transfer, B_T, Nu^* and F_T are obtained iteratively from:

$$B_T = (1+B_M)^\phi - 1 \quad \text{with} \quad \phi = \frac{C_{p,\mathrm{vap}}}{C_{p,\mathrm{m}}} \frac{\mathrm{Sh}^*}{\mathrm{Nu}^*} \frac{\mathrm{Pr_m}}{\mathrm{Sc_m}}. \tag{5.18}$$

The Spalding mass transfer number B_M is calculated from Eq. (5.19) and (5.20):

$$B_M = \frac{Y_\mathrm{vap}^\mathrm{surf} - Y_\mathrm{vap}^\mathrm{seen}}{1 - Y_\mathrm{vap}^\mathrm{surf}} \quad \text{with} \quad Y_\mathrm{vap}^\mathrm{surf} = X_\mathrm{vap}^\mathrm{surf} \frac{W_\mathrm{vap}}{\overline{W}}, \tag{5.19}$$

where Y_vap refers to the mass fraction of fuel vapor, and $\overline{W}$ is the mean molecular weight of the seen mixture. The mole fraction of fuel vapor $X_\mathrm{vap}^\mathrm{surf}$ at the droplet surface is calculated from the Clausius-Clapeyron equation (assuming that the equilibrium between gas and droplet surface has been reached at each time step):

$$X_\mathrm{vap}^\mathrm{surf} = \exp\left[\frac{L_v(T_\mathrm{surf})}{R/W_\mathrm{vap}}\left(\frac{1}{T_\mathrm{boil}} - \frac{1}{T_\mathrm{surf}}\right)\right]. \tag{5.20}$$

5.3.4. HEAT TRANSFER

With the Abramzon and Sirignano evaporation model, the heat transfer to the droplet can be obtained from the definition of the Spalding heat transfer number B_T as:

$$\dot{q}_\mathrm{drop} = \dot{m}_\mathrm{p}\left[\frac{C_{p,\mathrm{m}}(T_\mathrm{seen} - T_\mathrm{surf})}{B_T} - L_v(T_\mathrm{surf})\right], \tag{5.21}$$

where the first term on the right hand side represents the droplet temperature change due to the convective heat transfer, and the second term the droplet temperature decrease due to the evaporation. In the present model, we would rather keep the standard expression for convective heat transfer and express the heat transfer between the droplet and the gas-phase as:

$$\dot{q}_\mathrm{drop} = \dot{m}_\mathrm{p}\left[\frac{T_\mathrm{seen} - T_\mathrm{surf}}{\tau_{\mathrm{p},T}} - L_v(T_\mathrm{surf})\right] \quad \text{with} \quad \tau_{\mathrm{p},T} = \frac{\rho_\mathrm{liq} C_{p,\mathrm{liq}} D_\mathrm{p}^2}{6\mathrm{Nu}\lambda_\mathrm{m}}, \tag{5.22}$$

as already used in the derivation of the parabolic temperature profile (implying the first term in the bracket in Eq. (5.10) and the last term in Eq. (5.11)).

However, as explained before, since the gas-phase modeling is based on an adiabatic igniting FGM, described by mixture fraction and progress variable only (no enthalpy heat loss included), the contribution of $\dot{q}_\mathrm{drop}$ is not considered here.

5.3.5. EVALUATION OF FILM PROPERTIES AND INFLUENCE OF INTERNAL RECIRCULATION

Eqs. (5.10) to (5.20) completely describe the droplet heating and evaporation process under the assumptions of parabolic temperature profile, phase equilibrium and taking into account the effects of Stefan flow. The presence of evaporation creates large normal gradients of composition and temperature near the droplet surface. The gas-phase properties of the film mixture, denoted by subscript "m", are all evaluated at an intermediate temperature T_m and composition $\mathbf{Y}_\mathrm{m}$:

$$T_\mathrm{m} = (1-\alpha)\, T_\mathrm{surf} + \alpha T_\mathrm{seen} \quad \text{and} \quad \mathbf{Y}_\mathrm{m} = (1-\alpha)\,\mathbf{Y}_\mathrm{surf} + \alpha \mathbf{Y}_\mathrm{seen}. \tag{5.23}$$

Typically $\alpha = 1/3$ is widely accepted for spray combustion simulation. It is the well known "1/3 rule" [49]. However, many other possibilities exist, for example $\alpha = 1$ means to directly use the "seen" gas properties. The influence of whether employing the "1/3 rule" or not will be further analyzed in Section 5.5.

The slip velocity between droplet and gas phase may induce internal circulation inside large droplets, which may enhance the droplet internal heat transfer. It is possible to take into account the inner recirculation by replacing the liquid thermal conductivity λ_liq in Eq. (5.10) with the so-called "effective conductivity" [44]:

$$\lambda_\mathrm{eff} = \kappa \lambda_\mathrm{liq}, \tag{5.24}$$

where $\kappa = 1.86 + 0.86 \tanh\left[2.245 \log_{10}(\mathrm{Pe}_L/30)\right]$, with Pe_L the Peclet number for droplet interior. However, the droplet size in this study is relative small, and the droplet internal recirculation is assumed negligible. Therefore, the physical thermal conductivity, λ_liq, is used.

5.3.6. SEEN PROPERTIES AND DISTRIBUTION OF VAPORIZED FUEL

The seen gas velocity is described by the modified Generalized Langevin Model (GLM) proposed and implemented in PDFD by Naud [11]. This model generalizes the model of Minier [50] for the seen velocity based on the Simplified Langevin Model, ensuring that the modeling is consistent with a given Reynolds stress and scalar flux second moment closure in the limit of tracer particles by generalizing the derivation of Naud [13]. In this case, the chosen seen velocity GLM is consistent with the LRR-IPM Reynolds stress model used in the RANS submodel.

As indicated by Eq. (5.23), the droplet evaporation rate is very sensitive to the way the seen gas temperature T_seen and composition $\mathbf{Y}_\mathrm{seen}$ are evaluated. For most applications, these seen properties are evaluated using the mean values in RANS simulations [17] or filtered quantities in LES [5, 28, 51], neglecting the influence of turbulent fluctuations. Transported PDF methods potentially allow for more refined modeling of the seen composition and temperature. Jones and co-workers [20] developed a stochastic Markov model to account for the effect of the SGS fluctuations of gas-phase reactive scalars on droplet dispersion and evaporation in LES. In this study, as proposed by Naud and De Meester [23, 48], for all stochastic droplets the seen composition and temperature are obtained from the FGM at given values $(Z^\star, Y_c^\star)$. Every given characteristic time $T_{L,\mathrm{seen}}$ (corresponding to a seen Lagrangian scalar correlation time based on the seen velocity

GLM), these values are sampled from a given gas-phase stochastic particle present in the same computational cell. The gas-phase particle is chosen to be the one with enthalpy $h(Z^\star, Y_c^\star)$ the closest to the enthalpy of the saturated mixture, evaluated for every droplet at T_{surf} and $\mathbf{Y}_{\text{surf}}$. During the characteristic time $T_{L,\text{seen}}$, this seen composition $(Z^\star, Y_c^\star)$ evolves according to the IEM mixing model with the scalar variance decay frequency $\omega_\phi = 1/T_{L,\text{seen}}$. The seen properties are then obtained from the FGM table as $T_{\text{seen}} = T(Z^\star, Y_c^\star)$ and $\mathbf{Y}_{\text{seen}} = \mathbf{Y}(Z^\star, Y_c^\star)$.

Another important issue is how to distribute the fuel vapor generated by evaporation. Although more advanced methods exist [10], for simplicity, the vaporized fuel vapor is evenly distributed to all the gas phase particles present in the computational cell, similar scheme has been used in [6, 17]. This approach, essentially reduces the variance of the gaseous properties.

5.4. TEST CASE AND NUMERICAL SETUP

5.4.1. TEST CASE

5

In this Chapter we simulate one of the ethanol spray in hot-diluted coflow cases, namely the case H_{II}, in the DSHC database. Details of this case is described in section **??**.

5.4.2. NUMERICAL SETUP

COMPUTATIONAL DOMAIN

As mentioned in Section 5.1, in this study we restrict ourselves to the modeling of dilute spray combustion, no attempt is made on the modeling of film breakup and droplet formation during the atomization process. The droplet collisions, coalescence and agglomeration are also ignored. The inlet boundary is chosen such that it is sufficiently far from the atomizer tip to avoid the dense spray region but below the region where the ignition starts. In this case, the axial location $Z = 8$mm is chosen as the inlet boundary. This is also the first axial location where the dispersed phase properties were measured. As the flame is statistically axisymmetrical, a 2D axisymmetrical simulation is conducted. The computational domain is indicated by the yellow rectangle in Fig. 5.4.

GAS PHASE BOUNDARY CONDITIONS

Due to the presence of droplets, LDA measurements for the gas phase velocity were only conducted at the coflow exit ($Z = 0$mm), which can not be directly used for this study. Although the PDA results at $Z = 8$mm (inlet boundary of this simulation) for the small droplets ($D < 6\mu$m) can be used as gas velocity, they are only available at limited points due to the availability of the small droplets, see the symbols in Fig. 5.5. These limited data points do not provide enough information for the accurate assignment of the inlet boundary of the dilute spray combustion.

Furthermore, because the spray is issued into a hot coflow, some liquid fuel has already vaporized before $Z = 8$mm, and possibly some reaction has already started before the computational inlet boundary. Therefore, accurate mixture fraction and progress variable radial profiles have to be provided as boundary conditions in order to correctly predict the dilute spray combustion behavior downstream. However, the mixture fraction and progress variable are not directly available from experimental measurements.

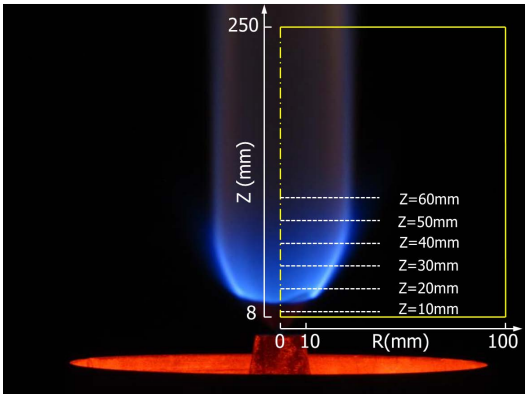

Figure 5.4: Picture of the DSHC flame, with indication of the computational domain and axial locations of experimental data.

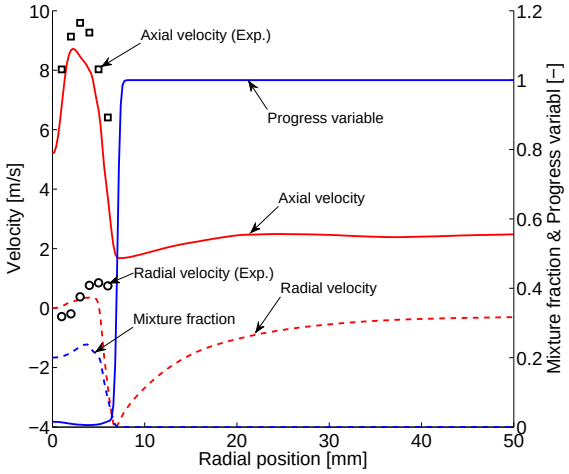

Figure 5.5: Boundary conditions for the dilute spray modeling and experimental data from PDA measurements of small droplets.

Nevertheless, the necessary properties are available at the coflow exit (Z = 0mm). A simulation of the entire spray flame, starting at Z = 0mm, including the spray atomization process was conducted with ANSYS Fluent 15.0 to derive reliable boundary conditions at Z = 8mm for the present study, following the approach reported in [52]. In the Fluent simulation, the pressure-swirl atomizer is modeled with Linearized Instability Sheet Atomization (LISA) model. Turbulence is modeled by Reynolds Stress Model (RSM). And the turbulence-chemistry interaction, to be consistent with the current study, is also modeled by FGM model but with presumed shape PDF method. β-PDF is used for both mixture fraction and progress variable. To examine the reliability of the boundary conditions provided by the Fluent simulation, not only the results at Z = 8mm but also at other axial locations are compared with experimental data. Good agreement with experiment data has been achieved by this Fluent simulation. The modeling details and results of the Fluent simulation will be reported separately. The profiles at Z = 8mm used as boundary conditions in the current simulation are shown in Fig. 5.5.

DISPERSED PHASE BOUNDARY CONDITIONS

The dispersed phase boundary conditions are assigned based on the experimental data for each droplet size class. Available dispersed phase boundary conditions include the droplet velocity components and their variance, the dispersed phase mass flow rate and the fraction of mass flow rate for each droplet class. The uncertainty exists in the droplet temperature at Z = 8mm. As described in Section 5.3.2, the modeled droplet temperature is determined by its own initial state as well as the experienced surrounding gas phase conditions. Therefore, it is difficult to accurately calculate the droplet temperature at Z = 8mm. However, single droplet simulations showed that due to the presence of high temperature coflow, the droplet temperature rises rapidly after injection. The Fluent simulation, in which the finite conductivity model is used, also confirms that the small droplets temperature at Z = 8mm are close to the boiling temperature. Here, two sets of droplet temperature boundary conditions will be tested to examine the sensitivity of the results on the droplet initial temperature. As shown in Table 5.1, droplet temperatures are assigned differently depending on their size to account for their different thermal innertia.

Table 5.1: Droplet temperature at inlet boundary (Z = 8mm)

Droplet diameter[μm]	[0,10]	[10,20]	[20,30]	[30,40]	[40,50]	[50,60]	[60,70]
Temperature [K] (T_p1)	330	330	325	325	325	320	320
Temperature [K] (T_p2)	344	343	342	341	340	336	331

NUMBER OF PARTICLES

With the time averaging and particle split/merge algorithms as described in [10], the required number of computational particles per cell is dramatically reduced. Two cases with 20 and 50 gas phase computational particles per cell are tested, no clear difference on the results is observed. According to the experiment, droplets with a diameter larger than 70μm are rarely detected. In the simulation, the droplets have been divided into

7 classes ranging from 0 to 70μm. For each droplet class, 10 nominal computational parcels per cell are used, which means a total of 70 dispersed phase parcels per cell. Within each hybrid outer iteration, 500 finite volume iterations, 10 gas particle Monte Carlo iterations and 10 droplet parcel Monte Carlo iterations are conducted respectively. More than 1000 hybrid iterations have been carried out for each case in this study to reach converged results. This is similar to the coal combustion modeling presented in [29], and in the same way, the use of a local time stepping algorithm also helped to increase the convergence rate since larger particle time steps can be used in regions with small velocities.

5.4.3. CASES

In the subsequent sections, the uncertainty of the boundary conditions, namely the droplet initial temperature at $Z = 8$mm, as well as the influence of different sub-models will be discussed. Four cases with different boundary conditions and sub-models will be analyzed, see Table 5.2. Cases "C" and "D" impose relatively low temperatures ("T_p1" in Table 5.1) as droplet boundary condition, while in the other two cases, "A" and "B", droplets are set to temperatures that are closer to the boiling temperature. In cases "A", "B" and "C", the parabolic temperature profile model is used in contrast with the infinite conductivity model used in case "D". The influence of the "1/3" rule is studied by setting α in Eq. (5.23) to 1 in case "A" and to 1/3 in the other cases.

Table 5.2: Droplet temperature at inlet boundary ($Z = 8$mm)

Case	T_p B.C.	Evap. model	α
A	T_p2	"parabolic profile"	1
B	T_p2	"parabolic profile"	1/3
C	T_p1	"parabolic profile"	1/3
D	T_p1	"infinite conductivity"	1/3

5.5. RESULTS AND DISCUSSION

5.5.1. ROLE OF THE "1/3" RULE

In Section 5.3, we saw that the film properties, λ_m, ρ_m, and $\mathscr{D}_{vap}$ are widely involved in the droplet sub-models. Due to the large normal gradients of composition and temperature near the droplet surface created by droplet evaporation, it is, theoretically, not straightforward to define a proper condition at which these properties should be evaluated. As discussed in Section 5.3.5, the empirical "1/3" rule is widely accepted for spray combustion.

Fig. 5.6 and Fig. 5.7 respectively show the predicted droplet mean axial and radial velocity components for the four cases considered in addition to experimental data. The results are plotted in a matrix of subplots with each subplot representing a certain droplet size class at a certain axial location. The droplet size increases from left to right in the matrix and the axial location increases from bottom to top. The difference between Case "A" and the other cases is only related to the way the gas phase properties used in

the droplet evaporation and dispersion models are evaluated. For cases “B”, “C” and “D” where the “1/3 rule" is applied, the gas phase mixture properties are evaluated at state $(T_{\mathrm{m}}, \mathbf{Y}_{\mathrm{m}})$ obtained from Eq. (5.23) with weighting factor $\alpha = 1/3$. In case “A”, $\alpha = 1$, the “seen" gas properties at $(T_{\mathrm{seen}}, \mathbf{Y}_{\mathrm{seen}})$ are directly used. These properties eventually affect the dispersed phase behavior via the droplet dispersion and evaporation models as described in Section 5.3. For the sake of clarity, in this section we only compare results of cases “A" and “B". It can be observed that case “A” considerably under-predicts the

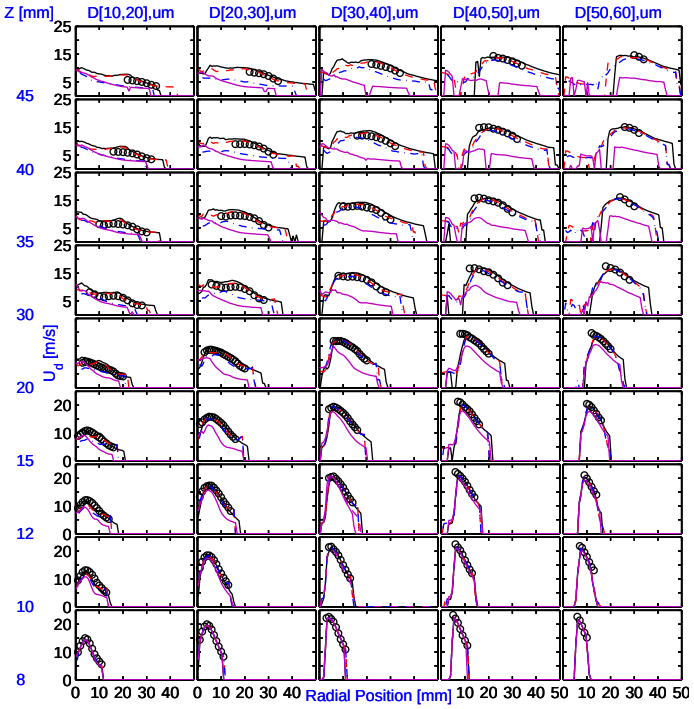

Figure 5.6: Radial profiles of droplet mean axial velocity. Black dots: experimental data, magenta solid line: case “A”, black solid line: case “B”, red dashed line: case “C”, blue dash-dotted line: case “D”.

droplet mean velocity while results of case “B" are in better agreement with experimental data. It is especially clear for large droplets at high axial locations (the up-right part of the subplots matrix). This means that the direct usage of “seen" gas properties leads to an over-prediction of the droplet velocity decay rate. Droplet velocity quickly reduces when traveling downstream.

In many spray applications, part of the droplets evaporate in a low temperature environment, where the difference between T_{surf} and T_{seen} is relative small, the averaging of gas phase properties may not make a significant difference. However, for conditions like the droplet-flame interaction and spray in hot-diluted coflow flame, where the conditions between droplet surface and surrounding gas are considerably different, this becomes very important. For example, in the current study, the gas temperature on droplet

surface, T_{surf}, is approximately equal to the droplet boiling temperature, T_{boil} = 351K. However, the "seen" gas temperature, T_{seen}, could vary in a wide range from fuel vapor temperature, ~ 351K, to flame temperature, above 2000K. The gas viscosity evaluated at (T_{seen}, Y_{seen}) is in general higher than when obtained with the "1/3" rule, according to Sutherland's law [53]. This in turn results in a shorter droplet relaxation time, see Eqs. (5.5) to (5.7). Droplets in this case tend to relax to the gas phase velocity more quickly, as demonstrated by the results of case "A" in Fig. 5.6 and Fig. 5.7. This example also illustrates the importance of droplet "seen" property model, since the "1/3 rule" is averaging the gas properties between the droplet surface and the "seen" gas. If the "seen" gas properties are not properly sampled, the results could also be different. Hereafter, we only show the simulation results obtained with the "1/3 rule", namely cases "B", "C" and "D".

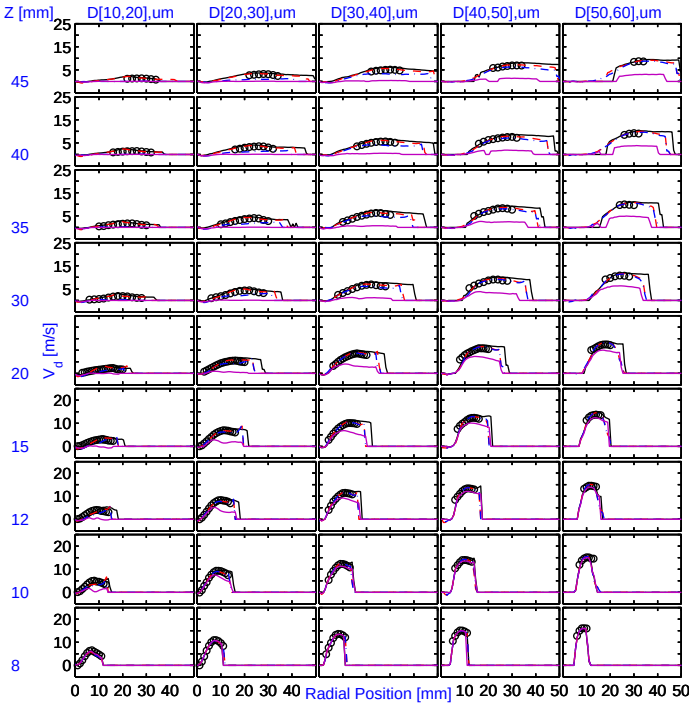

Figure 5.7: Radial profiles of droplet mean radial velocity. Black dots: experimental data, magenta solid line: case "A", black solid line: case "B", red dashed line: case "C", blue dash-dotted line: case "D".

5.5.2. INFLUENCE OF DROPLET TEMPERATURE BOUNDARY CONDITION

Since the droplet temperature boundary condition is the main uncertainty for the modeling of this flame, cases with two different sets of droplet temperature boundary conditions will be analyzed. In this section, we focus on the results predicted by cases "B" and "C".

As already shown in Fig. 5.6 and Fig. 5.7, the mean droplet velocity predicted by cases "B" and "C" do not exhibit considerable difference. With both sets of droplet initial temperature, the droplet Reynolds stresses $\overline{u_p'^2}$ are over-predicted in the near axis region for all the droplet classes, as depicted in Fig. 5.8. The reason for the over-prediction will be discussed later. It is fair to say that the different droplet temperature boundary conditions do not lead to significant differences in the droplet mean velocities and their higher moments. However, as expected, the droplet Sauter Mean Diameter (SMD), shown in

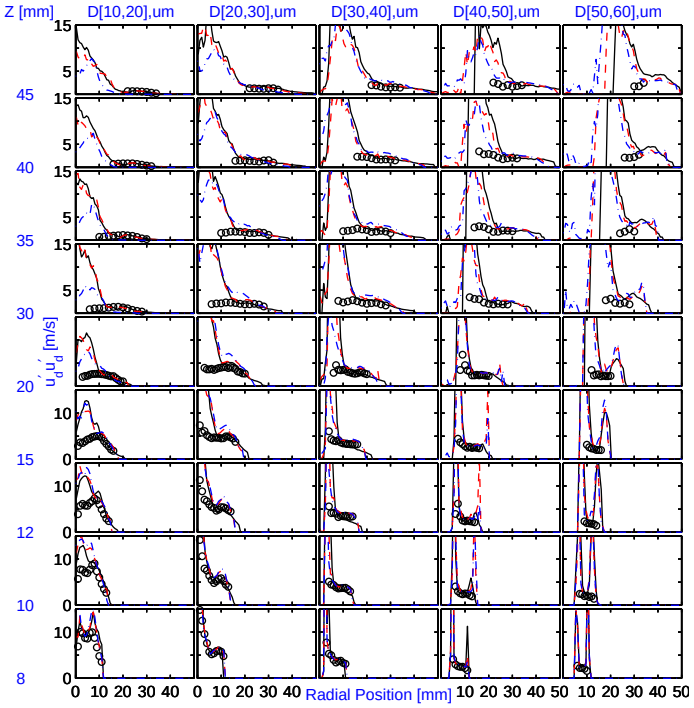

Figure 5.8: Radial profiles of droplet Reynolds stress $\overline{u'^2}$. Black dots: experimental data, black solid line: case "B", red dashed line: case "C", blue dash-dotted line: case "D".

Fig. 5.10, do unveil the differences caused by droplet temperature boundary condition. In general, both case "B" and "C" predict correct trend and magnitude of SMD, indicating the good performance of the droplet evaporation and dispersion model. Nonetheless, at the spray outer edge, the SMD is over-predicted by the "low" initial droplet temperature in case "C" and under-predicted by the "high" initial droplet temperature in case "B". These results mean that a better initial temperature for large droplet should be in between the value in "T_p1" and "T_p2" in Table 5.1. The predicted results for small value of SMD are almost identical. This is because the temperature of these small droplets rise very quickly to the so-called "wet bulb temperature" after injection. The initial temperature of the small droplets therefore has smaller influence on the results. The same trend is observed for the droplet number density in Fig. 5.11. The results for small droplets

predicted by these two cases are quite similar to each other, except that in case “B", the droplets have a wider radial distribution. The number density for large droplets is lower in case “B" than that in case “C", indicating that less large droplets survive due to faster evaporation. The influence of droplet initial temperature on gas phase velocity

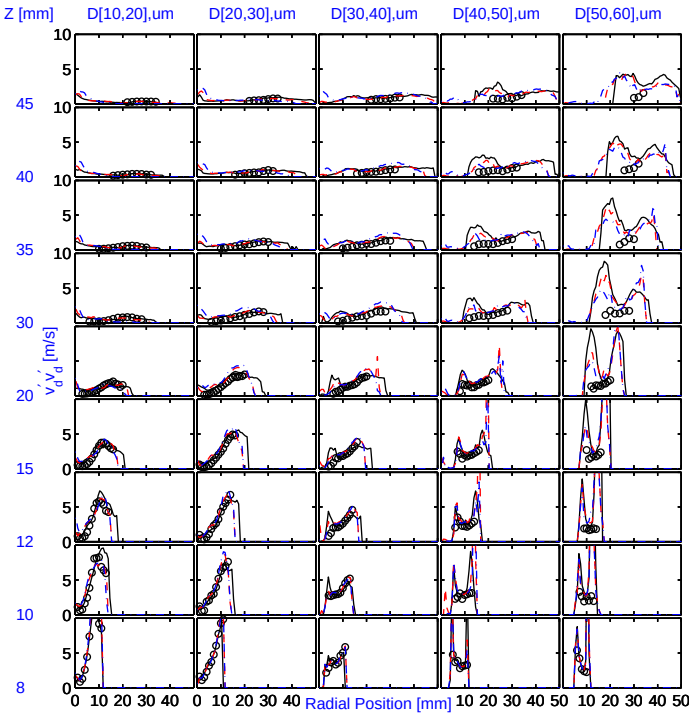

Figure 5.9: Radial profiles of droplet Reynolds stress $\overline{v'^2}$. Black dots: experimental data, black solid line: case “B”, red dashed line: case “C”, blue dash-dotted line: case “D”.

and Reynolds stresses is almost negligible, as shown in Fig. 5.12 and Fig. 5.13. A slight difference is observed on the gas phase temperature in Fig. 5.12 between case “B” and “C”, related to different mixture fraction source terms in both cases. However, this difference does not include the effects of heat loss due to droplet evaporation, which is not considered here.

5.5.3. INFLUENCE OF THE EVAPORATION MODEL

In this section, the two cases, “C” and “D”, which differ only in the droplet evaporation model will be analyzed. As explained in Section 5.3.2, the parabolic temperature profile model assumes that the temperature distribution inside the droplet is a parabola from surface to center, while the infinite conductivity model assumes isothermal conditions inside droplet. The parabolic temperature profile model can be categorized as “conduction limit” model, while the infinite conductivity model is also called “fast mixing” model. Fig. 5.14 shows the average difference between droplet surface and center

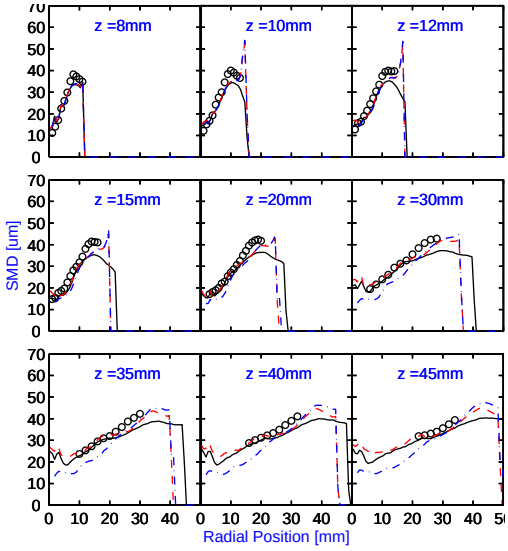

Figure 5.10: Radial profiles of droplet Sauter Mean Diameter. Black dots: experimental data, black solid line: case “B”, red dashed line: case “C”, blue dash-dotted line: case “D”.

temperature predicted by the parabolic temperature profile model as a function of axial location. It illustrates that after injection, the difference between the temperature at the droplet surface and at the center varies differently for the different droplet sizes. For small droplets, the difference continuously decreases as the droplets travel downstream. However, for droplets larger than 20μm, the droplet surface temperature first quickly increases and the surface-center temperature difference initially becomes larger. After some time, the heat conducts to the center and the difference decreases. The surface-center temperature difference in the infinite conductivity model case of course remains zero during the droplet lifetime. It was demonstrated by Dombrovsky and Sazhin [47] that the temporal evolution of the droplet temperature predicted by the parabolic temperature profile model closely resembles the one obtained by solving the heat conduction problem inside the droplets except in a very short time period at the beginning. In Fig. 5.10, it is observed that the droplet SMD predicted using the parabolic temperature profile matches well the experimental data, while it is obviously under-predicted at the near axis region when using the infinite conductivity model.

In case “D", where the infinite conductivity model is employed, the droplet number density of small droplets, Fig. 5.11, is over-predicted in the near axis region, and under-predicted in the spray outer edge. This is because the isothermal assumption in the infinite conductivity model results in a relatively lower droplet surface temperature, which determines the evaporation process. The droplet evaporation is therefore under-predicted by the infinite conductivity model compared to the parabolic temperature profile model. The small droplets in the near axis region do not vanish as fast as in Case “C”. Similarly, the relatively slow evaporation of large droplets at the spray outer region does not generate as many small droplets as in Case “C”. That also explains the

different behavior of SMD predicted by these two models as described above.

The different evaporation models also have a noticeable impact on the gas phase mean velocity via two-way coupling. Since the droplet velocity in case “D" has been under-predicted, the gas phase “feels" less acceleration from the evaporated mass. Therefore, the gas phase velocity in case “D" is lower than that in the case “C" as well as the experimental data. This is especially clear at high axial locations, see Fig. 5.12. Because of the fast evaporation of small droplets in the near axis region, combustible mixture has been quickly formed in this region. The ignition and combustion in this case therefore occur at a smaller radial location than that in case “C", as depicted in Fig. 5.15. The temperature fluctuation in case “D" is also stronger in the near axis region.

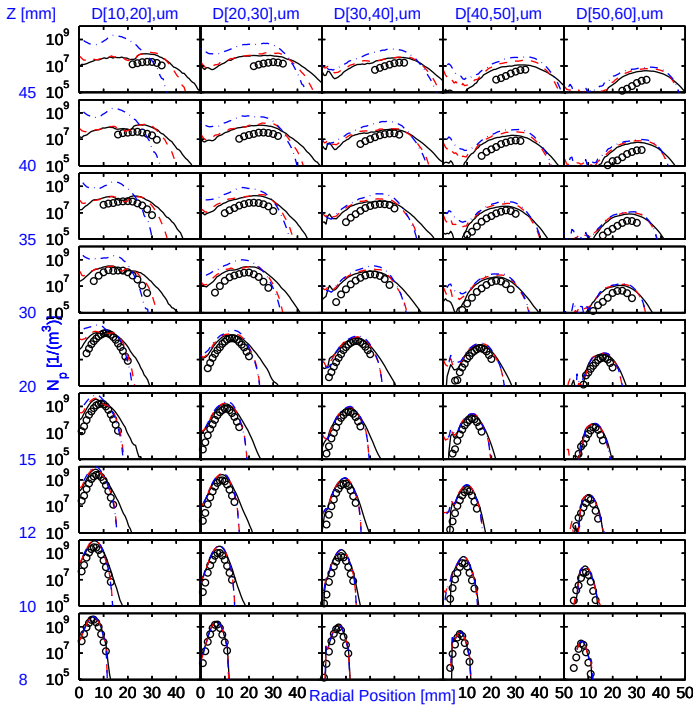

Figure 5.11: Radial profiles of droplet number density. Black dots: experimental data, black solid line: case “B”, red dashed line: case “C”, blue dash-dotted line: case “D”.

5.5.4. COMPARISON WITH EXPERIMENTAL DATA

From the previous analysis, it is already clear that the “1/3" rule should be applied in the simulation; the two different droplet temperature boundary conditions do not produce significant difference in the results, but a correct initial temperature for large droplets is important; and the parabolic temperature profile model outperforms the infinite conductivity model. We now proceed to an overall comparison of the predicted results with the experimental data. In this section, the results from case “C", which has been

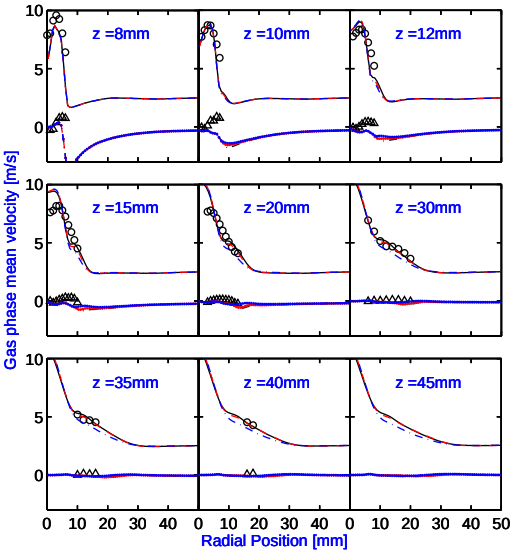

Figure 5.12: Radial profiles of gas phase mean velocity. Black circles: experimental axial velocity, black triangles: experimental radial velocity, black solid line: case "B" axial velocity, red dashed line: case "C" axial velocity, blue dash-dotted line: case "D" axial velocity, black solid line with dots: case "B" radial velocity, red dashed line with dots: case "C" radial velocity, blue dash-dotted line with dots: case "D" radial velocity.

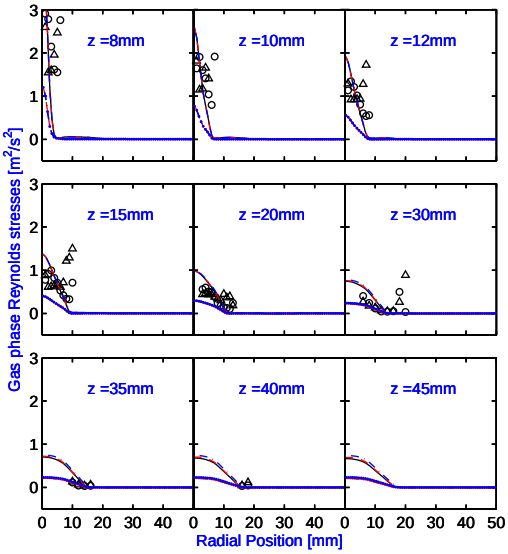

Figure 5.13: Radial profiles of gas phase Reynolds stresses. Black circles: experimental axial velocity, black triangles: experimental radial velocity, black solid line: case "B" $\widetilde{u''^2}$, red dashed line: case "C" $\widetilde{u''^2}$, blue dash dotted line: case "D" $\widetilde{u''^2}$, black solid line with dots: case "B" $\widetilde{v''^2}$, red dashed line with dots: case "C" $\widetilde{v''^2}$, blue dash dotted line with dots: case "D" $\widetilde{v''^2}$.

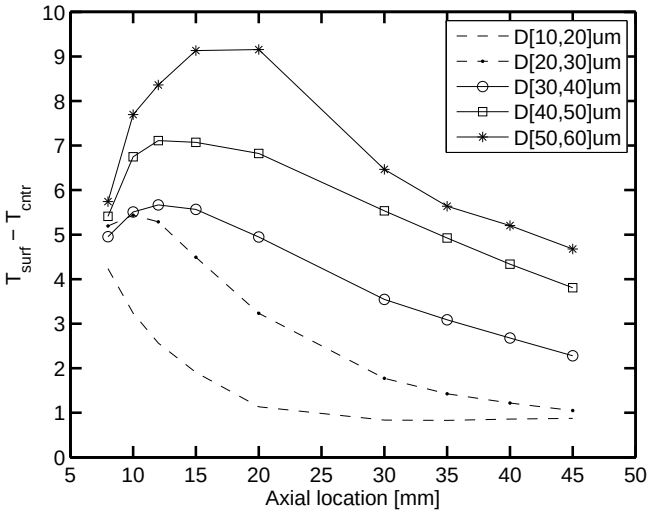

Figure 5.14: Mean difference between droplet surface and center temperature predicted by the "parabolic profile model (case "C") at varying axial locations.

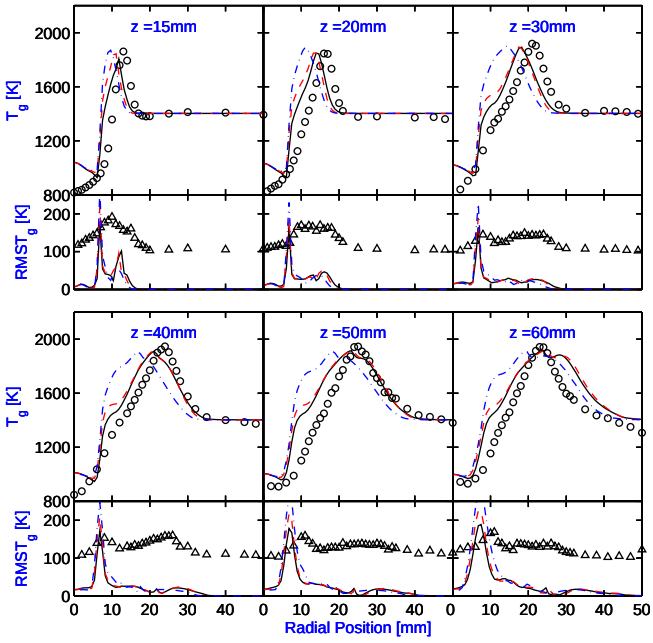

Figure 5.15: Radial profiles of gas phase mean and RSM temperature. Black circles: experimental temperature data, black triangles: experimental RMS temperature data, Black solid line: case "B", red dashed line: case "C", blue dash-dotted line: case "D".

shown to be the best among others, will be examined over experimental data to show the achievements and incapabilities of the current modeling approach.

First of all, as can be seen from Fig. 5.6 and Fig. 5.7, the droplet mean velocity components for all the droplet classes have been accurately reproduced at all the axial locations that have been checked. Note that the experimental data is only available within a certain radial range, this is related to the cone-shape spray structure and the number of sample data required to have a converged statistics in experiment. Out of the main spray region, the number density of the droplet becomes very small. In order to have a converged statistics, a sufficiently long measuring time is demanded, which is not always convenient for a spray combustion experiment. Therefore, only data in the main spray region, which is also considered of most interest, are available [3]. The same argument also holds for the simulation. Even though the iteration averaging algrithm is employed, the number of numerical parcels for droplets is only large enough to have converged statistics in the main spray region. Out of this region, the results include large statistical errors. For the droplet Reynolds stresses, $\overline{u_p'^2}$ and $\overline{v_p'^2}$, shown in Fig. 5.8 and Fig. 5.9, satisfying agreement with experimental data has been achieved in the main spray region. Significant over-prediction is observed in the near axis region and at large radius. These discrepancies of droplet Reynolds stresses are believed to be caused by the unconverged statistics due to the insufficient number of droplet parcels. The predicted $\overline{v_p'^2}$ is in general in better agreement with experiment data than $\overline{u_p'^2}$, see Fig. 5.9. However, the discrepancies for large droplets are obvious, and this may be related to the fact that the number density of large droplet is one to two orders of magnitude lower than that of the small droplets, as can be seen in Fig. 5.11.

Droplet Sauter Mean Diameter (SMD) is fairly well predicted by case "C", as shown in Fig. 5.10. As discussed before, the over-prediction at the outer edge of spray is attributed to the low temperature boundary condition for large droplets. The trend of the droplet number density is also well captured, Fig. 5.11. The slight over-prediction of the droplet number density may be due to the fact that some sample data were rejected during experiment when more than two droplets are present in the probe volume [3]. The above discussion demonstrates that the droplet sub-models, including the droplet dispersion model, evaporation model and seen gas model, are capable to accurately reproduce the dispersed phase behavior of the DSHC flame.

In Fig. 5.12 the modeled mean axial and radial gas-phase velocity components are compared to the experimental data obtained by PDA from the smallest droplets as tracers. Good agreement is obtained for the mean axial velocity. The discrepancy between the modeled and measured mean radial velocity could be explained by the fact that using small droplets as tracers in the near field corresponds to a non-uniform seeding of the flow. The small droplets, mainly moving outwards, do not represent in an unbiased manner the complete gas phase. A better, unbiased, mean velocity measurement would include more samples of coflow gas without droplets, with predominantly inwards velocity. From axial location $Z = 45$mm, not enough tracer droplets are available due to the evaporation, therefore no experimental data are available thereafter. The predicted gas phase Reynolds stress $\widetilde{u''^2}$ is in reasonable agreement with measured data. The $\widetilde{v''^2}$ is under-predicted at low axial location, which can also be explained by the bias in the

gas-phase radial velocity measurements based on a non-uniform small droplet seeding.

Gas phase temperature in the spray region has been measured with CARS technique [3]. A reasonable agreement with experimental data is obtained in case “C". The flame peak temperature as well as the flame width are correctly predicted. The radial position of the peak temperature is slightly shifted towards the center. This may mainly be caused by the mixture fraction profile specified at the inlet boundary. As explained in [52], the Fluent simulation used for providing inlet boundary information for this study predicts a smaller spray angle compared to the experiment. Consequently the distribution of the free vapor is also narrower. Close to the spray axis, an opposite temperature trend is predicted. The simulation shows a small temperature peak in the center, while the temperature progressively decreases towards the center in the experiment. This is because near the spray axis many small droplets exist, and considerable gas phase enthalpy loss happens in this region due to the fast evaporation of small droplets. The enthalpy loss, however, can not be accounted for by the 2D adiabatic FGM table used in the current study. As a consequence, the temperature has been over-predicted in this region. This problem can be solved by including enthalpy loss as another independent variable of the FGM table, namely using a non-adiabatic FGM table.

It is noticeable in Fig. 5.15, that the gas phase RMS temperature is significantly under-predicted. It is also noticed that the predicted RMS temperature is somehow systematically about 100 K lower than the experimental counterpart. This systematical difference in RMS temperature is believed to be mainly caused by the exclusion of temperature fluctuation at the inlet boundary. From the experimental data at radial position 20mm to 50mm in the first subplot in Fig. 5.15, we clearly see that the 100K deviation is equivalent to the temperature fluctuation in the coflow. The influence of temperature fluctuation at the inlet boundary will be further discussed in Section 5.5.6.

5.5.5. FLAME STRUCTURE

The fuel vapor released from the droplets makes the spray combustion show characteristics of both premixed and diffusion flames. The Flame index is a commonly used parameter to identify the premixed and non-premixed flame in the context of DNS or LES [38, 54]. Although the applicability of the flame index in the RANS simulation is still questionable, the “averaged" flame index can still reveal some major characteristics of the flame structure of the DSHC flame. The flame index is normally defined as the product of the spatial gradients of fuel and oxidizer mass fraction:

$$FI = \nabla Y_f \cdot \nabla Y_{O_2}.$$

In most literature, only the fuel from the inlet or from the droplet vapor is used in the calculation of the flame index. This is acceptable in the cases where the global one step reaction is used or the chemical reaction is infinitely fast [22]. In cases where the intermediate reactions are important, the intermediate species such as H_2 and CO should also been considered as fuel. Therefore, in this study, we define the following three flame indices:

$$FI_{C_2H_5OH} = \nabla Y_{C_2H_5OH} \cdot \nabla Y_{O_2},$$

$$FI_{H_2} = \nabla Y_{H_2} \cdot \nabla Y_{O_2},$$

$$FI_{CO} = \nabla Y_{CO} \cdot \nabla Y_{O_2}.$$

Their contour plots are shown in Fig. 5.16. The contour plots of mean mass fractions of C_2H_5OH, O_2, H_2, CO and H_2O are shown Fig. 5.17 to better illustrate the structure of this flame. In all these plots two iso-surfaces of gas temperature 1400K and 1600K are imposed to indicate the heat release region. According to the flame indices and the species

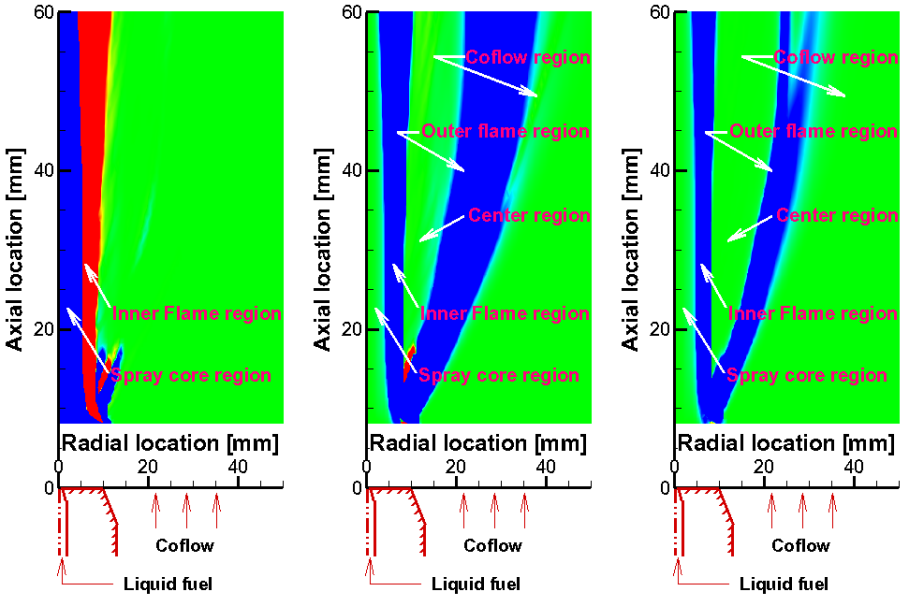

Figure 5.16: Flame index, left: $FI_{C_2H_5OH}$, middle: FI_{CO}, right: FI_{H_2}. Blue represents $FI < 0$, red represents $FI > 0$, green represents $FI = 0$.

mass fraction contour plots, the DSHC flame can be divided into the following five regions: the spray core region, the inner flame region, the center region, the outer flame region and the coflow region, they are indicated on the contour plot of flame indices Fig. 5.16. The spray core region is the region near the axis, where the small droplet accumulate and quickly evaporate. Next to it is the inner flame region, further outward is the center region, and the outer flame region. The coflow region is sitting most outside, and is not involved in any combustion.

In the spray core region, the O_2 entrained from the coflow before the lift-off of the flame coexists with the fuel vaporized from small droplets. The O_2 has a negative radial gradient while the fuel vapor has a positive gradient due to the cone shape spray generated by the pressure-swirl atomizer. Therefore in this region, the $FI_{C_2H_5OH}$ is negative, but it does not necessarily mean that a diffusion flame exists here, because the temperature in this region is relatively low. This negative $FI_{C_2H_5OH}$ is a sign of local production of fuel vapor, which is quite different from a gaseous flame case.

In the inner flame region, presence of a secondary flame front is revealed by a local peak in the RMS temperature profile in Fig. 5.15 (e.g. r=8 mm at Z=30 mm) and the posi-

tive $FI_{C_2H_5OH}$ in Fig. 5.16. This inner flame front is produced by the reaction of the premixed C_2H_5OH and O_2 coming from the spray core region. However, due to the dilution of the coflow, the O_2 in the spray core region is not enough to fully convert the C_2H_5OH to the final reaction products, CO_2 and H_2O. The temperature in this diluted rich region is relatively low and this is particularly suitable for pyrolytic or reforming stages leading to H_2 and CO [1], see Fig. 5.17. Therefore, we see also a negative FI_{CO} and FI_{H_2} in the inner flame region. Again, the negative FI_{CO} and FI_{H_2} do not correspond to a diffusion flame here, but to a local generation of CO and H_2. Supporting this observation, the high concentration of CO and H_2 have also been found in the furnace or well-stirred reactor (WSR) under MILD combustion conditions by other experimental [55] and numerical [56] studies. In the DSHC experimental results, the inner flame is only detectable at axial locations from 30mm onward, because the heat release from this inner flame front, has been partially compensated by the heat loss due to droplet evaporation. In the present simulations in which the heat loss is not considered, the inner flame front is clearly revealed by the shoulder in the mean temperature profile at the inner branch of the spray flame. The phenomenon that the inner flame front locates at more or less the same radial location with varying axial locations is also correctly captured by the simulation. The reason for this is that the inner flame front is mainly formed by the vaporized fuel vapor, and therefore behaves like a gaseous jet flame. The spreading rate is much lower than that of the outer flame region which is aligned with the spray outer edge.

Further outward, there is the center region. The peak of the temperature radial profile appears in this region, but it is mainly due to the heat released from the inner and outer flame regions rather than local combustion. Reaction barely happens in this region, because of the lack of O_2. The intermediate species will continuously react with the O_2 coming from the coflow at the outer flame region, which is also the main heat release region. In the outer flame region, a diffusion-like flame is formed, see the negative FI_{CO} and FI_{H_2} in this region in Fig. 5.16. The final combustion products are also formed in this region, see the contour plot of mean H_2O mass fraction in Fig. 5.17. Finally, almost no droplets survive beyond the outer flame region, and the flow composition in this region remains the same as that of the coflow.

As discussed above, under the hot-diluted coflow conditions the incomplete oxidation of fuel and the further reaction of the intermediate species are spatially separated. This results in a more distributed heat release region and a lower peak temperature, which are precisely desired in the MILD combustion technology for the reduction of NOx formation [2, 57].

5.5.6. TEMPERATURE PDF

Fig. 5.18 compares the gas phase temperature PDF obtained from experiment and simulation respectively. The solid red line represents the predicted temperature PDF and the solid black line is the temperature PDF obtained from the CARS measurements. To guarantee the convergence of the PDF, at least 1000 CARS samples are considered for each point in the experiment. The Monte Carlo particles are sampled over at least 5000 Langrangian time steps. The PDF comparison are carried out for 9 different locations as illustrated by the black dots on the temperature contour plot in Fig. 5.17.

The under-prediction of the temperature variance discussed in Section 5.5.4 is clearly

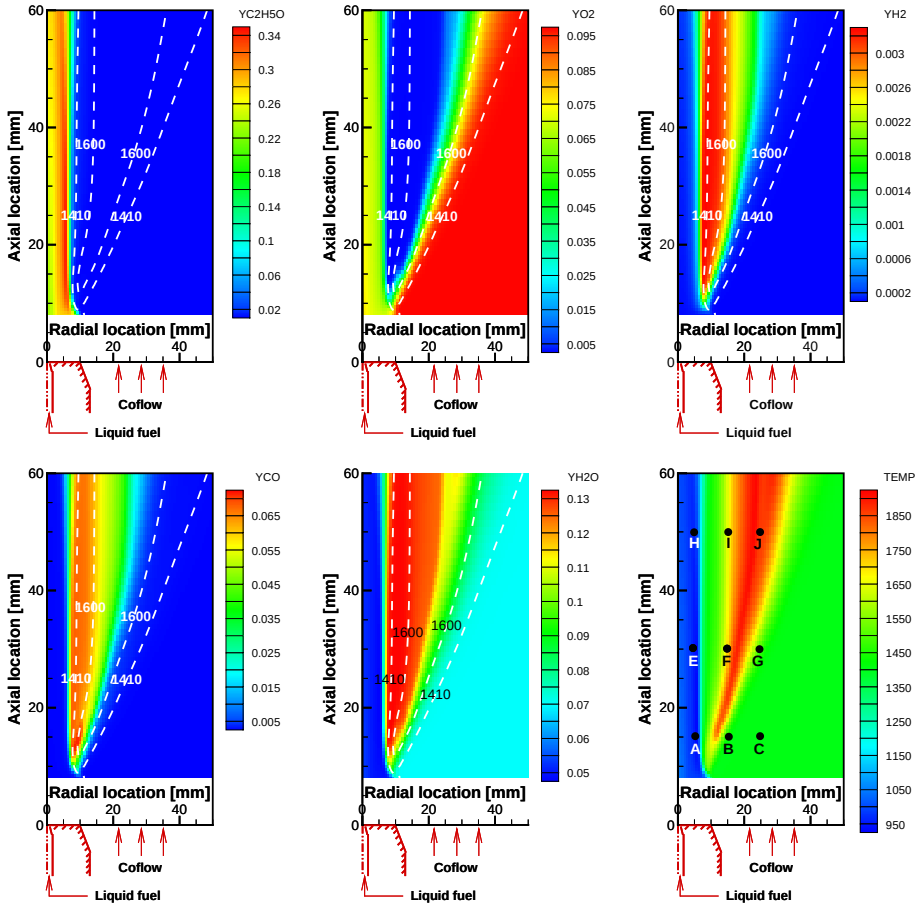

Figure 5.17: Contour plots of the simulation results, dashed lines are the iso-surface of T = 1410K and 1600K respectively. Top: C_2H_5OH, O_2, H_2; Bottom: CO, H_2O, temperature. Black dots on temperature contour indicate the locations where the temperature PDF is analyzed.

shown here by means of narrower temperature PDF distributions. The reason for this can be explained by the PDF at point “C", which is located in the coflow region and is only influenced by the coflow inlet boundary condition. The predicted temperature PDF of point “C" is a δ-function at the experimental mean temperature, whereas the experimental data show a Gaussian distribution within the range of 1000K – 1700K. This means that the mean temperature of the coflow has been exactly represented by the FGM table, but no temperature fluctuation at the inlet is considered. The exclusion of the temperature fluctuation at the flame inlet boundary consequently reduces the temperature fluctuations in the whole simulation domain. The temperature PDF prediction could be improved if the temperature fluctuations at the inlet would be included. The implementation of the inlet boundary temperature fluctuations can be done provided that the non-adiabatic FGM table is applied. Temperature fluctuations can be imposed by supplying gas phase Monte Carlo particles with fluctuating enthaly loss/gain values. This will be done in a future study.

The adiabatic FGM table also has a significant influence on the temperature PDF. The gas phase energy loss due to droplet evaporation can not be properly considered by the current adiabatic FGM table. This is the direct reason for the absence of the lower temperature tail of the PDF for points A, E, F, H, I, J , and the shift of the PDF towards the high temperature at these points. For points B and F, however, the whole PDF have been shifted towards the low temperature. This may be explained by the differential diffusion of H_2. In reality, the H_2 diffuses faster than other larger molecular species. In this case, the H_2 formed in the inner flame region diffuses faster outward than CO, therefore at the edge of the outer flame region, some pure H_2 combustion may occur. This can be proved by the very high temperature samples (> 2200K), which is higher than the adiabatic C_2H_5OH flame temperature under the diluted coflow condition, at points B and F. Correct account of differential diffusion of H_2 itself is still a big challenge for combustion modeling, and is out of the scope of current study. Readers interested in this topic are referred to [58]. Besides the two discrepancies mentioned above, comparison of the predicted temperature PDF with experimental data demonstrated the ability of transported PDF method.

5.6. CONCLUSION

In this paper, we reported a first numerical investigation of the Delft Spray-in-Hot-Coflow flame with transported PDF method and FGM model. The in-house hybrid finite-volume / particle transported PDF code “PDFD" is used for the simulation. A Lagrangian-Lagrangian approach is employed to describe the two-phase turbulent flow field in the dilute spray region. The continuous phase is described by a joint velocity-scalar PDF, and the dispersed phase is described by a joint PDF of droplet position, velocity, temperature, diameter, and gaseous properties “seen" by the droplet. The inlet boundary conditions for the dilute spray simulation was fulfilled by the results from a complete spray simulation with ANSYS Fluent 15.0 and the available experimental data. An uncertainty exists on the boundary condition for the droplet initial temperature. Two sets of different droplet temperature boundary conditions were tested. It was shown that the initial temperature of small droplets has a negligible effect on the results, while the initial temperature of large droplets considerably influences the droplet SMD and number density downstream. For

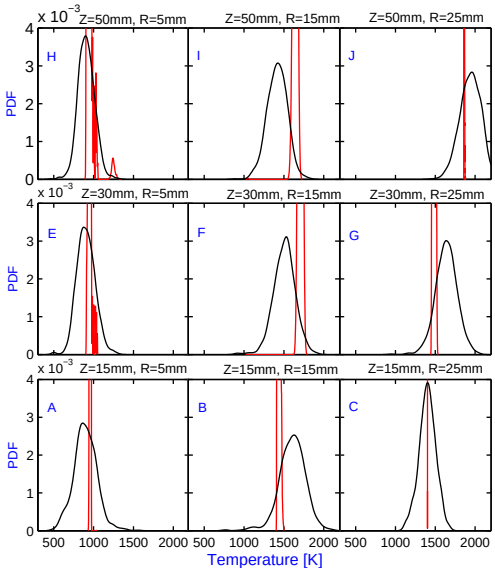

Figure 5.18: Temperature PDF, solid black line: from experiment, solid red line: from simulation.

future study, the temperature boundary condition is suggested to take values in between the two sets of temperature tested in this study. A parabolic temperature profile model was used to describe the droplet heating and evaporation process. Its performance was compared with the widely used infinite conductivity model. By being able to take into account the finite heat conduction process inside droplets, the former shows superior performance over the latter in terms of better agreement with experimental data on both gas and dispersed phase properties.

The influence of the “1/3" averaging rule was examined in detail. The results showed that the “1/3" averaging rule has a considerable influence on the droplet dispersion behavior, especially when the difference between the temperature at the droplet surface and in the surrounding environment is large: for example for droplet-flame interaction and in the spray-in-hot-coflow situations. A direct use of the “seen" gas properties for the evolution of the gas phase properties in the evaporation and dispersion models under these conditions leads to a too fast decay of droplet velocity.

The current modeling approach was further validated by comparing the results predicted by case “C", where the parabolic temperature profile model and the “1/3" rule were applied, with available experimental data. Droplet velocity, Sauter Mean Diameter and number density are all in good agreement with measured data, showing that the spray sub-models including the evaporation and dispersion models used in this study are suitable for modeling the DSHC flame. Gas phase velocity also matches well the available experimental data. The mean temperature was predicted with reasonable agreement with experimental data. However it was over-predicted in the central part of the spray where intensive droplet evaporation happens. The reason for this is that the heat

loss due to evaporation can not the properly considered by the adiabatic FGM table used in this study. The temperature variance has been significantly under-predicted due to the exclusion of the temperature fluctuations at the inlet boundary. The use of an adiabatic FGM table and leaving out the H_2 differential diffusion effects both contribute to the large discrepancy between the experimental and modeled temperature PDF.

The structure of the modeled flame was analyzed. It was found that two heat release regions exist. The inner flame region is formed by the reaction between the fuel vapor and the coflow oxidizer entrained from the flame base below lift-off height, and mainly behaves like a premixed flame. The outer flame region, which is the main heat release region, is mainly created by the further oxidation of the intermediate species formed at the inner flame region, and shows characteristics of diffusion flame. The incomplete oxidation of fuel and the further reaction of the intermediate species are spatially separated, resulting in a more distributed heat release region and a lower peak temperature, which are desired conditions in the MILD combustion technology for the reduction of NOx formation.

The transported PDF method together with the FGM model presented in this study show promising performance on modeling dilute spray combustion. The two phase flow field as well as the flame structure could be properly reproduced. However, further improvements are required in order to have a more precise prediction of the temperature PDF. These improvements include taking into account the enthalpy effects, considering differential diffusion effects, and including the temperature fluctuations at the inlet boundary.

REFERENCES

[1] A. Cavaliere and M. de Joannon, *Mild Combustion,* Progress in Energy and Combustion Science **30**, 329 (2004).

[2] J. A. Wünning and J. G. Wünning, *Flameless oxidation to reduce thermal no-formation,* Progress in Energy and Combustion Science **23**, 81 (1997).

[3] H. Correia Rodrigues, M. J. Tummers, E. H. van Veen, and D. Roekaerts, *Spray flame structure in conventional and hot-diluted combustion regime,* Combustion and Flame **162**, 759 (2015).

[4] P. Jenny, D. Roekaerts, and N. Beishuizen, *Modeling of turbulent dilute spray combustion,* Progress in Energy and Combustion Science **38**, 846 (2012).

[5] M. Chrigui, A. R. Masri, A. Sadiki, and J. Janicka, *Large Eddy Simulation of a polydisperse ethanol wpray flame,* Flow, Turbulence and Combustion **90**, 813 (2013).

[6] C. Heye, V. Raman, and A. R. Masri, *LES/probability density function approach for the simulation of an ethanol spray flame,* Proceedings of the Combustion Institute **34**, 1633 (2013).

[7] S. B. Pope, *PDF methods for turbulent reactive flows,* Progress in Energy and Combustion Science **11**, 119 (1985).

[8] D. Haworth, *Progress in probability density function methods for turbulent reacting flows,* Progress in Energy and Combustion Science **36**, 168 (2010).

[9] S. B. Pope, *Small scales, many species and the manifold challenges of turbulent combustion,* Proceedings of the Combustion Institute **34**, 1 (2013).

[10] B. Naud, *PDF modeling of turbulent sprays and flames using a particle stochastic approach*, Ph.D. thesis, Delft University of Technology (2003).

[11] B. Naud, *Particle dispersion modelling based on the Generalised Langevin Model for the seen velocity,* in *Turbulence, Heat and Mass Transfer 7* (2012).

[12] B. Naud, C. Jiménez, and D. Roekaerts, *A consistent hybrid PDF method : implementation details and application to the simulation of a bluff-body stabilised flame,* Progress in Computational Fluid Dynamics **6**, 146 (2006).

[13] B. Naud, B. Merci, and D. Roekaerts, *Generalised Langevin Model in correspondence with a chosen standard scalar-flux second-Moment closure,* Flow, Turbulence and Combustion **85**, 363 (2010).

[14] N. A. Beishuizen, *PDF modelling and particle-turbulence interaction of turbulent spray flames*, Ph.D. thesis, Delft University of Technology (2008).

[15] H.-W. Ge and E. Gutheil, *Simulation of a turbulent spray flame using coupled PDF gas phase and spray flamelet modeling,* Combustion and Flame **153**, 173 (2008).

[16] H.-W. Ge, Y. Hu, and E. Gutheil, *Joint gas-phase velocity-scalar PDF modeling for turbulent evaporating spray flows,* Combustion Science and Technology **184**, 1664 (2012).

[17] S. Bhattacharjee and D. C. Haworth, *Simulations of transient n-heptane and n-dodecane spray flames under engine-relevant conditions using a transported PDF method,* Combustion and Flame **160**, 2083 (2013).

[18] Y. Pei, E. R. Hawkes, and S. Kook, *A comprehensive study of effects of mixing and chemical kinetic models on predictions of n-heptane jet ignitions with the PDF method,* Flow, Turbulence and Combustion **91**, 249 (2013).

[19] Y. Pei, E. R. Hawkes, and S. Kook, *Transported probability density function modelling of the vapour phase of an n-heptane jet at diesel engine conditions,* Proceedings of the Combustion Institute **34**, 3039 (2013).

[20] W. Jones, A. Marquis, and K. Vogiatzaki, *Large-eddy simulation of spray combustion in a gas turbine combustor,* Combustion and Flame **161**, 222 (2014).

[21] J. A. van Oijen and L. P. H. de Goey, *Modelling of premixed laminar flames using flamelet-generated manifolds,* Combustion Science and Technology **161**, 113 (2000).

[22] H. Watanabe, R. Kurose, S. Hwang, and F. Akamatsu, *Characteristics of flamelets in spray flames formed in a laminar counterflow,* Combustion and Flame **148**, 234 (2007).

[23] R. de Meester, B. Naud, U. Maas, and B. Merci, *Transported scalar PDF calculations of a swirling bluff body flame SM1 with a reaction diffusion manifold,* Combustion and Flame **159**, 2415 (2012).

[24] C. Hollmann and E. Gutheil, *Modeling of turbulent spray flames including detailed chemistry,* in *26 th Symposium (International) on Combustion* (1996) pp. 1731–1738.

[25] C. Hollmann and E. Gutheil, *Flamelet-modeling of turbulent spray diffusion flames based on a laminar spray flame library,* Combustion Science and Technology **135**, 175 (1998).

[26] E. Gutheil and W. Sirignano, *Counterflow spray combustion modeling with detailed transport and detailed chemistry,* Combustion and Flame **113**, 92 (1998).

[27] H. Olguin and E. Gutheil, *Influence of evaporation on spray flamelet structures,* Combustion and Flame **161**, 987 (2014).

[28] M. Chrigui, J. Gounder, A. Sadiki, A. R. Masri, and J. Janicka, *Partially premixed reacting acetone spray using LES and FGM tabulated chemistry,* Combustion and Flame **159**, 2718 (2012).

[29] M. Stöllinger, B. Naud, D. Roekaerts, N. Beishuizen, and S. Heinz, *PDF modeling and simulations of pulverized coal combustion – Part 2: Application,* Combustion and Flame **160**, 396 (2013).

[30] G. Anand and P. Jenny, *Stochastic modeling of evaporating sprays within a consistent hybrid joint PDF framework,* Journal of Computational Physics **228**, 2063 (2009).

[31] J. A. van Oijen, *Flamelet-Generated Manifolds : Development and Application to Premixed Laminar Flames,* Ph.D. thesis, Eindhoven University of Technology (2002).

[32] M. Ihme and Y. C. See, *Prediction of autoignition in a lifted methane/air flame using an unsteady flamelet/progress variable model,* Combustion and Flame **157**, 1850 (2010).

[33] B. Naud, R. Novella, J. M. Pastor, and J. F. Winklinger, *RANS modelling of a lifted H2/N2 flame using an unsteady flamelet progress variable approach with presumed PDF,* Combustion and Flame **162**, 893 (2014).

[34] C. Duwig and M. J. Dunn, *Large Eddy Simulation of a premixed jet flame stabilized by a vitiated co-flow: Evaluation of auto-ignition tabulated chemistry,* Combustion and Flame **160**, 2879 (2013).

[35] P. Domingo, L. Vervisch, and D. Veynante, *Large-eddy simulation of a lifted methane jet flame in a vitiated coflow,* Combustion and Flame **152**, 415 (2008).

[36] CHEM1D, A one-dimensional laminar flame code, *Eindhoven University of Technology,* (URL:http://www. combustion. tue. nl/chem1d//).

[37] N. M. Marinov, *A Detailed Chemical Kinetic Model for High Temperature Ethanol Oxidation,* International Journal of Chemical Kinetics **31**, 183 (1998).

[38] Y. Baba and R. Kurose, *Analysis and flamelet modelling for spray combustion,* Journal of Fluid Mechanics **612**, 45 (2008).

[39] B. Franzelli, B. Fiorina, and N. Darabiha, *A tabulated chemistry method for spray combustion,* Proceedings of the Combustion Institute **34**, 1659 (2013).

[40] K. Luo, J. Fan, and K. Cen, *New spray flamelet equations considering evaporation effects in the mixture fraction space,* Fuel **103**, 1154 (2013).

[41] J. S. Shirolkar, C. F. M. Coimbra, and M. Q. Mcquay, *Flundamental aspects of modeling turbulent particle dispersion in dilute flows,* Progress in Energy and Combustion Science **22**, 363 (1996).

[42] S. S. Sazhin, *Advanced models of fuel droplet heating and evaporation,* Progress in Energy and Combustion Science **32**, 162 (2006).

[43] R. S. Miller, K. Harstad, and J. Bellan, *Evaluation of equilibrium and non-equilibrium evaporation models for many-droplet gas-liquid flow simulations,* International Journal of Multiphase Flow **24**, 1025 (1998).

[44] B. Abramzon and W. Sirignano, *Droplet vaporization model for spray combustion calculations,* International Journal of Heat and Mass Transfer **32**, 1605 (1989).

[45] C. Law, *Recent advances in droplet vaporization and combustion,* Progress in Energy and Combustion Science **8**, 171 (1982).

[46] W. A. Sirignano, *Advances in droplet array combustion theory and modeling,* Progress in Energy and Combustion Science , 1 (2014).

[47] L. A. Dombrovsky and S. S. Sazhin, *A Parabolic Temperature Profile Model for Heating of Droplets,* Journal of Heat Transfer **125**, 535 (2003).

[48] R. de Meester, *Analysis of scalar mixing in hybrid RANS-PDF calculations of turbulent gas and spray flames,* Ph.D. thesis, University Ghent (2012).

[49] G. Faeth, *Evaporation and combustion of sprays,* Progress in Energy and Combustion Science **9**, 1 (1983).

[50] J.-P. Minier and E. Peirano, *The pdf approach to turbulent polydispersed two-phase flows,* Physics Report **352**, 1 (2001).

[51] S. De and S. H. Kim, *Large eddy simulation of dilute reacting sprays: Droplet evaporation and scalar mixing,* Combustion and Flame **160**, 2048 (2013).

[52] L. Ma, S. Zhu, M. J. Tummers, T. H. van der Meer, and D. Roekaerts, *Numerical investigation of ethanol spray-in-hot-coflow flame using steady flamelet model,* in *Proceedings of Eighth Mediterranean Combustion Symposium* (2013) pp. 1–12.

[53] W. Sutherland, *The viscosity of gases and molecular force,* Philosophical Magazine Series 5 **36**, 507 (1893).

[54] J. Reveillon and L. Vervisch, *Analysis of weakly turbulent dilute-spray flames and spray combustion regimes,* Journal of Fluid Mechanics **537**, 317 (2005).

[55] R. Weber, S. Orsino, N. Lallemant, and A. Verlaan, *Combustion of natural gas with high-temperature air and large quantities of flue gas,* Proceedings of the Combustion Institute **28**, 1315 (2000).

[56] M. de Joannon, A. Saponaro, and A. Cavaliere, *Zero-dimensional analysis of diluted oxidation of methane in rich conditions,* Proceedings of the Combustion Institute **28**, 1639 (2000).

[57] R. Weber, J. P. Smart, and W. V. Kamp, *On the (MILD) combustion of gaseous, liquid, and solid fuels in high temperature preheated air,* Proceedings of the Combustion Institute **30**, 2623 (2005).

[58] A. W. Vreman, J. A. van Oijen, L. P. H. de Goey, and R. J. M. Bastiaans, *Direct numerical simulation of hydrogen addition in turbulent premixed Bunsen flames using flamelet-generated manifold reduction,* International Journal of Hydrogen Energy **34**, 2778 (2009).

6

IMPLEMENTATION AND VALIDATION OF LES/FGM METHOD IN OPENFOAM

This chapter reports the implementation and validation of the FGM method in the framework of OpenFOAM®. A methane/air jet in vitiated coflow flame that shares many common features with the DSHC case H_{II} is used as test case. Parameter studies using an Unsteady Reynolds Averaged Navier Stokes (URANS) technique, reveal that the auto-ignition process is highly sensitive to the model constants in the transport equations for the mixture fraction and progress variable variances. To overcome the uncertainties on the model constants choice, dynamic procedures are proposed in the context of Large Eddy Simulation (LES). A significant improvement on the prediction of the considered case is achieved with the dynamic model.

6.1. INTRODUCTION

The auto-ignition process is an important phenomenon of great practical interest, e.g. in Homogeneous Charge Compression Ignition (HCCI) or Premixed Charge Compression Ignition (PCCI) engines. However, a correct prediction of the auto-ignition process in flowing media is very difficult, because, the turbulent-chemistry interaction (TCI) plays an crucial role in it. Many studies already investigated this process with different computational approaches [1–4]. In this paper, we focus on the role of TCI in auto-ignition modeling when tabulated chemistry model is employed for combustion.

The auto-ignition process in hydrogen and low hydrocarbon flames is recognized as an accumulation of hydroperoxyl (HO_2) upstream of the flame base, followed by considerable heat release and accumulation of hydroxyl (OH). To correctly capture the auto-ignition process, a detailed chemical mechanism must be incorporated in the simulation. However, a direct use of a detailed chemical mechanism, as can be done with for example the transported PDF method or the Eddy Dissipation Concept model, not only significantly increases the computational cost, but also brings in extra numerical difficulties due to the strong stiffness of the chemical reaction system. Proper chemistry reduction is required for affordable yet accurate simulations. This is accomplished by either using reduced chemical mechanisms, or employing tabulated chemistry methods [5]. In this study the Flamelet Generated Manifolds model [6] is used, which is a tabulated chemistry method.

The FGM model builts on the flamelet concept [7] and combines it with a manifold approach [6]. The multi-dimensional turbulent flame is considered as a set of 1D flamelets. A low dimensional manifold that is capable of describing the mixing, reaction and other major processes or properties of the turbulent flame is then constructed based on the laminar flamelets calculation. In the turbulent flame simulation, only the transport equations of the controlling variables in addition to the continuity and momentum conservation equations are solved. In this way the costly chemical reaction process is decoupled from the main simulation, and therefore the FGM method is computationally very efficient.

When this tabulated chemistry method is applied, the TCI is accounted for normally by the probability density function (PDF) of the controlling parameters, e.g. mixture fraction and progress variable. The Artificially thickened flame (ATF) model can also be combined with FGM [8], however this is out of the scope of the current work. The PDFs can be obtained by solving modeled transport equations for the joint PDFs [9, 10]. But it is more common to simply assume that they obey a certain shape which can be determined by the first and second moments of the controlling parameters. Mean values of the controlling parameters, in most cases, are obtained by solving transport equations. To obtain the values for the second moments, namely the variances and possibly also co-variances, of the controlling parameters both a transport equation model and an algebraic model, have been used. LES simulations of Sandia Flames D and F performed by Vreman et al. [11] using the FGM model found that the inclusion of modeled subfilter variances of mixture fraction and progress variable as additional entries to the manifold had only small effects on the simulation of both Sandia Flame D and F. However, a LES study by Ihme and See [12] on a lifted methane/air jet flame showed that including or not the Sub-Grid Scale (SGS) variance of progress variable has a significant influence on the

predicted flame lift-off height. The seemingly contradictory conclusions are suggesting that the role of scalar variances on combustion modeling deserves careful investigation. Therefore, influence of the models for the mixture fraction and progress variable variances on the auto-ignition process is the focus of this study.

The lifted methane/air jet flame experimentally studied by Cabra et al [13] is chosen as a target flame. Gordon et al [1] modeled this flame with the transported composition PDF approach. By analyzing the transport budget and qualitative behavior of key species such as HO_2, they concluded that the stabilization of this flame is primarily controlled by auto-ignition, for which the TCI is important. Therefore this flame is a suitable validation case for this study. Ihme and See [12] investigated this flame by Large Eddy Simulation (LES) using the unsteady flamelet/progress variable model. Other studies on this flame can be found in the references of [12].

To handle the wide time and length scale range in turbulence and combustion, three levels of simulation exist: direct numerical simulation (DNS), large eddy simulation (LES) and Reynolds-Averaged Navier Stokes (RANS) simulation, with increasing extent of modeling requirement. Due to the enormous computational resources needed for DNS, its application is still limited to academic research. RANS has for long been the workhorse for industrial application, while LES is gradually entering this field. With this in mind, we will study the auto-ignition process using both unsteady RANS (URANS) and LES techniques. As stated in [12], the intermittent ignition events typically occur on scales that are computationally not resolved in LES. Therefore in LES, the SGS TCI still deserves careful investigation. The FGM model has been implemented by the authors in the open source CFD package OpenFoam [14], and the simulation of this study is carried out using this newly developed OpenFoam FGM solver.

The present research makes contributions in the following three ways: first, an advanced combustion model (FGM) and related sub-models were implemented in the open source CFD package OpenFOAM and validated in this paper. Second, new dynamic models for SGS variances of FGM controlling parameters are proposed, promising performance of which is demonstrated. Last but not least, both URANS and LES have been used for the simulation, making possible the comparison of the capability and limitation of each approach. The rest of the paper is structured as follows: the mathematical modeling approach for the FGM method is presented in section 6.2, followed by a detailed explanation on the turbulence modeling. In section 6.4, models for the FGM controlling parameters variances are discussed, especially dynamic procedures for calculating the SGS scalar variances are developed. Details of the numerical solver adopted are given in section 6.5 before the analysis of the results in section 6.6. Main conclusions are summarized in the last section.

6.2. MATHEMATICAL MODELING

6.2.1. FLAMELET GENERATED MANIFOLDS

Instead of directly solving the transport equations for each species, a tabulated chemistry method – the Flamelet Generated Manifolds model [6] – is used in this study. Neglecting the effect of radiative heat transfer, in this FGM approach, the scalars, such as temperature, species mass fractions, density or source term, are stored in the lookup ta-

ble as function of the mixture fraction and the progress variable. Mixture fraction quantifies the extent of mixing between fuel and oxidizer streams in non-premixed combustion. Bilger's formula is adopted here [15]:

$$Z = \frac{b - b_o}{b_f - b_o}, \tag{6.1}$$

where $b = 2\frac{Y_C}{W_C} + 0.5\frac{Y_H}{W_H} - \frac{Y_O}{W_O}$ for hydrocarbon fuels. Subscripts C, H and O correspond to the elements C, H and O, respectively. And subscripts o and f refer to the oxidizer and the fuel stream conditions, respectively. Progress variable C is a parameter that characterizes the evolution of "global" chemical status from purely mixing ($C = 0$) to "fully burnt" ($C = 1$). In this way, the high-dimensional chemical reaction system has been projected to a two dimensional manifold:

$$\phi = \phi(Z, C), \tag{6.2}$$

where ϕ can be any of the scalar properties of this system. This two dimensional manifold is refereed in the following as the FGM table. In this study, the FGM table is created by solving laminar counterflow diffusion flame at different strain rate in physical space and then transfer the results to mixture fraction and progress variable space.

Definition of progress variable

A progress variable is generally defined as a linear combination of species mass fractions.

$$Y_c = \sum_{k=1}^{N} w_k Y_k, \tag{6.3}$$

where w is the weight factor and Y_k is the mass fraction for k-th species, followed by normalisation

$$C = \frac{Y_c - Y_c^u}{Y_c^b - Y_c^u}, \tag{6.4}$$

where the superscripts b and u respectively represent the burnt and unburnt status. To avoid confusion, in this paper we refer Y_c as progress variable and C as scaled progress variable. A transport equation has to be solved for either progress variable or scaled progress variable. It is more convenient to solve for the unscaled progress variable Y_c, since this avoids the necessity of modeling extra source terms appearing in the transport equation of scaled progress variable C.

In the present study the following definition of progress variable is used:

$$Y_c = a\frac{Y_{H_2O}}{W_{H_2O}} + b\frac{Y_{CO_2}}{W_{CO_2}} + c\frac{Y_{H_2}}{W_{H_2}} + d\frac{Y_{CO}}{W_{CO}}. \tag{6.5}$$

After a parameter study, the progress variable with $a = 4$, $b = 2$, $c = 1/2$ and $d = 1$ has been selected in this study. Since the species involved in the definition of progress variable are experimentally measured, scatter plots of temperature and CH_4 mass fraction are shown as functions of two different definitions of progress variable in Fig. 6.1. The same quantities retrieved from the FGM tables are also plotted for comparison. First of all, it can be clearly seen that the change of measured temperature and Y_{CH_4}

with progress variable are well represented by the FGM table. Second, the progress variable that is employing the information of CO and H_2 can also represent the reaction at the rich region. Taking mass fraction of CH_4 as example, in the case of $Y_c = Y_{CO_2}/M_{CO_2} + Y_{H_2O}/M_{H_2O}$ the mass fraction of CH_4 drops almost vertically at a constant progress variable (around $Y_c = 8$) for high mixture fraction, meaning the reaction for rich mixture can not be indicated by this progress variable. With the second definition of progress variable, the consumption of CH_4 for both rich and lean mixture are well represented. A similar observation can also be made from the plot of CO_2 mass fraction (not shown here). With the progress variable used in this study, both temperature and Y_{CH_4} change monotonically with respect to progress variable, at fixed mixture fraction.

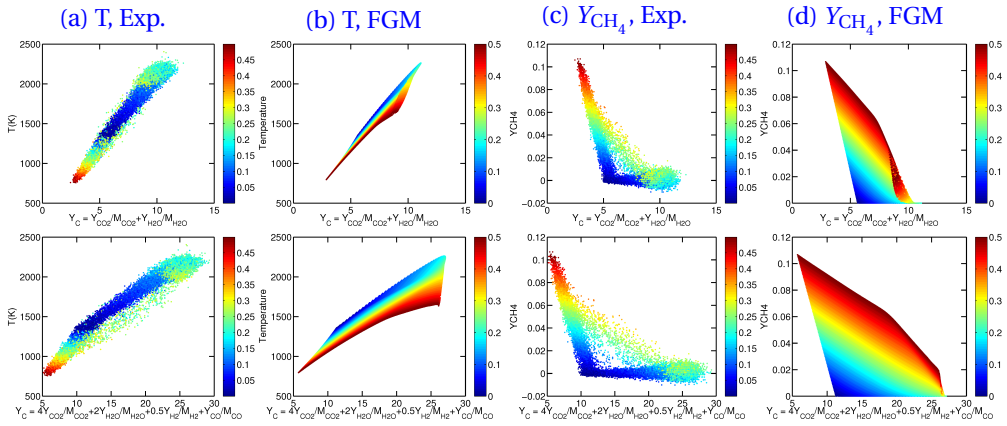

Figure 6.1: Scatter plots in $Y_c - T$ and $Y_c - Y_{CH_4}$ space, colored by mixture fraction.

PRESUMED PDF METHOD

The influence of turbulent fluctuations on the local flame structure is accounted for through the joint PDF of the independent variables. The Favre-averaged/filtered scalars are calculated as:

$$\tilde{\phi} = \int_0^1 \int_0^1 \phi(Z,C)\tilde{P}(Z,C)dZdC. \tag{6.6}$$

The Reynolds-averaged/filtered mean of scalar $\bar{\phi}$ and density $\bar{\rho}$ can be computed as follows:

$$\bar{\phi} = \bar{\rho}\int_0^1 \frac{\phi(Z,C)}{\rho(Z,C)}\tilde{P}(Z,C)dZdC, \tag{6.7}$$

and

$$\bar{\rho} = \left[\int_0^1 \frac{\tilde{P}(Z,C)}{\rho(Z,C)}dZdC\right]^{-1}, \tag{6.8}$$

where $\tilde{P}(Z,C)$ is the joint PDF of mixture fraction and scaled progress variable. It is possible to directly calculate the joint PDFs with transported PDF method, which eliminates any assumption on the shape of the joint PDFs. Such a combined FGM / transported PDF method has been used by the authors for the simulation of a spray jet flame [10].

Alternatively, a presumed PDF method can be adopted, in which the PDFs are assumed to obey a certain shape which can be determined by the first and second moments of the controlling parameters. In this study the latter approach, namely the FGM / presumed PDF method is used. It is a common practice to assume that Z and C are statistically independent of each other, namely

$$\tilde{P}(Z,C) = \tilde{P}(Z)\tilde{P}(C). \tag{6.9}$$

β-function is widely accepted as a good representation of the PDF of mixture fraction. The β-function PDF is defined as:

$$\tilde{P}(\phi) = \frac{\tilde{\phi}^{\alpha-1}(1-\tilde{\phi})^{\beta-1}\Gamma(\alpha+\beta))}{\Gamma(\alpha)\Gamma(\beta)}, \tag{6.10}$$

where the shape parameters α and β are determined by mean and variance of scalar ϕ.

$$\alpha = \tilde{\phi}\left[\frac{\tilde{\phi}(1-\tilde{\phi})}{\widetilde{\phi''^2}} - 1\right], \tag{6.11}$$

$$\beta = (1-\tilde{\phi})\frac{\alpha}{\tilde{\phi}}. \tag{6.12}$$

Both δ-function and β-function have been used as PDF of progress variable [16, 17]. The fluctuation of progress variable has been proven to be important for the target flame [12], so the β-function is also adopted for progress variable in the present study.

As can be seen from Eqs. (6.10) to (6.12), the mean and variance of mixture fraction and progress variable are required to obtain the PDFs. The mean value of mixture fraction is obtained by solving its transport equation:

$$\frac{\partial \bar{\rho}\tilde{Z}}{\partial t} + \frac{\partial \bar{\rho}\tilde{u}_j\tilde{Z}}{\partial x_j} = \frac{\partial}{\partial x_j}\left(\bar{\rho}\tilde{D}\frac{\partial \tilde{Z}}{\partial x_j} - \Phi_{Z,j}\right). \tag{6.13}$$

And the mean value of scaled progress variable, $\tilde{C}$, is obtained by firstly solving transport equation for $\tilde{Y}_c$ and then converting $\tilde{Y}_c$ to $\tilde{C}$. The transport equation for $\tilde{Y}_c$ reads:

$$\frac{\partial \bar{\rho}\tilde{Y}_c}{\partial t} + \frac{\bar{\rho}\tilde{u}_j\tilde{Y}_c}{\partial x_j} = \frac{\partial}{\partial x_j}\left(\bar{\rho}\tilde{D}\frac{\partial \tilde{Y}_c}{\partial x_j} - \Phi_{Y_c,j}\right) + \overline{\dot{\omega}}_{Y_c}. \tag{6.14}$$

$\tilde{Y}_c$ can be converted to $\tilde{C}$ by:

$$\tilde{C} = \frac{\tilde{Y}_c - \tilde{Y}_c^u}{\tilde{Y}_c^b - \tilde{Y}_c^u}, \tag{6.15}$$

where $\tilde{Y}_c^u$ and $\tilde{Y}_c^b$ are respectively the pdf-integrated minimum and maximum value of progress variable.

In Eqs. (6.13) and (6.14), there are several unclosed terms: SGS/turbulence fluxes for mixture fraction and progress variable, Φ_Z and Φ_{Y_c}, and the mean source term for

progress variable $\bar{\dot{\omega}}_{Y_c}$. The SGS turbulence fluxes for mixture fraction and progress variable are modeled with the standard gradient diffusion assumption:

$$\Phi_{Z,j} = -\bar{\rho} D_t \frac{\partial \tilde{Z}}{\partial x_j} = -\bar{\rho} \frac{\nu_t}{Sc_t} \frac{\partial \tilde{Z}}{\partial x_j}, \tag{6.16}$$

$$\Phi_{Y_c,j} = -\bar{\rho} D_t \frac{\partial \widetilde{Y_c}}{\partial x_j} = -\bar{\rho} \frac{\nu_t}{Sc_t} \frac{\partial \widetilde{Y_c}}{\partial x_j}, \tag{6.17}$$

where D_t is the turbulent diffusivity, μ_t is the turbulent viscosity, which will be discussed in Section 6.3. Sc_t is the turbulent Schmidt number, which was set to 0.7 in both the URANS and LES cases in this study.

Transport equations for the variances of mixture fraction and progress variable can be derived from the exact and averaged/filtered transport equations of mixture fraction and progress variable, making use of the continuity equation (see 6.7):

$$\frac{\partial \bar{\rho} \widetilde{Z''^2}}{\partial t} + \frac{\partial \bar{\rho} \tilde{u}_j \widetilde{Z''^2}}{\partial x_j} = \frac{\partial}{\partial x_j} \left(\bar{\rho} D \frac{\partial \widetilde{Z''^2}}{\partial x_j} - \Phi_{Z_v,j} \right) - 2\bar{\rho} \tilde{s}_{\chi_Z} - 2\Phi_{Z,j} \frac{\partial \tilde{Z}}{\partial x_j}, \tag{6.18}$$

$$\begin{aligned} \frac{\partial \bar{\rho} \widetilde{Y_c''^2}}{\partial t} + \frac{\partial \bar{\rho} u_j \widetilde{Y_c''^2}}{\partial x_j} = {} & \frac{\partial}{\partial x_j} \left(\bar{\rho} D \frac{\partial \widetilde{Y_c''^2}}{\partial x_j} - \Phi_{Y_{c,v},j} \right) - 2\bar{\rho} \tilde{s}_{\chi_{Y_c}} - 2\Phi_{Y_c,j} \frac{\partial \tilde{Y}_c}{\partial x_j} \\ & + 2\left(\overline{Y_c \dot{\omega}_{Y_c}} - \tilde{Y}_c \bar{\dot{\omega}}_{Y_c} \right). \end{aligned} \tag{6.19}$$

In Eqs.(6.18) and (6.19), the SGS/turbulent fluxes of mixture fraction and progress variable variances, $\Phi_{Z_v,j}$ and $\Phi_{Y_{c,v},j}$ are modeled with the Daly-Harlow generalized gradient diffusion model:

$$\Phi_{Z_v,j} = -\bar{\rho} D_t \frac{\partial \widetilde{Z''^2}}{\partial x_j} = -\bar{\rho} \frac{\nu_t}{S_{ct}} \frac{\partial \widetilde{Z''^2}}{\partial x_j}, \tag{6.20}$$

$$\Phi_{Y_{c,v},j} = -\bar{\rho} D_t \frac{\partial \widetilde{Y_c''^2}}{\partial x_j} = -\bar{\rho} \frac{\nu_t}{S_{ct}} \frac{\partial \widetilde{Y_c''^2}}{\partial x_j}. \tag{6.21}$$

Conversion of $\widetilde{Y_c''^2}$ to $\widetilde{C''^2}$ can be done using:

$$\widetilde{C''^2} = \frac{\widetilde{Y_c''^2} - \left(\widetilde{Y_c}\right)^2 - \widetilde{\left(Y_c^u\right)^2} - 2\tilde{C}\left[\widetilde{Y_c^u Y_c^b} - \widetilde{\left(Y_c^u\right)^2}\right]}{\left(\widetilde{Y_c^b} - \widetilde{Y_c^u}\right)^2} - \tilde{C}^2, \tag{6.22}$$

where $\left(\widetilde{Y_c}\right)^2$ and $\widetilde{Y_c^u Y_c^b}$ were pdf-integrated and tabulated as functions of of mean mixture fraction $\tilde{Z}$ and its variance $\widetilde{Z''^2}$ [18].

The unclosed terms in the transport equations of the mean and variance of mixture fraction and progress variable and their closure models are listed in Table 6.1.

Note that, Z and Y_c are in general not statistically independent, whereas Z and C come close to being statistically independent. We use $\tilde{Z}$ and $\tilde{C}$ as controlling parameters for tabulation. In the simulation, we solve transport equation for $\tilde{Y}_c$ and convert it to $\tilde{C}$ by relation (6.4) before table lookup. The range of variance depends on the mean

Table 6.1: Unclosed terms in RANS/LES transport equations for FGM controlling parameters

	RANS		LES	
Terms	Expression	Model	Expression	Model
$\Phi_{Z,j}$	$\bar{\rho}\widetilde{Z''u''_j}$	Eq. (6.16)	$\bar{\rho}\left(\widetilde{Zu_j}-\tilde{Z}\tilde{u}_j\right)$	Eq. (6.16)
$\Phi_{Y_c,j}$	$\bar{\rho}\widetilde{Y''_c u''_j}$	Eq. (6.17)	$\bar{\rho}\left(\widetilde{Y_c u_j}-\tilde{Y}_c\tilde{u}_j\right)$	Eq. (6.17)
$\Phi_{Z_v,j}$	$\bar{\rho}\widetilde{Z''^2 u''_j}$	Eq. (6.20)	$\Phi_{Z^2,j}-2\tilde{Z}\Phi_{Z,j}$	Eq. (6.20)
$\Phi_{Y_c,j}$	$\bar{\rho}\widetilde{Y''^2_c u''_j}$	Eq. (6.21)	$\Phi_{Y_c^2,j}-2\tilde{Y}_c\Phi_{Y_c,j}$	Eq. (6.21)
$\rho\widetilde{s}_{\chi_Z}$	$\bar{\rho}\tilde{\chi}_Z-\bar{\rho}\tilde{D}\left(\frac{\partial\tilde{Z}}{\partial x_j}\right)^2$	Eq. (6.39)	$\bar{\rho}\tilde{\chi}_Z-\bar{\rho}\tilde{D}\left(\frac{\partial\tilde{Z}}{\partial x_j}\right)^2$	Eq. (6.41)
$\rho\widetilde{s}_{\chi_{Y_c}}$	$\bar{\rho}\tilde{\chi}_{Y_c}-\bar{\rho}\tilde{D}\left(\frac{\partial\tilde{Y}_c}{\partial x_j}\right)^2$	Eq. (6.40)	$\bar{\rho}\tilde{\chi}_{Y_c}-\bar{\rho}\tilde{D}\left(\frac{\partial\tilde{Y}_c}{\partial x_j}\right)^2$	Eq. (6.42)
$\overline{\dot{\omega}_{Y_c}}$	$\overline{\dot{\omega}_{Y_c}}$	Tabulated	$\overline{\dot{\omega}_{Y_c}}$	Tabulated
$\overline{Y_c\dot{\omega}_{Y_c}}$	$\overline{Y_c\dot{\omega}_{Y_c}}$	Tabulated	$\overline{Y_c\dot{\omega}_{Y_c}}$	Tabulated

value, therefore to simplify the table construction, the scaled variances of mixture fraction and progress variable $\widetilde{\zeta_Z}$ and $\widetilde{\zeta_C}$ are used as controlling parameters in the lookup table. They are related to variances of mixture fraction and process variable by the following expressions:

$$\widetilde{\zeta_Z}=\frac{\widetilde{Z''^2}}{\tilde{Z}\left(1-\tilde{Z}\right)}, \tag{6.23}$$

$$\widetilde{\zeta_C}=\frac{\widetilde{C''^2}}{\tilde{C}\left(1-\tilde{C}\right)}. \tag{6.24}$$

Table 6.2: Relations between lookup table controlling parameters and parameters solved in simulation

Table controlling parameters		Parameters solved		Conversion
Parameter	Range	Parameter	Range	
$\tilde{Z}$	[0,1]	$\tilde{Z}$	[0,1]	
$\tilde{C}$	[0,1]	$\tilde{Y}_c$	$\left[\tilde{Y}_c^u,\tilde{Y}_c^b\right]$	Eq. (6.15)
$\widetilde{\zeta_Z}$	[0,1]	$\widetilde{Z''^2}$	$\left[0,\tilde{Z}\left(1-\tilde{Z}\right)\right]$	Eq. (6.23)
		$\widetilde{Y''^2_c}$		Eqs. (6.22)
$\widetilde{\zeta_C}$	[0,1]	$\widetilde{C''^2}$	$\left[0,\tilde{C}\left(1-\tilde{C}\right)\right]$	Eqs. (6.24)

The FGM table controlling parameters and parameters solved in simulation as well as their conversion are summarized in Table 6.2.

6.2.2. MODELED GOVERNING EQUATIONS

Summarizing the discussions given above, and substituting the unclosed terms with their corresponding models, the modeled (URANS or LES) transport equations for tur-

bulent combustion using FGM/presumed PDF method can be expressed as follows:

$$\frac{\partial \bar{\rho}}{\partial t}+\frac{\partial \bar{\rho}\tilde{u}_j}{\partial x_j}=0, \tag{6.25}$$

$$\frac{\partial \bar{\rho}\tilde{u}_i}{\partial t}+\frac{\partial\left(\bar{\rho}\tilde{u}_i\tilde{u}_j\right)}{\partial x_j}=-\frac{\partial \bar{p}}{\partial x_i}+\frac{\partial}{\partial x_j}\left(\bar{2}\mu\tilde{S}^D_{ij}-R_{ij}\right), \tag{6.26}$$

$$\frac{\partial \bar{\rho}\tilde{Z}}{\partial t}+\frac{\partial \bar{\rho}\tilde{u}_j\tilde{Z}}{\partial x_j}=\frac{\partial}{\partial x_j}\left[\bar{\rho}\left(\tilde{D}+D_t\right)\frac{\partial \tilde{Z}}{\partial x_j}\right], \tag{6.27}$$

$$\frac{\partial \bar{\rho}\tilde{Y}_c}{\partial t}+\frac{\bar{\rho}\tilde{u}_j\tilde{Y}_c}{\partial x_j}=\frac{\partial}{\partial x_j}\left[\bar{\rho}\left(\tilde{D}+D_t\right)\frac{\partial \tilde{Y}_c}{\partial x_j}\right]+\bar{\dot{\omega}}_{Y_c}, \tag{6.28}$$

$$\frac{\partial \bar{\rho}\widetilde{Z''^2}}{\partial t}+\frac{\partial \bar{\rho}\tilde{u}_j\widetilde{Z''^2}}{\partial x_j}=\frac{\partial}{\partial x_j}\left[\bar{\rho}\left(\tilde{D}+D_t\right)\frac{\partial \widetilde{Z''^2}}{\partial x_j}\right]+C_g\bar{\rho}D_t\left(\frac{\partial \tilde{Z}}{\partial x_j}\right)^2-C_{d,Zv}\bar{\rho}\tilde{s}_{\chi_Z}, \tag{6.29}$$

$$\frac{\partial \bar{\rho}\widetilde{Y_c''^2}}{\partial t}+\frac{\partial \bar{\rho}\tilde{u}_j\widetilde{Y_c''^2}}{\partial x_j}=\frac{\partial}{\partial x_j}\left[\bar{\rho}\left(\tilde{D}+D_t\right)\frac{\partial \widetilde{Y_c''^2}}{\partial x_j}\right]+C_g\bar{\rho}D_t\left(\frac{\partial \tilde{Y}_c}{\partial x_j}\right)^2-C_{d,Y_cv}\bar{\rho}\tilde{s}_{\chi_{Y_c}}+2\left(\overline{Y_c\dot{\omega}_{Y_c}}-\tilde{Y}_c\bar{\dot{\omega}}_{Y_c}\right), \tag{6.30}$$

$$S_{ij}=\frac{1}{2}\left(\frac{\partial u_i}{\partial x_j}+\frac{\partial u_j}{\partial x_i}\right), \tag{6.31}$$

where $S^D_{ij}=\left(S_{ij}-\frac{1}{3}\delta_{ij}S_{kk}\right)$ is the deviatoric part of the strain rate tensor S_{ij}. R_{ij} is the Reynolds stress (in URANS) or sub-grid scale (SGS) stress (in LES). C_g, $C_{d,Zv}$ and C_{d,Y_cv} are model constants for the generation and dissipation terms of mixture fraction and progress variable variances respectively. C_g in fact is not really a free model constant since a theoretical value 2 is found in the derivation of the exact transport equation, and this value is adopted here. A wide range of values for $C_{d,Zv}$ from 1 to 16 have been reported in literatures for different cases [8, 19]. However, as will be shown in section 6.6, the auto-ignition process is very sensitive to these two constants, and a dynamic procedure for determining these two constants is developed in this paper.

In Eqs. (6.25) to (6.30), the Reynolds/SGS stresses, R_{ij}, and turbulent/SGS scalar dissipation rate, $\bar{\rho}\tilde{s}_{\chi_Z}$ and $\bar{\rho}\tilde{s}_{\chi_{Y_c}}$ remain unclosed. Models for these terms will be discussed in following sections.

6.3. TURBULENCE MODELING

In this section we discuss the turbulence models that are used to close the Reynolds/SGS stresses R_{ij} in the Eq. (6.26). To calculate the Reynolds stress in URANS the $k-\epsilon$ model is used. A modified model constant $C_{1\epsilon}=1.6$ is used to predict the correct spreading rate for the round jet flame [20]. To model the SGS stresses in LES a dynamic Smagorinsky model is used, as explained next.

6.3.1. MODELING TURBULENCE IN LES

Similar to the closure of Reynolds stresses in RANS, the SGS stresses in LES can be modeled based on a turbulent viscosity hypothesis:

$$R_{ij} = \bar{\rho}\left(\widetilde{u_i u_j} - \tilde{u}_i \tilde{u}_j\right) = -2\mu_{sgs}\tilde{S}^D_{ij} + \frac{2}{3}\bar{\rho}k\delta_{ij}, \tag{6.32}$$

where μ_{SGS} is the SGS viscosity. k is the SGS kinetic energy defined by

$$\bar{\rho}k = \frac{1}{2}\tau_{kk} = \frac{1}{2}\bar{\rho}\left(\widetilde{u_k u_k} - \tilde{u}_k \tilde{u}_k\right). \tag{6.33}$$

The SGS viscosity μ_{SGS} and SGS kinetic energy k have to be modeled. Yoshizawa's formula is often used for modeling of the SGS kinetic energy [21]:

$$\tau_{kk} = 2\bar{\rho}k = C_I 2\bar{\rho}\Delta^2|\tilde{S}|^2, \tag{6.34}$$

where C_I is the model constant, and $|\tilde{S}| = \left(2\tilde{S}_{ij}\tilde{S}_{ij}\right)^{1/2}$ is the magnitude of the strain rate tensor. Erlebacher et al [22] pointed out that for turbulent Mach numbers $M_t < 0.4$ the kinetic energy is negligible. This term can also be incorporated into a modified pressure $P = p + \frac{2}{3}k$. This leads to the a modified equation of state, which takes the form [23]:

$$P = \bar{\rho}R\tilde{\upsilon} + \frac{3\gamma - 5}{6}\tau_{kk}, \tag{6.35}$$

where $\upsilon = \tilde{T} - \frac{1}{2C_v\bar{\rho}}\tau_{kk}$ is the modified temperature, γ is the specific heat ratio. This expression shows that with typical gas properties ($\gamma = 1.4$, $c_v = 718 J/Kg{\cdot}K$, $\rho = 1.25 Kg/m^3$ for air at room temperature) the second term is indeed negligible , unless τ_{kk} is very large. This means that the SGS stress trace can be incorporated in the pressure with no modification to the equation of state [24], this approach is adopted in current study.

SMAGORINSKY MODEL

The Smagorinsky SGS model assumes that the kinematic SGS viscosity ν_{SGS} (m^2/s) can be described in terms of one length (Δ) and one velocity ($\Delta|\tilde{S}|$) scale. Thus, the SGS viscosity is evaluated as follows:

$$\mu_{SGS} = \bar{\rho}\left(C_S\Delta\right)^2|\tilde{S}| = \bar{\rho}\left(C_S\Delta\right)^2\left|\sqrt{2\tilde{S}_{ij}\tilde{S}_{ij}}\right|. \tag{6.36}$$

The model constant C_S is case dependent, ranging from $C_S \approx 0.1$ for strongly anisotropic turbulence [25] to $C_S \approx 0.2$ homogeneous isotropic flow [26].

DYNAMIC SMAGORINSKY MODEL

The main drawback of the Smagorinsky model is that there is no single value of model constant C_s that is universally applicable to a wide range of flows. Germano et al. [27] proposed a procedure to dynamically calculate the model constant based on an algebraic identity between the subgrid-scale stresses arising from filtering at two different filter sizes. The basic idea in this model is to apply the same SGS stress model at two different scales, and thus to adjust the constant to agree with known information form

the resolved field. A test filter G, with filter width $\hat{\Delta}$ larger than the LES filter (size $\bar{\Delta}$) is introduced.

The dynamic Smagorinsky model has been extended to compressible flow by Moin et al [28] and Martin et al [24]. The Germano identity for compressible flow has the same form as the incompressible version,

$$L_{ij} - \frac{1}{3}L_{kk}\delta_{ij} = CM_{ij}, \tag{6.37}$$

where $M_{ij} = \beta_{ij} - \hat{\alpha}_{ij}$, $\alpha_{ij} = -2\overline{\Delta}^2\bar{\rho}|\tilde{S}_{ij}|\tilde{S}^D_{ij}$ and $\beta_{ij} = -2\hat{\Delta}^2\hat{\rho}|\breve{\tilde{S}}|\breve{\tilde{S}}^D_{ij}$, and C is the model constant. In compressible flow, the resolved turbulent stresses are $L_{ij} = \widehat{\overline{\rho u_i \rho u_j}/\bar{\rho}} - \widehat{\rho u_i}\widehat{\rho u_j}/\hat{\rho}$, and the test stresses are $T_{ij} = \hat{\rho}\breve{\tilde{u}}_i\breve{\tilde{u}}_j - \hat{\rho}\breve{\tilde{u}}_i\breve{\tilde{u}}_j$ (where $\breve{\tilde{f}} = \widehat{\rho f}/\hat{\rho}$).

Eq.(6.37) is over-determined, because it represents five independent equations for one unknown. The least squares method proposed by Lilly [29] is used here to minimize the error.

$$C = C_s^2 = \frac{\left\langle L^*_{ij}M_{ij}\right\rangle}{\langle M_{kl}M_{kl}\rangle}, \tag{6.38}$$

where $L^*_{ij} = L_{ij} - L_{kk}\delta_{ij}$. Although the angle brackets in the original formulation indicates averaging over homogeneous direction, it represents local average over computational volume [24] in the present study due to the absence of homogeneous direction in turbulent jet flames. It is well known that Eq. (6.38) may produce a negative value, which means negative SGS viscosity. This is interpreted, in some papers, as back-scattering (energy transfer from small scale eddies to large scale eddies). However, the model constant C is bounded to be non-negative in the present study, meaning $\mu_{SGS} \geq 0$. This ensures that the scalar dissipation rate of mixture fraction and progress variable variance remain non-negative, as will be discussed in Section 6.4.2.

6.4. SCALAR VARIANCES MODELING

6.4.1. MODELING VARIANCES IN RANS

The turbulent scalar dissipation rate for mixture fraction and progress variable variance $\bar{\rho}\tilde{s}_{\chi_Z}$ and $\bar{\rho}\tilde{s}_{\chi_{Y_c}}$ in Eqs. (6.29) and (6.30) can respectively be modeled as follows [26]:

$$\bar{\rho}\tilde{s}_{\chi_Z} = \bar{\rho}\tilde{\chi}_Z - \bar{\rho}\tilde{D}\left(\frac{\partial\tilde{Z}}{\partial x_j}\right)^2 = \bar{\rho}\frac{\epsilon}{k}\widetilde{Z''^2}, \tag{6.39}$$

and

$$\bar{\rho}\tilde{s}_{\chi_{Y_c}} = \bar{\rho}\tilde{\chi}_{Y_c} - \bar{\rho}\tilde{D}\left(\frac{\partial\tilde{Y}_c}{\partial x_j}\right)^2 = \bar{\rho}\frac{\epsilon}{k}\widetilde{Y''^2_c}, \tag{6.40}$$

where $\bar{\rho}\tilde{\chi}_Z$ and $\bar{\rho}\tilde{\chi}_{Y_c}$ are respectively the total scalar dissipation rate for mixture fraction and progress variable. Note that the dissipation rate in this study does not include the factor 2, different from the convention in [26]. The factor together with model constants for $\bar{\rho}\tilde{s}_{\chi_Z}$ and $\bar{\rho}\tilde{s}_{\chi_{Y_c}}$ are absorbed in the model constants $C_{d,Zv}$ and C_{d,Y_cv}, the value of which will be discussed latter. Substituting Eqs. (6.39) and (6.40) into Eqs. (6.29) and (6.30) we have the modeled transport equation for variances of mixture fraction and progress variable in URANS simulation.

6.4.2. MODELING VARIANCES IN LES

MODELING SGS SCALAR DISSIPATION RATE

The SGS part of scalar dissipation rate in Eqs. (6.29) and (6.30) can be modeled by linear relaxation models[8, 30]:

$$\bar{\rho}\tilde{s}_{\chi_Z} = \bar{\rho}\tilde{\chi}_Z - \bar{\rho}\tilde{D}\left(\frac{\partial \tilde{Z}}{\partial x_j}\right)^2 = D_t\frac{\widetilde{Z''^2}}{\Delta^2}, \tag{6.41}$$

and

$$\bar{\rho}\tilde{s}_{\chi_{Y_c}} = \bar{\rho}\tilde{\chi}_{Y_c} - \bar{\rho}\tilde{D}\left(\frac{\partial \tilde{Y}_c}{\partial x_j}\right)^2 = D_t\frac{\widetilde{Y_c''^2}}{\Delta^2}. \tag{6.42}$$

Similar to section 6.4.1, model constants for $\bar{\rho}\tilde{s}_{\chi_Z}$ and $\bar{\rho}\tilde{s}_{\chi_{Y_c}}$ are absorbed in the model constants $C_{d,Zv}$ and C_{d,Y_cv}. In [12], $\bar{\rho}\tilde{s}_{\chi_Z}$ is modeled similar to Eq. (6.41) with $C_{d,Zv} = 4$. But a distinction between conserved and non-conserved scalar was considered by linking $\bar{\rho}\tilde{s}_{\chi_{Y_c}}$ to $\bar{\rho}\tilde{s}_{\chi_Z}$ with a parameter that is evaluated using local progress variable. In the present study, dynamic procedures are proposed for determination of both $C_{d,Zv}$ and C_{d,Y_cv} as will be discussed in section 6.4.2. Substituting Eqs. (6.41) and (6.42) into Eqs. (6.29) and (6.30) we have the modeled transport equation models for SGS variances of mixture fraction and progress variable in LES simulation.

6

ALGEBRAIC MODEL

The Algebraic model can be obtained by assuming local equilibrium, namely the generation of scalar variance at SGS level is exactly balanced by its dissipation. Following this assumption, from Eqs. (6.29), (6.30), (6.41) and (6.42), the following algebraic models for mixture fraction and progress variable variance can be obtained respectively:

$$\widetilde{Z''^2} = C_{Zv}\Delta^2\left(\frac{\partial \tilde{Z}}{\partial x_i}\right)^2. \tag{6.43}$$

and

$$\widetilde{Y_c''^2} = C_{Y_cv}\Delta^2\left[\left(\frac{\partial \tilde{Y}_c}{\partial x_i}\right)^2 + \frac{Sc_t}{\mu_t}\left(\overline{Y_c\dot{\omega}_{Y_c}} - \tilde{Y}_c\tilde{\dot{\omega}}_{Y_c}\right)\right]. \tag{6.44}$$

Eq. (6.44) takes into account the influence of progress variable source term on its variance. We refer Eq. (6.43) and Eq. (6.44) as "AGM1". In many references, the influence of progress variable source term is simply neglected, resulting in the following expression:

$$\widetilde{Y_c''^2} = C_{Y_cv}\Delta^2\left(\frac{\partial \tilde{Y}_c}{\partial x_i}\right)^2. \tag{6.45}$$

We call Eq. (6.43) and Eq. (6.45) "AGM2". The model constants C_{Zv} and C_{Y_cv} for algebraic models are related to the model coefficients in transport equations by the following relations:

$$C_{Zv} = \frac{C_g}{C_{d,Zv}} \quad \text{and} \quad C_{Y_cv} = \frac{C_g}{C_{d,Y_cv}}. \tag{6.46}$$

We will discuss later the use of these relations to obtain proper model constants for the transport equation of mixture fraction and progress variable variances.

A wide range of C_{Zv} and C_{Y_cv} values from 1/12 to 0.3 have been reported in literature[11, 31–33]. Pierce and Moin [34] proposed a dynamic procedure for determination of C_{Zv}. Here we generalize this dynamic procedure to determine C_{Y_cv} for both "AGM1" and "AGM2".

Analogous to Yoshizawa's expression [21] for SGS kinetic energy, Eq. (6.43) can be rewritten as [34]:

$$\bar{\rho}\widetilde{Z''^2} = C_{Zv}\Delta^2\bar{\rho}\left(\frac{\partial\tilde{Z}}{\partial x_i}\right)^2. \tag{6.47}$$

Applying a test filter with larger filter width ($\hat{\Delta} = 2\bar{\Delta}$), the Leonard term for the left-hand side is defined as:

$$L_{Zv} = \lceil\bar{\rho}\tilde{Z}\tilde{Z}\rceil - \hat{\bar{\rho}}\tilde{\tilde{Z}}\tilde{\tilde{Z}}, \tag{6.48}$$

where $\lceil\ \ \rceil$ denotes filter at the test level, equals to $\hat{}$.

From the right-hand side of Eq. (6.48), one obtains the model term:

$$M_{Zv} = \hat{\Delta}^2\hat{\bar{\rho}}\left(\frac{\partial\tilde{\tilde{Z}}}{\partial x_i}\right)^2 - \Delta^2\lceil\bar{\rho}\left(\frac{\partial\tilde{Z}}{\partial x_i}\right)^2\rceil. \tag{6.49}$$

Assuming that the model coefficient varies slowly in space and that the same coefficient applies to both filter levels, one obtains $L_{Zv} = C_{Zv}M_{Zv}$. The least-squares method proposed by Lilly [29] is also adopted here.

$$C_{Zv} = \frac{\langle L_{Zv}M_{Zv}\rangle}{\langle M_{Zv}M_{Zv}\rangle}. \tag{6.50}$$

The Leonard term for the left-hand side of Eq. (6.44) is defined as:

$$L_{Y_cv} = \lceil\bar{\rho}\tilde{Y}_c\tilde{Y}_c\rceil - \hat{\bar{\rho}}\tilde{\tilde{Y}}_c\tilde{\tilde{Y}}_c, \tag{6.51}$$

and the model terms for "AGM1" and "AGM2" respectively read:

$$M_{Y_cv} = \hat{\Delta}^2\hat{\bar{\rho}}\left[\left(\frac{\partial\tilde{\tilde{Y}}_c}{\partial x_i}\right)^2 + \frac{Sc_t}{\hat{\mu}_t}\left(\lceil\overline{Y_c\dot{\omega}_{Y_c}}\rceil - \tilde{\tilde{Y}}_c\hat{\bar{\omega}}_{Y_c}\right)\right] - \Delta^2\lceil\bar{\rho}\left[\left(\frac{\partial\tilde{Y}_c}{\partial x_i}\right)^2 + \frac{Sc_t}{\mu_t}\left(\overline{Y_c\dot{\omega}_{Y_c}} - \tilde{Y}_c\bar{\dot{\omega}}_{Y_c}\right)\right]\rceil, \tag{6.52}$$

and

$$M_{Y_cv} = \hat{\Delta}^2\hat{\bar{\rho}}\left(\frac{\partial\tilde{\tilde{Y}}_c}{\partial x_i}\right)^2 - \Delta^2\lceil\bar{\rho}\left(\frac{\partial\tilde{Y}_c}{\partial x_i}\right)^2\rceil. \tag{6.53}$$

Similar to (6.50), the least-squares method is used to obtain the model constant:

$$C_{Y_cv} = \frac{\langle L_{Y_cv}M_{Y_cv}\rangle}{\langle M_{Y_cv}M_{Y_cv}\rangle}. \tag{6.54}$$

The developed dynamic algebraic models are referred to as "Dyn-AGM1" and "Dyn-AGM2", respectively corresponding to the calculation of M_{Y_cv} using Eq. (6.52) or (6.53).

DYNAMIC TRANSPORT EQUATION MODEL

The algebraic model assumes local equilibrium between the generation and dissipation of the scalar variances, which does not necessarily always hold [35]. The transport equation model does not have this limitation. However, on one hand, optimal value for the model constants $C_{d,Zv}$ and C_{d,Y_cv} in the transport equation for the variances of mixture fraction and progress variable are not available a priori to the simulation. On the other hand, as will be discussed in section 6.6.2, the flame lift-off height is very sensitive to these model constants. Kual et al [35] showed that these constants vary significantly depending on local condition and filter size, and they proposed a dynamic procedure to determine the model coefficients for the transport equation of mixture fraction variance. From the simulation with this dynamic transport equation, the $D_{d,Zv}$ was found in the range between 2 to 13 in the reaction region. However, this model requires time derivative of the variance Leonard term and is difficult to extend to the transport equation of $\widetilde{Y_c''^2}$.

In this study, we propose to use relations (6.46) to dynamically obtain the model constant for the transport equations of $\widetilde{Z''^2}$ and $\widetilde{Y_c''^2}$. As explained in section 6.4.2, C_{Zv} and C_{Y_cv} are obtained under equilibrium assumption, they lead to over-dissipation of SGS variances. To consider the non-equilibrium effect, two new constants $\gamma_{eq,Z}$ and γ_{eq,Y_c} are introduced in the relations between the algebraic and transport equation model constants. The new relations read:

$$C_{d,Zv} = \gamma_{eq,Z}\frac{C_g}{C_{Zv}} \quad \text{and} \quad C_{d,Y_cv} = \gamma_{eq,Y_c}\frac{C_g}{C_{Y_cv}}. \tag{6.55}$$

The physical meaning of $\gamma_{eq,Z}$ and γ_{eq,Y_c} can be interpreted as extent of local equilibrium that has been achieved, therefore they are referred to as equilibrium constants. They should be in the range of [0,1], $\gamma_{eq,Z} = 1$ and $\gamma_{eq,Y_c} = 1$ meaning a fully equilibrium condition. From simulations adopting dynamic algebraic models, C_{Zv}, C_{Y_cv} are found predominantly to have values smaller than 0.1, which means $C_{d,Zv}$ and C_{d,Y_cv} greater than 20 if $\gamma_{eq,Z} = \gamma_{eq,Y_c} = 1$. This values are much larger than the commonly used values for the transport equations models (around 2), which suggests that the non-equilibrium effect maybe significant. Therefore a small value of $\gamma_{eq,Z}$ and γ_{eq,Y_c} is reasonable, in this case $\gamma_{eq,Z} = \gamma_{eq,Y_c} = 0.35$ are used. A further study is needed in future to pursue a dynamic method to determine these equilibrium constants.

The procedure of solving the dynamic transport equation model is summarized as following:

Step1: the dynamic algebraic model Eqs. (6.50) and (6.54) are solved. Algebraic model constants, C_{Zv} and C_{Y_cv} are obtained according to local conditions.

Step2: model constants for the transport equation models, $C_{d,Zv}$ and C_{d,Y_cv} , are deduced via (6.55).

Step3: finally the transport equations (6.29) and (6.30) with the dynamically determined model constants are solved.

Since the dynamic transport equation can be formed by coupling either “AGM1” or “AGM2” with the transport equation model, the following two dynamic transport equation models should be distinguished: “DynTP-AGM1” and “DynTP-AGM2”.

6.5. NUMERICAL METHODOLOGY

6.5.1. FGMFOAM SOLVER

The simulation in this study is carried out with the open source CFD package – OpenFOAM [14]. New libraries have been created for the FGM storage and retrieval algorithms and are dynamically linked to a customized solver. The new solver is referred to as “FGMFoam". FGMFoam is based on the PIMPLE algorithm, a combination of PISO (Pressure implicit with splitting of operator) [36] and SIMPLE (Semi-Implicit Method for Pressure-Linked Equations) [25] algorithms. The algorithm of this solver is shown in Fig 6.2. Transport equations for the controlling variables are solved after the velocity prediction step. Then necessary properties, e.g. $\tilde{T}$, $\bar{\mu}$ and $\overline{\dot{\omega}}_{Y_c}$, are retrieved from the FGM libraries with the newly obtained controlling variables. Note that between the solution of the controlling parameter and the FGM lookup, there is a necessary step to convert the solved controlling parameters ($\tilde{Z}$, $\widetilde{Z''^2}$, $\tilde{Y}_c$, $\widetilde{Y_c''^2}$) to the controlling parameters used to construct the FGM libraries ($\tilde{Z}$, $\widetilde{\zeta_Z}$, $\tilde{C}$, $\widetilde{\zeta_C}$). The relations between these controlling parameters are given in Table. 6.2. After this, the velocity-pressure correction is conducted within the PISO loop. One PIMPLE loop and three PISO loops are carried for each time step in both URANS and LES simulation.

6.5.2. NUMERICAL DETAILS

For the URANS simulation, a 2D axisymmetric configuration was adopted. Mean velocity of fuel and coflow streams from experiment are specified as boundary conditions. For the LES, a 3D cylindrical geometry with radius of 22D and length of 100D is used, where D is the diameter of the fuel nozzle. The turbulent inlet boundary condition is provided by a separate pipe simulation using periodic boundary condition. The axial direction is discretized with 495 grid points, radial direction is discretized with 96 grid points and the circumferential direction is equally divided by 72 points, resulting in a total mesh size of 3.2 million. The smallest filter size is 0.12 mm (≈ 0.03D) at the centerline near the fuel jet exit, and the largest filter size is 5 mm (≈ 1.09D) at the largest radial distance on the exit plane. Two cross sections of the 3D mesh used in the LES cases are shown in Fig. 6.3.

The transport equations are spatially discretized with a Finite Volume Method (FVM). The convection and Laplacian terms are discretized respectively by second-order accuracy total variation diminishing (TVD) schemes ‘Gauss van Leer’ and ‘Gauss van Leer corrected’. Implicit second-order method CrankNicholson with blending factor $\phi = 1.0$ is used for the temporal integration. For the URANS simulation, an adjustable time step with maximum Courant number 0.5 is used to specify the simulation time step. In the LES cases, the time step is fixed as 5×10^{-7} s. The steady state is reached at around 0.03 s from the initial state. Averaging of properties starts at 0.05 s, corresponding to roughly 10 flow-through time based on the fuel jet mean velocity. Averaging duration is 0.1 s. The LES is carried out on the Cartesius supercomputer [37]; around 5000 CPU hours is required for one case.

6.6. RESULTS AND DISCUSSION

The results will be presented in three parts. The ignition process and flame structure of the studied flame is analyzed in the first part. In this part we show that the flame studied

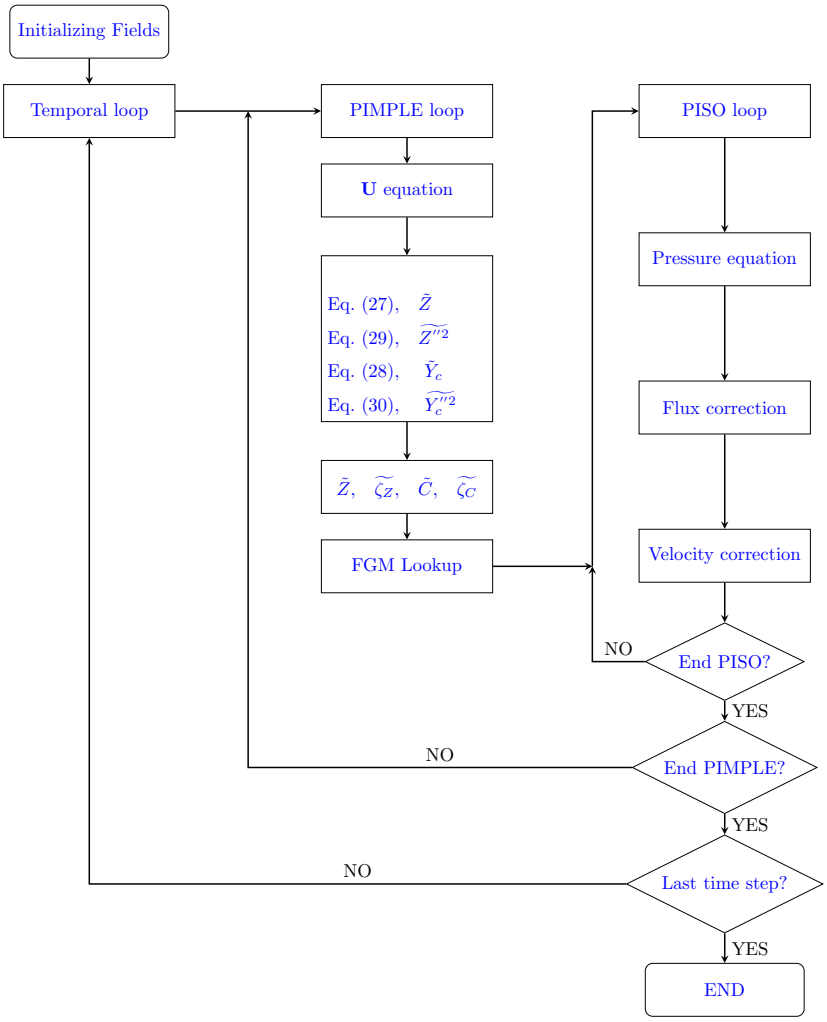

Figure 6.2: Algorithm of the FGMFoam slover

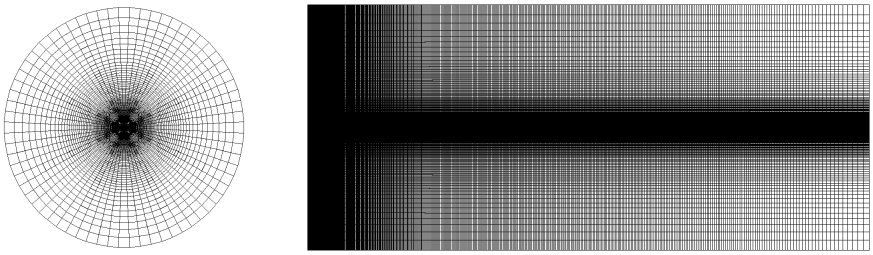

Figure 6.3: Two cross-sections of the 3D mesh for the LES case.

is mainly stabilized by auto-ignition. Based on this knowledge, the sensitivity of the auto-ignition process on the model constants in the transport equations of mixture fraction and progress variable variances are analyzed. In the last part, results obtained with the proposed new dynamic models for determining these model constants are shown and performance of different models are compared.

6.6.1. IGNITION PROCESS AND FLAME STRUCTURE

Fig. 6.4 shows a snapshot of instantaneous flow field. In this figure, the iso-surface of stoichiometric mixture fraction is used to show the mixing between fuel and oxidizer streams, the iso-surface of $T = 1800$K is plotted to represent the reaction region and the streamlines provide information on the flow patten. The mixing of the central jet with high-temperature coflow before the flame base is clearly visible from this figure. The flame stabilized at approximately 40 times the fuel jet diameter downstream the fuel exit. The temperature fields on a cross section with iso-line of $T = 1800K$ at four sequential time steps are depicted in Fig. 6.5. At time t_0, a few hot spots are firstly formed at the lean side of the jet. These ignited spots gradually increase as they are convected downstream and merge together at the flame base from time $t_0 + dt$ to $t_0 + 3dt$. As experimentally revealed by Oldenhof et al. [38] the occurrence and growth of the ignition kernels provide strong evidence for the auto-ignition mechanism of flame stabilization. Furthermore, the accumulation of HO_2 before the flame base as shown in Fig. 6.6 is another sign of auto-ignition. Comparing the contour plot of HO_2 and OH, the rich HO_2 regions are located right before the region where the high value of OH starts. Mir Najafizadeh et al [39] studied the chemical structure of a H_2/N_2 flame under similar coflow condition as the flame studied in this paper, they found that the auto-ignition has a large contribution to the stabilization of that flame and near the flame base the OH is formed by consuming HO_2 at a very lean condition. Based on these observations, it can be confirmed that the auto-ignition is indeed the main stabilization mechanism for this flame.

To further investigate the flame structure, two flame indices are defined respectively based on the reactions between CH_4 with O_2 and CO with O_2.

$$FI_{CH_4} = \nabla Y_{CH_4} \cdot \nabla Y_{O_2}, \tag{6.56}$$

and

$$FI_{CO} = \nabla Y_{CO} \cdot \nabla Y_{O_2}. \tag{6.57}$$

Snapshots of these two flame indices are given in Fig. 6.6. The FI_{CH_4} predominantly show positive values, especially before the flame base. This however, does not mean that the CH_4 is consumed in a premixed combustion mode in this region. The alignment of the CH_4 and O_2 gradients in this region is mainly caused by the fact that in this flame the central jet is already a premixed mixture with even higher content of O_2 than the coflow. The mixing with coflow as the jet developes actually dilutes both CH_4 and O_2, resulting in a positive values of FI_{CH_4} at the shear Layer. The heat release region indicated by the overlapping of OH and CH_2O ($Y_{OH} \times Y_{CH_2O}$) is also displayed in Fig. 6.6. Both negative and positive value of FI_{CH_4} are observed on the flame front. This reveals that the CH_4 reacts with O_2 in both premixed and non-premixed combustion modes. The flame index FI_{CO} shows rather interesting results in the sense that the regions with negative values of FI_{CO} corresponds well with the heat release region, meaning that the reaction of CO is substantially responsible for heat release and it happens predominantly in a non-premixed mode. This is quite reasonable, since the CO and H_2 are formed by fuel rich combustion, and can only be consumed by O_2 from coflow in the shear layer. Moreover, from the results of heat release region and flame indices, it is found that the reaction is mostly happening on a thin and distorted flamelet structure, justifying the applicability of FGM in the simulation of this flame.

The above analysis showed that this flame is mainly stabilized by the formation and growth of ignition kernels. Both premixed and non-premixed combustion modes are detected. As the β-function PDF is used for both mixture fraction and progress variable in the current study, the variances of these two scalars influence the local properties that are retrieved from the FGM table and consequently influence the auto-ignition process. The sensitivity of the results on the scalar variance model constants will be investigated using URANS results in the next section.

6.6.2. SENSITIVITY OF FLAME LIFT-OFF ON MODEL CONSTANTS

Results of a parameter study in order to explore the sensitivity of auto-ignition process on the mixture fraction and progress variable variances model constants are shown in this section. The value of model constants $C_{d,Zv}$ and C_{d,Y_cv} in the transport equation of mixture fraction and progress variances are varied around their commonly used values 2. A temperature contour plot is shown in Fig. 6.7 supplemented with an isoline of OH mass fraction equal to 0.0005. The flame lift-off height is defined in this study as the lowest axial location where the $Y_{OH} = 0.0005$ is reached. Fig. 6.7 shows a significant sensitivity of the flame lift-off height on the model constants $C_{d,Zv}$ and C_{d,Y_cv}. Since $C_{d,Zv}$ and C_{d,Y_cv} are the model constants for the dissipation terms in the transport equations of mixture fraction and progress variable variance, lower value of these two constants mean less dissipation, thus higher fluctuation. The flame lift-off height is influenced by these two parameters in a complicated manner. At relatively high fluctuation of mixture fraction ($C_{d,Zv} = 1$), the flame always ignite despite the change of progress variable fluctuation ($C_{d,Y_cv} = 1$, 2 and 3). However, the lift-off height of the flame decreases with decrease of progress variable variance (increasing of C_{d,Y_cv}). At relatively low fluctuation of mixture fraction ($C_{d,Zv} = 3$), the flame does not ignite when the fluctuation of

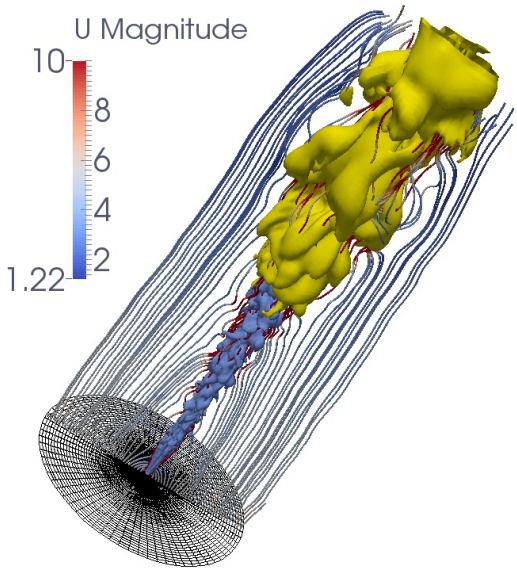

Figure 6.4: Flame configuration, iso-surface of stoichiometric mixture fraction ($Z = 1.77$, blue), iso-surface of $T = 1800$ K (yellow) and streamlines colored by flow velocity.

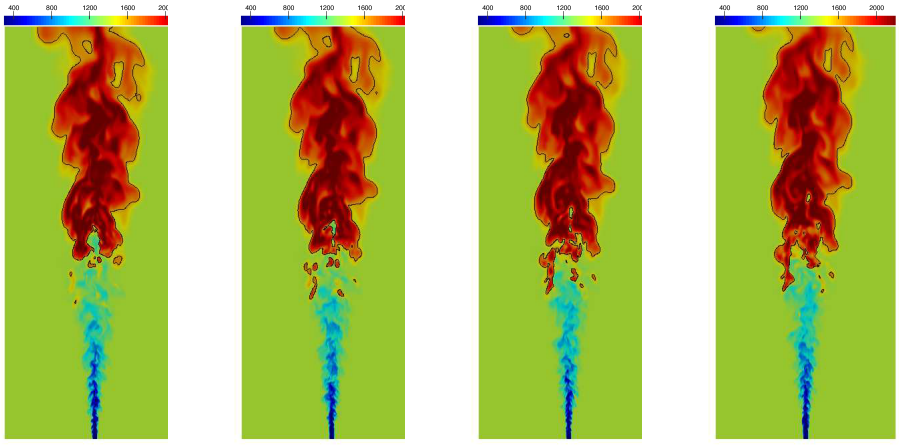

Figure 6.5: Snapshots of temperature contour plot.

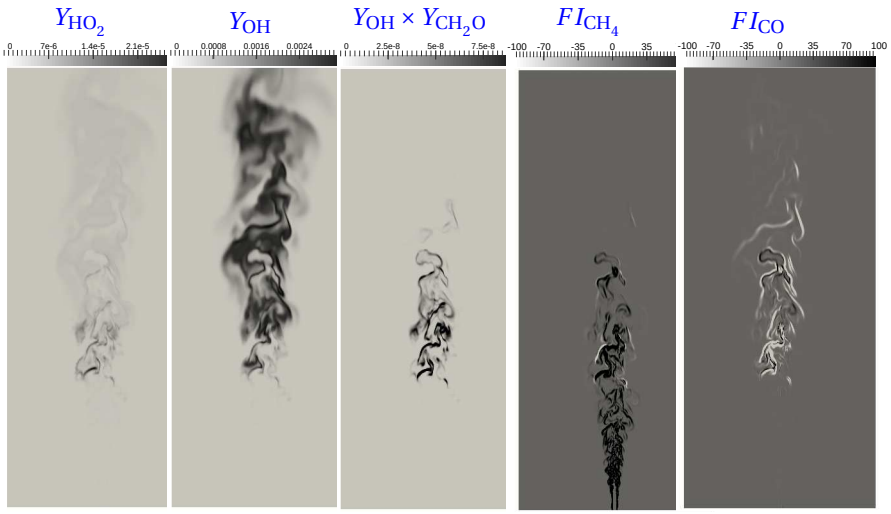

Figure 6.6: Snapshot of species mass fraction and flame index from LES simulation.

progress variable is high ($C_{d,Y_cv} = 1$ and 2). When the fluctuation of progress variable is further suppressed($C_{d,Y_cv} = 3$), the flame ignites and the lowest lift-off height among all the cases is observed. Fixing the value of C_{d,Y_cv} (column-wise comparison), the flame lift-off height first decreases with the increase of $C_{d,Zv}$, but further increase of $C_{d,Zv}$ may lead to no ignition, depending on the level of mixture fraction fluctuation. Given low level of mixture fraction fluctuation ($C_{d,Zv} = 3$), the flame lift-off height is extremely sensitive to the change of C_{d,Y_cv} within a certain range. A finer parameter study on this is shown in Fig. 6.8. A over- or under-prediction of the flame lift-off height is experienced by varying C_{d,Y_cv} from 2 to 3.

Radial profiles of the mean temperature from three representative cases are shown in Fig. 6.9. The sensitivity of the results on the model constants is evident when compared to experimental data. This sensitivity has two causes: on one hand, as investigated by Domingo et al [30] the ignition delay time of this flame reaches its minimum at the very lean side ($Z \approx 0.00427$) and rapidly increases away from this condition. This means that a small variation on the mixing at the lean side would lead to a large change in the ignition delay and therefore the flame lift-off height. On the other hand, the sensitivity is an essential feature of RANS simulation, where all the effects of turbulent fluctuations are modeled. These turbulence and scalar variance models rely on many empirical constants. Studies have shown that these model constants widely vary from case to case, and no optimal value is available in priori to the simulation of a new case. Therefore a wide range of these constants have been reported in the literature, even for simulation of similar or same experimental cases. By fine-tuning the model constants, a very good agreement on the mean properties can be achieved between simulation results and experimental data in the URANS, as shown by the case with $C_g = 2.86$ and $C_{d,Zv} = C_{d,Zv} = 1.0$ in Fig. 6.9. However, the general goal of the numerical combustion modeling research is to develop a predictable, robust and widely applicable tool for practical applications.

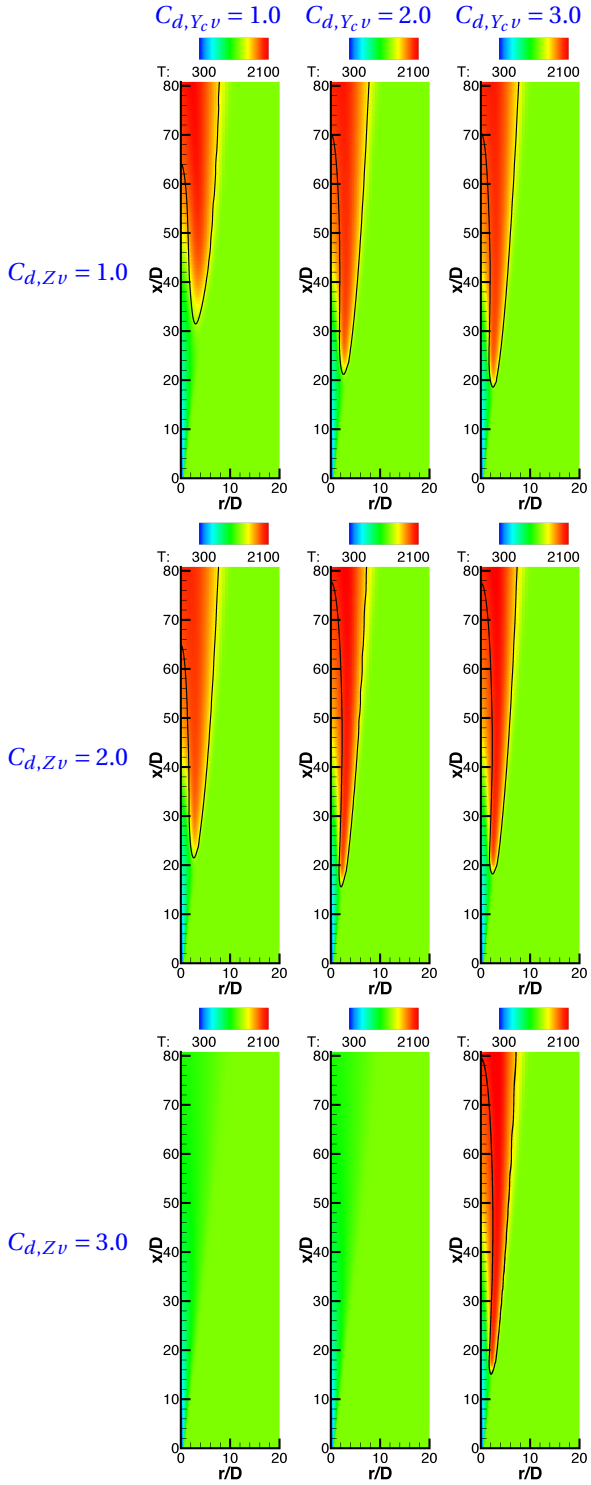

Figure 6.7: Contour plot of temperature with isoline of $Y_{OH} = 0.0005$ ($C_g = 2$), URANS.

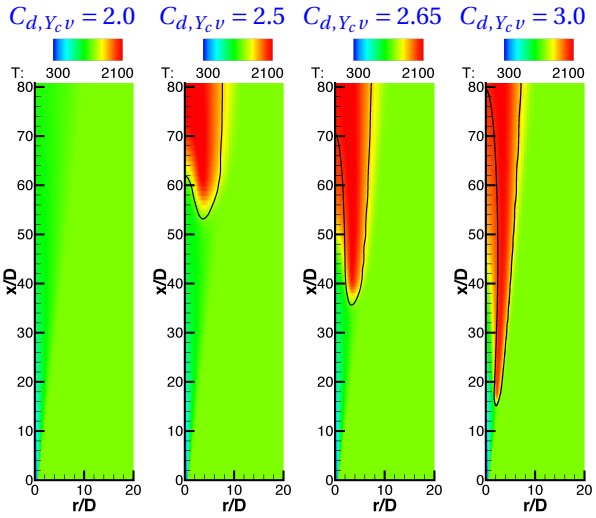

Figure 6.8: Contour plot of temperature with isoline of $Y_{OH} = 0.0005$ ($C_g = 2.0$, $C_{d,Zv} = 3.0$), URANS.

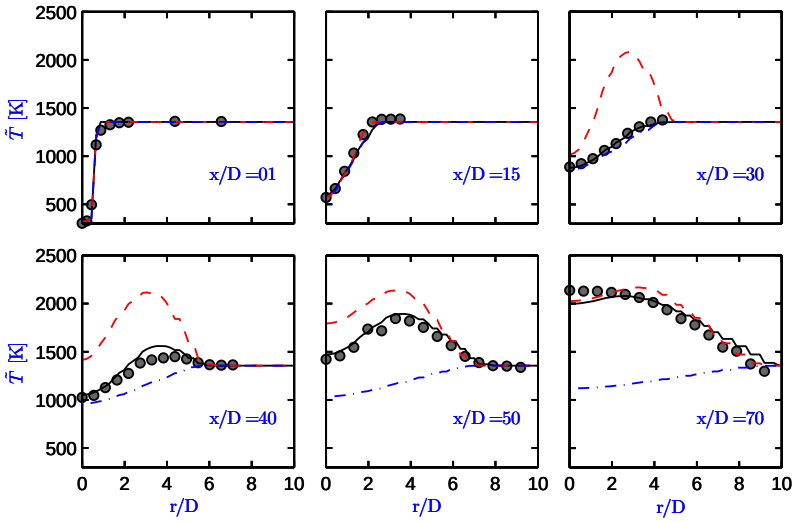

Figure 6.9: Radial profiles of mean temperature from URANS, $C_g = 2.86, C_{d,Zv} = 1, C_{d,Y_cv} = 1$ (——), $C_g = 2, C_{d,Zv} = 2, C_{d,Y_cv} = 2$ (– – –), $C_g = 2, C_{d,Zv} = 3, C_{d,Y_cv} = 1$ (– · – · –), Experiment (●).

Based on this criteria, it is clear that the tuning of model constants within RANS simulation for this kind of auto-ignition flame is ad-hoc and therefore less valuable.

6.6.3. RESULTS OF DYNAMIC SGS VARIANCE MODELS

LES provides possibilities to dynamically determine the uncertain model constants. In this section, results from LES simulation using dynamic Smagorinsky model and dynamic scalar variances model as proposed in Section 6.4 will be analyzed. Four cases that will be analyzed are summarized in Table. 6.3.

Table 6.3: LES cases description.

Case name	SGS variance model	coefficients
Ag1	DynAGM1	/
Ag2	DynAGM2	/
Tp1	DynTP-AGM1	$\gamma_{eq,Z} = \gamma_{eq,Y_c} = 1.0$
Tp2	DynTP-AGM1	$\gamma_{eq,Z} = \gamma_{eq,Y_c} = 0.35$

INFLUENCE OF FLUCTUATING SOURCE TERM ON $\widetilde{Y_c''^2}$

As shown by Eq. (6.44), the fluctuation of the progress variable source term also contributes to its variance. This term is however, most often neglected, for example in the commercial software ANSYS Fluent [40]. The importance of this term is investigated in the present section by comparing results from cases respectively using "Dyn-AGM1" and "Dyn-AGM2". The influence of fluctuating source term on progress variable variance is neglected in the latter model (see Eq.(6.45)).

Comparison between case "Ag1" and "Ag2" showed that the fluctuation of the progress variable source term indeed has a non-negligible effect when the algebraic model is used. In Fig. 6.10 and 6.11, in which the variances of mixture fraction and progress variables are shown, one can see that, as expected, case "Ag2" in general predicts smaller variances than case "Ag1", since the generation of $\widetilde{Y_c''^2}$ due to fluctuation of Y_c source term is neglected in case "Ag2". It is worth mentioning that the experimental data for progress variable variances plotted here are actually not accurate. Indeed, because based on the definition of the progress variable used in this study (Eq. (6.5)), the value of $\widetilde{Y_c''^2}$ requires the information on the covariances of the mass fraction of the involved species (CO_2, H_2O, CO and H_2). However, this information is not available in the experimental dataset. The plotted experimental $\widetilde{Y_c''^2}$ is simply the sum of the measured variances of each species. This value is plotted here only as a reference. If the mean temperature (Fig. 6.12) and mean species mass fraction (Fig. 6.13) are considered, results of case "Ag2" even have better agreement with the experimental data compared to those of case "Ag1". Similar to the observations made in section 6.6.2, again we found that the influence of the variances of FGM controlling parameters on the auto-ignition process is not really straightforward. This is of course due to the strong TCI, all the variables and processes are strongly coupled. Improvement on only one aspect of the entire model system does not necessarily lead to a better prediction of the whole system. So under the equilibrium

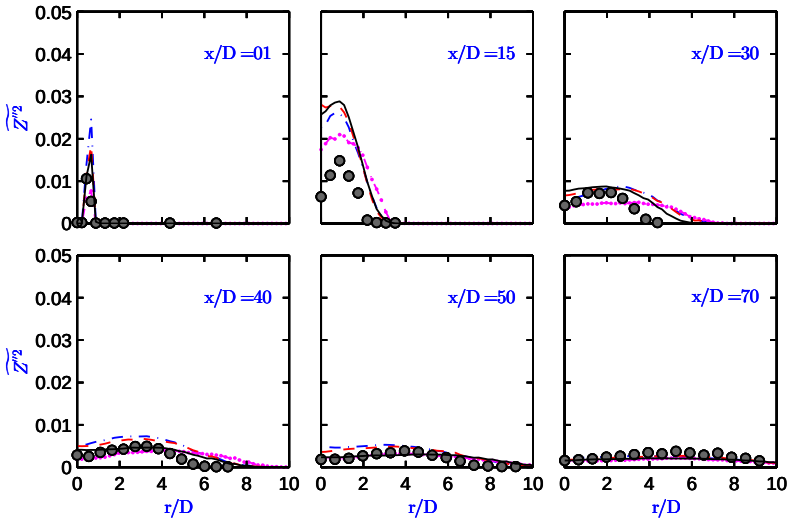

Figure 6.10: Radial profiles of mean mixture fraction variance, results of LES, Ag1: (- · - ·), Ag2:(- •-), Tp1 (- - -), Tp2 (——), Experiment (●).

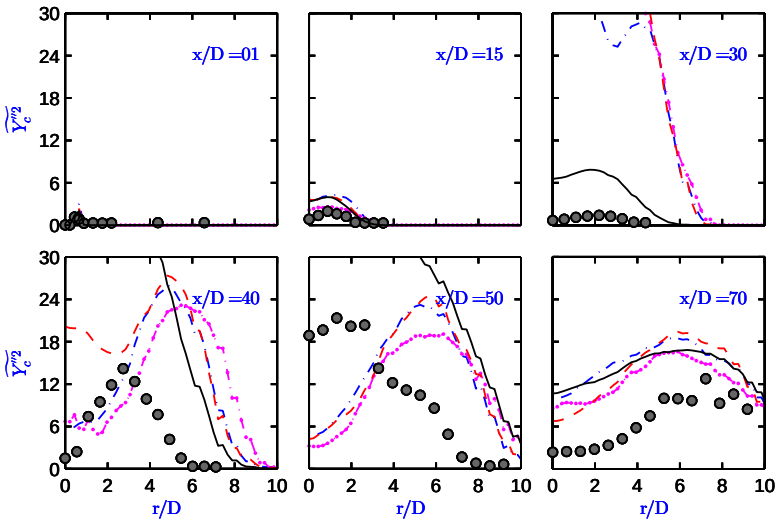

Figure 6.11: Radial profiles of mean progress variable variance, results of LES, Ag1: (- · - ·), Ag2:(- •-), Tp1 (- - -), Tp2 (——), Experiment (●).

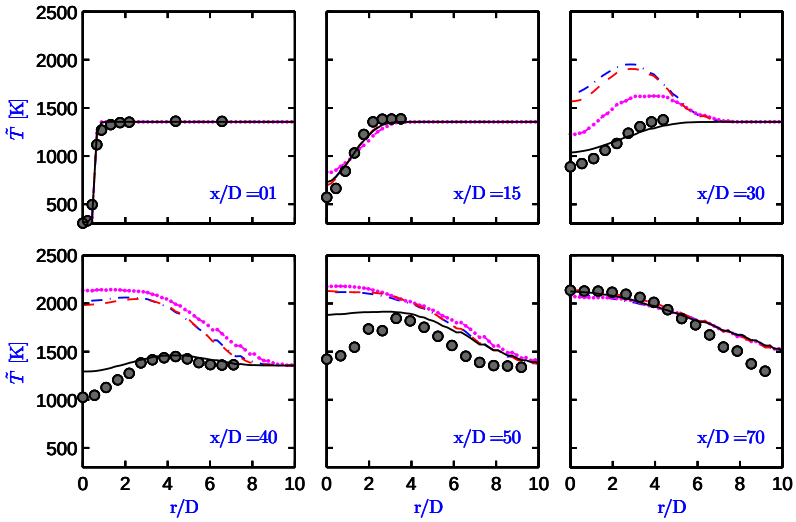

Figure 6.12: Radial profiles of mean temperature, results of LES, Ag1: (- · - ·), Ag2:(- • -), Tp1 (- - -), Tp2 (——), Experiment (●).

assumption, it is difficult to fairly assess the effect of the inclusion of the extra source term in the $\widetilde{Y_c''^2}$ model on the whole system. This also suggests that simulations using models "AGM2" or "Dyn-AGM2" may have success by luck, because the underestimation of the progress variable variances due to the equilibrium assumption may be compensated by the effect of exclusion of the fluctuating source term. Simulations respectively using dynamic transport equation models "DynTP-AGM1" and "DynTP-AGM2" were also carried out (not shown here for simplicity), the results showed that using "DynTP-AGM1" indeed slightly improved the prediction.

ALGEBRAIC MODE VS. TRANSPORT EQUATION MODEL

The performances of the dynamic algebraic model "DynAGM1" and dynamic transport equation model "DynTP-AGM1" are analyzed in this subsection. Compared to experimental data, case "Ag1" significantly over-predicts the mean temperature (Fig. 6.12), and mean progress variable (Fig. 6.14) between axial stations $x/D = 30$ to 50. The progress variable variance $\widetilde{Y_c''^2}$ (Fig. 6.11) was predicted much higher in case "Ag1" than the plotted experimental data and those of the case "Tp2" at $X/D = 30$, and the opposite was observed at $X/D = 40$ and $X/D = 50$. Similar results can also be seen in the root mean square (RMS) value of the mass fraction of main combustion products, i.e. CO_2 and H_2O, in Fig. 6.15. Meanwhile, over-prediction of these combustion products from $x/D = 30$ is also evident in case "Ag1", see Fig. 6.13. Based on these results, we can conclude that the flame stabilizes at around $X/D = 30$ in case "Ag1", which is lower than reported by experimental study [13] and a previous simulation [12]. This is because the ignition takes place too early and the flame lift-off height is under-predicted. In this case, the dynamic algebraic model "Dyn-AGM1" (Eq. (6.44)) was used for the determination of the mixture

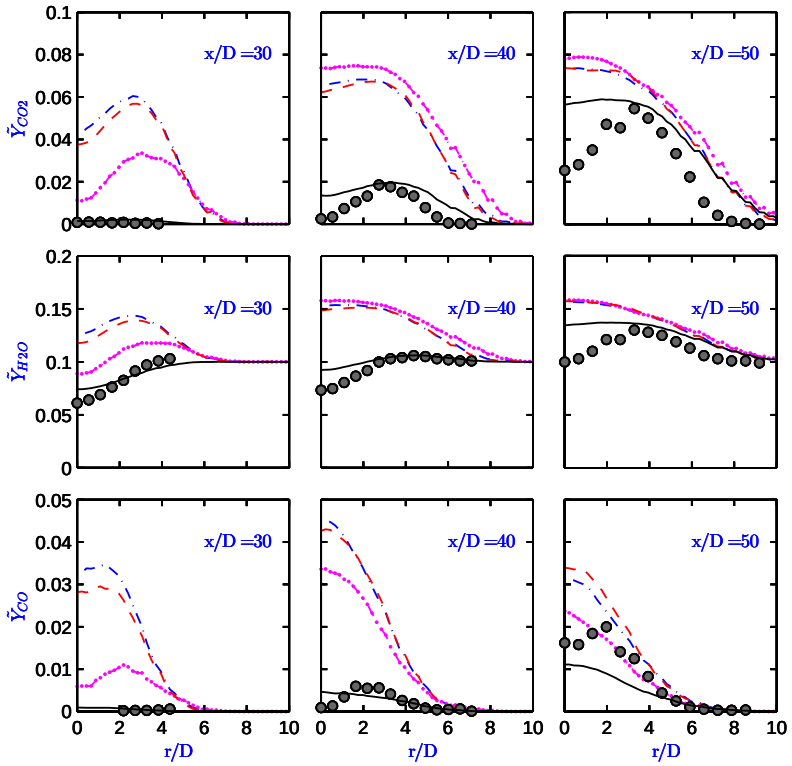

Figure 6.13: Radial profiles of mean species mass fraction, results of LES, Ag1: (– · – · –), Ag2:(– • –), Tp1 (– – –), Tp2 (——), Experiment (●).

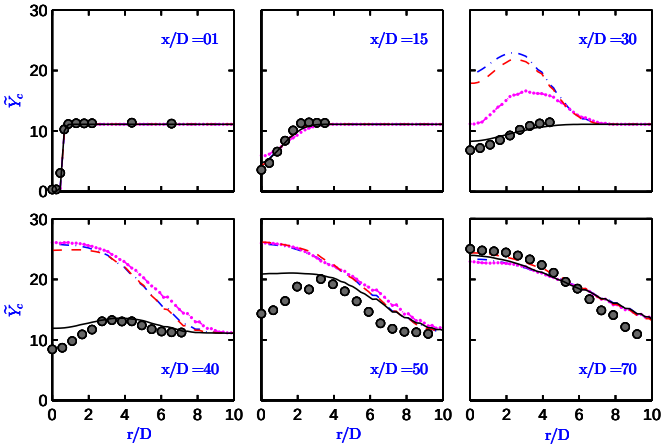

Figure 6.14: Radial profiles of mean progress variable, results of LES, Ag1: (– · – · –), Ag2:(– • –), Tp1 (– – –), Tp2 (——), Experiment (●).

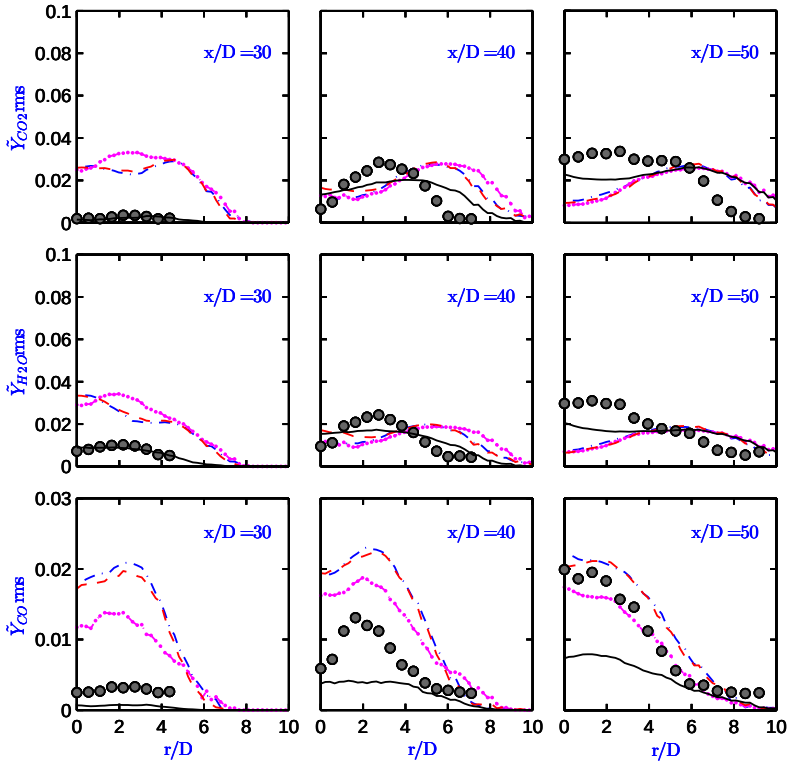

Figure 6.15: Radial profiles of species mass fraction root mean square (RMS), results of LES, Ag1: (– · – ·), Ag2:(–•–), Tp1 (– – –), Tp2 (——), Experiment (●).

fraction and progress variable variances. Unsurprisingly, in case “Tp1”, in which the dynamic transport equation model “DynTP-AGM1” with $\gamma_{eq,Z} = \gamma_{eq,Y_c} = 1.0$ is employed, only slight improvements have been achieved. This is because, in case “Tp1”, the dissipation term coefficients for the transport equations of $\widetilde{Z''}$ and $\widetilde{Y_c''^2}$ are directly converted form the dynamic algebraic model “Dyn-AGM1” using relations (6.46). In the algebraic model, the local equilibrium assumption was made. This assumption leads to an over-dissipation of the scalar variances in both “Ag1” and “Tp1” cases. The over-dissipation of the scalar variances, especially $\widetilde{Y_c''^2}$, tends to extend the sub-grid scale ignition event, which cannot be computationally resolved, and this in turn leads of under-prediction of flame lift-off height [12].

NON-EQUILIBRIUM EFFECT

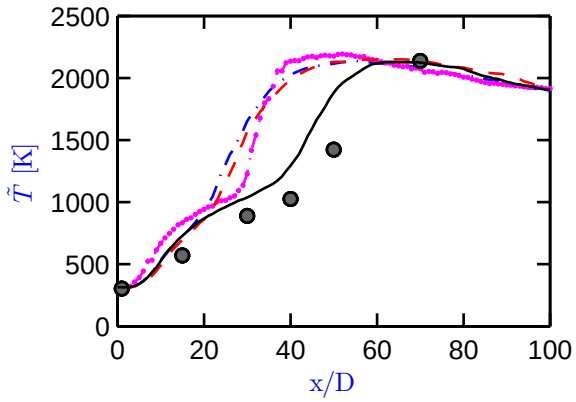

Figure 6.16: Centerline profiles of mean temperature, results of LES, Ag1: (– · –), Ag2:(– • –), Tp1 (– – –), Tp2 (——), Experiment (●).

When the non-equilibrium effect was considered by setting the coefficients $\gamma_{eq,Z} = \gamma_{eq,Y_c} = 0.35$, results were obtained with a considerable closer agreement with the experimental data in case “Tp2". The radial and centerline profiles of mean temperature (Figs. 6.12 and 6.16) indicate that a significant temperature rise occurred in regions between $x/D = 40$ and $x/D = 50$. This is in agreement with the conclusion drawn in a previous LES study of this flame using an unsteady flamelet/progress variable model [12]. However, the mean temperature in the near centerline region from $x/D = 15$ downstream was under-predicted. The mean mixture fraction is under predicted in the same region, as can be seen in Fig. 6.17. These observations all point to the fact that the fuel jet breakup happened in a shorter distance from the nozzle tip in the simulation as it should be. Consequently, a leaner condition which is favorable for ignition to take place was formed in the center. Ignition kernels may appear in this region, resulting in a over-prediction on the mean temperature. The early fuel jet breakup may relate to the specification of the inlet boundary condition, as argued by Müller et al in [41]. The mean mass fraction of CO_2, H_2O and their root mean square (RMS) values were well captured in case “Tp2”, as shown in Figs. 6.13 and 6.15. However CO was under-predicted, this may relate

to the definition of the progress variable used in this study (Eq. (6.5)), in which the contribution of CO is suppressed by using a relatively small weighting factor to maintain the monotonicity. To improve this, an optimization of the definition of progress variable is needed.

Summarizing the discussions in this section. We found that the fluctuating source term of progress variable has a considerable influence on the predicted results, however the inclusion of this term in the algebraic model does not necessarily lead to an improved prediction. This is due to the strong coupling between models. Furthermore, the equilibrium assumption made in the algebraic model has shown to be a poor assumption. The superior performance of the dynamic transport equation model with low value of equilibrium constant was demonstrated. This model is therefore recommended to be used with FGM for cases in which strong TCI exists.

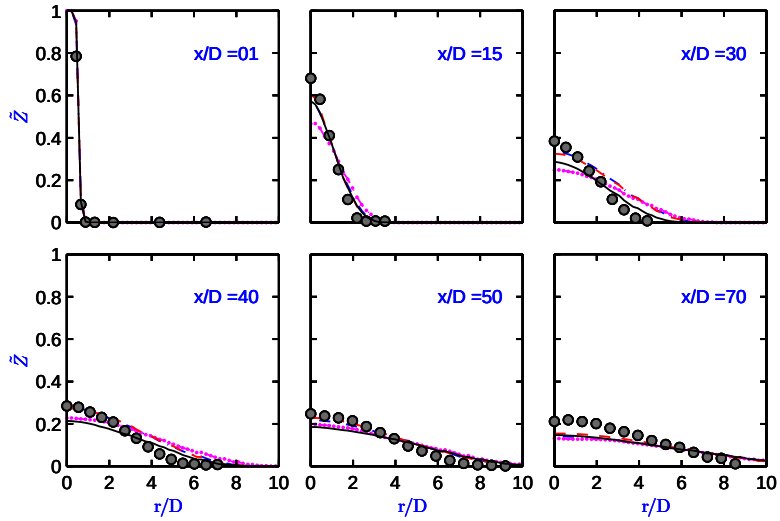

Figure 6.17: Radial profiles of mean mixture fraction, results of LES, Ag1: (– · –), Ag2:(– • –), Tp1 (– – –), Tp2 (——), Experiment (●).

6.7. CONCLUSIONS

In this Chapter we reported a new development in the modeling of sub-grid variances of the controlling parameters of the FGM model. In cases where the turbulence-chemistry interaction (TCI) is important, for example the auto-ignition process, the evaluation of the variances greatly influences the PDF of the controlling parameters, and therefore affects the prediction of TCI. The existing models for the scalar variances contain some empirical model constants of which no optimal value exists for wide range of applications. In this paper we have shown that in an URANS simulation, the auto-ignition process is very sensitive to even a small variation of these model constants. This brings in a considerable uncertainty when a new case is to be simulated with this model and no a priori information on these model constants is available. Therefore, the RANS technique

is not recommended for simulating cases in which strong TCI exists.

To overcome the uncertainties on the model constants choice, a dynamic procedure has been developed in the context of LES. In this model approach, the SGS Reynolds stresses are closed with the dynamic Smagorinsky model. The unknown model constants in the algebraic model and transport equation model for the controlling variable variances are calculated according to local conditions on the fly. The dynamic constants for the transport equation model are deduced from those of the dynamic algebraic model. The latter one builds on the local equilibrium assumption which was shown in this study to be a poor assumption. The non-equilibrium effect was considered by introducing a constant during the conversion of algebraic model constant to those of the transport model. The physical meaning of this constant can be interpreted as the extent of equilibrium that is achieved locally. A significant improvement on the prediction of the considered case was achieved with the dynamic transport equation model using a low value of equilibrium constants. The influence of the fluctuating source term on the variance of progress variable is also considered in the proposed dynamic SGS variance model, which has been shown to has a non-negligible influence on the prediction when algebraic model is used. The promising performance of the developed dynamic transport equation model was demonstrated.

APPENDIX:DERIVATION OF VARIANCE TRANSPORT EQUATIONS FOR Z AND Y_c

The derivation process for the transport equations of mixture fraction and progress variable variances will be given in this appendix. The continuity equation and exact transport equations for mixture fraction and progress variable are first given:

$$\frac{\partial \rho}{\partial t} + \frac{\partial \rho u_j}{\partial x_j} = 0 \tag{6.58}$$

$$\frac{\partial \rho Z}{\partial t} + \frac{\partial \rho u_j Z}{\partial x_j} = \frac{\partial}{\partial x_j}\left(\rho D \frac{\partial Z}{\partial x_j}\right) \tag{6.59}$$

$$\frac{\partial \rho Y_c}{\partial t} + \frac{\rho u_j Y_c}{\partial x_j} = \frac{\partial}{\partial x_j}\left(\rho D \frac{\partial Y_c}{\partial x_j}\right) + \dot{\omega}_{Y_c} \tag{6.60}$$

where $\dot{\omega}_{Y_c}$ is the source term for progress variable due to reaction.

Applying Reynolds averaging or filter function to Eqs. (6.59) and (6.60), one obtains:

$$\frac{\partial \bar{\rho} \tilde{Z}}{\partial t} + \frac{\partial \bar{\rho} \tilde{u}_j \tilde{Z}}{\partial x_j} = \frac{\partial}{\partial x_j}\left(\bar{\rho} D \frac{\partial \tilde{Z}}{\partial x_j} - \Phi_{Z,j}\right) \tag{6.61}$$

$$\frac{\partial \bar{\rho} \tilde{Y}_c}{\partial t} + \frac{\partial \bar{\rho} \tilde{u}_j \tilde{Y}_c}{\partial x_j} = \frac{\partial}{\partial x_j}\left(\bar{\rho} D \frac{\partial \tilde{Y}_c}{\partial x_j} - \Phi_{Y_c,j}\right) + \bar{\dot{\omega}}_{Y_c} \tag{6.62}$$

where Φ_Z and Φ_{Y_c} are respectively the (SGS) turbulent fluxes for mixture fraction and progress variable and are shown in Table 6.1.

The variance of progress variable can be obtained by:

$$Y_{c,v} = \widetilde{Y_c''^2} = \widetilde{Y_c^2} - \tilde{Y_c}^2 \tag{6.63}$$

The transport equation for Y_c^2 can be derived by multiplying Eq. (6.60) with $2Y_c$ and making use of continuity equation Eq. (6.58):

$$\frac{\partial \rho Y_c^2}{\partial t} + \frac{\partial \rho u_j Y_c^2}{\partial x_j} = \frac{\partial}{\partial x_j}\left(\rho D \frac{\partial Y_c^2}{\partial x_j}\right) - \rho \chi_{Y_c} + 2Y_c \dot{\omega}_{Y_c} \tag{6.64}$$

where the scalar dissipation rate for Y_c is $\chi_{Y_c} = D\left(\frac{\partial Y_c}{\partial x_j}\right)^2$, D being the diffusivity.

Applying Reynolds averaging or filter function to Eq. (6.64):

$$\frac{\partial \bar{\rho} \widetilde{Y_c^2}}{\partial t} + \frac{\partial \bar{\rho} \tilde{u}_j \widetilde{Y_c^2}}{\partial x_j} = \frac{\partial}{\partial x_j}\left(\bar{\rho} D \frac{\partial \widetilde{Y_c^2}}{\partial x_j} - \Phi_{Y_c^2,j}\right) - 2\bar{\rho}\tilde{\chi}_Z + \overline{2Y_c \dot{\omega}_{Y_c}} \tag{6.65}$$

where $\Phi_{Y_c^2,j} = \left(\overline{\rho u_j Y_c^2} - \bar{\rho}\widetilde{u_j}\widetilde{Y_c^2}\right)$ which for RANS can be written as $\Phi_{Y_c^2,j} = \bar{\rho}\widetilde{u_j'' \left(Y_c^2\right)''}$.

Similarly, the transport equation for $\tilde{Y_c}^2$ can be derived by $2\tilde{Y_c} \times$ Eq. (6.62) and a bit manipulation:

$$\frac{\partial \bar{\rho} \tilde{Y_c}^2}{\partial t} + \frac{\partial \bar{\rho} \tilde{u}_j \tilde{Y_c}^2}{\partial x_j} = \frac{\partial}{\partial x_j}\left(\bar{\rho} D \frac{\partial \tilde{Y_c}^2}{\partial x_j}\right) - 2\bar{\rho} D \left(\frac{\partial \tilde{Y_c}}{\partial x_j}\right)^2 - \frac{\partial}{\partial x_j}\left(2\tilde{Y_c}\Phi_{Y_c,j}\right) + 2\Phi_{Y_c,j}\frac{\partial \tilde{Y_c}}{\partial x_j} + 2\tilde{Y_c}\bar{\dot{\omega}}_{Y_c} \tag{6.66}$$

Subtracting Eq. (6.66) from Eq. (6.65), we finally obtain the transport equation for progress variable variance:

$$\begin{aligned}\frac{\partial \bar{\rho} \widetilde{Y_c''^2}}{\partial t} + \frac{\partial \bar{\rho} u_j \widetilde{Y_c''^2}}{\partial x_j} = \frac{\partial}{\partial x_j}\left(\bar{\rho} D \frac{\partial \widetilde{Y_c''^2}}{\partial x_j} - \Phi_{Y_{c,v},j}\right) - 2\bar{\rho}\tilde{s}_{\chi_{Y_c}} - 2\Phi_{Y_c,j}\frac{\partial \tilde{Y_c}}{\partial x_j} \\ + 2\left(\overline{Y_c \dot{\omega}_{Y_c}} - \tilde{Y_c}\bar{\dot{\omega}}_{Y_c}\right)\end{aligned} \tag{6.67}$$

The terms $\Phi_{Y_{c,v},j}$ and $\Phi_{Y_c,j}$ are explained in Table 6.1. The scalar dissipation rate has been decomposed into its resolved and SGS ($\bar{\rho}\tilde{s}_{\chi_{Y_c}}$) parts in LES, or laminar and turbulent part in RANS.

$$\underbrace{\bar{\rho}\tilde{\chi}_{Y_c}}_{\text{scalar dissipation rate}} = \overline{\rho D \left(\frac{\partial Y_c}{\partial x_j}\right)^2} = \underbrace{\bar{\rho} D \left(\frac{\partial \tilde{Y_c}}{\partial x_j}\right)^2}_{\text{resolved / laminar part}} + \underbrace{\bar{\rho}\tilde{s}_{\chi_{Y_c}}}_{\text{SGS / turbulent part}} \tag{6.68}$$

Transport equation for mixture fraction variance Eq.(6.29) can be obtained following similar procedure.

REFERENCES

[1] R. L. Gordon, A. R. Masri, S. B. Pope, and G. M. Goldin, *Transport budgets in turbulent lifted flames of methane autoigniting in a vitiated co-flow,* Combustion and Flame **151**, 495 (2007).

[2] C. S. Yoo, E. S. Richardson, R. Sankaran, and J. H. Chen, *A DNS study on the stabilization mechanism of a turbulent lifted ethylene jet flame in highly-heated coflow,* Proceedings of the Combustion Institute **33**, 1619 (2011).

[3] W. O'Loughlin and A. R. Masri, *The Structure of the Auto-Ignition Region of Turbulent Dilute Methanol Sprays Issuing in a Vitiated Co-flow,* Flow, Turbulence and Combustion **89**, 13 (2012).

[4] S. Bhattacharjee and D. C. Haworth, *Simulations of transient n-heptane and n-dodecane spray flames under engine-relevant conditions using a transported PDF method,* Combustion and Flame **160**, 2083 (2013).

[5] S. B. Pope, *Small scales, many species and the manifold challenges of turbulent combustion,* Proceedings of the Combustion Institute **34**, 1 (2013).

[6] J. A. van Oijen and L. P. H. de Goey, *Modelling of premixed laminar flames using flamelet-generated manifolds,* Combustion Science and Technology **161**, 113 (2000).

[7] N. Peters, *Laminar diffusion flamelet models in non-premixed turbulent combustion,* Progress in Energy and Combustion Science **10**, 319 (1984).

[8] A. Rittler, F. Proch, and A. M. Kempf, *LES of the Sydney piloted spray flame series with the PFGM/ATF approach and different sub-filter models,* Combustion and Flame **162**, 1575 (2015).

[9] D. Haworth, *Progress in probability density function methods for turbulent reacting flows,* Progress in Energy and Combustion Science **36**, 168 (2010).

[10] L. Ma, B. Naud, and D. Roekaerts, *Transported PDF Modeling of Ethanol Spray in Hot-diluted Coflow Flame,* Flow, Turbulence and Combustion , in press (2015).

[11] A. Vreman, B. Albrecht, J. A. van Oijen, L. P. H. de Goey, and R. Bastiaans, *Premixed and nonpremixed generated manifolds in large-eddy simulation of Sandia flame D and F,* Combustion and Flame **153**, 394 (2008).

[12] M. Ihme and Y. C. See, *Prediction of autoignition in a lifted methane/air flame using an unsteady flamelet/progress variable model,* Combustion and Flame **157**, 1850 (2010).

[13] R. Cabra, J. Chen, R. Dibble, A. Karpetis, and R. Barlow, *Lifted methane–air jet flames in a vitiated coflow,* Combustion and Flame **143**, 491 (2005).

[14] OpenFOAM, *OpenFOAM: The open source CFD Toolbox,* (2015).

[15] R. W. Bilger, *The structure of turbulent nonpremixed flames,* in *22rd International Symposium on Combustion* (1988) pp. 475–488.

[16] R. de Meester, B. Naud, U. Maas, and B. Merci, *Transported scalar PDF calculations of a swirling bluff body flame SM1 with a reaction diffusion manifold,* Combustion and Flame **159**, 2415 (2012).

[17] M. Chrigui, A. R. Masri, A. Sadiki, and J. Janicka, *Large Eddy Simulation of a polydisperse ethanol wpray flame,* Flow, Turbulence and Combustion **90**, 813 (2013).

[18] B. A. Albrecht, S. Zahirovic, R. Bastiaans, J. van Oijen, and L. de Goey, *A Premixed Flamelet - PDF Model for Biomass Combustion in a,* Energy & Fuels , 1570 (2008).

[19] B. Naud, R. Novella, J. M. Pastor, and J. F. Winklinger, *RANS modelling of a lifted H2/N2 flame using an unsteady flamelet progress variable approach with presumed PDF,* Combustion and Flame **162**, 893 (2014).

[20] B. B. Dally, D. F. Fletcher, and A. R. Masri, *Flow and mixing fields of turbulent bluff-body jets and flames,* Combustion Theory and Modelling **2**, 193 (1998).

[21] A. Yoshizawa, *Statistical theory for compressible turbulent shear flows, with the application to subgrid modeling,* Physics of Fluids **29**, 2152 (1986).

[22] G. Erlebacher, M. Y. Hussaini, C. G. Speziale, and T. A. Zang, *Toward the large-eddy simulation of compressible turbulent flows,* Journal of Fluid Mechanics **238**, 155 (1992).

[23] M. Lesieur, O. Metais, and P. Comte, *Large-Eddy Simulation of Turbulence* (Cambridge University Press, 2005).

[24] M. P. Mart, U. Piomelli, and G. V. Candler, *Subgrid-Scale Models for Compressible Large-Eddy Simulations,* Theoretical and Computational Fluid Dynnamics **13**, 361 (2000).

[25] H. Versteeg and W. Malalasekera, *An Introduction to Computational Fluid Dynamics (Second Edition)* (Pearson Education, 2007).

[26] T. Poinsot and D. Veynante, *Theoretical and Numerical combustion (Third Edition)* (Aquaprint, 2012).

[27] M. Germano, U. Piomelli, P. Moin, and W. H. Cabot, *A dynamic subgrid-scale eddy viscosity model,* Physics of Fluids A: Fluid Dynamics **3**, 1760 (1991).

[28] P. Moin, K. Squires, W. Cabot, and S. Lee, *A dynamic subgrid-scale model for compressible turbulence and scalar transport,* Physics of Fluids A: Fluid Dynamics **3**, 2746 (1991).

[29] D. K. Lilly, *A proposed modification of the Germano subgrid-scale closure method,* Physics of Fluids A: Fluid Dynamics **4**, 633 (1992).

[30] P. Domingo, L. Vervisch, and D. Veynante, *Large-eddy simulation of a lifted methane jet flame in a vitiated coflow,* Combustion and Flame **152**, 415 (2008).

[31] N. Branley and W. Jones, *Large Eddy simulation of a turbulent non-premixed flame,* Combustion and Flame **127**, 1914 (2001).

[32] W. Ramaekers, *Development of Flamelet Generated Manifolds for Partially-Premixed Flame Simulations*, Ph.D. thesis, Eindhoven University of Technology (2011).

[33] M. Chrigui, J. Gounder, A. Sadiki, A. R. Masri, and J. Janicka, *Partially premixed reacting acetone spray using LES and FGM tabulated chemistry,* Combustion and Flame **159**, 2718 (2012).

[34] C. D. Pierce and P. Moin, *A dynamic model for subgrid-scale variance and dissipation rate of a conserved scalar,* Physics of Fluids **10**, 3041 (1998).

[35] C. M. Kaul, V. Raman, E. Knudsen, E. S. Richardson, and J. H. Chen, *Large eddy simulation of a lifted ethylene flame using a dynamic nonequilibrium model for subfilter scalar variance and dissipation rate,* Proceedings of the Combustion Institute **34**, 1289 (2013).

[36] R. I. Issa, *Solution of the Implicitly Discretised Fluid Flow Equations by Operator-Splitting,* Journal of Computational Physics **65**, 40 (1986).

[37] Surfsara, *Cartesius: the Dutch supercomputer,* (https://surfsara.nl/systems/cartesius).

[38] E. Oldenhof, M. Tummers, E. van Veen, and D. Roekaerts, *Ignition kernel formation and lift-off behaviour of jet-in-hot-coflow flames,* Combustion and Flame **157**, 1167 (2010).

[39] S. M. Mir Najafizadeh, M. T. Sadeghi, R. Sotudeh-Gharebagh, and D. Roekaerts, *Chemical structure of autoignition in a turbulent lifted H2/N2 jet flame issuing into a vitiated coflow,* Combustion and Flame **160**, 2928 (2013).

[40] ANSYS, *Fluent 15.0 Theory Guide,* (2014).

[41] H. Müller, F. Ferraro, and M. Pfitzner, *Implementation of a Steady Laminar Flamelet Model for non-premixed combustion in LES and RANS simulations,* in *8th International openFOAM Workshop* (2013).

7

DEVELOPMENT AND VALIDATION OF LES/FGM METHOD FOR MODELING MILD SPRAY FLAMES

This chapter reports a numerical study of case H_{II} of the DSHC database with the new OpenFOAM FGM solver developed in Chapter 6. The enthalpy loss effect due to droplet vaporization is considered by employing an additional controlling parameter in the FGM library. Analysis of the DSHC experimental data suggested that flash boiling influences the atomization of liquid fuel in the DSHC burner. A conditional injection model is proposed to provide precise spray information at the injector exit plane ($\mathcal{Z} = 0\ mm$). The results show that this model significantly improves the prediction of all the properties examined compared to standard injection model. Comparison between URANS and LES is made, and it is found that the LES predicted similar gas phase velocity and better temperature profiles compared to experimental data than URANS, mainly due to the better performance of the dynamic model for mixture fraction variance used in LES. The improvement of the temperature prediction by the non-adiabatic FGM was clearly demonstrated by comparing the results obtained with an adiabatic FGM table.

Content in this has been published in the following paper:
L. Ma, D. Roekaerts, Modeling of spray jet flame under MILD condition with non-adiabatic FGM and a new conditional droplet injection model, Combustion and Flame, 165: 402-423, 2016.

7.1. INTRODUCTION

Spray combustion is widely utilized in energy systems, such as industrial furnaces and propulsion systems. Achieving low pollutant emissions while maintaining high efficiency and the required heat flux is a key goal for innovation in this area [1, 2]. Exploitation of the beneficial effects of dilution of the oxidizer with partially cooled combustion products, leading to so-called MILD (Moderate or Intense Low-oxygen Dilution) combustion or "flameless oxidation" [3, 4], has been such innovation. MILD combustion of gaseous fuels has been intensively studied both experimentally and numerically [5–8]. However, so far there has been much less research on liquid fuel MILD combustion [9–11]. The Delft Spray-in-Hot-Coflow (DSHC) burner was designed to study the flameless oxidation of light oils [12]. With different spray and gas phase properties measured and influences of coflow conditions and fuel flexibility studied, the DSHC dataset provides a valuable basis for the development and validation of modeling method towards the application of MILD spray combustion [12, 13].

Modeling of turbulent spray combustion is particularly challenging because many physical and chemical processes including turbulence, atomization, evaporation, combustion and radiative heat transfer are involved and interact with each other [14]. A set of models, hence has to be carefully chosen to accurately predict the aforementioned processes. Under MILD condition, new features and challenges emerge. The increase of liquid–gas interface temperature makes surface tension decrease leading to a better atomization with respect to the process without preheating. Depending on the configuration of the liquid fuel injection system, cavitation or flash boiling may happen because of sudden pressure drop and heat transfer from the preheated oxidizer stream. The high temperature of the reactants also influences the droplet evaporation that occurs in series and/or in parallel with the atomization process [3]. These new features all demand careful treatment when an accurate prediction of MILD spray combustion is expected. Analysis of the experimental data shows that flash boiling happens during the atomization process of the DSHC burner (see section 7.4.1). This imposes difficulties on modeling the atomization process with conventional models. To fully understand the complicated atomization process, a Direct Numerical Simulation (DNS) of the nozzle internal flow and atomization process should be carried out. However, this is beyond the scope of this study. In this paper we attempt to develop a (simple) method capable of providing reliable and accurate spray boundary conditions for DSHC flame using available experimental information.

Successful use of flamelet-based models under MILD conditions have been reported by many researchers [15, 16]. An early study [17] using flamelet models show comparable results with experiments across a range of conditions. Minamoto et al. [18] carried out DNS study of flame under MILD condition and found flamelet structure still exists under MILD condition. Further analysis on the scalar gradient behavior in MILD combustion confirmed this finding [19]. Flamelet interactions were observed, but these interactions do not make a strong difference in the time-averaged or spatial filtered sense. Compared to the Eddy Dissipation Concept (EDC) model, which is widely used for modeling of MILD combustion [5, 20, 21], the tabulated chemistry models are computationally very efficient. The Flamelet Generated Manifolds (FGM) model [22], conceptually similar to the Flamelet / Progress Variable (FPV) model [23], advances from the original

steady flamelet model by taking into account the chemical dynamics. Many important phenomena, such as auto-ignition and flame quenching can be captured with the FGM model [16, 24]. Based on these considerations, the FGM model was implemented into the open source CFD package — OpenFOAM [25] — by the authors, and used to model the DSHC flame in this study.

It was found from a previous study [26] that heat loss has to be incorporated in the FGM library in order to accurately reproduce the gas phase temperature. The heat loss in spray combustion mainly comes from two aspects: on one hand the convective heat transfer to raise the droplet temperature and on the other hand, the latent heat during droplet vaporization. Many approaches have been reported in the literature to extend flamelet-based models, including FGM, with heat loss effects, most of which are however for the application of radiative heat transfer [27–29]. In summary, these methods can be categorized in three groups: “method 1", neglecting the influence of enthalpy loss on the species composition, only the gas phase temperature is reduced to the new enthalpy levels, for example in the commercial CFD software ANSYS Fluent [30]; “method 2", decreasing the temperature at flamelet boundaries, and combining flamelets with different enthalpy loss in the library, [31]; “method 3", solve flamelet equations with source term taking into account the heat loss [32, 33]. In the present study, we develop a new lookup procedure based on “method 2".

The main objective of the current study is to develop and validate predictive models for spray combustion under MILD condition. Original contributions of this paper are made in two aspects: first, a new droplet injection model accounts for the influences of flash-boiling atomization is proposed and tested; Second, a new solver using non-adiabatic FGM model for modeling turbulent spray combustion is developed and validated in the framework of OpenFOAM. The paper is structured as follows: modeling approaches for both gas phase and dispersed phase are presented in section 7.2, followed by a detailed explanation on the construction and lookup procedures of the non-adiabatic FGM library in section 7.3. Based on analysis of experimental data, features of the atomization of DSHC flame is studied in section 7.4, a new droplet injection model is also proposed in this section. Details for the numerical solver adopted are given in section 7.5 before the analysis of the results in section 7.6. Main conclusions are summarized in the last section.

7.2. MATHEMATIC MODELING

In this Chapter we simulate one of the ethanol spray in hot-diluted coflow cases, namely the case H_{II}, in the DSHC database. Details of this case are described in section 1.4.

7.2.1. GAS PHASE MODELS

In the current study, the FGM model is adopted for the Turbulence-Chemistry Interaction (TCI). For FGM, instead of solving all the species and energy transport equations during simulation, the chemical process in turbulent combustion is assumed to happen in a low dimensional manifold. This means that there are only a few variables that can change independently in the whole composition space. Very often, the mixture fraction Z, which represents the extent of mixing between “fuel” and “oxidizer”, and progress

variable C, which denotes the progress of chemical reaction from pure mixing ($C = 0$) to fully burnt ($C = 1$), are chosen as independent variables in the FGM method. The dimension of the FGM lookup table can be extended to incorporate more physics when required, for example, adding enthalpy h to account for the heat loss/gain [34], adding scalar dissipation rate χ to consider the influence of strain [35] and adding pressure p to take into account the effect of pressure variation [36]. The modeled Unsteady Reynolds Averaged Navier Stokes (URANS) or Large Eddy Simulation (LES) transport equations for turbulent combustion using FGM method can be expressed as follows:

$$\frac{\partial \bar{\rho}}{\partial t} + \frac{\partial \bar{\rho}\tilde{u}_j}{\partial x_j} = \bar{S}_\rho, \tag{7.1}$$

$$\frac{\partial \bar{\rho}\tilde{u}_i}{\partial t} + \frac{\partial \left(\bar{\rho}\tilde{u}_i\tilde{u}_j\right)}{\partial x_j} = -\frac{\partial \bar{p}}{\partial x_i} + \frac{\partial}{\partial x_j}\left(\bar{2}\mu\tilde{S}^D_{ij} - \tau_{ij}\right) + \bar{S}_{u_i}, \tag{7.2}$$

$$\frac{\partial \bar{\rho}\tilde{Z}}{\partial t} + \frac{\partial \bar{\rho}\tilde{u}_j\tilde{Z}}{\partial x_j} = \frac{\partial}{\partial x_j}\left[\bar{\rho}\left(\tilde{D} + D_t\right)\frac{\partial \tilde{Z}}{\partial x_j}\right] + \bar{S}_Z, \tag{7.3}$$

$$\frac{\partial \bar{\rho}\tilde{Y}_c}{\partial t} + \frac{\bar{\rho}\tilde{u}_j\tilde{Y}_c}{\partial x_j} = \frac{\partial}{\partial x_j}\left[\bar{\rho}\left(\tilde{D} + D_t\right)\frac{\partial \tilde{Y}_c}{\partial x_j}\right] + \bar{\dot{\omega}}_{Y_c}, \tag{7.4}$$

$$S_{ij} = \frac{1}{2}\left(\frac{\partial u_i}{\partial x_j} + \frac{\partial u_j}{\partial x_i}\right), \tag{7.5}$$

where $S^D_{ij} = \left(S_{ij} - \frac{1}{3}\delta_{ij}S_{kk}\right)$ is the deviatoric part of the strain rate tensor S_{ij}. τ_{ij} is the Reynolds stresses (in URANS) or sub-grid scale (SGS) stresses (in LES). It is closed with standard $k-\epsilon$ model in URANS, and dynamic Smagorinsky model in the LES.

Y_c is the unscaled progress variable, and is defined as follows in the present study:

$$Y_c = \frac{Y_{CO_2}}{W_{CO_2}} + \frac{Y_{H_2O}}{W_{H_2O}} + \frac{Y_{H_2}}{W_{H_2}}, \tag{7.6}$$

where W and Y are the molar mass and mass fraction, respectively. Normalization of Y_c leads to C:

$$C = \frac{Y_c - Y_c^u}{Y_c^b - Y_c^u}, \tag{7.7}$$

where the superscripts b and u respectively represent the burnt and unburnt status. To avoid confusion, in this paper we refer to Y_c as progress variable and to C as scaled progress variable. A transport equation for the unscaled progress variable Y_c is solved in this study, since this avoids the necessity of modeling extra source terms appearing in the transport equation of scaled progress variable C.

The influence of turbulence fluctuations on the local flame structure is accounted for through the joint PDF of the independent variables. The Favre-averaged/filtered scalar ϕ, e.g. T, Y_i, are calculated as:

$$\tilde{\phi} = \int_0^1 \int_0^1 \phi(Z,C)\tilde{P}(Z,C)dZdC. \tag{7.8}$$

The Reynolds-averaged/filtered mean of scalar $\bar{\phi}$ and density $\bar{\rho}$ can be computed as follows:

$$\bar{\phi} = \bar{\rho} \int_0^1 \int_0^1 \frac{\phi(Z,C)}{\rho(Z,C)} \tilde{P}(Z,C) dZ dC, \tag{7.9}$$

and

$$\bar{\rho} = \left[\int_0^1 \int_0^1 \frac{\tilde{P}(Z,C)}{\rho(Z,C)} dZ dC \right]^{-1}, \tag{7.10}$$

where $\tilde{P}(Z,C)$ is the joint PDF of mixture fraction and scaled progress variable. It is possible to directly calculate the joint PDFs with transported PDF method, which eliminates any assumption on the shape of the joint PDFs [26]. Alternatively, a presumed PDF method can be adopted, in which the PDFs are assumed to obey a certain shape which can be determined by the first and second moments of the controlling parameters. In this study the latter approach, namely the FGM / presumed PDF method is used. It is a common practice to assume that Z and C are statistically independent of each other, namely

$$\tilde{P}(Z,C) = \tilde{P}(Z)P(C). \tag{7.11}$$

Information for the second moment of mixture fraction, namely its variance $\widetilde{Z''^2}$ has to be provided in order to calculate $\tilde{P}(Z)$ and use it for table lookup.

$$\frac{\partial \bar{\rho} \widetilde{Z''^2}}{\partial t} + \frac{\partial \bar{\rho} \tilde{u}_j \widetilde{Z''^2}}{\partial x_j} = \frac{\partial}{\partial x_j} \left[\bar{\rho} \left(\tilde{D} + D_t \right) \frac{\partial \widetilde{Z''^2}}{\partial x_j} \right] + C_g \bar{\rho} D_t \left(\frac{\partial \tilde{Z}}{\partial x_j} \right)^2 - C_{d,Zv} \bar{\rho} \tilde{s}_{\chi_Z} \tag{7.12}$$

C_g and $C_{d,Zv}$ are model constants for the generation and dissipation terms of mixture fraction variances, respectively. C_g is set to its theoretical value 2. $C_{d,Zv}$ is set to 2 in the URANS simulation. In the LES simulation, a dynamic algebraic model is used for the SGS variance of mixture fraction.

$$\widetilde{Z''^2} = C_{Zv} \Delta^2 \left(\frac{\partial \tilde{Z}}{\partial x_i} \right)^2. \tag{7.13}$$

The model constant C_{Zv} is computed dynamically [37].

The evaporation of droplets can influence the (SGS) variances of the controlling parameters, a model for the mixture fraction variance source term due to evaporation is proposed by Pera et al [38]. In the present study, this effect is neglected, because the resolution of the current LES simulation is sufficiently high, and the influences of SGS variance are expected to be small.

$\bar{S}_\rho$, $\bar{S}_{u_i}$ and $\bar{S}_Z$ in Eqs.(7.1) to (7.3) are respectively the source term for density ρ, momentum and mixture fraction Z due to droplet evaporation. Models for these terms will be provided in the following subsection.

7.2.2. SPRAY SUB-MODELS

For practical spray combustion, the droplet drag force and the gravitational force are dominant compared to other forces, for instance the buoyancy force and Basset force.

Therefore the particle momentum equation, also known as BBO (Basset-Boussinesq-Ossen) [39], is greatly simplified:

$$\frac{dU_{\mathrm{p},i}}{dt} = \frac{U_{\mathrm{seen},i} - U_{\mathrm{p},i}}{\tau_{\mathrm{p}}} + g_i. \tag{7.14}$$

The droplet relaxation time τ_{p} is determined by:

$$\tau_{\mathrm{p}} = \frac{4}{3}\frac{\rho_{\mathrm{p}}}{\rho_{\mathrm{g}}}\frac{D_{\mathrm{p}}}{C_D|\mathbf{U}_{\mathrm{seen}} - \mathbf{U}_{\mathrm{p}}|}, \tag{7.15}$$

where ρ_{p} and ρ_{g} respectively refer to the liquid droplet and gas phase densities, and D_{p} is the droplet diameter. The drag coefficient C_D is given by the Schiller-Naumann semi-empirical correlation:

$$C_D = \begin{cases} \frac{24}{\mathrm{Re}_{\mathrm{p}}}\left(1 + 0.15\mathrm{Re}_{\mathrm{p}}^{0.687}\right), & \text{if } \mathrm{Re}_{\mathrm{p}} \leq 1000 \\ 0.44, & \text{if } \mathrm{Re}_{\mathrm{p}} > 1000 \end{cases} \tag{7.16}$$

with the droplet Reynolds number:

$$\mathrm{Re}_{\mathrm{p}} = \frac{\rho_{\mathrm{g}}|\mathbf{U}_{\mathrm{seen}} - \mathbf{U}_{\mathrm{p}}|D_{\mathrm{p}}}{\mu_{\mathrm{m}}}. \tag{7.17}$$

In the above equations and in the following, the subscript “seen” refers to the properties seen by the droplets (the undisturbed fluid flow properties at the position of the droplet center). In the present study, the “Seen" properties are obtained by interpolating cell values to the droplet location. The subscripts “p” and “g” respectively refer to droplet and gas-phase properties, subscript “m” refers to the properties of the film gas mixture and is evaluated according to the “1/3" rule.

The infinite conductivity model is employed for droplet evaporation. The temperature of droplets evolves as follows:

$$\frac{dT_{\mathrm{p}}}{dt} = \frac{\pi D_{\mathrm{p}}\lambda_{\mathrm{m}}\mathrm{Nu}}{m_{\mathrm{p}}C_{p,\mathrm{liq}}}\left(T_{\mathrm{seen}} - T_{\mathrm{p}}\right) + \frac{1}{C_{p,\mathrm{liq}}}\frac{L_v\left(T_{\mathrm{p}}\right)}{m_{\mathrm{p}}}\dot{m}_{\mathrm{p}}. \tag{7.18}$$

The mass transfer rate is given as:

$$\frac{dm_p}{dt} = \pi D_p Sh\mathscr{D}_{\mathrm{vap}}\rho_g ln\left(1 + B_M\right). \tag{7.19}$$

Nusselt number Nu and Sherwood number Sh are used to consider the convective effect on heat and mass transfer, and are calculated according to the well known Ranz and Marshall correlation:

$$\mathrm{Nu} = 2 + 0.552\mathrm{Re}_{\mathrm{p}}^{1/2}\mathrm{Pr}_{\mathrm{m}}^{1/3}, \quad \text{and} \quad \mathrm{Sh} = 2 + 0.552\mathrm{Re}_{\mathrm{p}}^{1/2}\mathrm{Sc}_{\mathrm{m}}^{1/3}, \tag{7.20}$$

where Sc_{m} and Pr_{m} are the Schmidt and Prandtl number respectively.

Bird's correction [40] can be applied for Nu to account for the reduction of heat transfer due to evaporation:

$$\mathrm{Nu}' = \mathrm{Nu}\frac{\beta}{e^{\beta}-1}, \quad \text{and} \quad \beta = -\frac{C_{p,\mathrm{vap}}\dot{m}_{\mathrm{p}}}{\pi D_{\mathrm{p}}\lambda_{\mathrm{m}}\mathrm{Nu}}. \tag{7.21}$$

To apply correction (7.21), the Nu in Eq. (7.18) should be replaced by Nu'. Abramzon and Sirignano [41] proposed modified Nusselt and Sherwood numbers, Nu^*, Sh^*, deduced from "film theory", to account for the boundary layer thickening effect by the Stefan flow. The modified Sherwood and Nusselt numbers are obtained iteratively from:

$$\mathrm{Sh}^* = 2 + \frac{\mathrm{Sh}-2}{F_M}, \quad \text{and} \quad \mathrm{Nu}^* = 2 + \frac{\mathrm{Nu}-2}{F_T}. \tag{7.22}$$

$$F_M = (1+B_M)^{0.7}\frac{\ln(1+B_M)}{B_M}, \quad \text{and} \quad F_T = (1+B_T)^{0.7}\frac{\ln(1+B_T)}{B_T}. \tag{7.23}$$

$$B_T = (1+B_M)^{\phi} - 1, \quad \text{with} \quad \phi = \frac{C_{p,\mathrm{vap}}}{C_{p,\mathrm{m}}}\frac{\mathrm{Sh}^*}{\mathrm{Nu}^*}\frac{\mathrm{Pr}_{\mathrm{m}}}{\mathrm{Sc}_{\mathrm{m}}}. \tag{7.24}$$

B_M is the Spalding mass transfer number and is calculated as following:

$$B_M = \frac{X_{vap,surf} - X_{vap,seen}}{1 - X_{vap,seen}}, \tag{7.25}$$

Note here the Spalding mass transfer number is defined by the mole fraction instead of mass fraction as commonly done.

The vapor mole fraction at surface is obtained according to Raoult's law:

$$X_{vap,surf} = X_{vap,seen}\frac{p_{sat}(T_{\mathrm{p}})}{p_a} \tag{7.26}$$

where $X_{vap,seen}$ is the vapor mole fraction "seen" by the droplet in the surrounding gas. p_{sat} is the vapor saturation pressure at droplet temperature, and p_a the ambient pressure.

Evaluation of source terms due to evaporation in Eqs.(7.1) to (7.3) are given in Table. 7.1. In this table, V_c is the volume of a computational cell, and N_p is the number of droplets represented by a parcel.

Table 7.1: Sources terms due to evaporation

Source	Expression
$\bar{S}_{\rho}$	$-\frac{1}{V_c}\sum_p \dot{m}_p N_p$
$\bar{S}_{u_i}$	$\frac{1}{V_c}\sum_p m_p N_p\left[\left(U_{p,i}^{t_n+\Delta t} - U_{p,i}^{t_n}\right)/\Delta t - g_i\right] - \frac{1}{V_c}\sum_p \dot{m}_p N_p U_{p,i}^{t_n}$
$\bar{S}_Z$	$-\frac{1}{V_c}\sum_p \dot{m}_p N_p$

7

7.3. ENTHALPY DEFICIT IN FGM

Our previous study [26] suggested that an adiabatic FGM table predicts high gas phase temperature in the region where intense droplet evaporation takes place, and the enthalpy deficit effect has to be considered in order to improve the prediction. To take into account the enthalpy deficit effect in the context of FGM implies two steps. First, creating the FGM libraries with different levels of heat loss, and parameterizing these different libraries with an additional parameter. Second, obtaining this parameter during the turbulent combustion simulation, and using it for table lookup.

7.3.1. NON-ADIABATIC FGM LIBRARY

In the present study, we adopt the second method as listed in section 7.1 to create the non-adiabatic FGM library. In order to create the FGM library, a counter-flow diffusion flame is solved in physical space with CHEM1D [42]. The enthalpy loss effect is imposed by decreasing boundary temperature (enthalpy) at the oxidizer side. Different methods exist for the construction of the 2D FGM lookup table. A commonly used one is to first calculate different steady flamelet equations with scalar dissipation rate increasing from a very small value to the extinguishing value. These steady flamelets are then mapped in (Z, Y_c)-space together with the unsteady extinguishing flamelet solution [43]. Another approach is to solve the unsteady process of a 1D diffusion flame in physical space from pure mixing until the steady flame is established under constant scalar dissipation rate χ_{ign}. The flamelet solution at different time is then transformed into (Z, Y_c)-space. To include the equilibrium state, steady flamelets with scalar dissipation rate lower than χ_{ign} can also be combined with these igniting unsteady flamelets. FGM libraries generated from these two approaches are respectively referred to as “Extinguishing FGM" (EFGM) and “Igniting FGM" (IFGM) in this study. Fig. 7.1 illustrate the construction process of these two different FGM libraries.

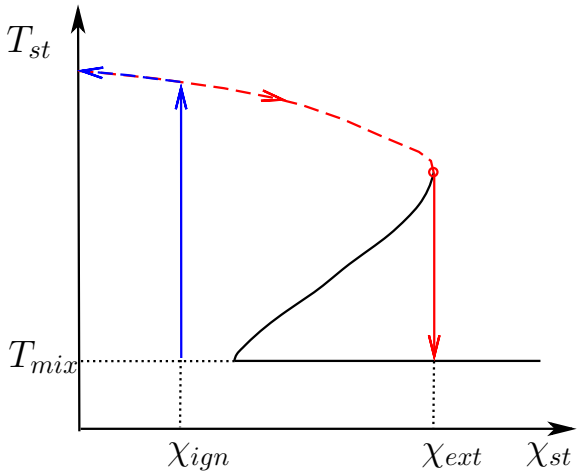

Figure 7.1: Construction process of EFGM (red) and IFGM (blue), dashed parts represent the steady flamelets at different χ_{st} and solid arrows are the unsteady flamelets at constant χ_{st}.

EFGM and IFGM libraries with different oxidizer boundary temperature T_o are shown in Fig 7.2, source term of progress variable in (Z,Y_c) space is shown in Fig. 7.3. Differences between the adiabatic and non-adiabatic FGM tables are obvious. The peak temperature and the progress variable source term are decreased with enthalpy loss. The area with high progress variable source term in the (Z,Y_c) space is greatly reduced. The differences between EFGM and IFGM lie in many aspects, among which the most noticeable one is the distribution of the Y_c source term in (Z,Y_c) space. For IFGM, reactions mainly take place at near stoichiometric values ($Z_{st} = 0.045$), whereas, for EFGM, large Y_c source term is found in a wide range of Z up to quite rich conditions ($Z = 0.2$). For IFGM, when $T_o = 1000\ K$, no significant temperature rise was observed within 2 s after the inert mixing during the calculation of unsteady igniting flamelets (at $\chi_{st} \approx 2\ s^{-1}$). However, when $T_o = 1400\ K$, ignition starts within less than 1 ms at the same scalar dissipation rate. This indicates that the ignition delay time increases quickly with the enthalpy loss. However, in the EFGM, since the table is built on the steady flamelet at low saclar dissipation rate and unsteady flamelet at extinguishing value, no “ignition time" information is included in the table. This feature of EFGM has some further influences when it is applied for simulation of auto-igniting flame. We will revisit this issue at the results section.

The parameter, normalized enthalpy deficit η_h, is introduced to index the FGM libraries from the adiabatic state ($\eta_h = 0$) to the one with maximum heat loss ($\eta_h = 1$). Note that here we use absolute (or total) enthalpy. In the case of equal diffusivity of all species and enthalpy, a state in the FGM library with a certain enthalpy deficit, can be uniquely represented with one enthalpy value at a certain mixture fraction as indicated in Fig. 7.4, because absolute enthalpy does not change with reaction progress. Here we use the value at $Z = 0$. The normalized enthalpy deficit η_h is defined as follows:

$$\eta_h = \frac{dh\,|_{Z=0}}{h_m\,|_{Z=0} - h_{ad}\,|_{Z=0}}. \tag{7.27}$$

Where $h_{ad}\,|_{Z=0}$ and $h_m\,|_{Z=0}$ are respectively the enthalpy of the adiabatic state in the FGM library and the one with maximum enthalpy loss when $Z = 0$, see Fig. 7.4 for illustration. The FGM table is now three dimensional, namely properties are depending on Z, C, and η_h:

$$\tilde{\phi} = \int_0^1 \int_0^1 \int_0^1 \phi(Z,C,\eta_h)\tilde{P}(Z,C,\eta_h)dZdC. \tag{7.28}$$

Statistical independence of the controlling parameters is assumed:

$$\tilde{P}(Z,C,\eta_h) = \tilde{P}(Z)P(C)P(\eta_h). \tag{7.29}$$

β-function PDF was found to be also a good representation of mixture fraction PDF in spray combustion by a DNS study [44], therefore it is used in this study. δ-function is used for PDFs of both C and η_h. The resulted pdf-integrated FGM libraries become four dimensional:

$$\tilde{\phi} = \phi\left(\tilde{Z},\widetilde{\zeta_Z},\tilde{C},\widetilde{\eta_h}\right) \tag{7.30}$$

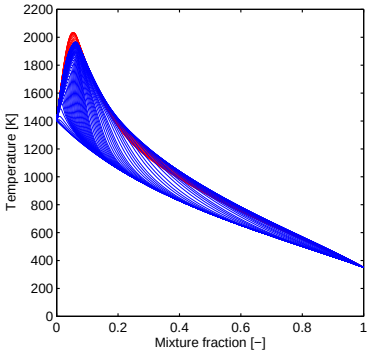

(a) IFGM ($a = 100\ s^{-1}$), $T_o = 1400K$

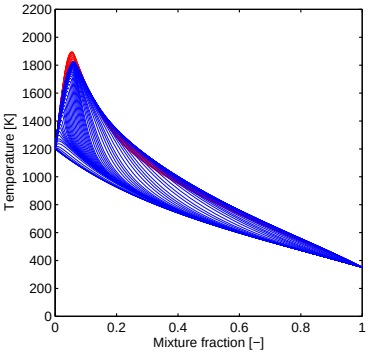

(b) IFGM ($a = 100\ s^{-1}$), $T_o = 1200K$

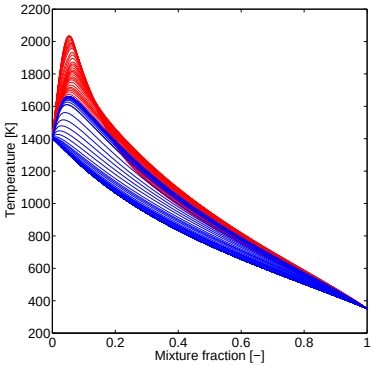

(c) EFGM, $T_o = 1400K$

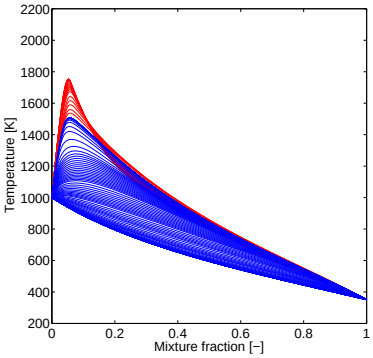

(d) EFGM, $T_o = 1000K$

Figure 7.2: Temperature profile in mixture fraction space for IFGM (top) and EFGM (bottom). Red lines are the steady flamelets (dashed part in Fig. 7.1) and blue lines are the unsteady flamelets (solid part in Fig. 7.1).

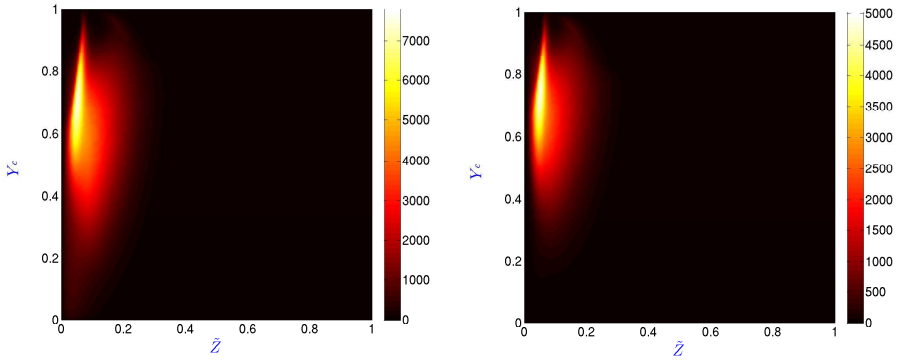

(a) IFGM, $T_o = 1400K$

(b) IFGM, $T_o = 1200K$

(c) EFGM, $T_o = 1400K$

(d) EFGM, $T_o = 1000K$

Figure 7.3: Progress variable source term in $Z - Y_c$ space, for EFGM and IFGM.

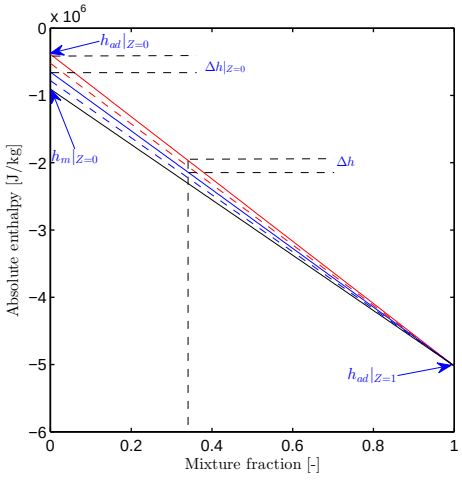

Figure 7.4: Enthalpy as function of mixture fraction for FGM tables with different T_o, $T_o = 1400K$: ——, $T_o = 1300K$: - - -, $T_o = 1200K$: ——, $T_o = 1100K$: - - -, $T_o = 1000K$: ——.

7.3.2. LOOKUP PROCEDURE

During the turbulent combustion simulation, transport equations (or algebraic models) are solved to obtain $\tilde{Z}$, $\widetilde{\zeta_Z}$ and $\tilde{C}$, see [37] for more details. As for η_h, some extra steps are required. A transport equation for enthalpy is firstly solved to obtain the local mean enthalpy.

$$\frac{\partial \bar{\rho}\tilde{h}}{\partial t} + \frac{\partial}{\partial x_i}\left(\bar{\rho}\tilde{u}_i\tilde{h}\right) = \frac{Dp}{Dt} + \frac{\partial}{\partial x_i}\left[\alpha_{eff}\frac{\partial \tilde{h}}{\partial x_i}\right] + \bar{S}_h \tag{7.31}$$

where $\alpha_{eff} = \mu_{eff}/\mathrm{Pr}_t$ is the effective thermal diffusivity for enthalpy, including laminar and turbulent effects, Pr_t the turbulent Prandtl number, set to 0.7. The local adiabatic enthalpy, $\tilde{h}_{ad}$, is calculated from $h_{ad}|_{Z=0}$, $h_m|_{Z=0}$ and the local mean mixture fraction $\tilde{Z}$ making use of the linear relation of enthalpy with mixture fraction, as shown in Fig. 7.4. Then the local enthalpy deficit can be obtained by:

$$\Delta\tilde{h} = \tilde{h} - \tilde{h}_{ad} \tag{7.32}$$

The enthalpy deficit at $Z = 0$ can be computed as follows:

$$\Delta\tilde{h}|_{Z=0} = \begin{cases} \frac{\Delta\tilde{h}}{1-\tilde{Z}}, & 0 \le \tilde{Z} < 1 \\ 0, & \tilde{Z} = 1 \end{cases} \tag{7.33}$$

Finally, the $\widetilde{\eta_h}$ is obtained from Eq. (7.27). Since the enthalpy changes linearly with mixture fraction for a certain flamelet at the same enthalpy deficit level, there is no need to pdf-integrate the enthalpy. The mean enthalpy equals the enthalpy at mean mixture fraction.

Now the procedures for creating FGM library with enthalpy loss, and to obtain the extra parameter to lookup this FGM table are clear. Before it can be applied to simulation, another question still has to be answered, namely, how many slices of FGM table with different levels of enthalpy loss have to be included in the final FGM library? A low number is preferred, because the table size grows linearly with this number. In Fig. 7.5, we plot the variations of several properties as function of η_h. These plots helps to clarify two things: first, to take into account the effect of enthalpy loss by frozen species and only decrease temperature (method 1) is not a good choice, because the species are also influenced by the enthalpy loss, especially the source term of progress variable. Second, assuming that properties change piecewise-linearly with η_h, only store a few, e.g. three, layers of FGM tables at different extent of enthalpy loss, and do linear interpolation in between theses layers during simulation for EFGM is acceptable. Since the temperature and species mass fraction change near linearly with enthalpy deficit in EFGM. The errors for the progress variable source term are also not large. In the following simulations, three FGM tables corresponding to $\eta_h = 0$, 0.5 and 1, respectively, will be used to construct the non-adiabatic EFGM table. For IFGM, at relative large strain rate ($a = 100\ s^{-1}$), no ignition takes place for the FGM at $\eta_h = 1.0$, corresponding to $T_o = 1000\ K$. Therefore a sharp decrease of properties is experienced when η_h goes beyond 0.5. This causes stability issues for the LES simulations using dynamic Smagorinsky model when this FGM library is used. At small strain rate ($a = 5\ s^{-1}$), ignition does happen at highest enthalpy loss. The temperature in the IFGM with low strain rate is very similar to that in the EFGM.

But large differences exist in the species mass fraction and source term of progress variable. To compare with the EFGM, two IFGM libraries respectively at strain rate 5 s^{-1} and 100 s^{-1} have been both generated with only three layers of enthalpy deficit in the current study. The results from these three FGM libraries (one EFGM and two IFGMs at different strain rate) will be compared in section 7.6.2.

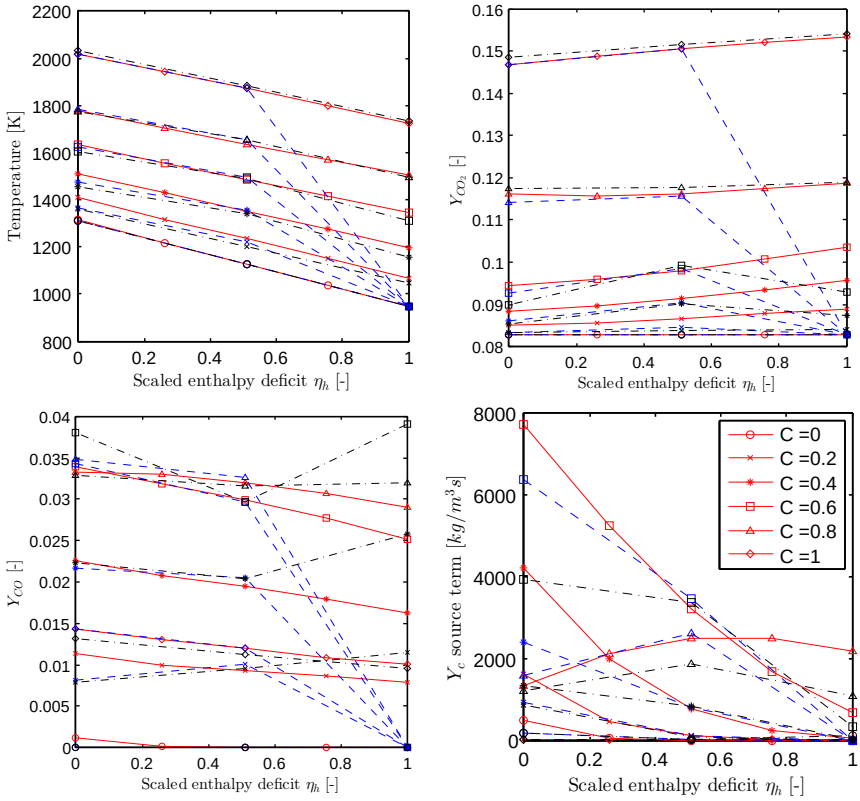

Figure 7.5: Change of FGM properties with enthalpy loss at Z_{st} and different C, red solid line: EFGM, blue dashed line: IFGM (a=100 s^{-1}), black dash-dotted line: IFGM (a=5 s^{-1}). Different symbols indicate different value of scaled progress variable C, shown in the bottom right figure.

7.4. SPRAY BOUNDARY CONDITIONS

A common practice in spray combustion study is to neglect the dense region, and only focus on the dilute spray regime [14]. The advantage of this approach is to avoid the complex phenomena such as liquid sheet breakup, ligament formation, droplet collision and possibly cavitation within the spray nozzle. In our previous study, the diluted spray approach has been employed [26]. With precise droplet boundary conditions specified at 8 mm downstream of the injector according to experimental data, the measured properties further downstream can be reproduced with very good accuracy. However, a simulation including the droplet formation process will be of more practical interest, because

the dense region can not be avoided in reality. For the DSHC flame, the spray is injected with high velocity (bulk velocity $U_p \approx 30\ m/s$) into low velocity coflow $U_{cf} = 2.5\ m/s$, leading to a strong two-way coupling effect in the near injector region. Also due to the presence of high temperature coflow, a significant amount of fuel vapor is already formed before the first measurement transverse ($\mathscr{Z} = 8\ mm$). These together make a dilute spray simulation starting from the first measured station difficult, because accurate information on the gas phase velocity, fuel vapor amount and spatial distribution have to be provided. In [26], these informations were obtained from a previous simulation which also considered the dense region [45]. In the present study, we still use the dilute spray approach. But based on an analysis of phenomena in the dense region and on available experimental data, we propose a refined formulation of the droplet injection process, providing accurate spray boundary conditions.

7.4.1. FLASH-BOILING ATOMIZATION

In the DSHC burner, the liquid fuel is injected into the coflow by a hollow-cone pressure-swirl atomizer. As reported by Rodrigues et al [12], the atomization mechanism is significantly changed from the conventional spray flame to those under hot-diluted coflow condition. Fig. 7.6 shows the near field visualization of the atomization process for cold and hot coflow conditions. A development of sinuous waves on the surface of liquid sheet followed by formation of toroidal structures, lobes and small droplets can be clearly observed in the cold coflow case. Whereas, for the hot coflow case, no wave growth is evident and liquid jet immediately disrupts after leaving the nozzle exit. A fast radial expansion at the vicinity of injector exit is also clear compared to the conical sheet development in the cold case. Readers are referred to the supplementary videos of [12] for further visualization of the atomization process of the spray under cold and hot coflow condition. This change of atomization mechanism was explained in [12] to be caused by the thinned liquid sheet due to fast evaporation. However, further analysis shows that the occurrence of flashing boiling can be a better explanation for this phenomenon. The cooling system surrounding the fuel pipe ends a few centimeters upstream of the exit of the pipe (See Fig. 1.3). Due to the heat received from the hot coflow surrounding the fuel injector, the liquid fuel inside the atomizer chamber may become superheated. The vapor saturation pressure increases with liquid temperature. Once it exceeds local static pressure (decreases when the liquid is accelerated in the atomizer nozzle), cavitation can occur within the atomizer chamber generating vapor bubbles. When this partially vaporized liquid fuel leaves the injector orifice, explosive expansion can happen due to low ambient pressure. This process is referred to as flash-boiling atomization [46, 47]. The occurrence of flash-boiling atomization in DSHC flame will be further evidenced by the following analysis.

First of all, the Weber number of the spray is 0.46 in this case [12]. According to Senecal et al [48], with this low We, the liquid sheet will breakup in “long wave" regime, and resulting in much longer breakup length and much larger droplet size compared to those measured in the DSHC flame. This means that the growth of Kelvin–Helmholtz (KH) wave on the liquid interface is no longer the dominant mechanism for the primary breakup in the DSHC flame case. The immediate disintegration of liquid jet is most probably triggered by the explosive growth of vapor bubble formed within the atomizer

nozzle.

In Fig. 7.7, the measured velocity vector for large droplets ($40\ \mu m < D_p \leq 50\ \mu m$) is presented. The movement of a large droplet is expected to be more or less ballistic because of the high inertia, which is indeed the case as will be shown in section 7.6.5. With the red-dashed lines in Fig. 7.7 we try to extrapolate droplet trajectories at outer side of the spray cloud back to the injector plane. It seems that the droplets at the edge of the spray cloud came from a radial location at $\mathscr{Z} = 0\ mm$ that is much larger than the atomizer exit diameter ($0.21\ mm$). This is a clear evidence for the explosive expansion at the exit of the atomizer.

Reitz [47] found from experimental study that, when flash-boiling occurs, the flow discharge coefficient can be decreased. In the case considered here, the injection pressure $p_{ij} = 11.5\ bar$, the liquid fuel mass flow rate is $\dot{m}_l = 1.46\ kg/h$, and the injector exit diameter $D_{ij} = 0.21\ mm$. The flow discharge coefficient can be calculated as follows:

$$C_d = \frac{\dot{m}_l}{A\sqrt{2\rho_l \Delta p}}, \tag{7.34}$$

where $\Delta p = p_{ij} - p_{atm} = 10.5\ bar$ is the net injection pressure, $p_{atm} = 1\ bar$ is the atmospheric pressure, and $\rho_l = 785\ kg/m^3$ is the density of ethanol at temperature $300\ K$, A the area of the injector exit. The value of C_d calculated using Eq. (7.34) is 0.288 for the considered hot coflow case, and 0.323 for the cold coflow case (case Aii in [12]). The discharge coefficient is indeed decreased in the hot coflow case, very likely due to the cavitation within the atomizer chamber. Note that the experimental injection pressure is questionable, as will be further discussed later, here the calculated discharge coefficient is only used to make a qualitative comparison, since the same experimental setup and measure technique has been used to both cases.

It was observed in both [46] and [47] that when flash-boiling atomization happens, the spray angle increases. To have some idea about the droplet distribution and movement after the flash-boiling atomization, available experimental data is mined. The first measured station is 8 mm downstream the atomizer. While trajectories of small droplets have already been significantly influenced by surrounding gas when traveling from $\mathscr{Z} = 0$ to $\mathscr{Z} = 8\ mm$, large droplets keep their initial injection direction for the same reason as explained above. Information on these large droplets at $\mathscr{Z} = 8\ mm$ provides valuable insight on the atomization process upstream and will be used in the characterization of the spray boundary condition. The axial and radial velocity of droplets have been simultaneously measured. We define here the droplet trajectory angle based on its axial and radial velocity, $U_{p,z}$ and $U_{p,r}$:

$$\theta = arctan(\frac{U_{p,r}}{U_{p,z}}). \tag{7.35}$$

The scatter plot and mean value of size-conditional droplet trajectory angle is given in Fig. 7.8. As can be clearly seen, the mean trajectory angle for large droplets converges to about 40° as droplet size increases, this angle can be interpreted as the spray half angle (mean droplet initial injection angle). This value is apparently larger than the nominal spray half angle — 30° [12].

In summary, we can conclude that the atomization of the liquid fuel for the DSHC burner is greatly influenced by the flash-boiling. Main proofs are: first, growth of KH instability wave on the liquid interface is no longer the dominant mechanism for atomization according to the low We, short breakup length and fine droplet size; second, the immediate disintegration of liquid sheet at the exit of atomizer and increased spray cloud radial width due to explosive expansion; last but not least, the enlarged spray angle.

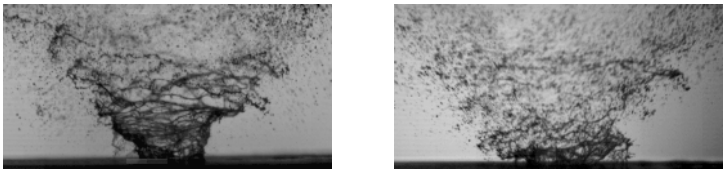

Figure 7.6: Atomization of liquid fuel under cold (left) and hot (right) coflow conditions, field-of-view dimensions, $6.8 \times 3.04\ mm^2$ [12].

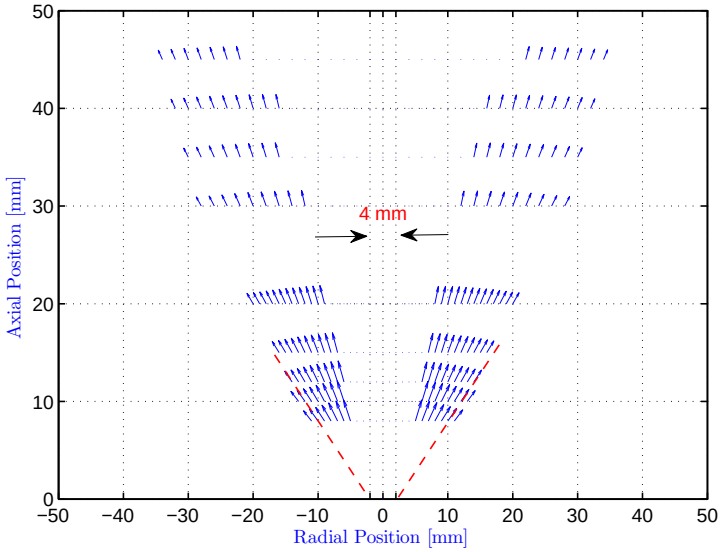

Figure 7.7: Velocity vector of measured large droplets ($40\ \mu m < D_p \leq 50 \mu m$).

7.4.2. MODELING ISSUES

The flash-boiling during the atomization has the following consequences on the downstream droplets distribution and combustion:

- The breakup length of liquid sheet is greatly shortened.
- Smaller droplet size and wider radial distribution.

- Changed trajectories of small droplets due to expulsion effect.
- Higher droplet temperature, and quick evaporation in the near injector region.

These effects impose difficulties on modeling the atomization process with conventional models. The Linearized Instability Sheet Atomization (LISA) model has been widely used for modeling the atomization of pressure-swirl atomizer. However, due to the changed atomization mechanism, the LISA model is not anymore applicable in the DSHC case. Zuo et al [16] proposed a modification for LISA model to take into account the flash boiling effect. However, in that modification, the droplet temperature is allowed to rise up to the critical value, which may cause convergence problems in the simulation due to the sharp variation of properties near the critical point. Furthermore, the original LISA model was established based on the KH wave growth theory, which as explained above is not the dominant mechanism for the primary breakup in this case. Therefore, a formulation based on LISA model in order to model this flash-boiling atomization is theoretically less sound. As an alternative approach, in this study, we ignore the primary breakup of the spray, and directly inject droplets into the domain. While doing so, special attention is paid on the providing of accurate droplet injection position, injection angle and initial droplet velocity and size distribution according to all available experimental data.

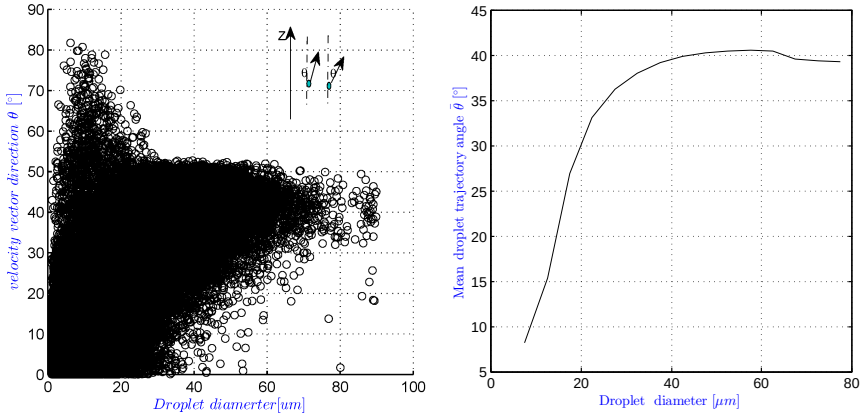

Figure 7.8: Scatter plot (left) and conditional average (right) of droplet trajectory angle from experimental data.

7.4.3. CONDITIONAL DROPLET INJECTION MODEL

Before proceeding to further discussion, we first define the spray half angle, θ_S, the minimum and maximum spray injection angle, θ_{min} and θ_{max}, as illustrated in Fig. 7.9. In many cases, the spray dispersion angle, θ_D is used, it is related to the θ_{min} and θ_{max} by $\theta_D = \theta_{max} - \theta_{min}$. The mean droplet trajectory angle in Fig. 7.8 indicates that 40° is the actual spray half angle in this case. In most studies, the spray cloud is assumed to be symmetric around the spray half angle, namely $\theta_{max} - \theta_S = \theta_S - \theta_{min}$. However, as indicated in the scatter plot of Fig. 7.8, this is clearly not the case for the DSHC flame. The dispersion of the spray cloud shows a strong asymmetric behavior in this case. This

asymmetric behavior is also droplet size (mass) dependent. Small droplets move in almost any direction, while large droplets are shooting along a narrower range of angles around 40°. The maximum angle for droplets larger than $20\mu m$ is almost constant; the minimum value however linearly increases with droplet size.

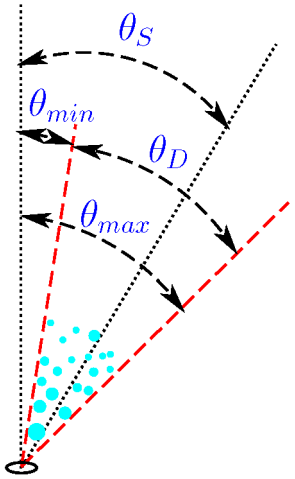

Figure 7.9: Illustration of spray half angle, θ_S, minimum and maximum possible injection angle, θ_{min} and θ_{max}, and dispersion angle, θ_D.

To take into account the aforementioned conditional injection effects, we propose the following correlations for droplet injection direction:

$$\theta_p = \begin{cases} \theta_{min,p}\left(D_p\right) + 2\Lambda\left[\theta_S - \theta_{min,p}\left(D_p\right)\right], & 0 \le \Lambda < 0.5 \\ \theta_S + (2\Lambda - 1)\left[\theta_{max,p}\left(D_p\right) - \theta_S\right], & 0.5 \le \Lambda \le 1 \end{cases} \tag{7.36}$$

where Λ is a random variable in the range $[0,1]$, $\theta_{min,p}$, $\theta_{max,p}$ are respectively the minimum and maximum possible injection angle dependent on droplet size D_p:

$$\theta_{min,p}\left(D_p\right) = \theta_{min,S} + \frac{D_p - D_{p,mid}}{D_{p,L} - D_{p,m}}\left(\theta_{min,L} - \theta_{min,S}\right), \tag{7.37a}$$

$$\theta_{max,p}\left(D_p\right) = \theta_{max,S} + \frac{D_p - D_{p,mid}}{D_{p,L} - D_{p,m}}\left(\theta_{max,L} - \theta_{max,S}\right). \tag{7.37b}$$

$\theta_{min,S}$, $\theta_{max,S}$, $\theta_{min,L}$, $\theta_{max,L}$ are respectively the possible minimum and maximum injection angle for small and large droplets. $D_{p,m}$ is the droplet diameter, larger than which the range of droplet injection angle will decrease, and $D_{p,L}$ is the largest droplet diameter. The values of these parameters are summarized in Table. 7.2, and they are estimated for experimental data shown in Fig. 7.8.

To take into account the influence of the radial expansion at the exit of the injector, the droplet injection position is randomly chosen within a circle centered at the origin

Table 7.2: Parameters for determining size-conditional droplet injection angle.

$\theta_{min,S}$	$\theta_{max,S}$	$\theta_{min,L}$	$\theta_{max,L}$	$D_{p,m}$	$D_{p,L}$
20°	50°	35°	45°	40 μm	80 μm

($\mathscr{Z} = r = 0\ mm$), which is referred to as injection disc hereafter. The diameter of the injection disc is set to 2 mm, 10 times larger than the nominal atomizer exit diameter.

Having determined the droplet injection direction and position, the next step is to determine the injection velocity. The bulk velocity of the liquid fuel can be estimated as follow:

$$U_l = \frac{\dot{m}_l}{\rho_p C_d A} \tag{7.38}$$

However, using the discharge coefficient calculated from Eq. (7.34), we get $U_l = 51.7\ m/s$. Simulation showed that using this as the droplet initial injection velocity, the downstream velocity will be significantly over-predicted. Note that in the experiment [12], the injection pressure was measured upstream the liquid fuel supply pipe, rather than directly in the atomizer chamber. The real injection pressure may be much lower than the reported one due to pressure drop in the fuel pipe. In the present study, a injection pressure $p_{ij} = 6\ bar$ is used, resulting in the fuel bulk velocity of $U_l = 35.7 m/s$. This value is leading to a good match between the predicted and experimental droplet velocity, as will be shown in section 7.6.

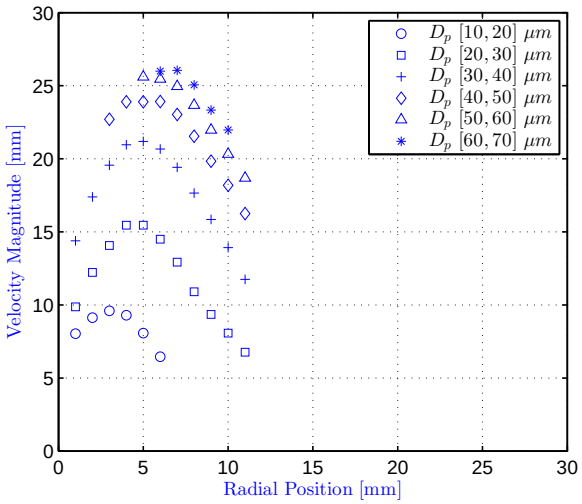

Figure 7.10: Magnitude of droplet velocity at $\mathscr{Z} = 8\ mm$.

Fig.7.10 shows the magnitude of the measured droplet mean velocity at $\mathscr{Z} = 8\ mm$ for different size class. It is found that the droplet velocity magnitude peaks at the center of the spray cloud and decreases towards the edges. This observation is also consistent

with the findings in [47], in which it was found that even under flash-boiling atomization condition, an intact liquid core still exists. This liquid core is probably the reason for the peak velocity magnitude in the center of spray cloud. To reproduce this phenomena, the droplet initial velocity magnitude should be conditioned upon its injection direction. Two methods to scale droplet velocity along the cross section of the spray cloud are proposed as follows.

Scale method 1: linear scale. In this method, the droplet velocity magnitude is scaled linearly from $\left(1+\alpha_p\right)U_l$ at the center of spray cloud ($\theta_p = \theta_S$) to $\left(1-\alpha_p\right)U_l$ at the edge of spray cloud ($\theta_p = \theta_{min}$ or $\theta_p = \theta_{max}$), with α_p is a parameter.

$$U_{p,mag} = \left(1-2\eta_p\alpha_p+\alpha_p\right)\bar{U}_l. \tag{7.39}$$

Scale method 2: cosinus scale. In this method, the droplet velocity magnitude is scaled following a cosine shaped curve from $\left(1+\alpha_p\right)U_l$ at the center of spray cloud ($\theta_p = \theta_S$) to $\left(1-\alpha_p\right)U_l$ at the edge of spray cloud ($\theta_p = \theta_{min}$ or $\theta_p = \theta_{max}$).

$$U_{p,mag} = \left[1+\alpha_p cos\left(\eta_p\pi\right)\right]\bar{U}_l. \tag{7.40}$$

η_p is the scaled offset of droplet injection direction from the spray half angle, defined as:

$$\eta_p = \mid 1-2\Lambda \mid \tag{7.41}$$

Λ is the same random variable as in Eq.(8.6). $\eta_p = 0$ means droplet moves along the center of spray cloud trajectory, and $\eta_p = 1$ at the edge.

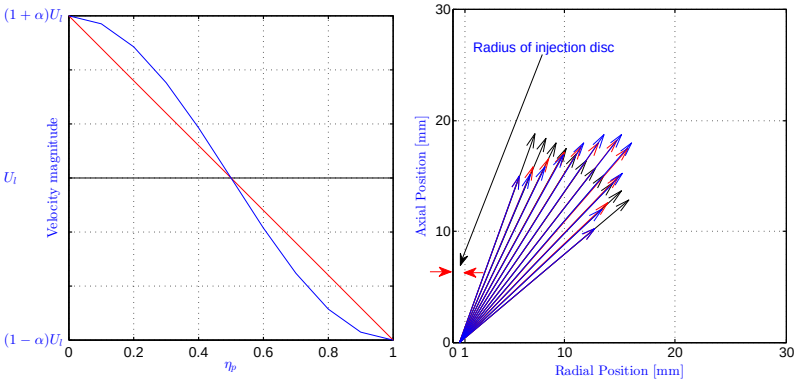

(a) (b)

Figure 7.11: Scale of droplet injection velocity magnitude (a) and illustration of the conditional droplet injection velocity (b). Black: no scale, blue: cosinus scale red: linear scale.

Fig. 7.11a compares the scaling of the droplet injection velocity magnitude with the two proposed methods. The “linear scale" provides a smoother change of velocity magnitude, and is applied in the present study with $\alpha_p = 0.05$. In summary, the proposed conditional droplet injection model is illustrated in Fig. 7.11b. Droplets are injected randomly at a location within the injection disc. The spray cloud is asymmetric around the

spray angle, namely the spray has a wider dispersion at the inner side of the spray angle and narrower dispersion at the outer side. The velocity magnitude is scaled such that the velocity peaks ($\left(1+\alpha_p\right)U_l$) at the spray half angle direction and reaches minimum ($\left(1-\alpha_p\right)U_l$) at the edges of spray cloud, Eq. (8.3) or (7.40). The possible angle of droplet injection direction is conditioned upon the droplet size (Eqs. (8.6) to (8.7b)). Smaller droplets have wider range of injection direction, while large droplets are injected in a small sector centered at the spray angle. We remark that the proposed model, which is introduced to represent effect of flash boiling on the initial spray structure, is sufficiently general to be used for representation of spray structure in the absence of flash boiling.

7.4.4. DROPLET SIZE DISTRIBUTION AT $\mathscr{Z} = 0\ mm$

Droplet initial size at the atomizer exit ($\mathscr{Z} = 0\ mm$) is specified as following:

$$D_{p,i} = D_{p,min} + \bar{D}_p \left[-ln\left(1-\Lambda K\right)^{\frac{1}{n}} \right], \tag{7.42}$$

with

$$K = 1 - e^{-\left(\frac{D_{p,max}-D_{p,min}}{\bar{D}_p}\right)^n} \tag{7.43}$$

$D_{p,min}$, $D_{p,max}$ and $\bar{D}_p$ are the minimum, maximum and mean droplet diameter after atomization, n is a constant. $D_{p,min}$, $D_{p,max}$ and $\bar{D}_p$ are obtained from experiment data, and the values of these parameters are given in Table. 7.3. The resulting PDF of droplet size at $\mathscr{Z} = 0\ mm$ obtained from 50000 samples is given in Fig. 7.12, in the form of a histogram with bin size 1.6 μm.

Table 7.3: Parameters for droplet initial size distribution.

$D_{p,min}$	$D_{p,max}$	$\bar{D}_p$	n
5 μm	80 μm	40 μm	3

7.5. NUMERICAL DETAIL

The simulation in this study is carried out using the open source CFD package — OpenFOAM [25]. New libraries have been created for the FGM storage and retrieval algorithms and are dynamically linked to a customized solver for spray combustion. The new solver is referred to as “sprayFGMFoam". A validation of the flow and combustion models of this new solver with gaseous auto-ignition flame is reported in [37]. sprayFGMFoam is based on the PIMPLE algorithm, a combination of PISO (Pressure implicit with splitting of operator) [49] and SIMPLE (Semi-Implicit Method for Pressure-Linked Equations) [50] algorithms. Transport equations for the controlling variables are solved after the velocity prediction step. Then necessary properties, e.g. $\tilde{T}$, $\bar{\mu}$ and $\overline{\dot{\omega}_{Y_c}}$, are retrieved from the FGM libraries with the newly obtained controlling variables. After this, the velocity-pressure correction is conducted within the PISO loop. One PIMPLE loop and three PISO loops are carried for each time step.

The transport equations are spatially discretized with a Finite Volume Method (FVM). The convection and Laplacian terms are discretized respectively by second-order accu-

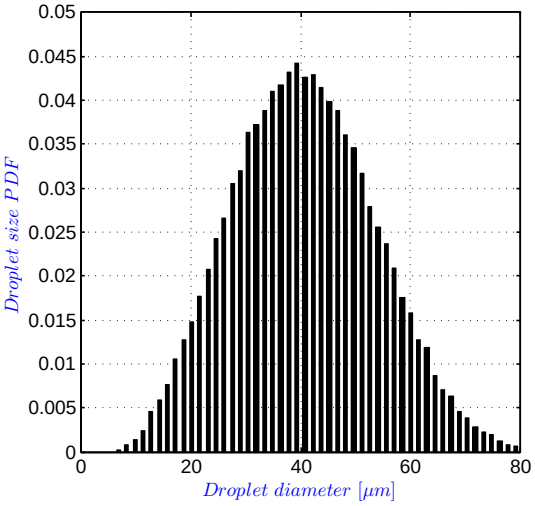

Figure 7.12: Droplet size PDF at $\mathcal{Z} = 0$ mm.

racy total variation diminishing (TVD) schemes Gauss vanLeer and Gauss vanLeer corrected. Implicit second-order method CrankNicholson is used for the temporal integration.

For both the URANS and LES cases, a 3D cylindrical mesh is used. The diameter of the numerical mesh is 200 mm, larger than the diameter of coflow (160 mm) to ensure correct momentum entrainment of the coflow. Two different values of length of the domain were tested, respectively 300 mm and 150 mm. From the simulation using the large mesh, it was observed that the axial gradient of many properties are already very small at 150 mm thanks to the low Reynolds number in this case. The results from these two different domains show no considerable difference. Therefore a shorter domain with length of 150 mm is used for the rest simulations. For the URANS simulation, the mesh has about 0.3 million cells. The smallest cell size is 0.6 mm at the near injector region, and the largest cell size is 3 mm and appears at the very end of the computational domain. The computational domain is initialized with coflow condition ($Z = 0$, $C = 0$ everywhere), and the droplet injection starts at $t = 0$ s. The ignition takes place by itself when sufficient fuel vapor has been produced and mixed with the oxidizer, because in this case the coflow temperature is high enough to have auto-ignition. Run-time adjustable time step was used, the maximum Courant number is limited to 0.5. The steady state is established within 0.05 s, and the total simulation time is 0.15 s.

For the LES, we have reached the limit of resolution both spatially and temporally. The axial direction is discretized with 250 grid points (short mesh, $L = 150$ mm), radial direction is discretized with 130 grid points and the circumferential direction is equally divided by 72 points, resulting in a total mesh size of 2.2 million. The cell size along axial and radial directions for the mesh used respectively for LES and URANS is given in Fig. 7.13. In LES, the smallest cell size is 0.3 mm at the near injector region, and is about four times the diameter of the largest droplet diameter, using a finer mesh may cause

statistical instabilities. A very small growth ratio of 1.004 is used for the stream-wise grid points in the LES mesh, leading to a uniformly fine mesh in the region of interest. The cell size is only 0.65 mm at 90 mm downstream the atomizer. The radial and circumferential grid points were set such that the aspect ratio is close to unity at the center region of $R < 80$ mm and $Z < 90mm$, which is the region where spray injection and reaction happens. The growth ratio is large in region of $R > 80$ mm, because no droplet exists there, and the flow is essentially laminar. The diameter of the flame at the highest measured elevation ($\mathcal{Z} = 60$ mm) is 50 mm, indicated by location of the peak on the measured temperature profile, fits well in the fine mesh region. The time step is set such that within each time step, only 10 parcels are injected. The corresponding maximum Courant number is about 0.4. The ratio between μ_{SGS} and μ (not shown here) in this LES is below unity in the whole domain. Based on these high temporal and spatial resolution, our LES can be referred to as high-fidelity LES.

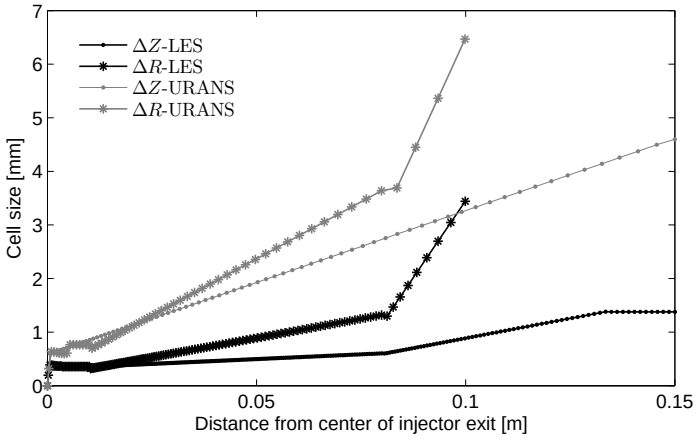

Figure 7.13: Mesh cell size along axial (ΔZ) and radial direction (ΔR) for the URANS and LES grid used in the current study.

It is computationally unaffordable to actually track each droplet during simulation, instead the concept of "parcel" is introduced. Each parcel represents a number of real droplets with identical properties. The parcels evolve like the real droplets (in terms of heat, mass and momentum transfer), but the influence on the gas phase is multiplied by N_p, the number of droplets that the parcel represents, see Table. 7.1.

7.6. RESULTS AND DISCUSSION

In this section, we analyze results from simulation and compare them with experimental data to verify and validate the proposed models. Droplet distribution at $\mathcal{Z} = 8$ mm and properties at various axial cross-sections are examined first in order to check the performance of the proposed conditional droplet injection model. Two configurations of FGM tables and two different droplet heat and mass transfer correction models are compared in subsection 7.6.2 in the context of URANS simulation. In subsection 7.6.3,

based on the information and confidence obtained from these URANS simulations, LES simulation with selected best combination of submodels are performed, and its results are compared with those of the corresponding URANS case to show the advantage of LES. Droplet-flame interaction is finally analyzed in 7.6.5 using the LES results.

7.6.1. CONDITIONAL VS. NON-CONDITIONAL DROPLET INJECTION

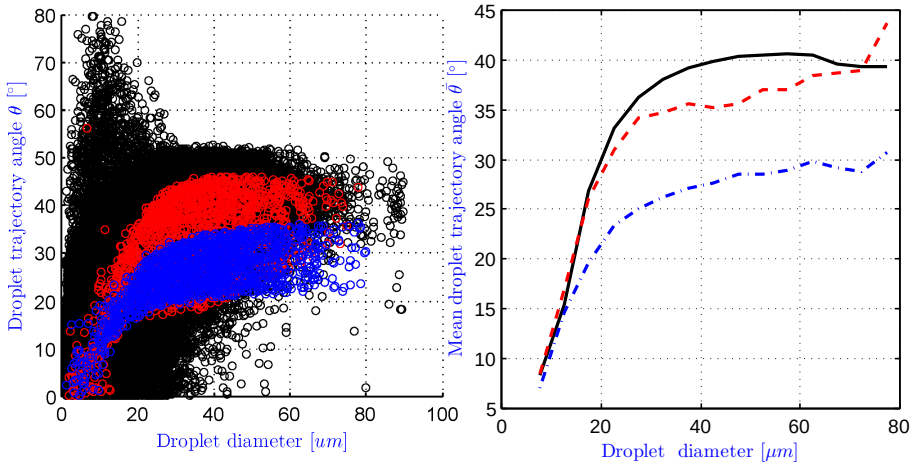

Figure 7.14: Scatter plot (a) and conditional averaged (b) droplet trajectory angle at $\mathcal{Z} = 8\ mm$. Black: experimental data, red: simulation with conditional droplet injection model, blue: simulation without conditional droplet injection model.

The scatter plot and conditional averaged droplet trajectory angle at Z = 8 mm from simulation have superimposed on the experimental data and are presented in Figs. 7.14a and 7.14b. It can be seen that main features observed in the experimental data such as the near constant maximum trajectory angle and linearly increasing of minimum trajectory angle for large droplets are well reproduced with the proposed conditional injection model. As expected, the trajectory angle for large droplets without the conditional injection is uniformly distributed between the specified maximum and minimum value. The averaged trajectory angle increases with droplet size in both simulation cases, reflecting the trend in the experimental data. However, without conditional injection, the mean trajectory angle for large droplets is greatly under-predicted, and with conditional injection, it is close to the experimental value of 40°. The trajectory angle of small droplets in both simulations is found to be concentrated in a relatively small range compared to experiment. This may be related to the numerical treatment of the droplets.

As mentioned before the droplets are represented by parcels, each representing N_p droplets. N_p can be determined in many ways. In this study, all parcels are assigned the same initial mass, and therefore N_p is inversely proportional to the mass of each droplet. In the simulation the number of parcels injected at each time step is calculated according to the experimental mass flow rate and the mass of largest droplets to be injected,

such that each parcel represents at least one real droplet. The resulting total number of parcels to be injected within one second is 1.9×10^6. This guarantees that the influence of a large droplet is not spatially divided. However, this has a negative influence on the representation of the dispersion of small droplets. Maintaining identical mass for each parcel, N_p values for parcels that represents smallest and largest droplets satisfy the following relation:

$$\frac{N_{p,min}}{N_{p,max}} = \left(\frac{D_{p,max}}{D_{p,min}}\right)^3 \tag{7.44}$$

This means that a very large amount of small droplets are represented by one parcel if polydispersity over wide range of droplet size is considered. The consequence of this is that the small droplets behave too coherently, show too little relative dispersion and are only distributed in a very small region, as shown in Fig. 7.14.

The droplet size PDF at $\mathcal{Z} = 8\ mm$ is shown in Fig. 7.15, the measured droplet size distribution is very well reproduced by both the URANS and LES case. Droplets at this axial location are mainly small droplets, and two peaks of the size PDF at around 18 mm and 5 mm are well captured. The PDFs of droplets smaller than 5 μ is however underpredicted, possibly resulting from the fact that the number of parcels that represent small droplets is quite small.

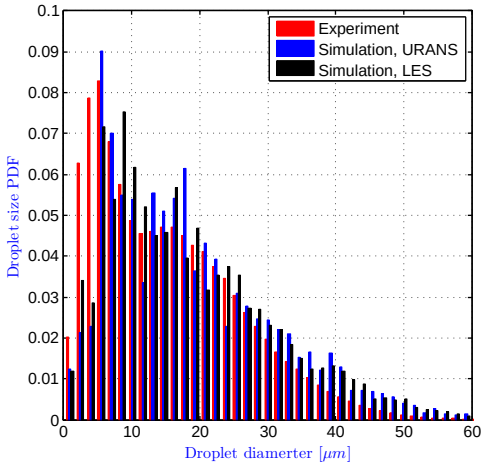

Figure 7.15: Droplet size PDF at $\mathcal{Z} = 8\ mm$ from simulation and experiment.

Figure 7.16 displays the droplet mean axial velocity. Since the conditional droplet injection model is used to provide the boundary condition of the droplets, its direct influence on the value of droplet velocity is mainly in the near injector region, the droplet velocity at further downstream is mainly influenced by the dispersion model. Fig. 7.16 shows that the conditional injection model indeed predicts better droplet velocity at $\mathcal{Z} = 8\ mm$ and $\mathcal{Z} = 10\ mm$. The droplet Sauter Mean Diameter (SMD, Fig. 7.17) exhibits considerable improvement when the conditional injection is applied. In the case without conditional injection, injection parameters are directly adopted from the nominal atomizer data, a typical conical shape spray was predicted. At low axial locations,

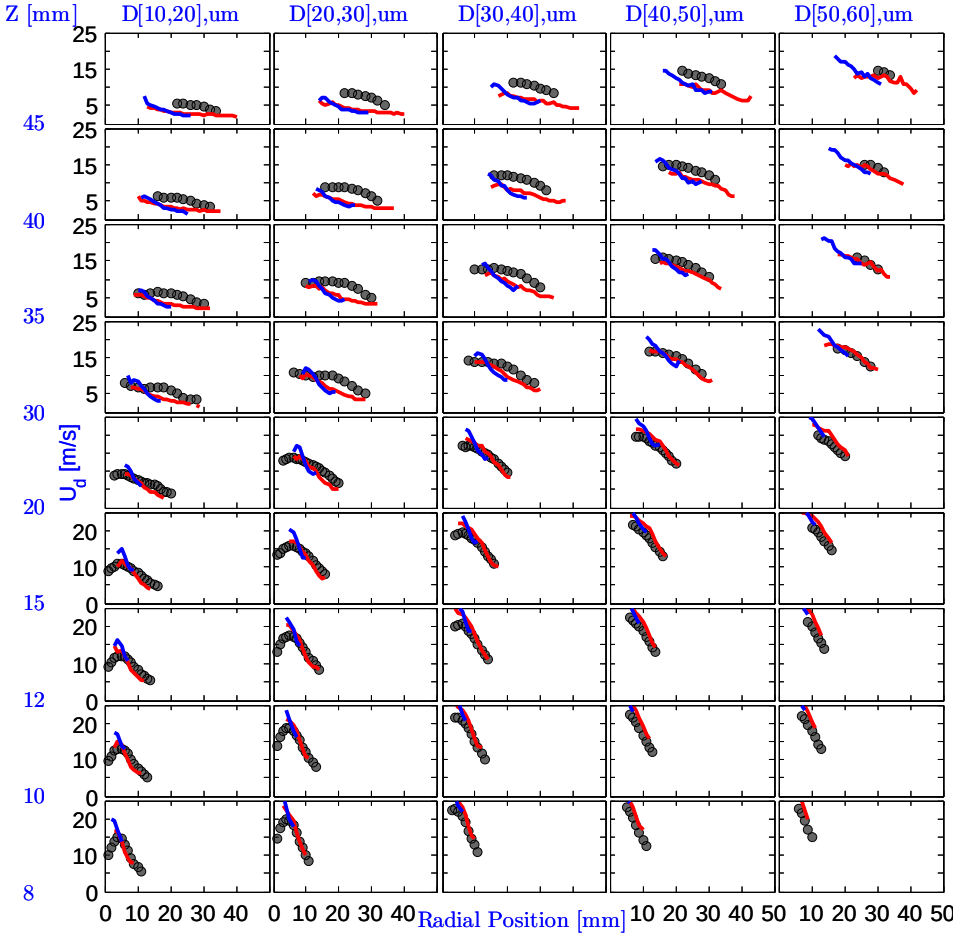

Figure 7.16: Radial profiles of droplet mean axial velocity for different droplet size (colum-wise) at different axial locations (row-wise), gray dot: experimental data, blue line: without conditional injection, red line: with conditional injection.

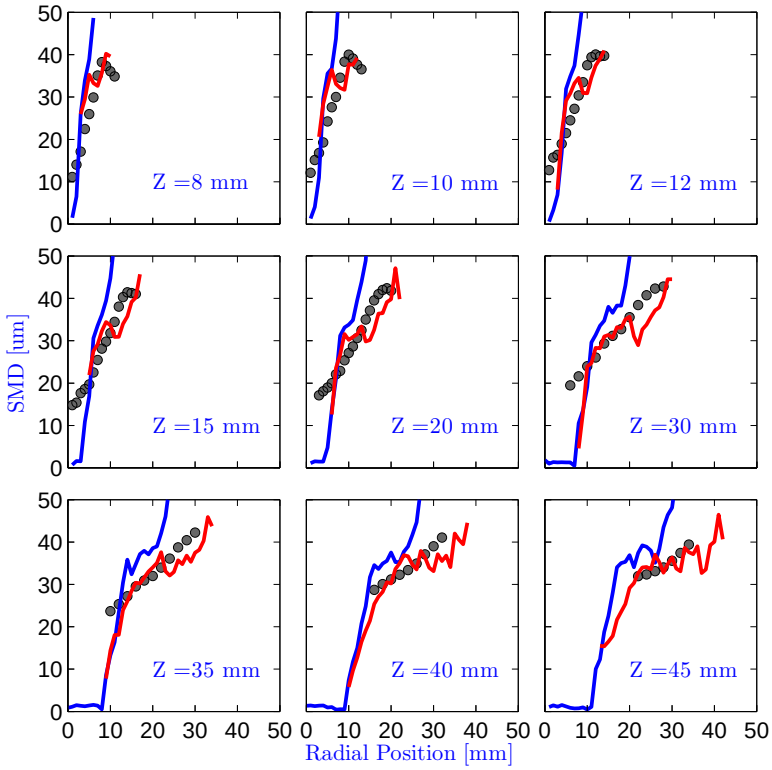

Figure 7.17: Radial profiles of Sauter Mean Diameter (SMD) at different axial locations, gray dot: experimental data, blue line: without conditional injection, red line: with conditional injection.

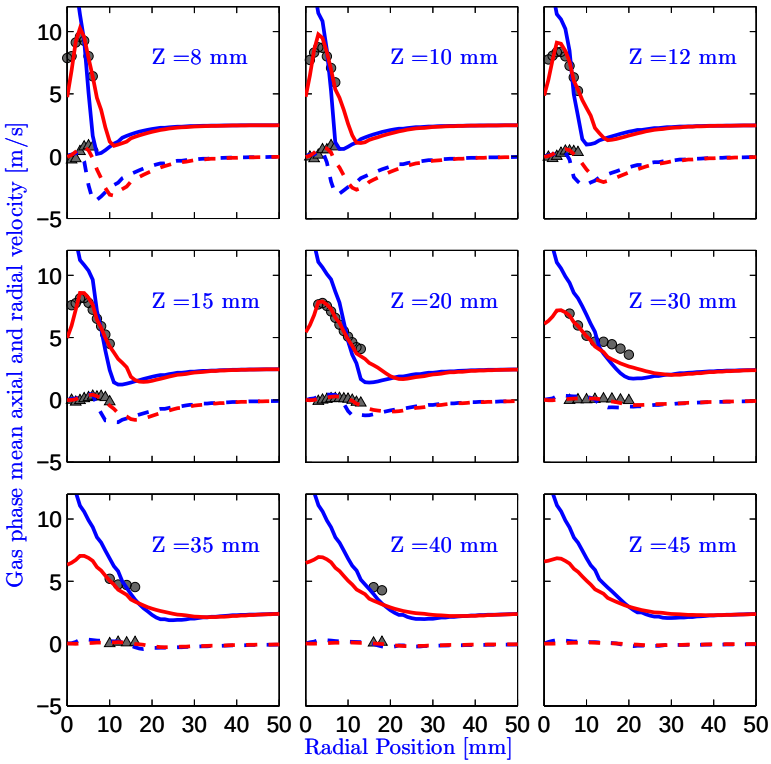

Figure 7.18: Radial profiles of mean gas phase velocity at different axial locations, gray dot: experimental data, blue line: without conditional injection, red line: with conditional injection, circle and solid lines: axial velocity, triangle and dashed lines: radial velocity.

droplets concentrate in only a small radial range, that becomes wider further downstream. As can be seen from the visualization of atomization process in Fig. 7.6, and the experimental data in Fig. 7.16, close to the atomizer, the droplets already have a relatively wide radial distribution due to the expansion caused by flash boiling. This effect is to a large extent reproduced by the conditional injection model. From the experimental data, it is also clear that the nominal spray half angle is smaller than those obtained from the actual spray distribution. This is caused by the radial expansion of spray cloud due to flash-boiling atomization.

The trend and magnitude of droplet SMD were both correctly captured in the case using conditional injection model. Without conditional injection case, the model predicts a very steep SMD profile and at the spray outer edge the SMD is over-estimated. In the conditional injection, large droplets are injected within a small range of angle around the spray half angle, and small droplets are injected in a much wider range, therefore the SMD is small at the edges of the spray cloud. Fluctuations in the radial profiles of SMD especially at high axial locations are due to low number density of droplets. Significantly longer simulation time is required in order to have a smooth droplet profile at high elevations, but statistical convergence of gas phase properties have already been well established within the current simulation time (0.15 s). Therefore, longer simulation time has not been carried out due to the high computational cost.

The advantage of the conditional injection is even more obvious when gas phase velocity is examined. As shown in Fig. 7.18. A very good agreement of gas phase mean axial and radial velocity is achieved in the case of using conditional injection. On the contrary, a steeper radial profile with significant over-prediction in the center and under-predication at the spray edge is observed in the other case, when the conditional injection model is not applied. Gas phase temperature profiles were also better captured with the conditional injection model in terms of radial spreading of high temperature region (not shown).

Above analysis clearly demonstrated the superior performance of the proposed conditional droplet injection model, therefore it will be applied to all cases involved in the remaining discussions.

7.6.2. IGNITING FGM VS. EXTINGUISHING FGM

In section 7.3.1, we have discussed different approaches for constructing a FGM library, involved in this study are EFGM and IFGM. In this section, we compare the performance of these two FGM configurations by examining the gas phase mean temperature and mixture fraction. The results presented in this section are obtained with URANS. Two IFGM libraries respectively generated at strain rate $a = 100\ s^{-1}$ and $a = 5\ s^{-1}$ will also be compared to study the influence of strain rate on the IFGM. Besides comparison of different lookup tables, two different models for the correction of droplet heat and mass transfer rate due to effects of convective flow, namely the Abramzon-Sirignano (A) model and Bird's correction (B) as presented in section. 7.2.2 are also evaluated. Cases are named by the FGM tables and correction models used.

Temperature profiles from five cases are shown in Fig. 7.19. As can be seen, the basic flame structure, namely the radial spreading and the radial position of the peak temperature, is well captured. However, the value of the peak temperature is under-estimated in

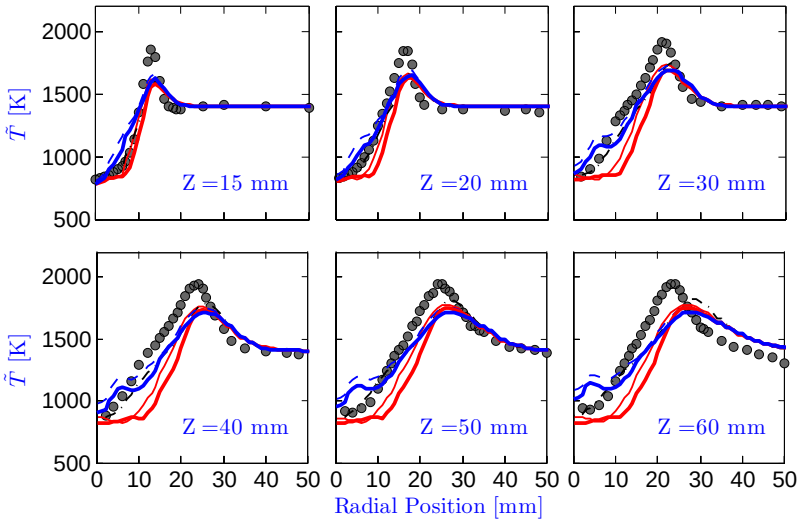

Figure 7.19: Radial profiles of mean gas phase temperature, gray dot: experimental data, thick red line: IFGM-A-$a = 100\ s^{-1}$, thin red line: IFGM-B-$a = 100\ s^{-1}$, thin black line: IFGM-B-$a = 5\ s^{-1}$, thick blue line: EFGM-A, thin blue line: EFGM-B.

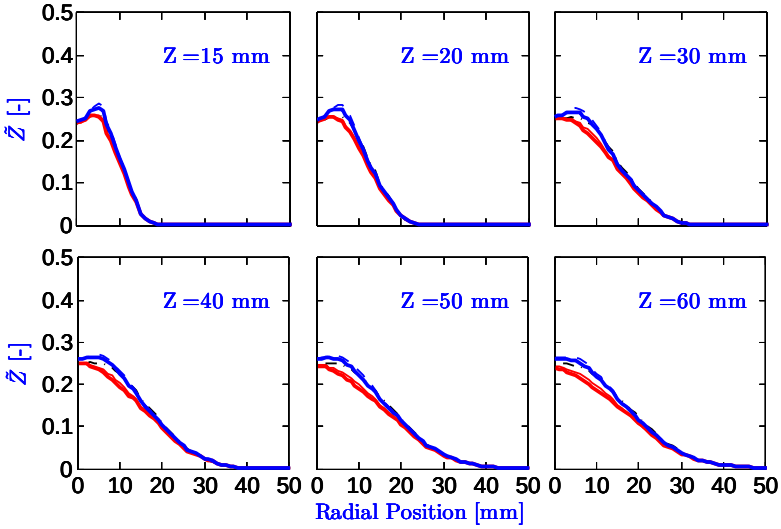

Figure 7.20: Radial profiles of mean mixture fraction, gray dot: experimental data, IFGM-A-$a = 100\ s^{-1}$, thin red line: IFGM-B-$a = 100\ s^{-1}$, thin black line: IFGM-B-$a = 5\ s^{-1}$, thin red line: IFGM-B, thick blue line: EFGM-A, thin blue line: EFGM-B.

all five cases, and this is due to the model for the mixture fraction variance which will be further discussed in the next section. The two EFGM cases over-predicted the thempera-ture in the near axis region, whereas the two cases using IFGM at high strain rate under-predicted the temperature in the same region. The case using IFGM at lwo strain rate reproduces quite well the temperature in the center region. An explanation for this goes as following: small droplets and evaporated fuel are convected towards the central part of the flame by the entraining coflow, resulting in a fuel rich region there. This can be evidenced with the mixture fraction profiles as shown in Fig. 7.20. As indicated with the progress variable source in the (Z, Y_c) space (Fig. 7.3), in the EFGM, reaction can happen in a wide range of Z up to 0.2, which leads to a secondary reaction region in the center rich part. On the contrary, in the IFGM generated at high strain rate, only a mixture close to stoichiometric is reactive, and also large enthalpy deficit leads to no ignition at all, and this is the reason for the under-prediction of the temperature in the center region of the spray flame. In the low-straining IFGM table, ignition still occurs at large enthalpy loss region, but it only happens at near stoichiometric condition, therefore the secondary re-action region is created at larger radial location (around $r = 10\ mm$), and leads to a local slope change on the mean temperature profile. According to the Correia Rodorigues et al. [12], this is the so-called "weakened inner flame front".

As can be seen from Fig. 7.19, besides the difference in a small region close to the axis, the results predicted by the EFGM and low-straining IFGM are quite similar. In the remaining of this paper, the EFGM will be used. There are two reasons to do so: first, as shown in this subsection, the results of IFGM is strongly influenced by the strain rate at which it is generated. The chosen of this strain rate is a bit arbitrary, the IFGM at $a = 5\ s^{-1}$ predicts good results in the case, but it will not necessarily work well in a different case. There are some solutions proposed in the literature. Ihme and See [35] suggested to add scalar dissipation rate as an additional controlling parameter in the FGM library to ac-count for the effect of strain. Alternately, Abtahizadeh et al. [51] have developed a novel FGM configuration based on the Igniting Mixing Layer (IML), and demonstrated that the effect of scalar dissipation rate can be incorporated well with IML manifolds. Neverthe-less, as a first step of model develop, EFGM is shown to be sufficient to accurately capture main flame properties. Second, the EFGM is more generally applicable compared to the IFGM. Because the generation of IFGM relies on auto-ignition of the reactants, which only happens when the reactant temperature is high enough. In the case where auto-ignition is not happening, for example the spray in air coflow (Hii) case as reported in [12], only EFGM can be generated.

The difference between results from the two evaporation correction models are small. The evaporation predicted by the Bird's correction is slightly faster, as indicated by the slightly higher mixture fraction from cases "B" in Fig. 7.20. Difference is more clear on the temperature profile — the Bird's correction produces higher temperature at the in-ner part of the profile up to the peak temperature position. Based on these results, it is difficult to judge which model is better. Since the Abramzon-Sirignano model involves iterative procedures to calculate Nu^* and Sh^*, Bird's correction is used in the LES simu-lation to reduce the computational cost.

7.6.3. URANS vs. LES

In the previous section, we observed that the peak temperature is under-predicted in all URANS cases regardless the FGM tables used. This can be improved with LES. The differences between the LES and URANS cases in the current study mainly lie in two aspects: first, the resolution in the LES in finer. Second, the model for mixture fraction variance is different. In the URANS, a transport equation for the mixture fraction variance (Eq. (7.12)) has been solved with model constant $C_{d,Zv} = 2$, while in LES, the mixture fraction variance is calculated with a dynamic model (Eq. (7.13)), for which no prescribed model constant is needed. A LES case performed on a coarser mesh is also reported here in order to identify the influence of grid resolution on the results. The mesh size of the coarse LES is similar to that for the URANS case in the near injector region but has a smaller growth ratio than the latter one.

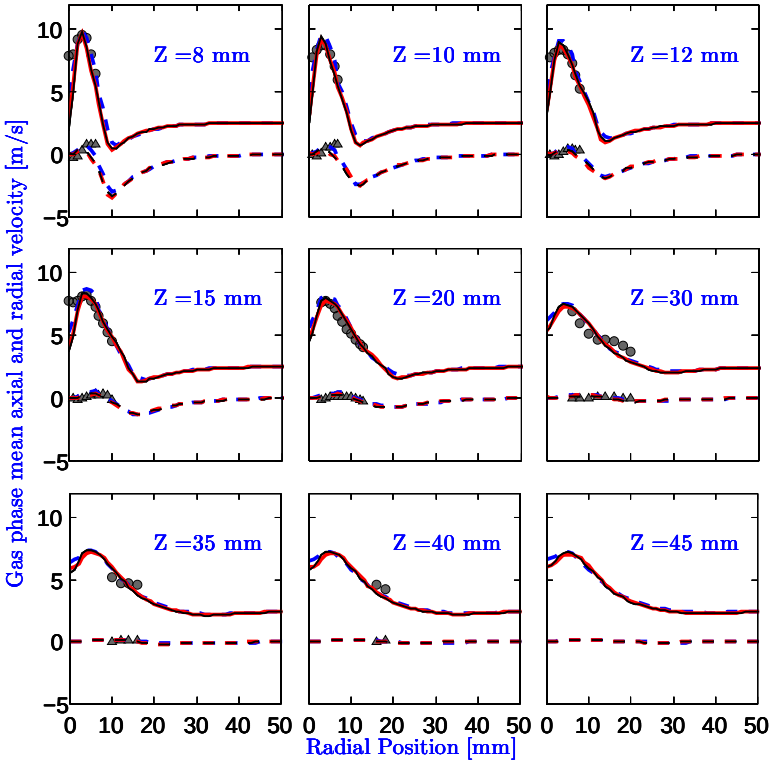

Figure 7.21: Radial profiles of mean gas phase velocity, solid red line: EFGM-LES-fine, solid black line: EFGM-LES-coarse, dashed blue line: EFGM-URANS.

The gas phase mean velocity is predicted quite similar in both the URANS and LES cases, see Fig. 7.21, which means that the combination of turbulence model and grid resolution in the URANS case also performs well. The gas phase velocity predicted by two LES cases are identical to each other. The mean gas phase temperature is significantly

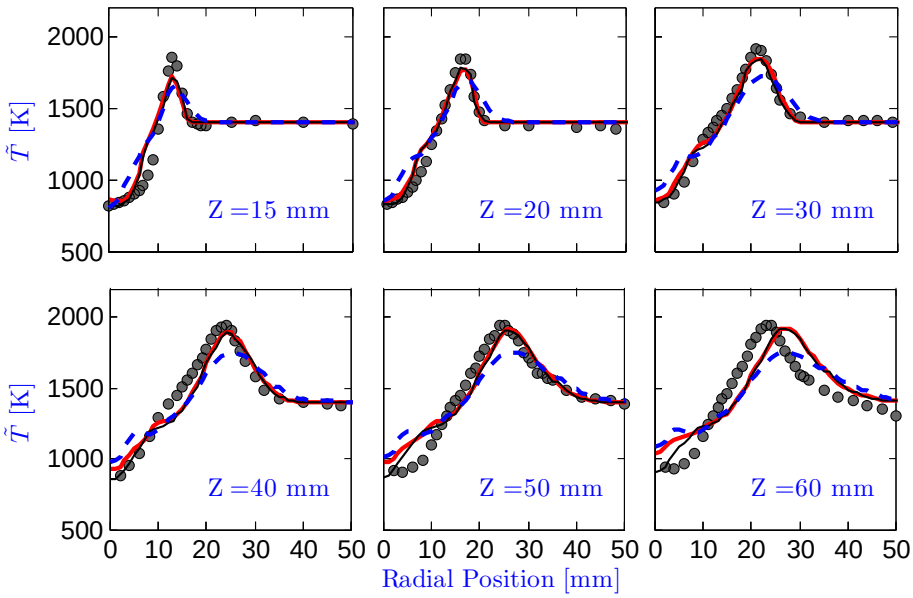

Figure 7.22: Radial profiles of mean gas phase temperature, gray dot: experimental data, solid red line: EFGM-LES-fine, solid black line: EFGM-LES-coarse, dashed blue line: EFGM-URANS.

improved in the LES case, see Fig. 7.22, in terms of well captured peak temperature as well as the radial width of temperature peak. The shoulder on the temperature profile at around $r = 10\ mm$, which represents the inner flame front, is well captured at $\mathcal{Z} = 20$, 30 and 40 mm, and the temperature in the near axis region is also in closer agreement with experiment. Again, the results from two LES cases are very similar. This means that the better prediction of temperature field in the LES is mainly due to the better performance of the dynamic algebraic model used for the mixture fraction variance in LES cases.

Fig. 7.23 presents the time-averaged temperature and its standard deviation on a cross-section from the fine grid LES case. The smooth appearance of the averaged field is demonstrating that the time duration used to obtain average value in the LES case is sufficient. The flame is clearly lifted from the injector plane, in agreement with the experimental visualization (Fig. 1.4). In the center, due to evaporation of small droplets, a low temperature region is present. From the contour plot of temperature standard deviation, it is clear that a secondary flame front present in the center. This secondary flame front is created after creation of a fuel rich mixture in the near axis region as revealed by flame index analysis in our previous study [26].

7.6.4. ADIABATIC VS. NON-ADIABATIC FGM

In this subsection, two cases respectively using adiabatic and non-adiabatic FGM tables will be compared in order to evaluate the significance of enthalpy loss on the spary combustion simulation. These two cases are both simulated with LES on the fine grid. The

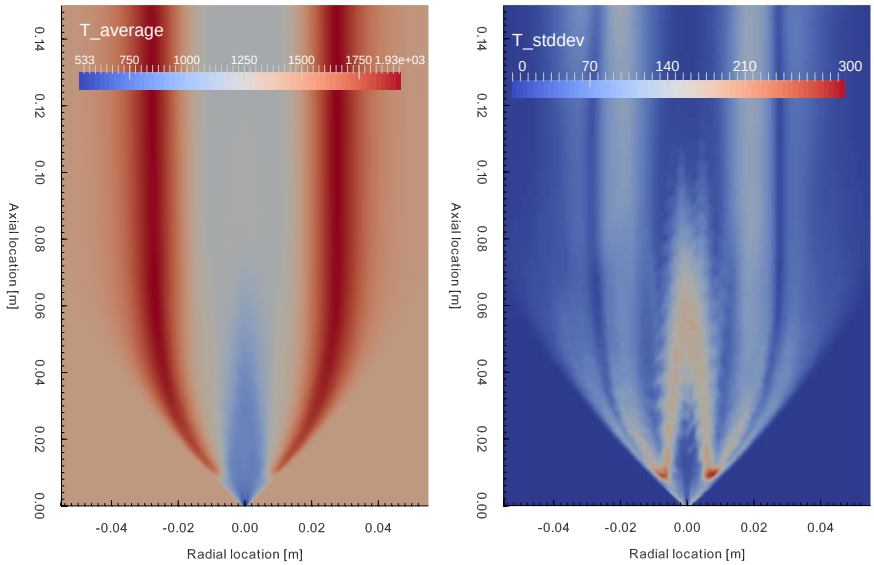

Figure 7.23: Averaged temperature and its standard deviation on a cross-section.

temperature profiles from these two cases are given in Fig. 7.24. Similar to the results reported in [26], in which an adiabatic IFGM table was used, the gas phase temperature is significantly over-predicted in the near axial region, indicating the influence of enthalpy loss in this region is non-negligible. Fig. 7.25, in which a snapshot of the enthalpy loss is shown on a cross-section, shows that largest enthalpy loss occurs in the center region. This is due to fast evaporation of large amount of small droplets that are convected to this region by the entraining coflow. On the other hand, the case that using non-adiabatic FGM library shows closer agreement with experimental data, especially in the center region.

7.6.5. DROPLET-FLAME INTERACTION

In the spray combustion system, the distribution of droplets plays a crucial role due to the strong coupling between the two phases [14]. On one hand the evaporated vapor provides the fuel for gas phase combustion, and on the other hand, the presence of dispersed phase strongly modulates the continues phase turbulence and reaction via momentum, energy and mass transfer. Thanks to the dynamic nature and high resolution of LES, the interaction between droplets and combustion can be analyzed in a more realistic and accurate way.

Trajectories of parcels were extracted from simulation and are displayed in Fig. 7.26. The time step between two sample (symbols on the trajectory) is constant (5×10^{-4} s), therefore the distance between two data points on each trajectory reflects the droplet velocity information. It is obvious that droplet velocity decays when they traveling downstream, as data points become closer to each other at high axial locations. Three groups of parcels where chosen based on their original injection position, as indicated by dif-

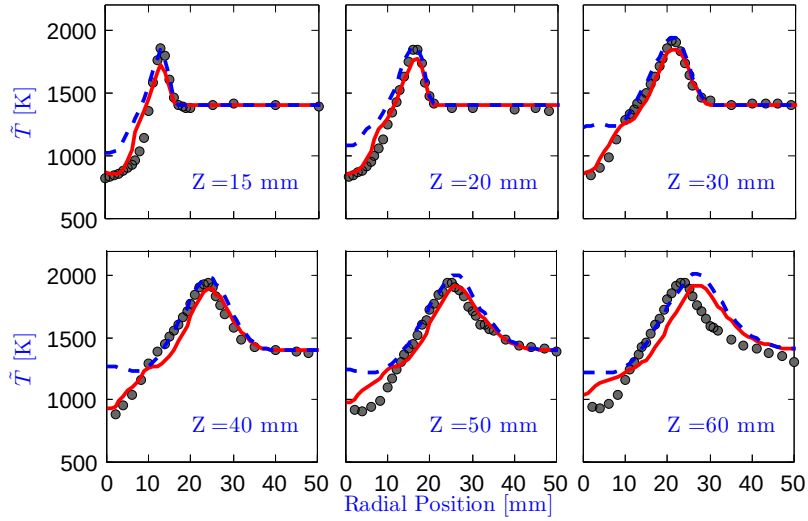

Figure 7.24: Radial profiles of mean gas phase temperature from LES with fine grid, gray dot: experimental data, solid red line: non-adiabatic, dashed blue line: adiabatic.

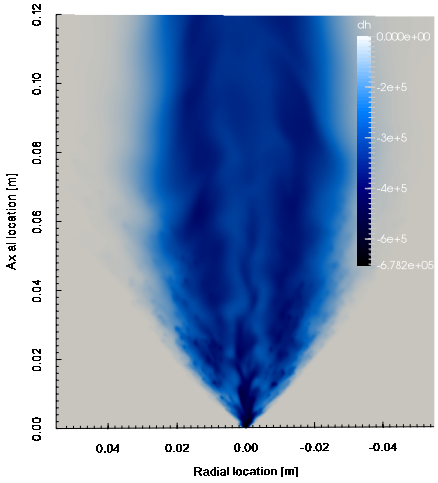

Figure 7.25: Snapshot of the enthalpy deficit on a vertical cross-section.

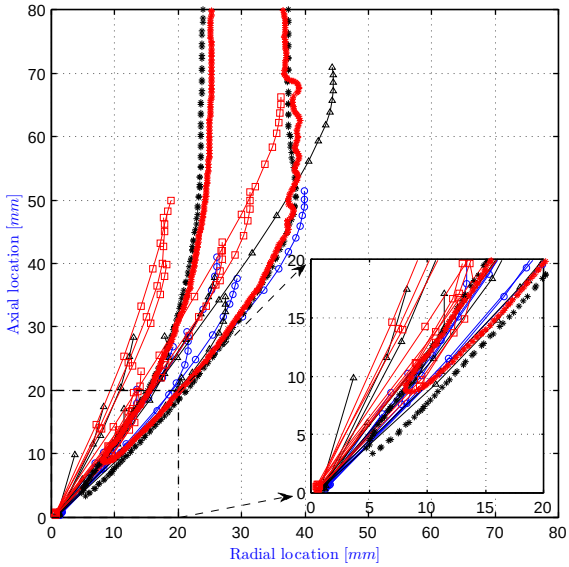

Figure 7.26: Droplet trajectory from simulation. Each line represents the trajectory of one parcel, different color indicating different droplet initial injection position. Red line with square: injected from center of injection disc, blue line with circle: injected from edge of injection disc, black line with triangle: injected from central annulus of injection disc. Stars are the averaged position of $Y_{OH} = 5 \times 10^{-4}$, black: URANS, red: LES.

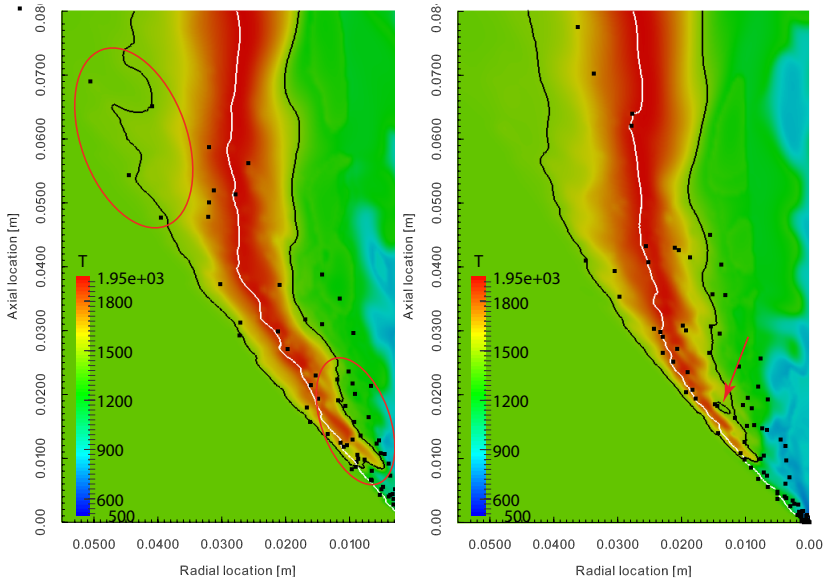

Figure 7.27: Snapshots of temperature field on a cross-section from LES. White line: isosurface of $Z_{st} = 0.045$, black line: isosurface of $T = 1450\ K$, black dots are representative of the instantaneous spray cloud within 1 mm perpendicular to the plane.

ferent color in Fig. 7.26. Five parcels were randomly chosen at each injection place so that behavior of different sized droplets can be represented. As clearly shown, the large droplets indeed have ballistic trajectories at the early period of their lifetime, which justifies the hypothesis made in section 7.4.1 during the analysis of experimental data. Some large droplets penetrated the reaction region (indicated by the averaged OH isosurface in Fig. 7.26) and survives until far downstream. These large droplet are expected to greatly influence the flame by momentum, heat and mass transfer. Small droplets vanish very soon, their trajectory angles were changed within a short distance after injection and turned towards the axis. This figure also shows that a large portion of droplets was traveling in the reaction region and finally disappeared there. The evaporation of these droplets on one hand decreases the flame temperature, and on the other hand supports the reaction by supplying fuel. This implies that if the non-adiabatic effect is not considered correctly in the simulation, not only the temperature in the near axis region, where lots of small droplet evaporate, but also in the reaction region will be over-predicted.

Fig. 7.26 shows that different lift-off heights have been predicted in URANS and LES, with the one in LES being closer to the experimental observation, if the $Y_{OH} >= 5\times10^{-4}$ is considered as the criteria of ignition. However, the flame shape at further downstream is quite similar in these two cases. Also interesting is that the flame stabilizes at the outside of the spray cloud, as is clear in the small plot in Fig. 7.26. This is in agreement with findings in gaseous auto-ignition flame, which shows that ignition mainly starts at lean and low-strain region [37, 52]. In this spray flame, the lean and low-strain region is formed at the outside of the spray cloud. This result implies that IFGM created at low strain rate physically more correctly represents the auto-ignition process and may produce better prediction, but to achieve this, careful tabulation of IFGM has to be studied as suggested in section 7.6.2.

The droplet-flame interaction is clear in the contour plot of instantaneous temperature on a vertical cross section. In Fig. 7.27 the stoichiometric mixture fraction and the isosurface of $T = 1450\ K$ (50 K higher than the coflow temperature) as well as the instantaneous spray cloud on the same plane are superimposed on the temperature contour plot. The flame has a very irregular shape both at the bottom, and at the outside. At outside of flame, some “long tails" occasionally appear. If we draw a straight line parallel to these tails, they all converge at the injector location at $\mathcal{Z} = 0\ mm$. These long tails are believed to be created by the wake of large droplets that passed through the main reaction region, as shown in Fig. 7.26. In Fig. 7.27, we also see some low temperature spots at the flame region, some even create a hole in the reaction region (pointed by red arrow), indicating local quenching due to large heat loss caused by droplet evaporation in the reaction region. The dynamic behavior of the droplet-flame interaction in LES can be seen in the videos provided as supplementary material.

7.7. CONCLUSION

In this paper, we report a numerical study on the Delft Spray-in-Hot-Coflow (DSHC) flame. This simulation was carried out with a customized OpenFoam solver. In this solver, the Flamelet Generated Manifolds (FGM) model has been implemented, and used to account for the Turbulence-Chemistry Interaction (TCI). The enthalpy loss effect due to droplet vaporization is considered by employing an additional controlling

parameter in the FGM libraries. Two different FGM configurations, namely the extinguishing FGM (EFGM) and igniting FGM (IFGM) are both used for the construction of the non-adiabatic FGM library. Two IFGMs generated at different strain rate were also compared. Considerable differences have been observed. Results of IFGM were strongly influenced by the strain rate. The high-straining FGM under-predicted the temperature in the center. The results from EFGM is similar to those form the low strain IFGM, and is close to experimental data, although the former slightly over-estimated the temperature in the near axis region. Abramzon-Sirignano model and the Bird's correction for droplet heat and mass transfer rate for the current case have similar performance.

Based on the analysis of the experimental data, it was concluded that flash-boiling atomization occurs in the DSHC flame. A conditional droplet injection model was proposed to take into account the influences of the flash-boiling atomization on downstream droplet distribution. In this conditional injection model, the droplets have an asymmetric distribution around the mean spray trajectory. Also, the possible range of injection angle is conditioned upon the droplet size (mass). Small droplets can be injected to a very wide range, while large droplets move within a small range of angle around the mean spray trajectory. Droplets are injected from a position randomly chosen within the injection disc at $\mathcal{Z} = 0\ mm$, the diameter of which was set 10 times the experimental atomizer exit diameter. Droplet initial velocity magnitude is scaled such that it peaks at the spray half angle direction and reaches minimum at the edge of the spray cloud. Two cases employing or not the proposed conditional injection model were compared. The results show that the conditional injection model significantly improves the prediction for all the properties examined.

The LES predicted similar gas phase velocity profiles to those from the URANS, supporting reliability of the employed URANS approach. The temperature field prediction was considerably improved in the LES case, in terms of well captured peak temperature and closer agreement with experimental data in the near axis region, mainly due to the better performance of the dynamic model for mixture fraction variance used in LES. Comparison between cases respectively using adiabatic and non-adiabatic clearly demonstrated the superiority of the latter on the simulation of spray combustion. Strong droplet-flame interaction was shown to exist in the DSHC flame. Large droplets have ballistic trajectories at the early stage of their lifetime, and can penetrate the flame and survive until far downstream outside the main reaction region. Movement of these large droplets strongly deforms the shape of the flame. Rapid evaporation of droplet in the reaction region may also cause local quenching. Small droplets are quickly convected towards the central region and vanish soon, forming a low temperature - fuel rich condition in the center. These phenomena have been captured with the developed LES/non-adiabatic FGM approach.

REFERENCES

[1] H. J. Kim, S. H. Park, K. S. Lee, and C. S. Lee, *A study of spray strategies on improvement of engine performance and emissions reduction characteristics in a DME fueled diesel engine,* Energy **36**, 1802 (2011).

[2] G. Valentino, L. Allocca, S. Iannuzzi, and A. Montanaro, *Biodiesel/mineral diesel fuel mixtures: Spray evolution and engine performance and emissions characterization,* Energy **36**, 3924 (2011).

[3] A. Cavaliere and M. de Joannon, *Mild Combustion,* Progress in Energy and Combustion Science **30**, 329 (2004).

[4] J. A. Wünning and J. G. Wünning, *Flameless oxidation to reduce thermal no-formation,* Progress in Energy and Combustion Science **23**, 81 (1997).

[5] F. Christo and B. Dally, *Modeling turbulent reacting jets issuing into a hot and diluted coflow,* Combustion and Flame **142**, 117 (2005).

[6] P. Li, J. Mi, B. B. Dally, F. Wang, L. Wang, Z. Liu, S. Chen, and C. Zheng, *Progress and recent trend in MILD combustion,* Science China Technological Sciences **54**, 255 (2011).

[7] E.-S. Cho, B. Danon, W. de Jong, and D. Roekaerts, *Behavior of a 300kWth regenerative multi-burner flameless oxidation furnace,* Applied Energy **88**, 4952 (2011).

[8] M. Sánchez, F. Cadavid, and A. Amell, *Experimental evaluation of a 20kW oxygen enhanced self-regenerative burner operated in flameless combustion mode,* Applied Energy **111**, 240 (2013).

[9] R. Weber, J. P. Smart, and W. V. Kamp, *On the (MILD) combustion of gaseous, liquid, and solid fuels in high temperature preheated air,* Proceedings of the Combustion Institute **30**, 2623 (2005).

[10] M. Derudi and R. Rota, *Experimental study of the mild combustion of liquid hydrocarbons,* Proceedings of the Combustion Institute **33**, 3325 (2011).

[11] J. Ye, P. R. Medwell, E. Varea, S. Kruse, B. B. Dally, and H. G. Pitsch, *An experimental study on MILD combustion of prevaporised liquid fuels,* Applied Energy **151**, 93 (2015).

[12] H. Correia Rodrigues, M. J. Tummers, E. H. van Veen, and D. Roekaerts, *Spray flame structure in conventional and hot-diluted combustion regime,* Combustion and Flame **162**, 759 (2015).

[13] H. Correia Rodrigues, M. Tummers, E. van Veen, and D. Roekaerts, *Effects of coflow temperature and composition on ethanol spray flames in hot-diluted coflow,* International Journal of Heat and Fluid Flow **51**, 309 (2015).

[14] P. Jenny, D. Roekaerts, and N. Beishuizen, *Modeling of turbulent dilute spray combustion,* Progress in Energy and Combustion Science **38**, 846 (2012).

[15] M. Ihme, J. Zhang, G. He, and B. Dally, *Large-Eddy Simulation of a Jet-in-Hot-Coflow Burner Operating in the Oxygen-Diluted Combustion Regime,* Flow, Turbulence and Combustion **89**, 449 (2012).

[16] E. Abtahizadeh, A. Sepman, F. Hernández-Pérez, J. van Oijen, A. Mokhov, P. de Goey, and H. Levinsky, *Numerical and experimental investigations on the influence of preheating and dilution on transition of laminar coflow diffusion flames to Mild combustion regime,* Combustion and Flame **160**, 2359 (2013).

[17] P. Coelho and N. Peters, *Numerical simulation of a mild combustion burner,* Combustion and Flame **124**, 503 (2001).

[18] Y. Minamoto, T. Dunstan, N. Swaminathan, and R. Cant, *DNS of EGR-type turbulent flame in MILD condition,* Proceedings of the Combustion Institute **34**, 3231 (2013).

[19] Y. Minamoto and N. Swaminathan, *Scalar gradient behaviour in MILD combustion,* Combustion and Flame **161**, 1063 (2014).

[20] A. De, E. Oldenhof, P. Sathiah, and D. Roekaerts, *Numerical Simulation of Delft-Jet-in-Hot-Coflow (DJHC) Flames Using the Eddy Dissipation Concept Model for Turbulence–Chemistry Interaction,* Flow, Turbulence and Combustion **87**, 537 (2011).

[21] B. Danon, E.-S. Cho, W. de Jong, and D. Roekaerts, *Numerical investigation of burner positioning effects in a multi-burner flameless combustion furnace,* Applied Thermal Engineering **31**, 3885 (2011).

[22] J. A. van Oijen and L. P. H. de Goey, *Modelling of premixed laminar flames using flamelet-generated manifolds,* Combustion Science and Technology **161**, 113 (2000).

[23] C. D. Pierce and P. Moin, *Progress-variable approach for large-eddy simulation of non-premixed turbulent combustion,* Journal of Fluid Mechanics **504**, 73 (2004).

[24] A. Vreman, B. Albrecht, J. A. van Oijen, L. P. H. de Goey, and R. Bastiaans, *Premixed and nonpremixed generated manifolds in large-eddy simulation of Sandia flame D and F,* Combustion and Flame **153**, 394 (2008).

[25] OpenFOAM, *OpenFOAM: The open source CFD Toolbox,* (2015).

[26] L. Ma, B. Naud, and D. Roekaerts, *Transported PDF Modeling of Ethanol Spray in Hot-diluted Coflow Flame,* Flow, Turbulence and Combustion , in press (2015).

[27] J. J. Louis, J. B. Kok, and S. A. Klein, *Modeling and measurements of a 16-kW turbulent nonadiabatic syngas diffusion flame in a cooled cylindrical combustion chamber,* Combustion and Flame **125**, 1012 (2001).

[28] P. Coelho, O. Teerling, and D. Roekaerts, *Spectral radiative effects and turbulence/radiation interaction in a non-luminous turbulent jet diffusion flame,* Combustion and Flame **133**, 75 (2003).

[29] G. Kim and Y. Kim, *Non-adiabatic flamelet modeling for combsution processes of oxy-natural gas flame,* Journal of Mechanical Science and Technology **19**, 1781 (2005).

[30] ANSYS, *Fluent 15.0 Theory Guide,* (2014).

[31] B. Marracino and D. Lentini, *Radiation Modelling in Non-Luminous Nonpremixed Turbulent Flames,* Combustion Science and Technology **128**, 23 (1997).

[32] M. K. Stöllinger and D. Roekaerts, *PDF modelling of soot formation in turbulent non-premixed flames using tabulated chemistry,* in *Proceedings of the European Combustion Meeting (2013)* (2013) pp. 1–6.

[33] G. Frank and M. Pfitzner, *ON THE GENERATION OF NON-ADIABATIC , NON- PREMIXED FLAMELET LIBRARIES WITH SPECIAL EMPHASIS ON WALL HEAT LOSSES,* in *Proceedings of 9th Mediterranean Combustion Symposium (2015)* (2015) pp. 1–11.

[34] N. Peters, *Laminar diffusion flamelet models in non-premixed turbulent combustion,* Progress in Energy and Combustion Science **10**, 319 (1984).

[35] M. Ihme and Y. C. See, *Prediction of autoignition in a lifted methane/air flame using an unsteady flamelet/progress variable model,* Combustion and Flame **157**, 1850 (2010).

[36] C. Bekdemir, L. M. T. Somers, and L. P. H. de Goey, *Modeling diesel engine combustion using pressure dependent Flamelet Generated Manifolds,* Proceedings of the Combustion Institute **33**, 2887 (2011).

[37] L. Ma and D. Roekaerts, *Dynamic procedures for sub-grid scale scalar variances of FGM method,* Submitted for publication (2015).

[38] C. Pera, J. Reveillon, L. Vervisch, and P. Domingo, *Modeling subgrid scale mixture fraction variance in LES of evaporating spray,* Combustion and Flame **146**, 635 (2006).

[39] J. S. Shirolkar, C. F. M. Coimbra, and M. Q. Mcquay, *Flundamental aspects of modeling turbulent particle dispersion in dilute flows,* Progress in Energy and Combustion Science **22**, 363 (1996).

[40] R. Bird, W. Stewart, and W. Lightfoot, *Transport Phenomena* (Wiley, US, 1960).

[41] B. Abramzon and W. Sirignano, *Droplet vaporization model for spray combustion calculations,* International Journal of Heat and Mass Transfer **32**, 1605 (1989).

[42] CHEM1D, A one-dimensional laminar flame code, *Eindhoven University of Technology,* (URL:http://www. combustion. tue. nl/chem1d//).

[43] M. Chrigui, J. Gounder, A. Sadiki, A. R. Masri, and J. Janicka, *Partially premixed reacting acetone spray using LES and FGM tabulated chemistry,* Combustion and Flame **159**, 2718 (2012).

[44] H. Wang, K. Luo, and J. Fan, *Direct numerical simulation and CMC (conditional moment closure) sub-model validation of spray combustion,* Energy **46**, 606 (2012).

[45] L. Ma, S. Zhu, M. J. Tummers, T. H. van der Meer, and D. Roekaerts, *Numerical investigation of ethanol spray-in-hot-coflow flame using steady flamelet model,* in *Proceedings of Eighth Mediterranean Combustion Symposium* (2013) pp. 1–12.

[46] R.D. Oza, *On the mechanism of flashing injection of initially subcooled fuels,* Journal of Fluids Engineering **106**, 105 (1984).

[47] R. D. Reitz, *A Photographic Study of Flash-Boiling Atomization,* Aerosol Science and Technology **12**, 561 (2007).

[48] P. Senecal, D. Schmidt, I. Nouar, C. Rutland, R. Reitz, and M. Corradini, *Modeling high-speed viscous liquid sheet atomization,* International Journal of Multiphase Flow **25**, 1073 (1999).

[49] R. I. Issa, *Solution of the Implicitly Discretised Fluid Flow Equations by Operator-Splitting,* Journal of Computational Physics **65**, 40 (1986).

[50] H. Versteeg and W. Malalasekera, *An Introduction to Computational Fluid Dynamics (Second Edition)* (Pearson Education, 2007).

[51] E. Abtahizadeh, P. de Goey, and J. van Oijen, *On the effect of preferential diffusion in autoignition of CH4/H2 flames. Part 1: Development of a flamelet-based model,* Combustion and Flame **162**, 4358 (2015).

[52] P. Domingo, L. Vervisch, and D. Veynante, *Large-eddy simulation of a lifted methane jet flame in a vitiated coflow,* Combustion and Flame **152**, 415 (2008).

8

INVESTIGATION ON THE FLAME STRUCTURE OF MILD SPRAY COMBUSTION

In this chapter, the influence of coflow conditions on the structure of the DSHC flames is studied using the modeling approach developed in Chapter 7. Three different experimental cases are first simulated in order to further validate the modeling approach. Then the study was extended to four more virtual cases, which differ from each other only by coflow temperature or oxygen concentration. The purpose of this step is to eliminate the simultaneous change of multiple parameters as was done in the experiment and to isolate the influences of coflow temperature and O_2 concentration, which are important parameters for a MILD furnace design and operation. Two reaction regions have been identified in the DSHC hot coflow flames.

Content in this chapter has been published in the following paper:
L. Ma, D. Roekaerts, "Structure of spray in hot-diluted coflow flames under different coflow conditions: a numerical study", Combustion and Flame, under review (2016).

8.1. INTRODUCTION

Achieving low pollutant emissions while maintaining high efficiency and the required heat flux is a key goal for innovation in combustion research [1, 2]. The MILD (Moderate or Intense Low-oxygen Dilution) combustion or "flameless oxidation" [3–5], has been such innovation. MILD combustion of gaseous fuels has been intensively studied both experimentally and numerically [6–9]. However, so far there has been much less research on liquid fuel MILD combustion [10–13].

Weber et al [10] performed experimental study of MILD combustion of various fuels and found that similar to nature gas, no visible flame is present for the light oils in a vitiated coflow. Mahendra Reddy et al [14] investigated kerosene combustion in a two stage flameless combustor. Experimental measurements showed that MILD combustion mode was achieved. An order of magnitude of reduction in CO and NOx emission was also reported. More recently, they [15] performed an experimental study of biodiesel fuel MILD combustion in a high swirl combustor, and found that the emission is drastically reduced when the pure biodiesel is blended with conventional diesel. They concluded that the reason is that the viscosity, surface tension and boiling temperature of biodiesel can be reduced by the blending, which in turn leads to a reduced droplet Sauter Mean Diameter (SMD) and increased evaporation rate. MILD combustion of another biofuel — Butyl Nonanoate (BN) was investigated by Khalil and Gupta [16] under gas turbine condition. 15% reduction in NO emission compared to JP8 was observed, CO emission was also lower than JP8. No startup issues and combustion instabilities were observed. These studies have undoubtedly demonstrated the promising performance of the MILD combustion technology for liquid fuels. However, the flame structure, stabilization mechanism and the parameter optimization of the liquid-fueled MILD combustion are not fully understood.

The Delft Spray-in-Hot-Coflow (DSHC) burner was designed to study the fundamental aspects of flameless oxidation of representative biofuels — ethanol and acetone [17] . With different spray and gas phase properties measured and influences of coflow conditions and fuel flexibility studied, the DSHC dataset provides a valuable basis for the development and validation of modeling methods towards the application of MILD spray combustion [18]. The study in this paper is part of a multi-stage project that is dedicated to the numerical study of the DSHC flames, with the goal of developing a reliable modeling approach, and to better understand the mechanism of MILD spray combustion. In our previous studies, different modeling strategies have been applied to the DSHC dataset, and in general, decent results compared to experimental data were obtained [19–21].

For MILD combustion of gaseous fuels, a range of operating parameters, such as coflow conditions, fuel compositions etc., have been shown to affect the establishment of MILD condition [6, 22]. To better understand the MILD spray combustion, similar parameter studies for liquid fuels are necessary. Recently, Ye et al [13] investigated the combustion of pre-vaporized liquid fuel in a reverse-flow combustor. MILD combustion mode was successfully realized for all studied fuels (ethanol, acetone and n-heptane). They found that the air jet velocity, pressure and carrier gas of the liquid fuel all influence the combustion stability and emission levels. From experimental visualization [23] and previous numerical studies [19, 20] it was confirmed that the DSHC flames are lifted

from the spray injector exit. The lift off phenomenon in spray combustion is resulted from the disparity between time and length scales for different processes, e.g., evaporation, convection and reaction [24, 25]. The coflow conditions, e.g. temperature and oxygen concentration, all have a certain influence on the lift-off height through the influence on these time scales. For example, increasing coflow temperature can significantly shorten the droplet evaporation and reaction time scale, therefore leading to a reduction of lift-off height. The decrease of O_2 concentration in the coflow, leads to the formation of the mixture condition that is less favorable for ignition, hence the flame can only be stabilized further downstream. A clear insight in the influence of these parameters on flame structures may provide valuable references for the design of liquid-fueled combustion systems that are intended to work in MILD conditions.

In the DSHC burner, the hot-diluted coflow is generated by a secondary burner that operates on a lean mixture of Dutch Nature Gas (DNG) and air [18]. A limitation of this configuration is that the coflow temperature and O_2 concentration can only change simultaneously, increase of one is always accompanied with decrease of the other. However these two can be independent parameters in a real MILD furnace, by different degrees of air preheating and internal recirculation [4]. Computational Fluid Dynamics (CFD) is an ideal too to carry out parameter studies that are not possible or difficult to do with experiment. In this paper, three experimental cases from the DSHC dataset with various coflow conditions are first simulated and the results are carefully compared to available experimental data. The purpose of this first step is to check the reliability of the proposed numerical approaches and developed solver [21], and its capability in capturing the trend of flame properties with change of coflow conditions. Based on the confidence obtained in the first step, some virtual cases that differ from each other only by one coflow parameter (temperature or O_2 concentration) are simulated.

The remaining of the paper is structured as follows: The experimental dataset and numerical approaches are first presented in section 8.2, a description of the cases that will be studied in the present paper is also given in this section. The results and discussions will be given in section 8.3 along the line first experimental validation and then numerical parameter study. Main findings of this study are summarized in section 8.4.

8.2. TEST CASES AND MODELING APPROACHES

8.2.1. SIMULATION CASES

As explained in the introduction, in this Chapter we first simulate three cases from the DSHC dataset, namely the case "H_I", "H_{II}" and "H_{III}" [23]. These three cases all use ethanol as fuel, and the coflow are consists of hot combustion products generated by the secondary burner. The main parameters for these cases are described in Table 8.1. Subscript "cf" refers to the property of coflow, and the last two columns are the turbulent intensity and mass flow rate of the liquid fuel at the injector. One may notice that the coflow temperature and O_2 mole fraction shown in Table 8.1 are different from those reported in [23]. This is because the whole profile including the boundary layer was considered for the averaging in [17], while a representative condition at the plateau of the coflow profile is used in this study. There are also four other numerical cases named "H_{II}-A" to "H_{II}-D" shown in Table. 8.1. Conditions of these cases are based on H_{II}, with

changes only in coflow temperature (cases H_{II}-A and H_{II}-B) or O_2 concentration (cases H_{II}-C and H_{II}-D). As explained in section 8.1 that these four new cases are created to isolate the influences of coflow temperature and O_2 concentration on the MILD spray combustion.

Table 8.1: Boundary conditions for different cases.

Case	$\overline{T}_{cf}$ [K]	$\overline{X}_{O_2,cf}$ [%]	$\overline{X}_{N_2,cf}$ [%]	$\overline{X}_{H_2O,cf}$ [%]	$\overline{X}_{CO_2,cf}$ [%]	$\bar{U}_{cf}$ [m/s]	$\bar{I}_{cf}$ [%]	$\dot{m}_{liquid}$ [kg/hr]
Hi	1600	6.89	74.26	12.51	6.34	3.5	3.0	1.36
Hii	1400	8.71	74.81	10.94	5.54	2.5	2.0	1.46
Hii-A	1200	8.71	74.81	10.94	5.54	2.5	2.0	1.46
Hii-B	1600	8.71	74.81	10.94	5.54	2.5	2.0	1.46
Hii-C	1400	6.00	74.07	13.23	6.70	2.5	2.0	1.46
Hii-D	1400	12.00	75.94	8.01	4.05	2.5	2.0	1.46
Hiii	1350	9.30	75.02	10.41	5.27	2.0	2.5	1.48

8.2.2. NON-ADIABATIC FLAMELET GENERATED MANIFOLDS

One of the main features of MILD combustion is the low Damköhler number, which implies comparable time scales for flow and chemical reaction. Therefore, models that is able to account for finite rate chemistry are indispensable for modeling of MILD combustion. Direct use of detailed chemistry mechanism is computationally expensive, especially when great detail of the turbulent flow field is intended to be resolved, like in Large Eddy Simulation (LES) or Direct Numerical Simulation (DNS). To this end, chemistry reduction method has to be applied. Use of flamelet-based models under MILD conditions has been reported by several researchers [26, 27]. Compared to the Eddy Dissipation Concept (EDC) model, which is widely used for modeling of MILD combustion [6, 28, 29], the tabulated chemistry models are computationally very efficient. The Flamelet Generated Manifolds (FGM) model [30], conceptually similar to the Flamelet / Progress Variable (FPV) model [31], has been demonstrated by previous studies to be applicable to DSHC cases and produces good results both with transported PDF (probability density function) [20] and presumed PDF methods [21]. To take into account the effect of enthalpy loss due to liquid fuel evaporation, the authors proposed a three dimensional non-adiabatic FGM approach. Details and validation of this approach were reported in [21]. The same modeling approach is employed in the current study.

Both premixed and non-premixed combustion regimes have been found in spray combustion [32]. Therefore, to better represent the reaction process, in principle, tabulated chemistry manifolds based on hybrid premixed and non-premixed flamelets should be used to model spray combustion, as suggested by Franzelli et al [33]. However, in many situations using only one type of flamelets works well. Vreman et al [34] modeled Sandia Flame D and F with both premixed based and non-premixed based FGM, and found that the latter yields significantly better results. Tillou et al [35] tested different configurations for tabulated chemistry method, and concluded that they don't make much difference on prediction of auto-ignition. So, as a first attempt, the non-premixed

flamelets based FGM is used in the present study.

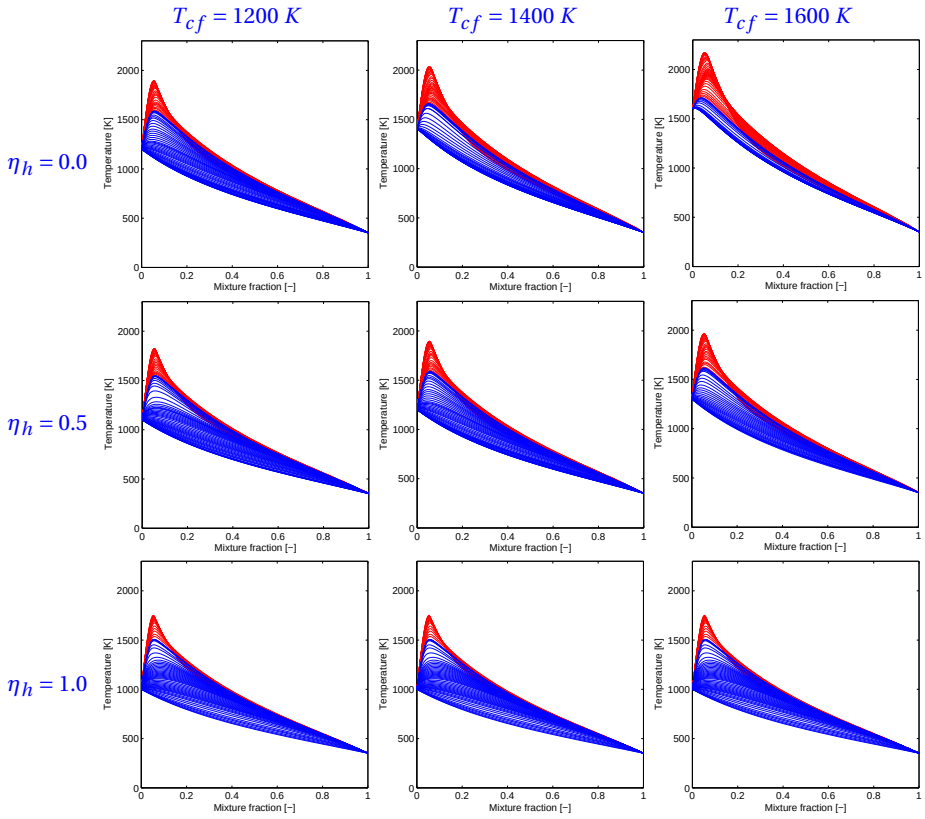

Figure 8.1: FGM data for temperature versus mixture fraction at different coflow temperature (T_{cf}) and different scaled enthalpy loss (η_h), coflow oxygen concentration $X_{O_2,cf}$ = 8.7%.

In Figs. 8.1 and 8.2, the non-adiabatic FGM tables used in cases H_{II} and H_{II}-A to H_{II}-D are compared. In these figures, each small plot represents temperature data from a two dimensional FGM table. Each 2D FGM was constructed from steady flamelets with increasing strain rate (red lines) and unsteady flamelets at the extinction strain rate (blue lines). The flamelets are obtained by calculating counter-diffusion flame using CHEM1D [36]. Different rows in Figs. 8.1 and 8.2 represent FGM tables at different enthalpy loss. ζ_h is the scaled enthalpy loss parameter, $\zeta_h = 0$ means adiabatic and $\zeta_h = 1$ means maximum enthalpy loss levels. The enthalpy loss effect was accomplished by decreasing inlet temperature at the oxidizer side ($Z = 0$). Three 2D FGM tables in each column then form the final 3D, (Z, C, ζ_h), non-adiabatic FGM tables used for simulations. For more details regarding construction of non-adiabatic FGM table and the lookup procedure, readers are referred to [21].

We can read form Fig. 8.1 that the coflow temperature can significantly change the content of the FGM table. When $T_{cf} = 1200\ K$, the maximum strain rate to have a stable flamelet solution is 2000 s^{-1}, it increases to 10000 s^{-1} when $T_{cf} = 1600\ K$. This implies

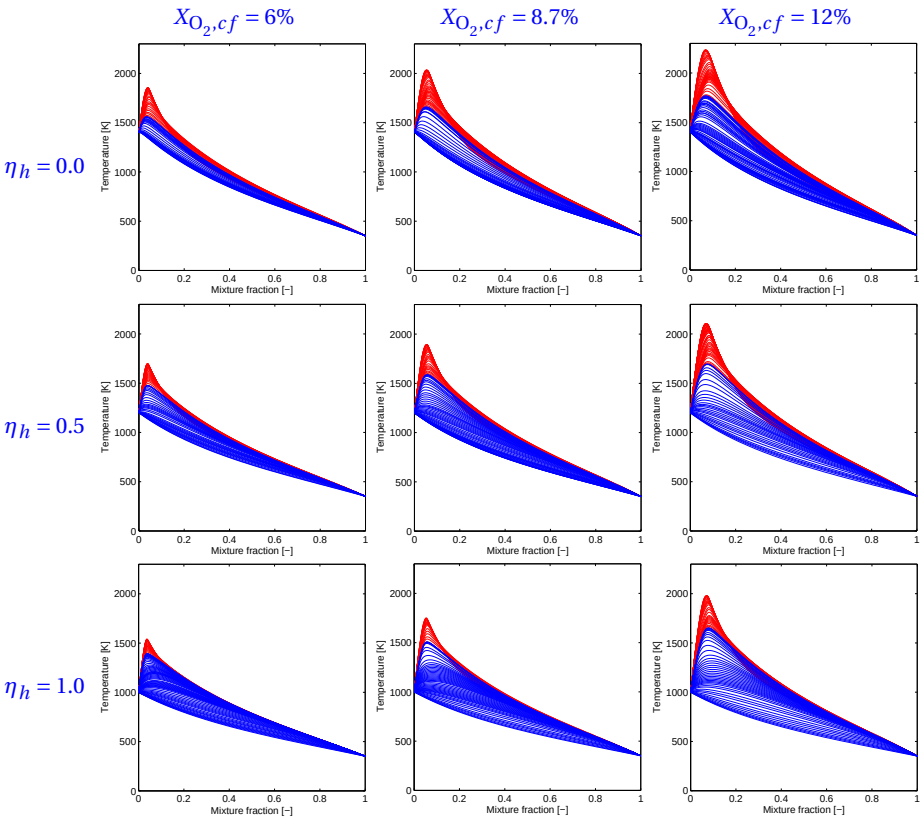

Figure 8.2: FGM data for temperature versus mixture fraction at different coflow O_2 concentration ($X_{O_2,cf}$) and different scaled enthalpy loss (η_h), coflow temperature $T_{cf} = 1400\ K$.

that a reaction status is much easier to establish and maintain in case H_{II}-B than in case H_{II}-A. The adiabatic flame temperature, T_{ad}, also increased at high coflow temperature condition. From Fig. 8.1, we can see that a strong influence on the T_{ad} comes from the coflow O_2 concentration. T_{ad} reaches 2230 K when $X_{O_2,cf}$ = 12%, while it is only 1841 K when $X_{O_2,cf}$ = 6%. This confirms the effectiveness of reducing the flame peak temperature by dilution of the oxidizer, as used in the MILD technology. These changes in the FGM tables will have further influences on the structure and other properties of the flame when they are used for simulation of DSHC flames, as will be further discussed in section 8.3.

8.2.3. SPRAY SUB-MODELS AND BOUNDARY CONDITIONS

Analysis of experimental data has shown that the flash-boiling phenomenon occurs in the atomization process of the DSHC burner [21]. When flash-boiling atomization happens, the dominant mechanism for liquid sheet breakup, and ligament formation is no longer the growth of Kelvin-Helmholtz waves on the liquid-gas interface, but the explosion of fuel vapor bubbles formed due to cavitation inside the atomizer chamber. This precludes the applicability of a conventional atomization model, such as the LISA (Linearized Instability Sheet Atomization) model [37]. A conditional droplet injection model was proposed based on analysis of available DSHC experimental data. In this model, the primary breakup is not simulated and poly-dispersed droplets are directly injected into the computational domain. The droplet injection direction and initial velocity both depend on its size, see the appendix for formulation of this model. This model was applied to the H_{II} case of the DSHC flame, and significantly improvements of all examined properties have been achieved compared with non-conditional injection model [21]. This model is applied to all cases studied here. Model parameters have been estimated from experimental data and are given also in the appendix.

The infinite conductivity model is employed together with Bird's correction to calculate the droplet heating and evaporation process. No sub-grid dispersion model is used for droplets, due to the very fine grid resolution. The droplet initial size distribution is given as Rosin-Rammler distribution. About two million numerical parcels are injected per second, but the specific number varies in different cases according to the liquid mass flow rate. The floww is calculated using an Eulerian-Lagrangian approach in Large Eddy Simulation (LES). Sub-grid stresses are closed with dynamic Smagorinsky model.

8.2.4. NUMERICAL DETAILS

The simulation in this study is carried out using the open source CFD package — OpenFOAM [38]. New libraries have been created for the FGM storage and retrieval algorithms and are dynamically linked to a customized solver for spray combustion. The new solver is referred to as "sprayFGMFoam". This new solver has been first validated against a gaseous lifted flame [39], and then applied to the H_{II} case from the DSHC dataset [21].

A 3D cylindrical mesh is used. The diameter of the domain is 200 mm, larger than the outer diameter of the coflow annulus (160 mm) to ensure correct coflow entrainment. Two different values of length of the domain were tested, respectively 300 mm and 150 mm. From the simulation using the large mesh, it was observed that the axial gradient of many properties are already very small at 150 mm thanks to the low Reynolds

number in these cases. The results from these two different domains show no considerable difference. Therefore a shorter domain with length of 150 mm is used for the simulations in the present study.

For the LES, we have reached the limit of resolution both spatially and temporally. The axial direction is discretized with 250 grid points (short mesh, $L = 150\ mm$), radial direction is discretized with 130 grid points and the circumferential direction is equally divided by 72 points, resulting in a total mesh size of 2.2 million. The smallest cell size 0.3 mm is about four times the diameter of the largest droplet diameter, using a finer mesh may violate the point source assumption. A very small growth ratio of 1.004 is used for the stream-wise grid points, leading to a nearly uniform fine mesh in the region of interest. The cell size is only 0.65 mm at 90 mm downstream the atomizer. The radial and circumferential grid spacing were set such that the aspect ratio is close to unity at the center region of $D < 80\ mm$ and $z < 90mm$, which is the region where spray injection and reaction happens. The diameter of the flame at the highest measured elevation ($Z = 60\ mm$) is 50 mm, indicated by location of the peak on the measured temperature profile, fits well in the fine mesh region. The time step is set such that within each time step, only about 10 parcels are injected. The corresponding maximum Courant number is less than 0.4. The ratio between sub-grid scale viscosity (μ_{sgs}) and molecular viscosity (μ) in this LES is below unity in the whole domain. Based of the high temporal and spatial resolution, our LES can be referred to as high-fidelity LES.

8.3. RESULTS AND DISCUSSION

In this section, the results of the simulations will be presented. Three cases from the DSHC database will be analyzed at first to validate the employed modeling approaches. The results of case H_{II} is then studied in detail in order to understand the flame structure. Based on the knowledge gained so far, the influence of coflow temperature and O_2 concentration will be investigated subsequently. Finally, these cases will be discussed in the framework of MILD combustion.

8.3.1. VALIDATION AGAINST EXPERIMENTAL CASES

Three experimental cases with varying coflow conditions have been simulated, and the results are carefully compared with experimental data in order to check the capability of the developed solver and modeling approaches in capturing variations of various flame properties with change of coflow conditions. The cases studied here are the H_I, H_{II} and H_{III} flames in the DSHC database [23]. As described in Table. 8.1, differences between these three cases lie in many aspects, including the coflow temperature, O_2 concentration, velocity as well as the mass flow rate of liquid fuel. Subsequently, the resulting spray and gaseous properties also differ from each other in these cases. In the following discussions, the droplet mean axial velocity, Sauter Mean Diameter (SMD) together with gas phase velocity and temperature are chosen as representative properties.

Spray combustion is distinguished from its gaseous counterpart mainly by the way the fuel (and oxidizer) is fed to the reaction process. For the former, the fuel is injected in the form of droplets, and supplied to the local environment via dispersion and evaporation. For a simulation, even if the combustion model correctly describes the generation

of products and heat, a deficiency in the local fuel concentration resulting from poor evaporation modeling can still ruin the accuracy of the results. This implies a crucial role of spray sub-models on an accurate prediction. With this in mind, droplet properties are first examined to reveal the performance of spray sub-models and their boundary conditions. Size-conditioned droplet mean axial velocity profiles at three stations increasingly far from the atomizer exit ($Z = 0\ mm$) are shown in Fig. 8.3. A general good agreement between simulation results and experimental data is observed for all three cases. The radial distribution of droplet velocity profiles from different cases are rather similar, except that in case H_I the droplets are only available within a small region. The reason for this is the rapid evaporation resulting form high coflow temperature. Due to high Stokes number, large droplets experience less velocity reduction from $Z = 10\ mm$ to $Z = 30\ mm$ in all three cases. This is well captured in the simulation. These results show that the dispersion and evaporation model employed perform reasonably well. Apart from this, the conditional droplet injection model proposed by the authors also contributes to the good agreement, as demonstrated in a previous study [21].

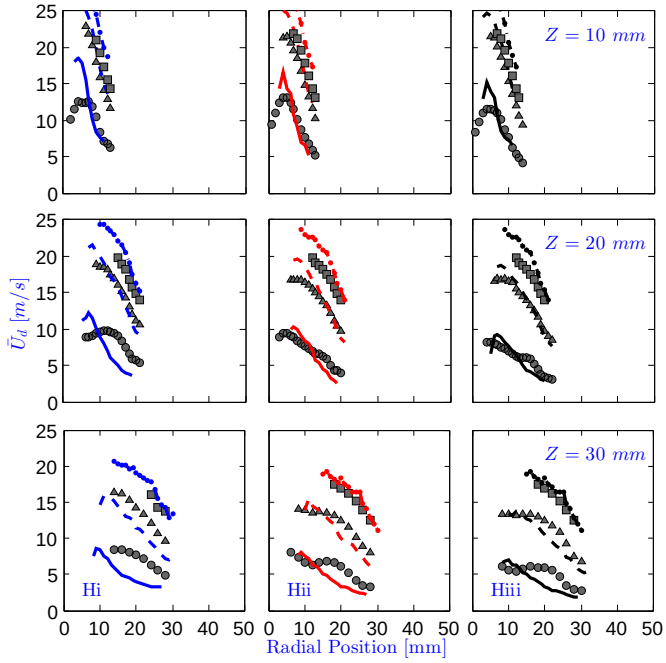

Figure 8.3: Radial profiles of mean axial velocity for different size droplets at various elevations. First column: case H_I, second column: case H_{II}, third column: case H_{III}. Lines: simulation results, symbols: experimental data. Solid-thick line: $10\ \mu m \leq D_p \leq 20\ \mu m$, dashed-thick line: $30\ \mu m \leq D_p \leq 40\ \mu m$, dotted line: $50\ \mu m \leq D_p \leq 60\ \mu m$.

Sauter Mean Diameter (SMD) is one of the parameters used to characterize the droplet size distribution. The advantage of using SMD over other mean diameter definitions is that it preserve the total volume-to-surface ratio of the spray cloud compared to a mono-

size spray with this SMD as droplet diameter, which is important for characterization of trends in the spray evaporation. Fig. 8.4 gives the SMD of the three cases. Both the trend and magnitude of the SMD are correctly reproduced by the simulations. Large droplets have more ballistic trajectories and remain at the outer edge of the spray cloud. Small droplets have shorter relaxation time, and therefore can be easily convected toward the region near the axis of the atomizer by the entrainment of the coflow. As expected, SMD is smaller in case H_I compared to the other two cases due to rapid evaporation. The droplet diameter at the outer edged of the spray is over predicted in case H_{III}, probably related to the large spray angle specified in the conditional injection model for this case.

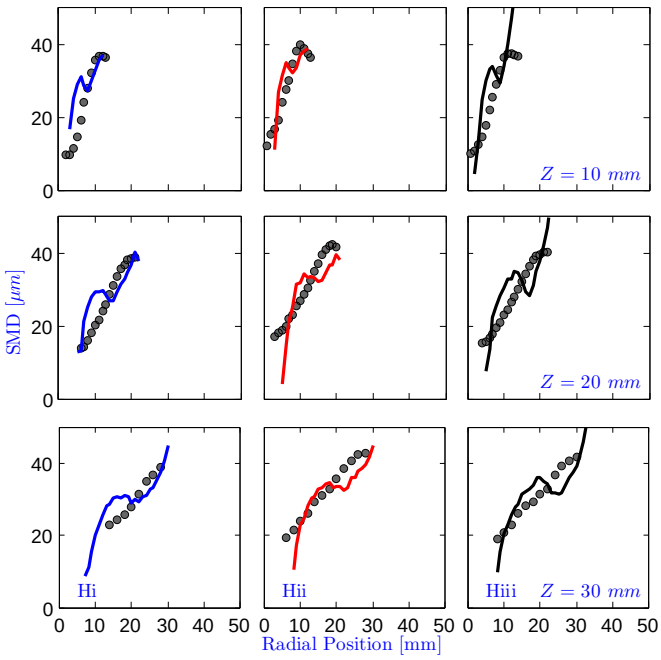

Figure 8.4: Radial profiles of droplet SMD at several elevations. First column: case Hi, second column: case Hii, third column: case Hiii. Lines: simulation results, symbols: experimental data.

Gas phase velocity (Fig. 8.5) is in very good agreement for all three cases. At $Z = 10\ mm$, the dips on both the axial and radial velocity profiles indicating strong entrainment of coflow towards the spray central region. In Fig. 8.6, good agreement on the gas phase mean temperature is observed. The H_{II} matches best with experimental data in terms of the values and radial locations of peak temperature as well as the width of the high temperature region, indicating an accurate reproduction of the turbulence-chemistry interaction process by the current modeling approach. Despite the overall agreement, some deficiencies are noticeable in the results of cases H_I and H_{III}. For H_I, the temperature in the center region is over-predicted. A exact responsibility for this mismatch is not clear due to the strong coupling between different models and processes. The radial position of the peak temperature in cases H_I and H_{III} are both predicted a bit

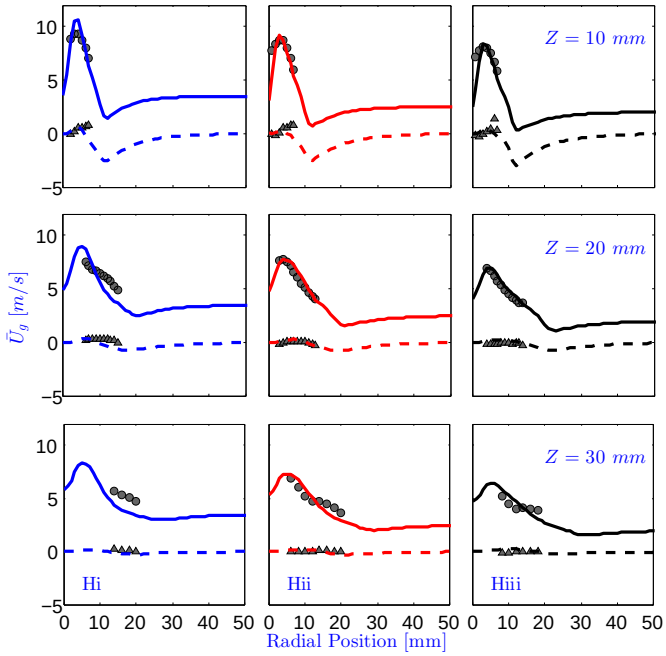

Figure 8.5: Radial profiles of gas phase mean velocity at several elevations. First column: case Hi, second column: case Hii, third column: case Hiii. Lines: simulation results, symbols: experimental data. Circle and solid line: axial velocity, triangle and dashed line: radial velocity.

larger than those measured at $Z = 50\ mm$. This is believed to be related to the large spray angle specified for these two cases.

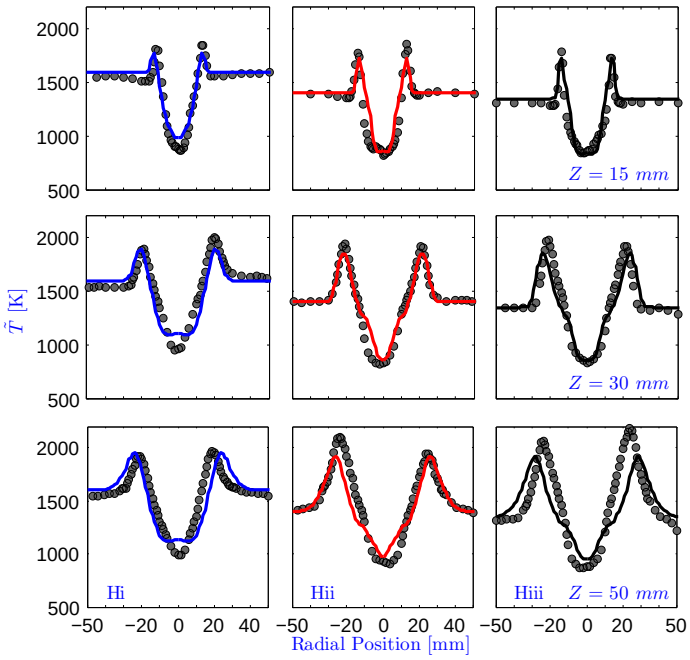

Figure 8.6: Radial profiles of gas phase mean temperature at several elevations. First column: case Hi, second column: case Hii, third column: case Hiii. Lines: simulation results, symbols: experimental data.

The peak temperature at $Z = 50\ mm$ is under-estimated in case H_{III}. An explanation for this goes as follows: the DSHC burner has a relative large diameter of coflow ($D_{cf} = 160\ mm$) to prevent ruining of desired MILD condition by the entrainment of laboratory air. However, as shown in [23], from $Z = 50\ mm$ downstream, the influence of laboratory air is non-negligible. The room temperature air influences the DSHC flame in two ways: first, a decrease of mixture temperature; second a increase of O_2 concentration. These two effects have opposite impact on the flame temperature. However, as will be shown in sections 8.3.3 and 8.3.4, the rise of flame temperature due to increased O_2 is stronger than its reduction due to decreased initial mixture temperature. Therefore the entrained air increases the flame peak temperature. Comparing the experimental temperature profiles between $r = 30$ to 50 at two axial stations $Z = 30$ and 50 in case H_{III}, the decrease of the coflow temperature is clear at $Z = 50\ mm$, this is a sign of air entrainment. The consequence of this is the high peak temperature, around 2200 K, in case H_{III}. This air entrainment is not considered in the current two-stream FGM model, therefore, an under-prediction of the peak temperature at high elevations is not surprising.

In conclusion, although some deficiencies exist, main features and trends for the three experimental cases are correctly captured. At $Z = 30\ mm$, where influence of laboratory air is negligible, the peak temperatures of these three cases are in very good

agreement with experimental data. The flame lift-off height is an important parameter for model validation. Because the accurate prediction of lift-off height requires correct representation of dominating physics by individual models, and more importantly, the coupling between them. In [23] the lift-off heights of these three flames were defined based on the average flame luminescence from photographs. A correct reproduction of the luminescence demands the concentration of OH*, which is not included in the chemical mechanism employed in the current study [40]. Furthermore, it is the trend of flame properties with respect to change of coflow conditions that is the main focus of the current study. Therefore, a exact match of the experimentally defined lift-off height is not attempted. Here two different criteria have been adopted to define lift-off height in the numerical results. The first one is the lowest axial location where the temperature has increased by 50 K with respect to the inlet coflow value (T_{cf}), and the second one is based on the iso-surface of $\tilde{Y}_{\mathrm{OH}} = 0.001$. Values of lift-off height are listed in Table. 8.2. As can be seen, the increasing trend of lift-off height from case $\mathrm{H_I}$ to $\mathrm{H_{III}}$ is correctly predicted. The two definitions for lift-off height in the simulation show a little difference on the specific values, but are reflecting the same trend. Hereafter, the definition based on the temperature increase will be used.

Table 8.2: Lift-off hight in cases Hi, Hii and Hiii.

Case	Sim. ($\tilde{Y}_{\mathrm{OH}} = 0.001$, mm)	Sim. ($T_{cf} + 50\ K$, mm)	Exp. (luminescence, mm)
$\mathrm{H_I}$	6	5	7.5
$\mathrm{H_{II}}$	10	9	13
$\mathrm{H_{III}}$	12	11	18

Based on visualization, it was also found the flame width increases from case $\mathrm{H_I}$ to $\mathrm{H_{II}}$, as shown in Fig. 8.7a. This phenomenon is well captured in the present study, as can be seen form the OH iso-surface shown in Fig. 8.7b. A possible explanation for the change of flame width can be given like this: as the coflow temperature increases from case $\mathrm{H_{III}}$ to $\mathrm{H_I}$, the droplet evaporation rate increases, leading to a fast reduction of droplet size. Trajectories of these smaller droplets are easier changed by coflow, therefore they can not reach far radial location and deliver fuel vapor there. Therefore the flame front is formed at a smaller radius. This explaination implies that good prediction of the flame width is especially a test for the dispersion and evaporation models.

8.3.2. FLAME STRUCTURE

In the previous section, we have demonstrated that the current modeling approach is capable of accurately predicting major spray and gaseous properties as well as their change with variation of coflow conditions. In this section, we aim to make a detailed analysis of the structure of the DSHC flame, to elucidate the mechanism of the influence of coflow conditions on the flame structure.

In Fig. 8.8 we present the mean gas phase temperature, its standard deviation, and snapshots of the mass fraction of $\mathrm{O_2}$, $\mathrm{C_2H_5OH}$, CO and $\mathrm{HO_2}$ as well as two flame indices on a vertical cross section. de Joannon et al [41] found that fuel actually undergoes a two-stage combustion under MILD condition. In the first stage, diluted rich mixture is

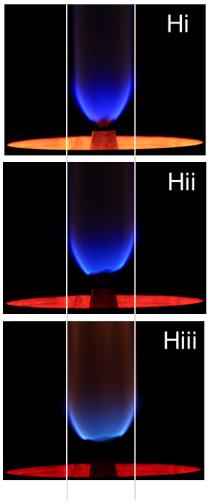

(a) Experimental visualization of three cases [23].

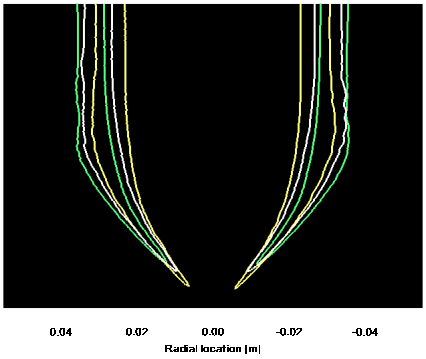

(b) Iso-surface of $\tilde{Y}_{OH} = 0.001$, yellow: H_I, white: H_{II}, green: H_{III}.

Figure 8.7: Comparison of flame width.

formed, the mixture temperature is relatively low but still higher than the self-ignition value, and this is particularly suitable for pyrolytic or reforming stages leading to H_2 and CO. The second stage is the further oxidation of these intermediate fuels. Therefore the commonly used flame index, which is defined based on the gradients of major fuel and oxygen, is insufficient for the analysis of MILD combustion. The authors introduced flame indices also based on the intermediate fuels. The two flame indices used in this study to analyze the flame structure are defined as follows:

$$FI_{C2H5OH} = \frac{\nabla Y_{C_2H_5OH} \cdot \nabla Y_{O_2}}{|\nabla Y_{C_2H_5OH} \cdot \nabla Y_{O_2}|}, \tag{8.1}$$

and

$$FI_{C2H5OH} = \frac{\nabla Y_{CO} \cdot \nabla Y_{O_2}}{|\nabla Y_{CO} \cdot \nabla Y_{O_2}|}. \tag{8.2}$$

On the contour plot of mean temperature, the iso-surface of $T = T_{cf} + 50\ K$ was superimposed to help identifying the high temperature region. Sidey et al [42] carried out 1D laminar simulation of MILD combustion of kerosene, and they found that the $Y_{OH} \times Y_{CH_2O}$ is still a good representation of the reaction zone in MILD combustion. Same conclusion was drawn also by Minamoto et al [43] from DNS results. Medwell and Dally [22] et al have measured the simultaneous OH, CH_2O and temperature fields on a jet in hot coflow burner, and the results showed that the temperature indeed increases from the region where O_2 and CH_2O overlaps. Based on these results, iso-surface of $Y_{CH_2O} \times Y_{OH} = 1 \times 10^{-9}$ (white lines) are superimposed on the contour plots of species mass fraction and flame indices to help identify main reaction regions (RRs).

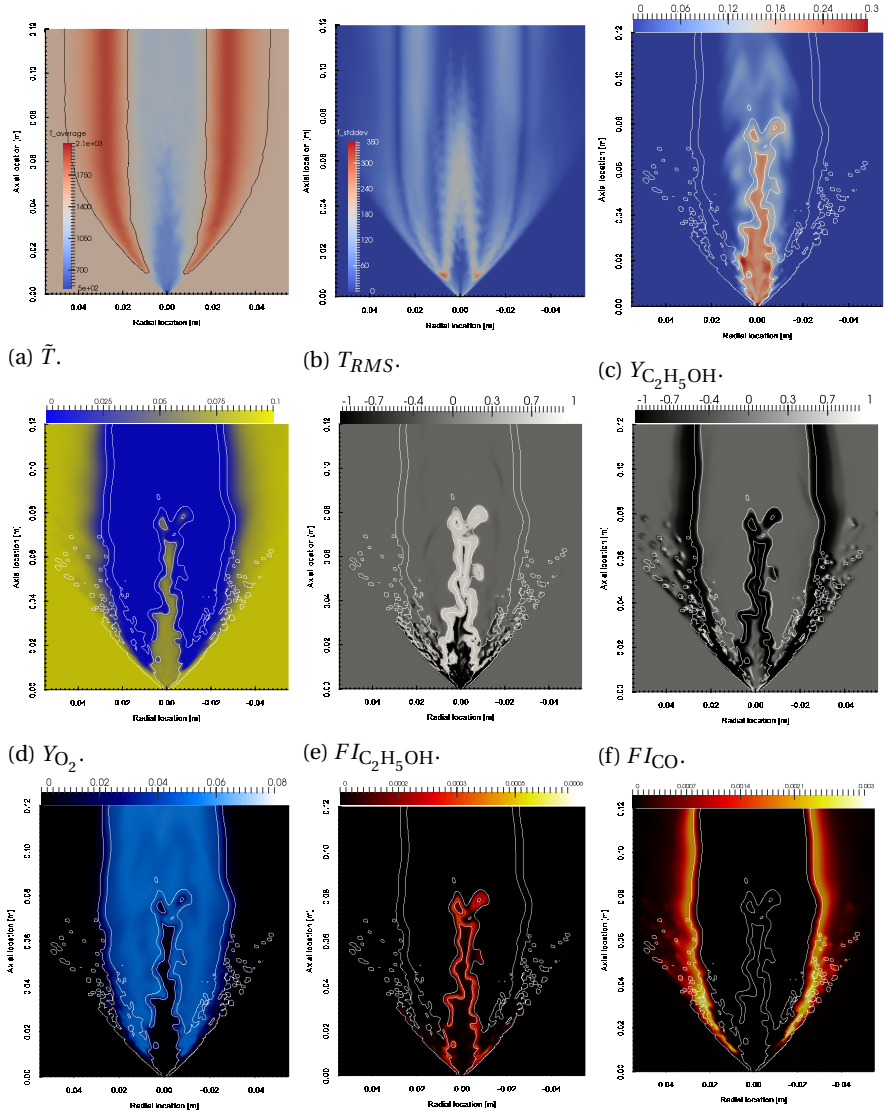

(a) $\tilde{T}$.

(b) T_{RMS}.

(c) $Y_{C_2H_5OH}$.

(d) Y_{O_2}.

(e) $FI_{C_2H_5OH}$.

(f) FI_{CO}.

(g) Y_{CO}.

(h) Y_{HO_2}.

(i) Y_{OH}.

Figure 8.8: Various properties on a vertical cross section for case Hii.

First of all, we can clearly infer from these plots that there are two main RRs, the outer “U" shape one and the inner “inversed-V" shape one. These two RRs are connected to each other in the near injector region. These two RRs are further evidenced in Fig. 8.9, where mean and standard deviation of gas phase temperature for the case H_{II} are given. The regions between two red or two black dashed lines have high value of T_{RMS} from measurement. The near axis one corresponds to the change of slope on the mean temperature profile, is the inner RR. The outer region coincides well with the peak temperature, and is the outer RR. The temperature fluctuation is under-estimated in the far radial region by the simulation, but in the reaction region the underestimation is by a factor of about two only. Especially, peaks of T_{RMS} related to the two RRs are also observed in the simulation results, and their radial locations are close to their experimental counterpart at low elevations but shifted inwards at high elevations ($Z = 50\ mm$). The under-prediction of T_{RMS} in far radial regions can be attributed to the exclusion of fluctuations at the inlet boundary, as revealed in our previous study [20]. A first attempt has been made to consider the temperature fluctuations at boundary via random fluctuation of enthalpy at inlet. However, it turns out that these uncorrelated fluctuations damps very quickly, and do not provide the desired level of fluctuations at downstream. Therefore, those results are not shown here, and all cases in the present study do not include the temperature fluctuation at the inlet.

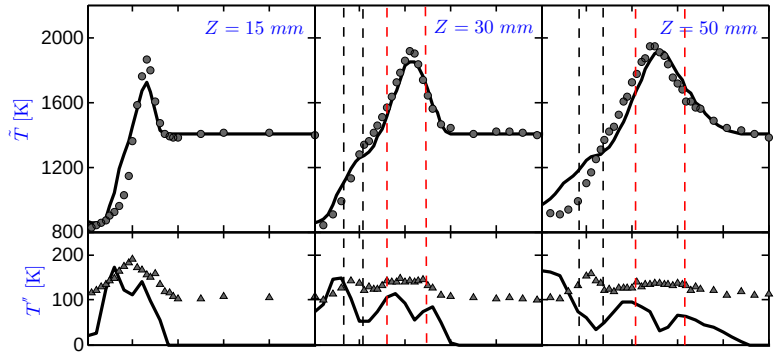

Figure 8.9: Radial profiles for mean and standard deviation of gas phase temperature for case H_{II}, black lines indicating inner RR and red lines the outer RR.

Now we have evidenced the existence of the two RRs in the DSHC flame. Then the next question is what is the reason for the two-RRs structure. It can be seen from Figs. 8.8d and 8.8g that the inner and outer RRs coincide well with the boundaries of the CO rich region, which is also the O_2-free region. $FI_{C_2H_5OH}$ clearly shows that premixed reaction of C_2H_5OH happens at the inner RR, and non-premixed reaction of C_2H_5OH occurs at the bottom of the outer RR. Care has to be taken to interpret the results of FI_{CO}, which shows negative value in both RRs. The negative value at outer RR reflects that this flame front is actually created by the non-premixed reaction of CO with O_2 that comes from the coflow. The negative value of FI_{CO} in the inner RR is actually due to the local production of CO from pyrolysis of C_2H_5OH in the inner RR. In the center region, high concentration of C_2H_5OH is generated due to the rapid evaporation of small droplets.

Entrainment of coflow also brings O_2 into this region. Therefore a rich mixture is formed in this region owing to the low O_2 concentration in the coflow. Due to the high temperature of the coflow, the temperature of the mixture in this region is still higher than the self-ignition point of C_2H_5OH (638.15 K). These hot-fuel rich mixture is favorable for pyrolysis process, as evidenced by the high HO_2 concentration at the inner RR. Almost all O_2 is consumed in this inner RR, but there is still some C_2H_5OH left that continuously to react outside the inner RR. During the pyrolysis process, large amounts of CO and H_2 (not shown here) are produced. These intermediate fuels are transported outwards, and finally react with the O_2 from coflow at the outer RR. The high concentration of OH is only observed at the outer RR, this is in consistent with the experimental flame luminescence (see Fig. 8.7a). The mean temperature field clearly shows that the outer RR is the main heat release region.

In summary, the DSHC H_{II} flame consists of two RRs. The inner one is created by the fuel decomposition in high temperature - fuel rich mixture formed from the rapidly evaporated small droplets in entrained hot-diluted coflow. The reaction at the inner RR converts C_2H_5OH to intermediate species like CO and H_2, and the non-premixed reaction of the latter forms the outer RR. The outer RR is the main heat release region, while the inner one only leads to local peak of T_{RMS} and change of slope of the $\tilde{T}$ profiles. The two-RR structure flame agrees with the two stage combustion theory of de Joannon et al [41]. The ballistic motion of large droplets and the fuel wake left behind them also forms a small non-premixed reaction region of C_2H_5OH at the bottom of the “U" shape outer RR. Single or group droplet combustion is also observed in the simulation from the isolated pockets of heat release region ($Y_{CH_2O} \times Y_{OH}$). It can be expected that coflow conditions — T_{cf}, $X_{O_2,cf}$ — can significantly influence the structure via the influences on the droplet evaporation rate, the mixture conditions formed in the center and the ignition delay times. Further investigation on these influences will be presented in the following sections.

8.3.3. INFLUENCE OF COFLOW TEMPERATURE

To gain further insight on the influence of coflow temperature on the flame structure, we present in this section three cases that differ from each other only on the coflow temperature. The cases analyzed in this section are “H_{II}-A”, “H_{II}” and “H_{II}-B”, respectively having coflow temperature 1200 K, 1400 K and 1600 K, as listed in Table. 8.1.

The mean temperature and its standard deviation fields for these three cases, shown in Fig. 8.10 and 8.11, are good starting points for discussion. It is interesting to observe that the appearance of the flame changes significantly with the coflow temperature. For case H_{II}-A, which has the lowest coflow temperature, the flame is lifted to far downstream ($Z \approx 45\ mm$) of the atomizer exit, whereas, in case H_{II}-A, $T_{cf} = 1600\ K$, the flame is stabilized very close to the atomizer exit ($Z \approx 5\ mm$). Also interesting, from the supplementary video (showing the transient ignition and stabilization phase) one can clearly see that the H_{II}-A flame first ignites far downstream, and then propagates upstream and stabilizes at around $Z \approx 45\ mm$. While for case H_{II}-B, the reaction starts almost immediately after the droplets been injected into the domain, and local auto-ignition plays an important role on the flame stabilization. The contours of T_{RMS} show that strong temperature fluctuations are present in the inner RR for case H_{II}-A and the outer RR for case

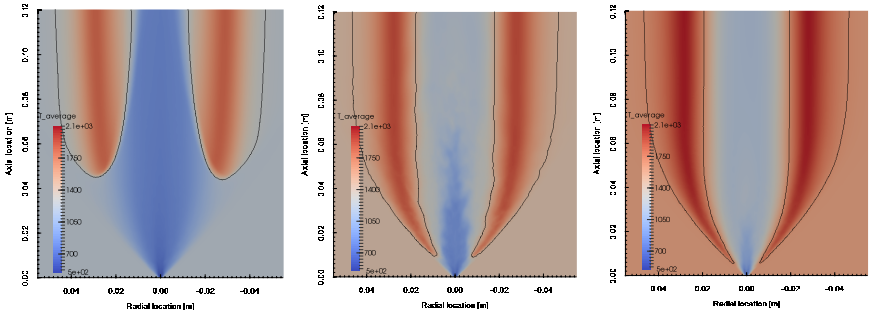

(a) Case H_{II}-A, $T_{cf} = 1200\ K$ (b) Case H_{II}, $T_{cf} = 1400\ K$ (c) Case H_{II}-B, $T_{cf} = 1600\ K$

Figure 8.10: Average temperature on a vertical cross section from cases with different coflow temperature.

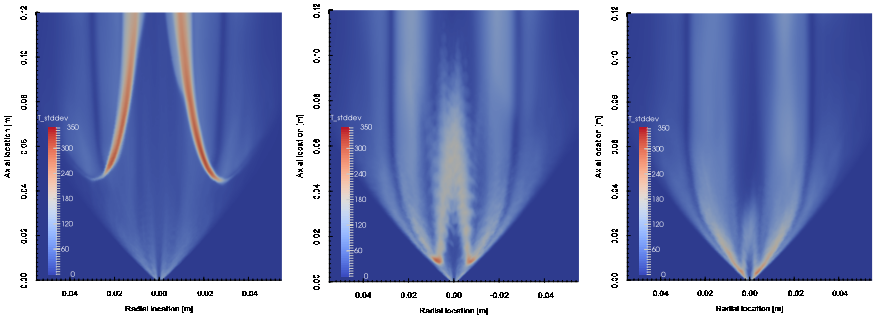

(a) Case H_{II}-A, $T_{cf} = 1200\ K$ (b) Case H_{II}, $T_{cf} = 1400\ K$ (c) Case H_{II}-B, $T_{cf} = 1600\ K$

Figure 8.11: Temperature standard deviation on a vertical cross section from cases with different coflow temperature.

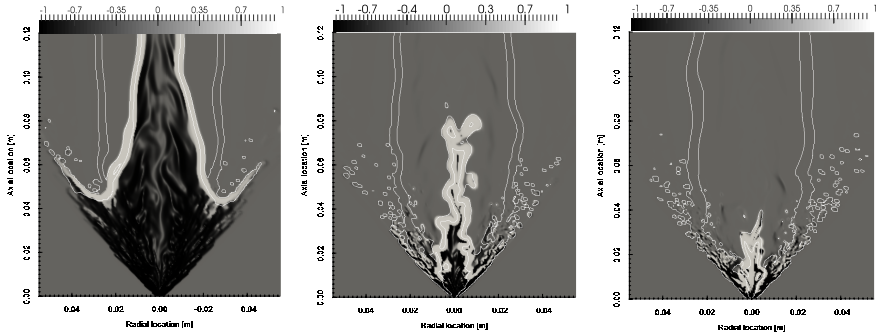

(a) Case H_{II}-A, $T_{cf} = 1200\ K$ (b) Case H_{II}, $T_{cf} = 1400\ K$ (c) Case H_{II}-B, $T_{cf} = 1600\ K$

Figure 8.12: Snapshots of FI_{C2H5OH} on a vertical cross section from cases with different coflow temperature, positive value indicating premixed combustion, negative value meaning non-premixed combustion.

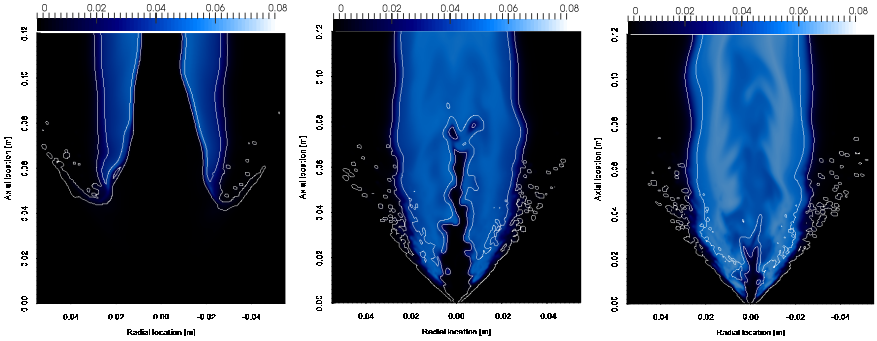

(a) Case H_{II}-A, $T_{cf} = 1200\ K$ (b) Case H_{II}, $T_{cf} = 1400\ K$ (c) Case H_{II}-B, $T_{cf} = 1600\ K$

Figure 8.13: Snapshots of Y_{CO} on a vertical cross section from cases with different coflow temperature.

H_{II}-B. And for case H_{II}, temperature fluctuations in both RRs are roughly on the same order. This implies that the role and importance of the two RRs are changed by varying T_{cf}.

The flame index of C_2H_5OH shown in Fig. 8.12 sheds light on the reason of the aforementioned changes. For cases H_{II} and H_{II}-B, there are still two RRs present. In case H_{II}-B although the diffusion reaction at the bottom of the outer RR is stronger, and the area of the inner RR considerably shorter. In case H_{II}-A, however, it is very interesting to see that the flame is stabilized by a triple flame which is typically seen in gaseous partially premixed combustion [44]. Triple flame for spray combustion has also been observed in the studies of [24, 25]. We can infer from Fig. 8.12a that the two branches sitting at the sides are created by the non-premixed combustion of C_2H_5OH. The inner one being fuel rich, which leads to a formation of CO, see Fig. 8.13a. The outer branch is fuel lean and all C_2H_5OH are directly converted to final products CO_2 and H_2O; no high concentration of CO is generated in this RR. The middle RR sits exactly on the outer border of the high CO region, and is the formed by the non-premixed combustion of CO generated from the inner RR. Evidence for this argument has been given in the previous section.

Table 8.3: Lift-off hight in cases with different coflow temperature.

Case	H_{II}-A	H_{II}	H_{II}-B
Lift-off height $[mm]$	45	9	5

The lift-off height of these three cases is given in Table. 8.3. It increases with decrease of T_{cf}. From case H_{II} to H_{II}-A, less than 15% reduction of coflow temperature results in a five times larger lift-off height.

Summary of findings in this section: the temperature of the coflow has a significant influence on the spray flame structure. The flame lift-off height decreases quickly with increase of T_{cf}. The inner premixed RR is strengthened at low T_{cf}. The outer RR changes from premixed RR at low T_{cf} to non-premixed RR at high T_{cf}, and is actually the main heat release region. A triple flame is observed in case H_{II}-A, which has the lowest T_{cf}.

Two branches at the inner and outer sides of the flame base are created respectively from the lean and rich premixed combustion of C_2H_5OH. The middle RR is due to the non-premixed reaction of CO generated at the inner RR. In the experimentally studied cases discussed in section 8.3.1, the triple flame phenomenon did not occur showing that it is limited to a narrow range of operating conditions.

8.3.4. INFLUENCE OF COFLOW O_2 CONCENTRATION

The O_2 concentration is another important parameter that can influence the structure of the flame. In a real MILD furnace, the O_2 concentration in the reaction zone is directly related to the mixing of air with recirculated combustion products. A better understanding of the O_2 concentration on the MILD condition is essential for the design and optimization of the furnace. The cases examined in this section are H_{II}-C, H_{II} and H_{II}-D, respectively containing 6%, 8.7% and 12% O_2 by volume in the coflow, $T_{cf} = 1400\ K$ for all three cases, see Table. 8.1.

Table 8.4: Lift-off hight in cases with different coflow O_2 concentration.

Case	H_{II}-C	H_{II}	H_{II}-D
Lift-off height $[mm]$	12	9	6

As shown in Table. 8.4, the lift-off height of the flame decreases almost linearly with increase of O_2 volume fraction in the coflow. This is because at lower O_2 concentration, larger amount of coflow is required to burn unit mass of fuel. To provide it, entrainment over a large distance is needed, resulting in a higher lift-off height. This is also consistent with the experimental observation that the lift-off height increases almost linearly with increase of liquid mass flow rate. Another impact of the coflow O_2 concentration is the strength of the inner RR, as shown in Figs. 8.14 and 8.15. With more O_2 contained in the coflow, the equivalence ratio is closer to unity in the center premixed region in case H_{II}-D. Therefore, intense premixed combustion of C_2H_5OH can take place in a small region. This is the reason that the inner RR in the H_{II}-D case is smaller and stronger, as indicated by the higher T_{RMS} in the center region in Fig. 8.15c. In the H_{II}-C, the inner RR is no longer a connected area, but there are distributed irregular shape structures, this can be called “distributed reaction” [24].

Considerable change of CO concentration is observed in these three cases, see Fig. 8.16. The Y_{CO} in case H_{II}-D is much higher than in case H_{II}-C. This is related to the reaction happening in the inner RR. In case H_{II}-D, most C_2H_5OH is converted to CO in the inner RR, whereas in case H_{II}-C, only a small part of fuel vapor is oxidized due to lack of O_2, and a considerable amount of C_2H_5OH still remains at the outlet of the computational domain, see Fig. 8.17. The peak temperature of the flame significantly increases with the O_2 concentration contained in the coflow, shown in Fig. 8.14; some further discussion on this aspect will be given in next section. Fig. 8.18 shows that decrease of the O_2 level in the coflow, leads to a suppression of OH as a result of the reduced temperature, this is consistent with findings from the gaseous methane jet in hot-vitiated coflow flame [45].

Summary of findings in this section: The flame lift-off height varies almost linearly with the coflow O_2. The $X_{O_2,cf}$ alters the role of the two RRs. At high $X_{O_2,cf}$, the inner

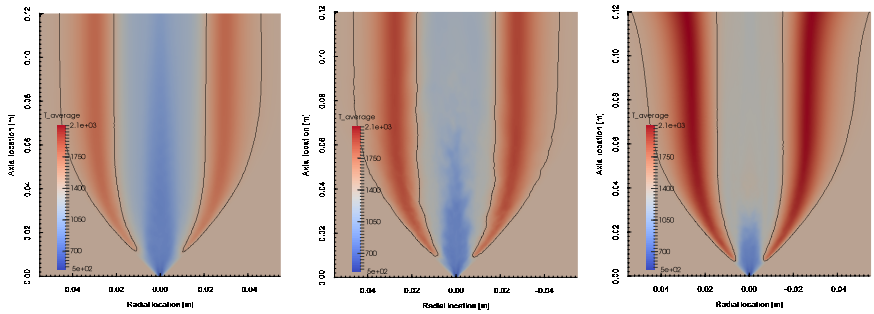

(a) Case H_{II}-C, $X_{O,cf} = 6\%$ (b) Case H_{II}, $X_{O,cf} = 8.7\%$ (c) Case H_{II}-D, $X_{O,cf} = 12\%$

Figure 8.14: Average temperature on a vertical cross section from cases with different coflow O_2 concentration.

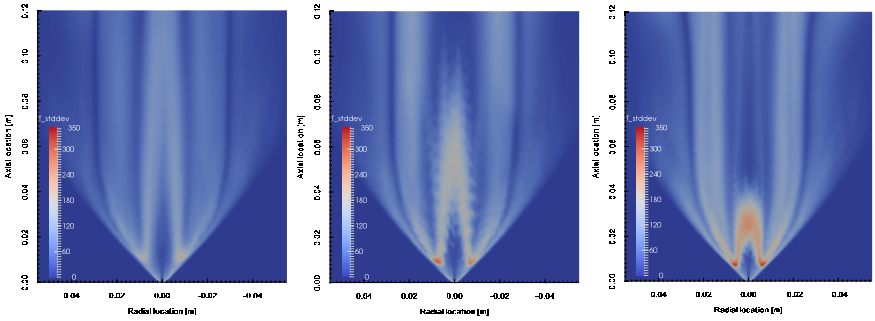

(a) Case H_{II}-C, $X_{O,cf} = 6\%$ (b) Case H_{II}, $X_{O,cf} = 8.7\%$ (c) Case H_{II}-D, $X_{O,cf} = 12\%$

Figure 8.15: Temperature standard deviation on a vertical cross section from cases with different coflow O_2 concentration.

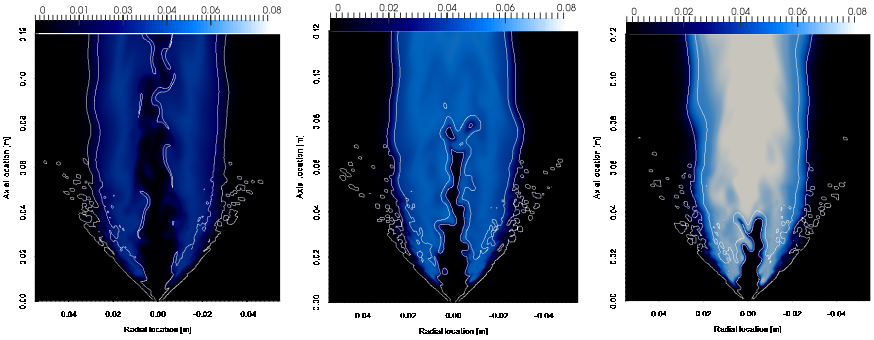

(a) Case H_{II}-C, $X_{O,cf} = 6\%$ (b) Case H_{II}, $X_{O,cf} = 8.7\%$ (c) Case H_{II}-D, $X_{O,cf} = 12\%$

Figure 8.16: Snapshots of Y_{CO} on a vertical cross section from cases with different coflow temperature.

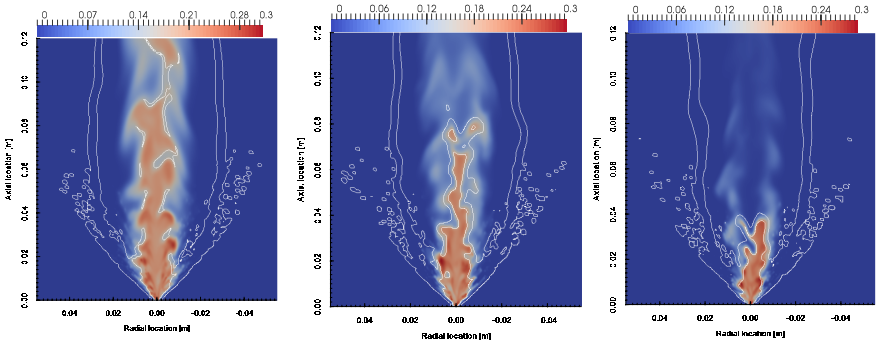

(a) Case H_{II}-C, $X_{O,cf} = 6\%$ (b) Case H_{II}, $X_{O,cf} = 8.7\%$ (c) Case H_{II}-D, $X_{O,cf} = 12\%$

Figure 8.17: Snapshots of $Y_{C_2H_5OH}$ on a vertical cross section from cases with different coflow temperature.

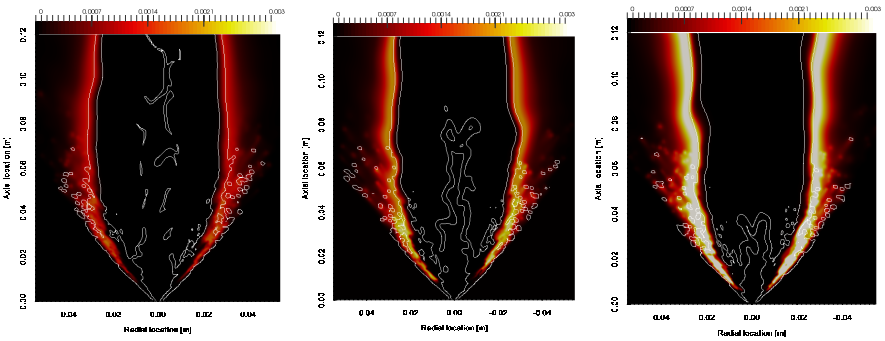

(a) Case H_{II}-C, $X_{O,cf} = 6\%$ (b) Case H_{II}, $X_{O,cf} = 8.7\%$ (c) Case H_{II}-D, $X_{O,cf} = 12\%$

Figure 8.18: Snapshots of Y_{OH} on a vertical cross section from cases with different coflow temperature.

premixed RR is shorter and stronger due to more O_2 entrained with the coflow. The inner RR becomes disconnected and distributed at low $X_{O_2,cf}$. The flame peak temperature is significantly increased in the case with highest $X_{O_2,cf}$. Considerable increase of CO was observed in the case with highest $X_{O_2,cf}$.

8.3.5. MILD OR NOT?

The above analysis has revealed the profound influences of coflow conditions on the flame structure. In the present section, we will make an overall comparison of all cases studied and try to answer the question which cases can be categorized as MILD combustion, and how the coflow conditions influence the combustion regime. First, in Fig. 8.19, temperature profiles from the H_{II} case and four auxiliary cases are shown at various elevations. No noticeable temperature rise was observed in case H_{II}-A below $Z = 50\ mm$. This is due to the high lift-off distance in this case, as shown before. It can also be seen that the overall temperature rises as the coflow temperature increases, when case H_{II}-A, H_{II} and H_{II}-B are compared. The O_2 level in the coflow mainly affects the inner branch (including the peak) of the temperature profiles. The higher concentration of O_2 in the coflow provides more O_2 for the inner premixed region leading to a enhanced inner RR. $X_{O_2,cf}$ has a considerable impact on the flame peak temperature, the highest value of which is observed in case H_{II}-D with $X_{O_2,cf} = 12$.

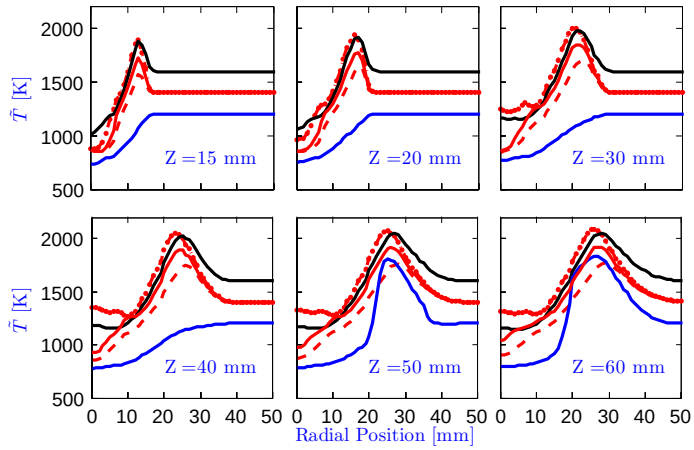

Figure 8.19: Radial profiles for mean gas phase temperature, red solid line: case H_{II}, blue slide line: case H_{II}-A, black solid line: case H_{II}-B, red dashed line: case H_{II}-C, red dotted line: case H_{II}-D.

According to Cavaliere and de Joannon [3], a combustion process is named Mild if the following two conditions are satisfied: (1) the inlet temperature of the reactant mixture is higher than mixture self-ignition temperature, (2) the maximum allowable temperature increase with respect to inlet temperature during combustion is lower than mixture self-ignition temperature (in Kelvin). As shown in Table. 8.1, the first condition is satisfied in all cases, namely $T_{cf} > T_{si} = 638.15\ K$.

All seven cases studied in the current paper are placed in $T_{peak} - T_{cf}$ space in Fig. 8.20.

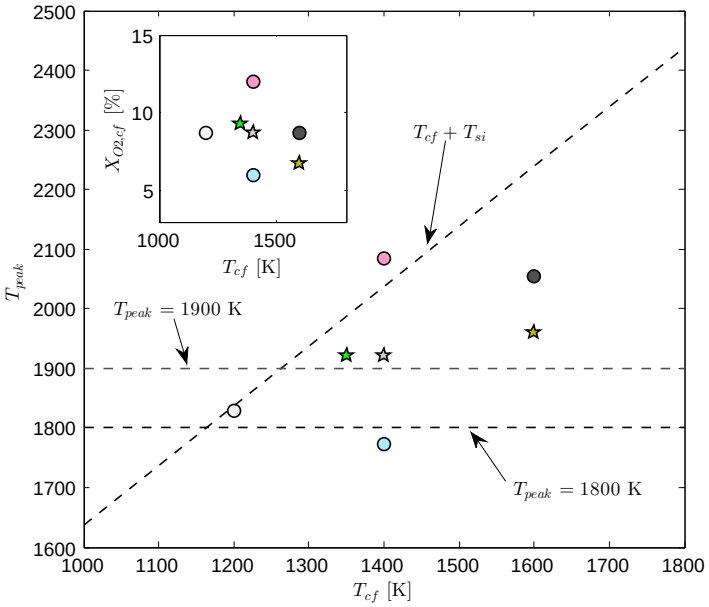

Figure 8.20: Peak temperature for all cases studied. Small plot describes cases in the $X_{O_2,cf} - T_{cf}$ space.

Their position in $X_{O_2,cf} - T_{cf}$ space is also shown in the small plot of Fig. 8.20 to help to identify each other. The line of $T_{peak} + T_{si}$ is also displayed. When a case is under this line means its temperature increase is lower than the self-ignition value, and satisfies condition (2) of Cavaliere and de Joannon' definition, and therefore is in MILD mode. As can be clearly seen, only case H_{II}-D (pink circle) is above this limit and all other cases are in the MILD regime. As explained in section 8.3.1, the real DSHC flame is influenced by the surrounding air at $Z = 50\ mm$ downstream. Due to the air entrainment, the measured flame peak temperature at high elevations is quite high, and if those data are used to calculate the $T_{peak} - T_{cf}$, then the cases H_I and H_{III} would not be in the MILD regime. But when the influence of environmental air is eliminated in the simulation, these three cases are well in the MILD regime. This suggests that a wider coflow is necessary for further experimental study to shift the influence of surrounding air further downstream, and to create a larger region that is under the MILD condition.

The case H_{II}-A is just below the border of the MILD/non-MILD regimes, meaning that it can easily be shifted to non-MILD condition with little change in coflow conditions. We find from Fig. 8.20 that cases with high air preheating and high O_2 dilution are well below the MILD limit, while cases with low air preheating and high O_2 dilution are very close or even above the MILD limit. This clearly suggests that to achieve MILD conditions for spray combustion, high air preheating and O_2 dilution are required. These are consistent with those for gaseous MILD combustion [3].

One of the main targets of MILD combustion is to minimize emission of NOx, which is achieved by suppression of peak temperature in the combustion system. The above definition of MILD combustion does not reflect this aspect. It was reported that forma-

tion of NOx, especially the thermal NOx, increases significantly when the flame temperature is above 1600°C [4]. If this condition is also applied in the diagram (Fig. 8.20), one sees that only two cases are under the T_{peak} = 1900 K line. If the limitation of the flame peak temperature is further restricted to 1800 K, only case H_{II}-C, which has the lowest coflow O_2 level and moderate coflow temperature, meets all requirements.

The control of CO emission is also of importance. Weber et al [10] found that in a MILD furnace, the light fuel oil flame shows substantially larger CO concentration than the heavy fuel oil flame. Comparing Fig. 8.13 and 8.16, we find that the “best" MILD case in the present study (case H_{II}-D) has the highest CO mass fraction. This issue deserves attention in future studies.

Another aspect deserving attention is the combustion stability. The dilution of the oxidizer in the MILD combustion regime essentially prolongs the ignition delay time. In sections 8.3.3 it was shown that the flame lift-off height strongly depends on the coflow temperature. At high temperature the flame stabilizes very close to the injector exit, whereas, at relative low coflow temperature, the flame can only stabilize at far downstream, where the strain is low. The message from this result is that although the H_{II}-A case can be categorized as MILD combustion based on the definition of Cavaliere and de Joannon, it may not be possible to establish a stable reaction zone if such a condition is applied to real furnace. In this sense, the air preheating in MILD combustion does not only increases the thermal efficiency but is also essential to establish and maintain the reaction.

8.4. CONCLUSION

In the present paper, we have studied the influence of coflow conditions on the structure of the Delft Spray in Hot Coflow (DSHC) flames. The developed modeling approach was first applied to three different experimental cases. Results of these cases were carefully compared with experimental data. It was shown that major properties like droplet velocity, SMD, gas phase velocity and temperature can be reproduced with good accuracy. The trends of flame lift-off height and flame width with change of coflow conditions were also properly captured. This first step has demonstrated the capability of the developed modeling approaches and solver for predicting a spray in different conditions. The second step was to extend the simulations to four more virtual cases, which differ from each other only be coflow temperature or O_2 concentration. The purpose of this step is to isolate the influences of these two parameters which are important for a real MILD furnace design and operation. This strict parameter study was not made in the experimental study due to limitations of the setup. Major findings in the present paper are summarized as following:

1. Two reaction regions (RRs) have been identified in the DSHC flame. The inner RR is created by the premixed reaction of ethanol and coflow entrained below the lift-off height under hot and fuel rich condition. The reaction in the inner RR creates significant amounts of intermediate fuels, e.g. CO and H_2. The non-premixed reaction of these intermediate fuels with the O_2 in the coflow downstream of the lifg-off height forms the outer RR, which is actually the main heat release region.

2. To correctly capture the flame structure, use of a detailed chemical mechanism is

indispensable due to the importance of the finite rate reaction under MILD condition.

3. The coflow temperature (T_{cf}) has a significant influence on the DSHC flames. Five times increase of flame lift-off height was observed when the coflow temperature was decreased from 1400 K to 1200 K. The flame changed from having a two-RRs structure to a triple flame when the coflow temperature is reduced. The outer reaction region shifted from non-premixed combustion at high T_{cf} to premixed combustion at low T_{cf}.

4. A change of the O_2 concentration in the coflow ($X_{O_2,cf}$) alters the characteristics of the two RRs. At high $X_{O_2,cf}$ (12%), the inner premixed RR is shorter and stronger due to availability of more O_2 (12%). The inner RR becomes more distributed at low $X_{O_2,cf}$. The flame peak temperature is significantly increased in the case with highest $X_{O_2,cf}$.

5. According to Cavaliere and de Joannon's definition [3], all studied cases except H_{II}-D, which has the highest $X_{O_2,cf}$, fall into the MILD regime. But when the restriction of flame peak temperature ($T_{peak} < 1800\ K$) is also applied, only the case with the lowest $X_{O_2,cf}$ can be strictly called MILD.

APPENDIX: CONDITIONAL DROPLET INJECTION MODEL

Table 8.5: Parameters for determining size-conditional droplet injection angle and velocity.

case	$\theta_{min,S}$ [°]	$\theta_{min,S}$ [°]	$\theta_{max,S}$ [°]	$\theta_{min,L}$ [°]	$\theta_{max,L}$ [°]	$D_{p,m}$ [μm]	$D_{p,L}$ [μm]	P_{inj} [bar]
H_I	42	20	50	38	45	40	80	6.5
H_{II}	40	20	50	35	45	40	80	6
H_{III}	44	20	55	40	50	40	80	6

To provide reliable spray boundary conditions under flash-boiling atomization condition, the conditional droplet injection model was proposed [21]. The magnitude of initial droplet velocity has a non-uniform distribution across the spray cloud:

$$U_{p,mag} = \left(1 - 2\eta_p \alpha_p + \alpha_p\right) \bar{U}_l. \tag{8.3}$$

where α_p is a parameter. η_p is the scaled offset of droplet injection direction from the spray half angle, defined as:

$$\eta_p = |\,1 - 2\Lambda\,| \tag{8.4}$$

Λ is a random variable in the range $[0,1]$. $\eta_p = 0$ means droplet moves along the center of spray cloud trajectory, and $\eta_p = 1$ at the edge. The bulk velocity of the liquid fuel, U_l, is be estimated from the injection pressure P_{inj}:

$$U_l = \sqrt{\frac{2\left(P_{inj} - P_{amb}\right)}{\rho_l}} \tag{8.5}$$

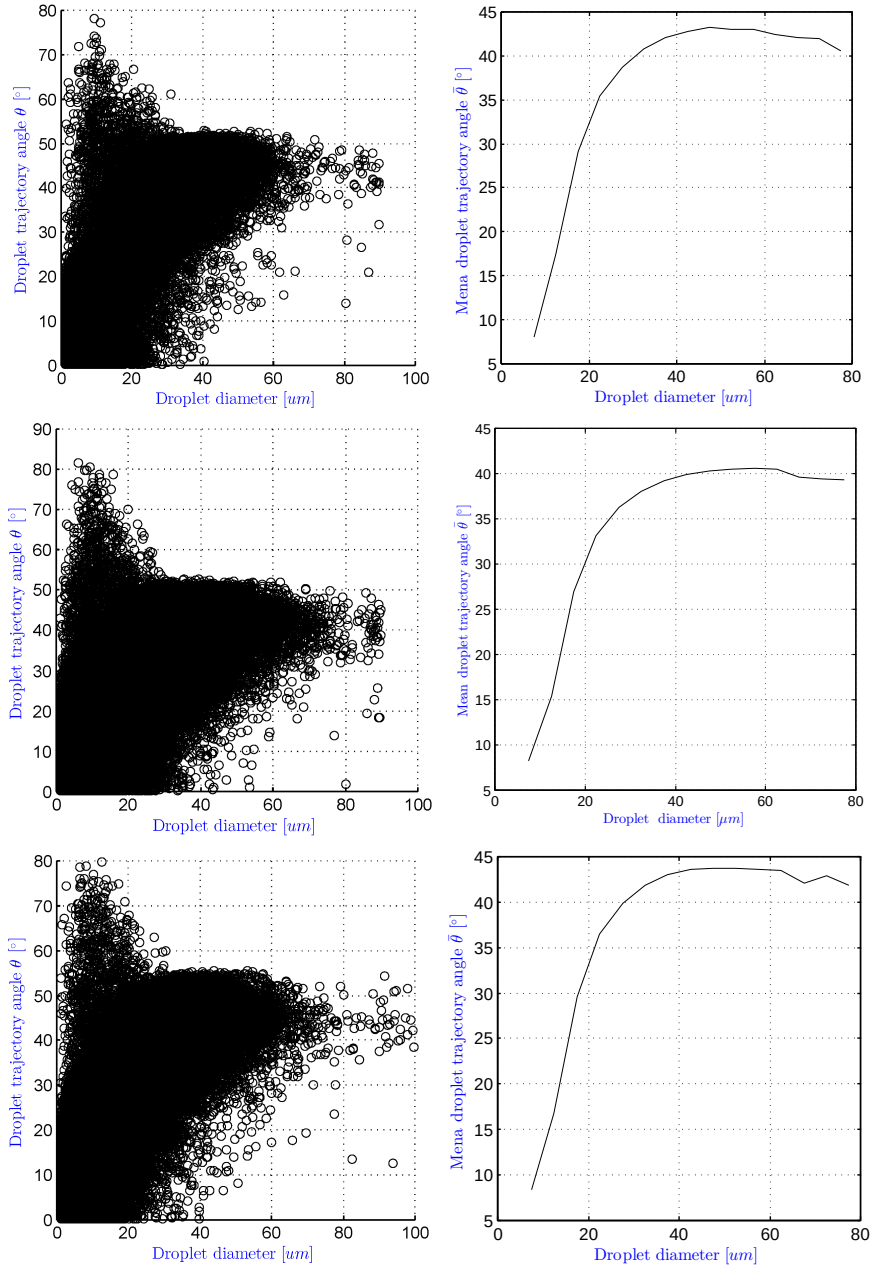

Figure 8.21: Scatter plot (left) and conditional average (right) of droplet trajectory angle from experimental data.

where P_{amb} is the ambient pressure, and ρ_l the liquid fuel density.

The droplet initial injection direction is conditioned upon its size, and is determined by:

$$\theta_p = \begin{cases} \theta_{min,p}\left(D_p\right) + 2\Lambda\left[\theta_S - \theta_{min,p}\left(D_p\right)\right], & 0 \le \Lambda < 0.5 \\ \theta_S + (2\Lambda - 1)\left[\theta_{max,p}\left(D_p\right) - \theta_S\right], & 0.5 \le \Lambda \le 1 \end{cases} \tag{8.6}$$

where $\theta_{min,p}$, $\theta_{max,p}$ are respectively the minimum and maximum possible injection angle dependent on droplet size D_p:

$$\theta_{min,p}\left(D_p\right) = \theta_{min,S} + \frac{D_\mathrm{p} - D_{p,mid}}{D_{p,L} - D_{p,m}}\left(\theta_{min,L} - \theta_{min,S}\right), \tag{8.7a}$$

$$\theta_{max,p}\left(D_p\right) = \theta_{max,S} + \frac{D_\mathrm{p} - D_{p,mid}}{D_{p,L} - D_{p,m}}\left(\theta_{max,L} - \theta_{max,S}\right). \tag{8.7b}$$

$\theta_{min,S}$, $\theta_{max,S}$, $\theta_{min,L}$, $\theta_{max,L}$ are respectively the minimum and maximum possible injection angle for small and large droplets. $D_{p,m}$ is the droplet diameter, larger than which the range of droplet injection angle will decrease, and $D_{p,L}$ is the largest droplet diameter. The values of these parameters are summarized in Table. 8.5, and they are estimated from experimental data shown in Fig. 8.21.

To take into account the influence of the radial expansion at the exit of the injector, the droplet injection position is randomly chosen within a circle centered at the origin ($Z = r = 0\ mm$), which is referred to as injection disc. The diameter of the injection disc is set to 2 mm for all cases studied here, 10 times larger than the nominal atomizer exit diameter.

REFERENCES

[1] H. J. Kim, S. H. Park, K. S. Lee, and C. S. Lee, *A study of spray strategies on improvement of engine performance and emissions reduction characteristics in a DME fueled diesel engine,* Energy **36**, 1802 (2011).

[2] G. Valentino, L. Allocca, S. Iannuzzi, and A. Montanaro, *Biodiesel/mineral diesel fuel mixtures: Spray evolution and engine performance and emissions characterization,* Energy **36**, 3924 (2011).

[3] A. Cavaliere and M. de Joannon, *Mild Combustion,* Progress in Energy and Combustion Science **30**, 329 (2004).

[4] J. A. Wünning and J. G. Wünning, *Flameless oxidation to reduce thermal no-formation,* Progress in Energy and Combustion Science **23**, 81 (1997).

[5] S. Kruse, B. Kerschgens, L. Berger, E. Varea, and H. Pitsch, *Experimental and numerical study of MILD combustion for gas turbine applications,* Applied Energy **148**, 456 (2015).

[6] F. Christo and B. Dally, *Modeling turbulent reacting jets issuing into a hot and diluted coflow,* Combustion and Flame **142**, 117 (2005).

[7] P. Li, J. Mi, B. B. Dally, F. Wang, L. Wang, Z. Liu, S. Chen, and C. Zheng, *Progress and recent trend in MILD combustion,* Science China Technological Sciences **54**, 255 (2011).

[8] E.-S. Cho, B. Danon, W. de Jong, and D. Roekaerts, *Behavior of a 300kWth regenerative multi-burner flameless oxidation furnace,* Applied Energy **88**, 4952 (2011).

[9] M. Sánchez, F. Cadavid, and A. Amell, *Experimental evaluation of a 20kW oxygen enhanced self-regenerative burner operated in flameless combustion mode,* Applied Energy **111**, 240 (2013).

[10] R. Weber, J. P. Smart, and W. V. Kamp, *On the (MILD) combustion of gaseous, liquid, and solid fuels in high temperature preheated air,* Proceedings of the Combustion Institute **30**, 2623 (2005).

[11] M. Derudi and R. Rota, *Experimental study of the mild combustion of liquid hydrocarbons,* Proceedings of the Combustion Institute **33**, 3325 (2011).

[12] V. K. Arghode, A. E. Khalil, and A. K. Gupta, *Fuel dilution and liquid fuel operational effects on ultra-high thermal intensity distributed combustor,* Applied Energy **95**, 132 (2012).

[13] J. Ye, P. R. Medwell, E. Varea, S. Kruse, B. B. Dally, and H. G. Pitsch, *An experimental study on MILD combustion of prevaporised liquid fuels,* Applied Energy **151**, 93 (2015).

[14] V. Mahendra Reddy, D. Sawant, D. Trivedi, and S. Kumar, *Studies on a liquid fuel based two stage flameless combustor,* Proceedings of the Combustion Institute **34**, 3319 (2013).

[15] V. Mahendra Reddy, P. Biswas, P. Garg, and S. Kumar, *Combustion characteristics of biodiesel fuel in high recirculation conditions,* Fuel Processing Technology **118**, 310 (2014).

[16] A. E. Khalil and A. K. Gupta, *Clean combustion in gas turbine engines using Butyl Nonanoate biofuel,* Fuel **116**, 522 (2014).

[17] H. Correia Rodrigues, M. J. Tummers, E. H. van Veen, and D. Roekaerts, *Spray flame structure in conventional and hot-diluted combustion regime,* Combustion and Flame **162**, 759 (2015).

[18] H. Correia Rodrigues, *Spray combustion in moderate and intense low-oxygen conditions - An experimental study*, Ph.D. thesis, Delft University of Technology (2015).

[19] L. Ma, S. Zhu, M. J. Tummers, T. H. van der Meer, and D. Roekaerts, *Numerical investigation of ethanol spray-in-hot-coflow flame using steady flamelet model,* in *Proceedings of Eighth Mediterranean Combustion Symposium* (2013) pp. 1–12.

[20] L. Ma, B. Naud, and D. Roekaerts, *Transported PDF Modeling of Ethanol Spray in Hot-Diluted Coflow Flame,* Flow, Turbulence and Combustion , DOI:10.1007/s10494 (2015).

[21] L. Ma and D. Roekaerts, *Modeling of spray jet flame under MILD condition with non-adiabatic FGM and a new conditional droplet injection model,* Combustion and Flame (2016, in print).

[22] P. R. Medwell and B. B. Dally, *Effect of fuel composition on jet flames in a heated and diluted oxidant stream,* Combustion and Flame **159**, 3138 (2012).

[23] H. Correia Rodrigues, M. Tummers, E. van Veen, and D. Roekaerts, *Effects of coflow temperature and composition on ethanol spray flames in hot-diluted coflow,* International Journal of Heat and Fluid Flow **51**, 309 (2015).

[24] D. Martínez-Ruiz, J. Urzay, a. L. Sánchez, a. Liñán, and F. a. Williams, *Dynamics of thermal ignition of spray flames in mixing layers,* Journal of Fluid Mechanics **734**, 387 (2013).

[25] A. L. Sánchez, J. Urzay, and A. Liñán, *The role of separation of scales in the description of spray combustion,* Proceedings of the Combustion Institute **35**, 1549 (2015).

[26] M. Ihme, J. Zhang, G. He, and B. Dally, *Large-Eddy Simulation of a Jet-in-Hot-Coflow Burner Operating in the Oxygen-Diluted Combustion Regime,* Flow, Turbulence and Combustion **89**, 449 (2012).

[27] E. Abtahizadeh, A. Sepman, F. Hernández-Pérez, J. van Oijen, A. Mokhov, P. de Goey, and H. Levinsky, *Numerical and experimental investigations on the influence of preheating and dilution on transition of laminar coflow diffusion flames to Mild combustion regime,* Combustion and Flame **160**, 2359 (2013).

[28] A. De, E. Oldenhof, P. Sathiah, and D. Roekaerts, *Numerical Simulation of Delft-Jet-in-Hot-Coflow (DJHC) Flames Using the Eddy Dissipation Concept Model for Turbulence–Chemistry Interaction,* Flow, Turbulence and Combustion **87**, 537 (2011).

[29] B. Danon, E.-S. Cho, W. de Jong, and D. Roekaerts, *Numerical investigation of burner positioning effects in a multi-burner flameless combustion furnace,* Applied Thermal Engineering **31**, 3885 (2011).

[30] J. A. van Oijen, *Flamelet-Generated Manifolds : Development and Application to Premixed Laminar Flames*, Ph.D. thesis, Eindhoven University of Technology (2002).

[31] C. D. Pierce and P. Moin, *Progress-variable approach for large-eddy simulation of non-premixed turbulent combustion,* Journal of Fluid Mechanics **504**, 73 (2004).

[32] K. Luo, H. Pitsch, M. Pai, and O. Desjardins, *Direct numerical simulations and analysis of three-dimensional n-heptane spray flames in a model swirl combustor,* Proceedings of the Combustion Institute **33**, 2143 (2011).

[33] B. Franzelli, B. Fiorina, and N. Darabiha, *A tabulated chemistry method for spray combustion,* Proceedings of the Combustion Institute **34**, 1659 (2013).

[34] A. Vreman, B. Albrecht, J. A. van Oijen, L. P. H. de Goey, and R. Bastiaans, *Premixed and nonpremixed generated manifolds in large-eddy simulation of Sandia flame D and F,* Combustion and Flame **153**, 394 (2008).

[35] J. Tillou, J.-B. Michel, C. Angelberger, and D. Veynante, *Assessing LES models based on tabulated chemistry for the simulation of Diesel spray combustion,* Combustion and Flame (2013), 10.1016/j.combustflame.2013.09.006.

[36] CHEM1D, A one-dimensional laminar flame code, *Eindhoven University of Technology,* (URL:http://www. combustion. tue. nl/chem1d//).

[37] P. Senecal, D. Schmidt, I. Nouar, C. Rutland, R. Reitz, and M. Corradini, *Modeling high-speed viscous liquid sheet atomization,* International Journal of Multiphase Flow **25**, 1073 (1999).

[38] OpenFOAM, *OpenFOAM: The open source CFD Toolbox,* (2015).

[39] L. Ma and D. Roekaerts, *Dynamic procedures for sub-grid scale scalar variances of FGM method,* Submitted for publication (2015).

[40] N. M. Marinov, *A Detailed Chemical Kinetic Model for High Temperature Ethanol Oxidation,* International Journal of Chemical Kinetics **31**, 183 (1998).

[41] M. de Joannon, A. Saponaro, and A. Cavaliere, *Zero-dimensional analysis of diluted oxidation of methane in rich conditions,* Proceedings of the Combustion Institute **28**, 1639 (2000).

[42] J. Sidey, A. Giusti, and E. Mastorakos, *Simulation of laminar non-premixed flames of kerosene with hot combustion products as oxidizer,* in *ninth Mediterranean Combustion Symposium* (2015).

[43] Y. Minamoto and N. Swaminathan, *Scalar gradient behaviour in MILD combustion,* Combustion and Flame **161**, 1063 (2014).

[44] S. Chung, *Stabilization, propagation and instability of tribrachial triple flames,* Proceedings of the Combustion Institute **31**, 877 (2007).

[45] P. R. Medwell, P. a.M. Kalt, and B. B. Dally, *Simultaneous imaging of OH, formaldehyde, and temperature of turbulent nonpremixed jet flames in a heated and diluted coflow,* Combustion and Flame **148**, 48 (2007).

9

NUMERICAL STUDY OF CONVENTIONAL AND MILD SPRAY FLAMES

In this chapter, we investigate the multi-flame phenomenon often seen in spray combustion. To do so, simulations are made of cases H_{II} and A_{II} of the DSHC database. These two cases have the same fuel (ethanol) but differ in the type of coflow: room temperature air (case A_{II}) or products of lean premixed combustion (case H_{II}), and they exhibit remarkably different flame structure, respectively with a "double flame" and a "single flame". Simulation results reveal that four spatially separated reaction regions exist in the flame A_{II} and two in the flame H_{II}. These regions are of different types, premixed or non-premixed, and are formed by different species, major fuel (ethanol) or intermediate species, e.g. carbon monoxide. The mechanism underlying the multi-flame structure is investigated and explained in terms of the relative magnitude of different time scales, namely of droplet evaporation, dispersion, convection and reaction. Parameter studies on the effect of spray polydispersity and coflowing air temperature are carried out, demonstrating an even wider range of flame structures. An important observation is that the "single flame" structure usually present in the hot-diluted coflow case (H_{II}), is also generated in a case of room temperature air coflow, provided the injected droplets are small. This is attributed to the fact that representative droplets in all cases with single flame have similar evaporation time scale. Or stated more generally, by matching important time scales, similar flame structure can be created under considerably different conditions.

Content in this chapter has been published in the following paper:
L. Ma, D. Roekaerts, Numerical study of the multi-flame structure in spray combustion, Proceedings of the Combustion Institute, under review (2016).

9.1. INTRODUCTION

Spray combustion differs from its gaseous counterpart in many aspects [1, 2]. An interesting and important one is the rich variety of structures that a spray flame can exhibit. In 1990, Continillo and Sirignano [3] firstly predicted the existence of double flame structure in spray combustion through numerical study of a counterflow configuration. Later on, Greenberg and Sarig [4] also demonstrated that three possible scenarios (single, double or triple flames) can appear depending on the characteristics of the spray. Cessou et al. [5] were the first to experimentally confirm the existence of double flame structure in spray flame. Later studies by Marley et al. [6] also observed the double flame structure via OH-PLIF. They found that the entrainment of coflow plays an important role in determining the flame structure; without coflow the flame exhibits a single flame structure and addition of low speed coflow results in a double flame structure. Two recent experimental datasets on spray combustion further revealed the complexity of spray flame topology. Correia Rodrigues et al. [7] performed CARS (Coherent Anti-Stokes Raman Spectroscopy) measurement on the Delft Spray in Hot Coflow (DSHC) flames. And they initially reported that the temperature radial profile has only one peak in the case where the spray is issued into a hot-diluted coflow, but has two separate peaks when the coflow is replaced by room temperature air. Cléon et al. [8] carried out experimental studies on a series of spray oxyfuel flames. In their study, the double flame structure is present for all cases, but three different types of flame can occur depending on the degree of CO_2 dilution and coflow velocity.

Understanding of the flame structure can benefit spray combustion system design and optimization as well as emission control. The above studies have provided valuable information towards these goals. However, an insight on the mechanism that controls the change of spray flame structure is still missing due to the limited information available in experiment. Numerical studies on the structure of spray flames are still sparse in literature. Most of them are on a simplified counterflow configuration, including early studies by Continillo and Sirignano [3], Gutheil and Sirignano [9], and more recently by Olguin and Gutheil [10]. Vié et al. [11] performed a DNS study of a 3D spray counterflow configuration. It was found that the structure is strongly related to droplet size and strain rate. Under certain combinations of these two parameters, both single and double flame modes can occur. Reveillon and Vervisch [12] analyzed the dilute spray flame structure using DNS, and observed that the flame structures can be classified with three dimensionless quantities which characterize the fuel/air equivalence ratio within the core of the spray jet, the mean inter-droplet distance to flame thickness ratio, and the evaporation time to flame time ratio. While providing valuable insight on the spray flame topology, the simulated configuration is not close to an experimental spray combustion system. Enjalbert [13] has successfully reproduced the double flame structure of [8] with Large Eddy Simulation (LES) and a tabulated chemistry method. But the simulation was only carried out for a single case, and the ability of predicting spray flames under different conditions was not shown. In the current study, a 3D LES of two cases in the DSHC dataset mentioned above will be reported. The focus is on predicting different structures in spray jet flames and on understanding of the mechanism underling the transition between structures.

The remainder of the paper is structured as follows: The experimental cases and the

numerical approaches employed will be described in section 9.2. The results and discussions are presented in section 9.3. Main findings and conclusions are then given in section 9.4.

9.2. TARGET CASES AND MODELING APPROACH

Two cases from the DSHC database have been chosen as target flames for the current study. Schematic of the DSHC burner is shown in Fig. 9.1. The liquid fuel (ethanol) is injected by a pressure-swirl atomizer at $\mathscr{Z} = 0\ mm$. A secondary burner matrix is placed upstream of the coflow exit. When the secondary burner is switched off, only room temperature air is supplied as coflow, the burner works in 'conventional' mode (case A_{II}). When the secondary burner works on lean premixed Dutch Nature Gas (DNG) / air, hot combustion products with lower O_2 concentration is supplied as coflow, the burner then works in MILD (Moderate or Intense Low Oxygen Dilution) mode (case H_{II}) [7]. The different appearance of these two flames (see Fig. 9.3b) is one of the major observations in experiment. For details about the DSHC burner and the database, readers are referred to [7]. Conditions for two experimental cases that will be studied are listed in Table 9.1. Subscript "cf" denotes the coflow condition, $\dot{m}_{liq}$ is the mass flow rate of the liquid fuel.

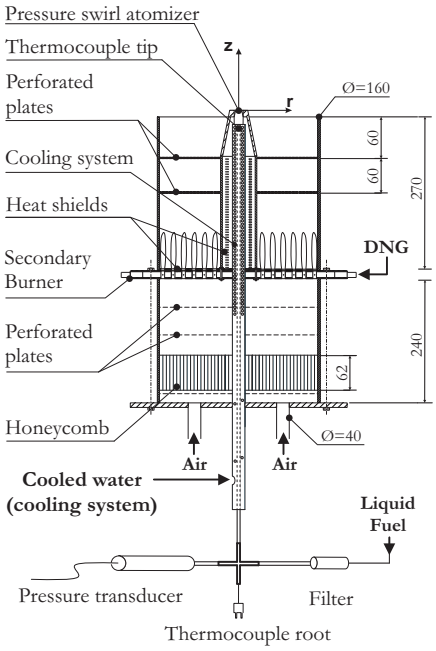

Figure 9.1: Schematic of the DSHC burner

An Eulerian-Lagrangian approach is used in the current study to account for the two-phase flow field. The continuous phase is resolved with the Large Eddy Simulation (LES) technique. Including of detailed chemistry is important for capturing correct flame structure [9], and this is realized here by making use of a Flamelet Generated

Table 9.1: Boundary conditions.

Case	$\overline{T}_{cf}\,[K]$	$\overline{X}_{O_2,cf}\,[\%]$	$\tilde{U}_{cf}\,[m/s]$	$\dot{m}_{liq}\,[kg/hr]$
A_{II}	300	21	0.25	1.70
H_{II}	1400	8.71	2.5	1.45

Manifolds (FGM) method. The influence of turbulence fluctuations on the local flame structure is accounted for through the joint Probability Density Function (PDF) of the independent variables. In this study a presumed β-function is used for the PDFs of both mixture fraction and progress variable. A transport equation (Eq. (9.1)) and an algebraic model (Eq.(9.2)) have been used for the SGS variances of mixture fraction and progress variable respectively, following the approach in [14].

$$\begin{aligned}\frac{\partial \bar{\rho}\widetilde{Z''^2}}{\partial t}+\frac{\partial \bar{\rho}\tilde{u}_j\widetilde{Z''^2}}{\partial x_j}&=\frac{\partial}{\partial x_j}\left[\bar{\rho}\left(\tilde{D}+D_t\right)\frac{\partial \widetilde{Z''^2}}{\partial x_j}\right]\\&+2\bar{\rho}D_t\left(\frac{\partial \tilde{Z}}{\partial x_j}\right)^2-2\bar{\rho}D_t\frac{\widetilde{Z''^2}}{\Delta^2}+\alpha\widetilde{Z''^2}\left(\frac{\bar{S}_Z}{\bar{Z}}\right),\end{aligned} \tag{9.1}$$

the last term in Eq. (9.1) accounts for the creation of mixture fraction variance due to droplet evaporation as suggested by Pera et al. [15]. Model constant value $\alpha = 0.5$ is used in the current study, following the recommendation of Hollmann and Gutheil [16].

$$\widetilde{Y_c''^2}=C_v\Delta^2\left(\frac{\partial \tilde{Y}_c}{\partial x_i}\right)^2, \tag{9.2}$$

the model constant C_v is set to 0.15 according to [17].

The FGM libraries were generated based on the counterflow configuration, with on one side the pure fuel vapor, and the other side a mixture that is representative of coflow conditions, given in Table. 9.1. To take into account the effect of enthalpy loss due to liquid fuel evaporation, the authors proposed a three dimensional non-adiabatic FGM approach. In this method, the 2D FGM tables at different enthalpy levels were built by decreasing the temperature at the oxidizer side ($Z = 0$). An extra parameter η_h representing the scaled enthalpy loss was introduced. This method is used for case H_{II}. More details and validation of this approach were reported in [18]. In case A_{II}, because of the already very low coflow temperature, only little heat loss can be accommodated via the above method and it is not effective. Instead, a 2D adiabatic FGM library is directly used. This adiabatic approach has limitations in the zone where heat involved in evaporation is dominant compared to combustion heat release, but has little or no impact on predicted fllame structure. An extra simulation for H_{II} using adiabatic FGM table (not shown here) showed that the flame structures predicted are indeed rather similar.

The droplets are injected from the atomizer ($\mathcal{Z} = 0\ mm$) using the Conditional Injection Model (CIM) proposed by the authors [18]. No sub-grid dispersion model is used for droplets, in view of the very fine grid resolution. The droplet initial size distribution is given as Rosin-Rammler distribution. About two million numerical parcels are injected per second, but the specific number varies in different cases according to the liquid mass

flow rate and maximum droplet size. Droplets heat and mass transfer are modeled with infinite conductivity model.

The simulations in this study were carried out using a new OpenFOAM solver — “sprayFGMFoam", developed by the authors. This solver has been first validated against a gaseous lifted flame, and then applied to the H_{II} case [18]. A 3D cylindrical domain of diameter 200 mm and length 150 mm was used for the LES. The axial, radial and circumferential directions of the computational domain were discretized with 250, 130 and 72 grid points, respectively, resulting in a total mesh size of 2.2 million. The smallest cell size 0.3 mm is about four times the diameter of the largest droplet diameter, using a finer mesh may violate the point source assumption. A very small growth ratio of 1.004 is used for the stream-wise grid points, leading to a nearly uniform fine mesh in the region of interest. The time step is set such that within each time step, only about 10 parcels are injected. The corresponding maximum Courant number is less than 0.4. Simulation of both A_{II} and H_{II} cases have also been carried out on a coarser grid with cell size almost doubled at all three directions compared to the fine grid described above. No considerable difference has been observed, demonstrating the adequate resolution of the current LES. In the following, only results on the fine mesh will be shown.

9.3. RESULTS AND DISCUSSION

In this section, the simulation results will be first validated against the experimental data. Detailed discussion on the flame structures will be given in the second subsection. Then different time scales involved in spray combustion will be analyzed to understand the mechanism behind the wide variety of flame topologies. Finally, several new cases will be investigated to verify the findings in previous subsections.

9.3.1. VALIDATION WITH EXPERIMENTAL DATA

Radial profiles of droplet Sauter Mean Diameter (SMD) and mean gas phase temperature are displayed in Fig. 9.2. In general, good agreement with experimental data has been achieved. The droplet SMD has been under-estimated at the outer edge of the spray in case A_{II}, but the radial spreading and the trend of increasing SMD with increasing radial position have been correctly captured. The SMD in the H_{II} case agrees well with the measurement. Compared to the result of case H_{II}, the droplets show a much wider radial spreading in this cold coflow case. This is a consequence of increased droplet evaporation time scale due to cooler surrounding environment as will be demonstrated in section 9.3. The droplet and gas phase velocity components are also in satisfactory agreement with experiment in both cases, for simplicity, they are not shown here.

The most important message from Fig. 9.2 is that there are two peaks present on the temperature radial profiles in case A_{II}, whereas, in case H_{II}, only one peak exists. This phenomenon has been correctly captured in the simulation. The double-peak temperature profile is an important sign of the so-called ‘double flame’ structure that has been observed in many experiments but seldomly reported by numerical study. Detailed discussions on the spray flame morphology will be presented in next subsection. Although the hot region in case A_{II} was predicted slightly wider, and the outer temperature peak has been under-estimated, the overall shape, the inner peak and the position of both

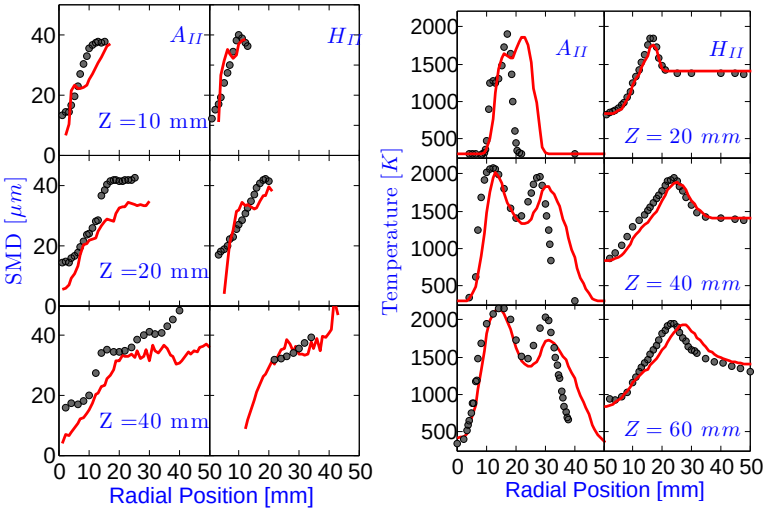

Figure 9.2: Radial profiles of droplet SMD (left), mean temperature (right) at several elevations from case A_{II} and H_{II}. Line: LES results, symbols: experimental data.

peaks have been accurately reproduced. Furthermore, the predicted temperature profiles in case H_{II} match very well with experiment. These results suggest that the current modeling approach is adequate for analyzing the spray flame structures under both conventional and MILD conditions.

To have an overall impression of the flame structures in these two cases, snapshots of the predicted OH fields supplemented with instantaneous spray cloud and the flame photos from experiment are given in Fig. 9.3. As one can see that the flame structures are considerably different in these two cases. In case A_{II}, the OH exhibits two high concentration regions, one near the center axis and the other at large radial distance, consistent with the double temperature peaks shown in Fig. 9.2. Similar phenomena are also present in the flame picture of case A_{II} where two separate luminous regions are clear, especially at the bottom part of the flame. Both simulation and experiment show that there is a brighter-thicker core flame surrounded by blueish-thin outer flame. This is the reason that it is referred to as 'double flame' structure in literature. Whereas, in the H_{II} case, only one 'U' shape region exhibits high concentration of OH. This agrees with the flame picture of case H_{II}, where only one intense luminous region is observable.

The flame photos show that the A_{II} flame is in general brighter than the H_{II} flame which was designed to work in MILD, also known as "flameless", condition. This is reflected in the simulation in terms of higher OH concentration in case A_{II} than that in case H_{II}. In Fig. 9.3a the inner OH layer is thinner than the outer one near the flame base. A similar observation was made by Marley et al. [6] with OH-PLIF in an experimental study of a case that is very similar to case A_{II}. They reasoned this as a consequence of high strain in the inner flame front due to high droplet flux. This argument is supported in the present study. As shown in Fig. 9.3a, most droplets directly approach the bottom part of the inner flame front. From the supplementary videos, local extinctions

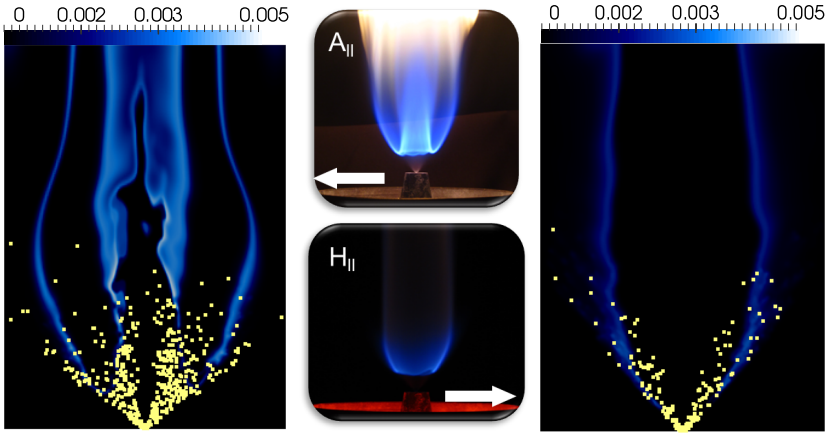

Figure 9.3: Instantaneous OH mass fraction field (a and c) on a vertical cross-section from LES, and flame photography from experiment (b) for cases A_{II} and H_{II}. Dots: instantaneous spray cloud near the cut plane.

on the inner flame front caused by passing and local evaporation of droplets are clearly observable.

9.3.2. DETAILS OF THE FLAME STRUCTURE

In this section, we will study in detail the flame structures of the A_{II} and H_{II} cases. To facilitate the discussion, the isosurface of $Y_{OH} \times Y_{CH_2O} = 1 \times 10^{-9}$, which can be used as marker of reaction region (RR) [19], is superimposed on top of all contour plots that will be shown hereafter. It was confirmed from the simulation results that the RRs marked by $Y_{OH} \times Y_{CH_2O} > 1 \times 10^{-9}$ coincide well with the regions that have high progress variable source value. As indicated in Fig. 9.4, the structure of the A_{II} flame is very complicated. In total, four RR branches exist, and they are labeled as RR1 to RR4 from the center to the far radial location, see Fig. 9.4a. The RR1 and RR2 originate from the same RR that extends from the flame base to about 90 mm, for convenience it is also named RR1. All RRs join together at the flame base. RR4 shows strong intermittency. We can find from Figs. 9.3a and 9.4a, that the high concentration of OH in case A_{II} are present in the zones between RR1/RR2 and RR3/RR4. The flame structure of H_{II} is much simpler. It consists of two RRs, the outer “U" shape one (RR2) and the inner “inversed-V" shape one (RR1). Comparisons between the OH field and the RRs shows that only the RR2 produces large amount of OH, in agreement with the experimentally observed single luminous region (Fig. 9.3b).

In Fig. 9.4, the Flame Index (FI) and the mass fraction of CO are also displayed. The FI is defined as:

$$FI = \frac{\nabla Y_{C_2H_5OH} \cdot \nabla Y_{O_2}}{|\nabla Y_{C_2H_5OH} \cdot \nabla Y_{O_2}|}, \tag{9.3}$$

positive value denotes premixed reaction of C_2H_5OH, and negative value indicates non-premixed reaction. The FI shown in Figs. 9.4b and 9.4e demonstrate that the inner RRs

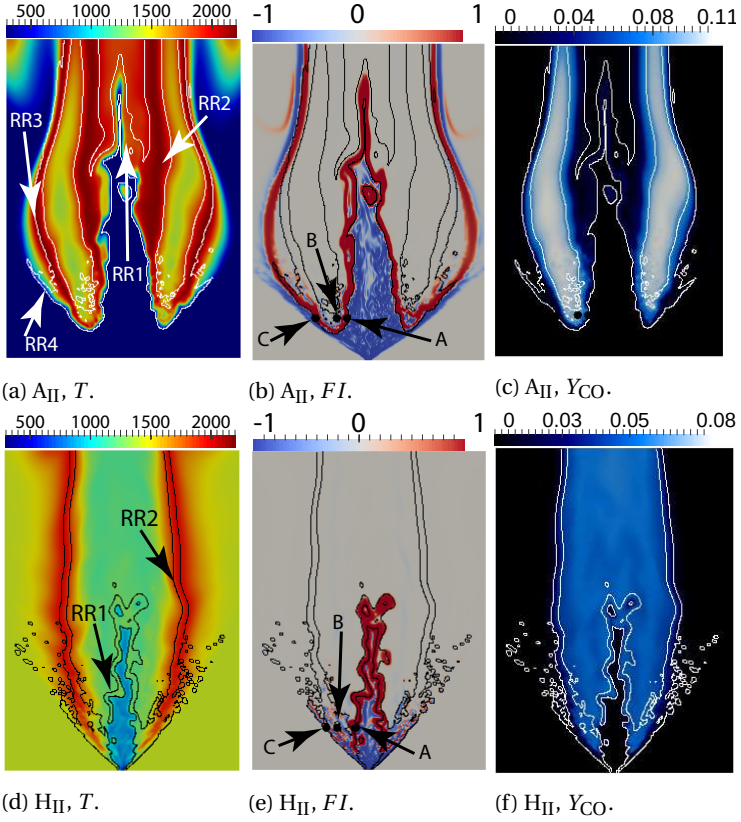

(a) A_{II}, T. (b) A_{II}, FI. (c) A_{II}, Y_{CO}.

(d) H_{II}, T. (e) H_{II}, FI. (f) H_{II}, Y_{CO}.

Figure 9.4: Snapshots of temperature (T), FI and Y_{CO} on a vertical cross section from cases A_{II} (top) and H_{II} (bottom). White lines: isosurfaces of $Y_{OH} \times Y_{CH_2O} = 1 \times 10^{-9}$.

(RR1) in both cases are formed by the premixed reaction of the ethanol vapor. The fuel vapor in the core region is from the evaporation of droplets that are present in the center, and may also from the fuel vapor formed outside but brought to the center by the entrained coflow. O_2 coexists in the same region due to the coflow entrained below the flame base.

Figure 9.5 shows the scatter plots in the $T-Z$ space with data sampled at three different points from each case. The locations of data sampling points are given in Fig. 9.5, and are also displayed on Figs. 9.4b and 9.4e. Points "A" in both cases are located roughly on the most inner reaction region — RR1. It is shown that although in both cases premixed reaction happen in RR1, they are at absolutely different conditions. The core region of case A_{II} is mostly fuel lean, whereas it is very rich in the H_{II} case. As a consequence, in case A_{II}, all the fuel vapor in the center is consumed in RR1, but O_2 is in excess there. In case H_{II}, the condition in RR1 — hot and fuel rich — is suitable for pyrolysis, which decomposes the fuel vapor to intermediate species rather than directly converting to final combustion products. Fig. 9.4f shows that a large amount of CO is produced in RR1 of case H_{II}. As shown in our previous study [20], the RR2, which is also the main heat release region is actually created by the non-premixed reaction between the CO and the O_2 from coflow. Figure 9.5 also shows that the RR2 (points "B") of both cases are similar, in most situations are fuel rich but also fuel lean spots can occur. Point "C" in case H_{II} is located at the outer edge of RR2, it is fuel lean, because only few large droplets can penetrate the RR2. And in case A_{II}, this point sits at the bottom of RR4, and is also mostly fuel lean.

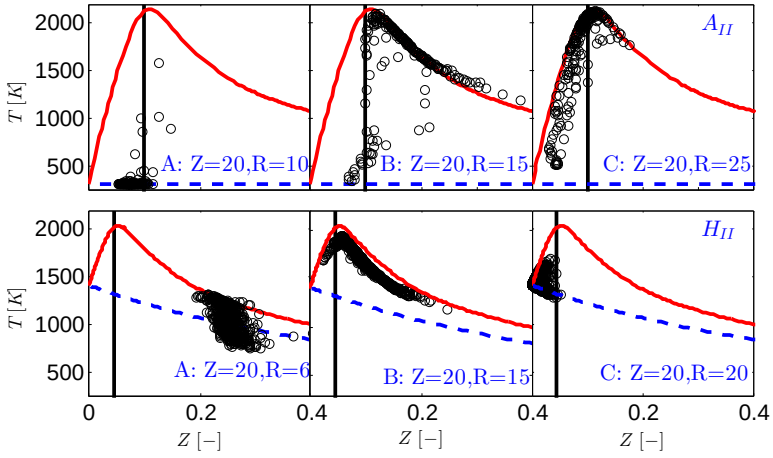

Figure 9.5: Scatter plot in $T-Z$ space. Top: case A_{II}, bottom: case H_{II}. Sample point coordinate in mm. Red solid line: fully burnt flamelet (adiabatic), blue dashed line: pure mixing flamelet (adiabatic). Vertical lines: stoichiometric mixture fraction (Z_{st}).

The different conditions in the core region of each case is related to the coflow temperature. In H_{II}, due to the presence of hot coflow, the injected droplets quickly shrink through fast evaporation. These smaller droplets are easier convected towards the center region by the entrained coflow, and produce large amount of fuel vapor there. In the

A_{II} case, the droplets undergo slow evaporation before they reach the RR1 because of the low surrounding temperature, and therefore could keep a more ballistic trajectory. A consequence is that less droplets are available in the center, and also less fuel vapor is produced there. Higher O_2 concentration in the coflow of the A_{II} case than in the H_{II} case also contributes to different condition in the core regions.

Analogous to Eq.(9.3), a FI can also be defined based on CO (results not shown here). The CO FI reveals that the RR2 and RR3 in case A_{II} are generated by the non-premixed reaction of CO with the excess O_2 respectively from RR1 and RR4 (or coflow). Fig. 9.4c shows that there indeed is a CO rich region between RR2 and RR3, and it is clear that the CO in this region in not generated from RR1 as happens in the case H_{II}. CO can be produced from incomplete hydrocarbon combustion, as is the case in the RR1 of case H_{II}, and can also come from fuel thermal decomposition. The latter is probably the reason for CO generation in the case A_{II}. Sampled data (not given here) show that droplets in the near axis region almost keep their initial temperature (300 K), while those have crossed the RR1 all reach the so called wet-bubble temperature, which is very close to the boiling temperature (351 K). This indicates a very fast evaporation of these droplets in the post-combustion region. However, simulation results show that no C_2H_5OH is present in this region. A good explanation is that due to the high temperature in this region (see Fig. 9.4a), the generated C_2H_5OH is immediately decomposed to smaller molecular fuels, producing a region rich of CO. It is then clear that the RR2 is formed by the diffusion combustion of excess O_2 from RR1 and the CO generated in the post-combustion region. RR3 is similar to RR2, but the O_2 comes from the coflow or left by RR4.

Support for the above arguments can be found in literature. Gutheil and Sirignano [9] observed the double flame structure in a counterflow spray combustion simulation. They explained the occurrence of the second flame to be caused by diffusion of air from the counterflow and diffusion of cracked fuel components from the location where the local minimum in the profile of gas temperature exists. They also found that the single step mechanism predicts two peaks on the fuel vapor profiles which was not seen when detailed mechanism was used, and argued that this is due to the negligence of fuel cracking into radicals in hot flame regions. Olguin and Gutheil [10] also found that when a double flame structure appears in the counterflow spray, the local maximal of the evaporation rate is coincident with the local minimal of the temperature profile, and the mixture fraction and CO peak in the same region.

9.3.3. TIME SCALE ANALYSIS

The above analysis has shown that the spray flame structure is strongly related to droplet behavior — being convected to the core region and create a fuel rich condition there or crossing the first RR and quickly evaporate in the post-combustion region. Sánchez et al. [21] showed that the disparity between time scales influences the spray flame structure. In Table. 9.2, we compare time scales of droplet evaporation (τ_e), dispersion (τ_p), convection (τ_c) as well as reaction (τ_r). These time scales have been evaluated for three representative droplet size classes under a range of surrounding temperature. 300 K to 1200 K were chosen as possible conditions that droplets can meet before reaching the RR. 2000K was used as a representative temperature in the post-combustion region. For all calculations, the droplet initial temperature was assumed to be $T_{p,0} = 300$ K, and the

droplet/gas slip velocity was kept as $U_s = 30\ m/s$ (liquid bulk velocity at injector exit is about 35 m/s). Calculation using a smaller slip velocity ($U_s = 20\ m/s$) only influences specific values, the trends and relative magnitude between different time scales remain the same.

τ_e is defined as the lifetime of a single droplet, calculated using the infinite conductivity model. τ_p equals to the droplet relaxation time:

$$\tau_{\mathrm{p}} = \frac{4}{3}\frac{\rho_{\mathrm{p}}}{\rho_{\mathrm{g}}}\frac{D_{\mathrm{p}}}{C_D U_s}, \tag{9.4}$$

where ρ_{p} and ρ_{g} respectively refer to the liquid and gas phase density, and D_{p} is the droplet diameter. The drag coefficient C_D is given by the Schiller-Naumann semi-empirical correlation. The convection time scale characterizes the time that is needed for a droplet to travel from the injector exit to the flame base (assuming no evaporation), and is defined as the flame lift-off hight (H_{lift}) divided by the slip velocity, $\tau_c = H_{lift}/U_s$. Since the coflow velocity is very low, U_s roughly equals to droplet velocity U_p. H_{lift} is set to 20 mm according to the $\mathrm{A_{II}}$ case. The reaction time scale is defined as $\tau_r = \rho/\dot{\omega}_{Yc}|_{Z=Z_{st},C=0.5}$, where $\dot{\omega}_{Yc}|_{Z_{st},C=0.5}$ ($kg/m^3 \cdot s$) is the source term of unscaled progress variable (Y_c) conditioned on $Z = Z_{st}$ (stoichiometric) and $C = 0.5$, Z and C are mixture fraction and progress variable, respectively. For the interpretation of data in Table 9.2, only the trend and the order of magnitude are of interest, specific values can change under different definitions.

In Table 9.2, $\tau_c \approx 0.7\ ms$ for all droplets. This means that if the initial droplet velocity does not decay, it takes about 0.7 ms for a droplet to reach the flame base. However, we see that small droplets ($D_p = 20\ \mu m$) have very small dispersion time scale, meaning that they will very quickly adapt to local gas flow, and be convected to the core region by the entraining coflow rather than directly shooting to the flame front. On the other hand, large droplet ($D_p = 60\ \mu m$) have much larger dispersion time scale, indicating that they will keep ballistic trajectory before reach the flame base. The intermediate-sized droplet will travel directly towards the RR, because their dispersion time scale is larger than the convection time scale. But their trajectories will probably be modified by local gas, and they will have a broader distribution, since their dispersion and convection time scales are not far from each other. Now, we can infer that probably it is the small droplets and their evaporation in the core region that mainly responsible for the formation of RR1 of both $\mathrm{A_{II}}$ and $\mathrm{H_{II}}$ cases. Largest droplets are related to the RR4 in case $\mathrm{A_{II}}$ and distributed reaction spots in case $\mathrm{H_{II}}$ at large radial positions. Intermediate droplets will arrive in the post-combustion region, and will probably also vanish there.

Table 9.2: Time scales for droplet evaporation (τ_e), dispersion (τ_p), convection (τ_c) and gas phase reaction (τ_r), unit: ms.

	$D_p = 20\ \mu m$					$D_p = 40\ \mu m$					$D_p = 60\ \mu m$				
	$T_{seen}\ [K]$					$T_{seen}\ [K]$					$T_{seen}\ [K]$				
	300	600	900	1200	2000	300	600	900	1200	2000	300	600	900	1200	2000
τ_e	21.3	1.8	0.8	0.5	0.02	69.3	6.2	2.8	1.8	0.6	136.5	12.5	5.7	3.8	1.7
τ_p	0.3	0.4	0.4	0.4	0.4	1.0	1.2	1.3	1.3	1.3	1.8	2.3	2.5	2.6	2.6
τ_c			0.7					0.7					0.7		
τ_r	2.6	0.2	0.03	0.009		2.6	0.2	0.03	0.009		2.6	0.2	0.03	0.009	

Droplet evaporation time scale τ_e is strongly related to both its size and the surrounding gas temperature. Large droplets evaporate considerably slower. Since many small droplets can evaporate simultaneously, it requires much shorter time to vaporize the same amount of liquid fuel in the form of small droplets than as large droplets. Drastic change in τ_e is observed when the surrounding temperature is increased. Under room temperature, the evaporation time scale is much longer than all other time scales considered here, implying that local availability of fuel vapor is limited by the evaporation process. When small droplets arrives in the hot RR, they will immediately vanish due to the very small evaporation time scale. This fast production of fuel vapor in the post-combustion region, followed by its decomposition eventually contribute to the formation of RR2 and RR3 in the case A_{II}. It is possible for the largest droplets to survive when they pass through the hot regions as we have seen in the two studied cases, because even under this situation their evaporation and dispersion time scales are comparable and longer than the convection time scale.

The reaction time scale is independent of droplet size but strongly depends on the temperature. The τ_r decreases by three orders of magnitude when temperature increases from 300 K to 1200 K, and is smaller than all other time scales when surrounding gas temperature is higher than the boiling point (351 K). This means that single or group droplet combustion can happen provided that the produced fuel vapor can be quickly mixed with oxidizer. As shown in Fig. 9.4, there are lots of isolated RR spots appearing outside the RR2 in case H_{II}. Those spots are possibly created by the single or group combustion of large droplets that have escaped from the main RRs.

9.3.4. INFLUENCES OF DROPLET SIZE AND AIR PREHEATING

We have seen that the droplet size and surrounding gas temperature influence the values and their relative magnitude of different time scales that eventually determine the spray flame topologies. Parameter studies on these two factors will be presented to verify the analysis made above. In all cases that will be investigated, initially mono-sized droplets were injected into the domain. The cases are named by the initial droplet size and coflow temperature. For example, “40 – 900" refers to the case in which droplets of diameter 40 μm have been injected at the atomizer position, and the coflowing air has been preheated to 900 K. Note that in the following discussions, we follow the conventions in the literature to refer the structure of A_{II} as double flame and H_{II} as single flame. But as has already been shown, there are actually more RRs exist in both cases — four in A_{II} and two in H_{II}. So the name of the ‘double flame’ or ‘single flame’ structures are not really accurate, and the ‘flame’ here mainly refers to luminous regions that can be experimentally observed but not necessarily are the RRs.

Snapshots of temperature field, the isosurface of $Y_{OH} \times Y_{CH_2O} = 1 \times 10^{-9}$, as well as the instantaneous spray cloud are presented in Fig. 9.6. The results demonstrated that the initial droplet size distribution indeed plays a crucial role in determining the spray flame structure. A single flame structure is observed in case “20 – 300", while the double flame structure occurs in other cases. In case “20 – 300" all droplets are convected to the center region, and preferential droplet distribution along the inner shear layer downstream can be observed. This is the consequence of small dispersion time scale of these small droplets. The flame stabilizes at the periphery of the spray cloud, and looks very

similar to a gaseous diffusion flame. This is because indeed all droplets in the center, especially those close to the flame front, evaporate locally, and form a fuel rich condition, which to some extent resembles a gaseous jet flame. It is interesting to note that the flame structure in the "20 – 300" case is also similar to that in the H_{II} case, in terms of fuel rich condition in the center and single temperature peak on a radial transverse. It is remarkable that similar flame structure could be created under considerably different coflow conditions — cold air in case "20–300", and hot combustion products in H_{II}. This is related to the fact that intermediate-sized droplets, which dominate in case H_{II}, can have similar evaporation time scale in hot surroundings ($D_p = 40\ \mu m$, $T_{seen} = 1200\ K$) as small droplets under cooler conditions ($D_p = 20\ \mu m$, $T_{seen} = 600\ K$), see Table. 9.2.

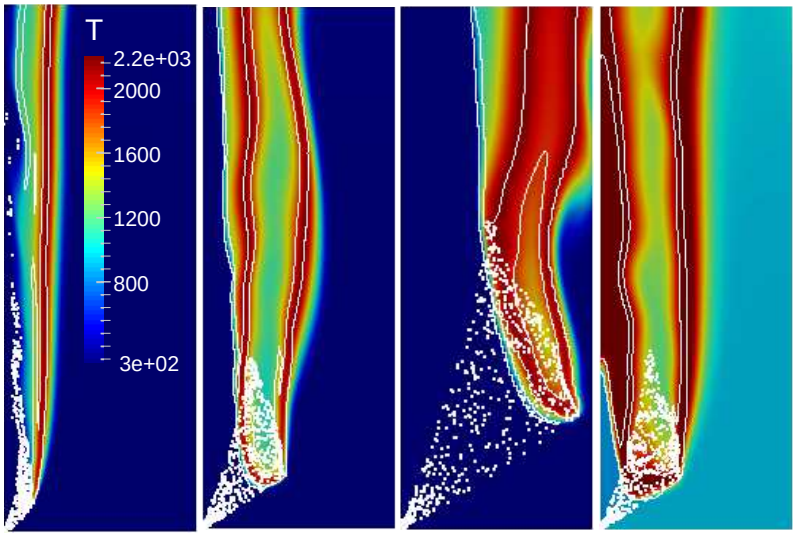

(a) 20 – 300. (b) 40 – 300 (c) 60 – 300 (d) 40 – 900

Figure 9.6: Snapshots of temperature field. Dots: instantaneous spray cloud. White lines: isosurfaces of $Y_{OH} \times Y_{CH_2O} = 1 \times 10^{-9}$.

The flame structure in case "40 – 300" is similar to that of A_{II}, but the relatively low temperature region between RR2 and RR3 is longer and no RR4 exist. This is because all droplets arrive and quickly evaporate in the region behind RR1. This creates a much richer condition locally than in the case A_{II}, where small droplets went to the center and large ones escaped. If only large droplets are injected (case "60 – 300"), the double flame structure still exists but can only stabilize further downstream and at larger radial positions due to small convection time scale and large evaporation time scale. The major influence of air preheating is on the inner flame fronts RR1 and RR2. At higher coflow temperature, the evaporation and reaction time scales become very small. The mixture before RR1 is still fuel lean, but already quite close to stoichiometric. Therefore a shorter but stronger RR1 is established in case "40 – 900", and not much O_2 is left after RR1, so RR2 becomes smaller and closes at the center axis.

In summary, the four cases presented here confirm that the structure of spray flames

is strongly related to the time scales which determine the motion and evaporation of droplets and gas phase reaction. Droplet polydispersity significantly affects the basic flame topology and lift-off height, while air preheating mainly modulates the strength of each RR.

9.4. CONCLUSION

In the current study, two cases from the Delft Spray in Hot Coflow (DSHC) database have been numerically investigated with an LES/FGM method. The focus of the present study was on the multi-flame structure that is particular to two-phase combustion. The double and single flame structures respectively observed in the experimental cases A_{II} and H_{II} have been successfully reproduced in the simulation. Detailed analysis further revealed that four and two reaction regions exist in the flame A_{II} and H_{II}, respectively. They are of different types, premixed or non-premixed, and are formed by different species, major fuel (ethanol) or products of fuel decomposition, for example CO. The relevant time scales are strongly influenced by droplet size and surrounding gas temperature. Change in these two parameters can change relative magnitude of time scales, which eventually leads to transition of flame topologies. Parameter studies on these two factors showed that an interestingly wide range of flame structure can occur when time scales and their relative magnitude are varied. With only small droplets injected, a single flame structure very similar to that in the case H_{II} was produced, in spite of considerably different coflow conditions. It was found that this is related to the fact that representative droplets in the two cases have similar evaporation time scale. This means that by matching important time scales, similar flame structure can be created under considerably different conditions. Air-preheating mainly modulates the strength of each RR by decreasing the evaporation and reaction time scales.

REFERENCES

[1] P. Jenny, D. Roekaerts, and N. Beishuizen, *Modeling of turbulent dilute spray combustion,* Progress in Energy and Combustion Science **38**, 846 (2012).

[2] M. Linne, *Imaging in the optically dense regions of a spray: A review of developing techniques,* Progress in Energy and Combustion Science **39**, 403 (2013).

[3] G. Continillo and W. Sirignano, *Counterflow spray combustion modeling,* Combustion and Flame **81**, 325 (1990).

[4] J. B. Greenberg and N. Sarig, *An Analysis of Multiple Flames in Counterflow Spray Combustion,* Combustion and Flame **104**, 431 (1996).

[5] A. Cessou, P. Goix, and D. Stepowski, *Simple description of the combustion structures in the stabilization stage of a spray jet flame,* Atomization and Sprays **9**, 1 (1999).

[6] S. K. Marley, K. M. Lyons, and K. A. Watson, *Leading-Edge Reaction Zones in Lifted-Jet Gas and Spray Flames,* Flow Turbulence and Combustion **72**, 29 (2004).

[7] H. Correia Rodrigues, M. J. Tummers, E. H. van Veen, and D. Roekaerts, *Spray flame structure in conventional and hot-diluted combustion regime,* Combustion and Flame **162**, 759 (2015).

[8] G. Cléon, D. Honoré, C. Lacour, and A. Cessou, *Experimental investigation of structure and stabilization of spray oxyfuel flames diluted by carbon dioxide,* Proceedings of the Combustion Institute **35**, 3565 (2015).

[9] E. Gutheil and W. Sirignano, *Counterflow spray combustion modeling with detailed transport and detailed chemistry,* Combustion and Flame **113**, 92 (1998).

[10] H. Olguin and E. Gutheil, *Influence of evaporation on spray flamelet structures,* Combustion and Flame **161**, 987 (2014).

[11] A. Vié, B. Franzelli, Y. Gao, T. Lu, H. Wang, and M. Ihme, *Analysis of segregation and bifurcation in turbulent spray flames : A 3D counterflow configuration,* Proceedings of the Combustion Institute **35**, 1675 (2015).

[12] J. Reveillon and L. Vervisch, *Analysis of weakly turbulent dilute-spray flames and spray combustion regimes,* Journal of Fluid Mechanics **537**, 317 (2005).

[13] N. Enjalbert, *Modélisation avancée de la combustion turbulente diphasique en régime de forte dilution par les gaz brûlés,* Ph.D. thesis, INSA de Rouen, France (2011).

[14] A. Rittler, F. Proch, and A. M. Kempf, *LES of the Sydney piloted spray flame series with the PFGM/ATF approach and different sub-filter models,* Combustion and Flame **162**, 1575 (2015).

[15] C. Pera, J. Reveillon, L. Vervisch, and P. Domingo, *Modeling subgrid scale mixture fraction variance in LES of evaporating spray,* Combustion and Flame **146**, 635 (2006).

[16] C. Hollmann and E. Gutheil, *Flamelet-modeling of turbulent spray diffusion flames based on a laminar spray flame library,* Combustion Science and Technology **135**, 175 (1998).

[17] M. Chrigui, J. Gounder, A. Sadiki, A. R. Masri, and J. Janicka, *Partially premixed reacting acetone spray using LES and FGM tabulated chemistry,* Combustion and Flame **159**, 2718 (2012).

[18] L. Ma and D. Roekaerts, *Modeling of spray jet flame under MILD condition with non-adiabatic FGM and a new conditional droplet injection model,* Combustion and Flame (2016, in print).

[19] Y. Minamoto and N. Swaminathan, *Scalar gradient behaviour in MILD combustion,* Combustion and Flame **161**, 1063 (2014).

[20] L. Ma, B. Naud, and D. Roekaerts, *Transported PDF Modeling of Ethanol Spray in Hot-Diluted Coflow Flame,* Flow, Turbulence and Combustion , DOI:10.1007/s10494 (2015).

[21] A. L. Sánchez, J. Urzay, and A. Liñán, *The role of separation of scales in the description of spray combustion,* Proceedings of the Combustion Institute **35**, 1549 (2015).

III

CONCLUSION

10

Conclusions & Recommendations

In this chapter, the studies conducted in this thesis are summarized and recommendations for future studies are provided.

10.1. MODEL DEVELOPMENT

In this thesis we have focused on the computational modeling of MILD spray combustion. Many different modeling approaches, including different computational platforms, different turbulence models, different combustion models, different spray models, etc., have been developed and tested. In summary these model strategies can be categorized into three levels, as shown in Table 10.1.

Table 10.1: Categorization of different modeling levels in this thesis.

Modeling	Code	Two-Phase	Turbulence	Combustion	Spray
Level 1	ANSYS Fluent®	E-L	RANS	Steady Flamelet	Full spray
Level 2	PDFD	L-L	RANS/TPDF	FGM	Dilute spray
Level 3	OpenFOAM®	E-L	LES	FGM	Full spray

At modeling level 1, the commercial code ANSYS Fluent® (Version 15.0) was used. The turbulent two-phase flow field was described by the Eulerian-Lagrangian (E-L) method, with gas phase turbulence modeled by RANS technique. The combustion was described with the standard Steady Flamelet model available in Fluent. And a full spray simulation including the atomization process was conducted. The atomization was modeled with the standard LISA (Linearized Instability Sheet Atomization) model.

The numerical domain of a full spray simulation for DSHC flames is shown in the right part of Fig. 10.1. Given the complexity and difficulty of the atomization modeling, it is a common practice to ignore the dense region, and only focus on the dilute region in spray combustion simulation. This approach is called dilute spray simulation, shown in the left part of Fig. 10.1. The dilute spray simulation of the DSHC flame starts at 8 mm downstream the atomizer exit, where the first measurement of droplet properties has been made. The measured droplet information was directly provided as boundary conditions. As for the gas phase boundary condition, because the fuel vapor was not measured in experiment, the results of a full spray simulation from modeling level 1 has been used.

The dilute spray simulation approach was adopted in modeling level 2, where the in-house code “PDFD" was employed. In this simulation, the hybrid TPDF/RANS method was used to model the turbulence. Lagrangian descriptions of both gas phase and the spray droplets were adopted, so it is referred to as Lagrangian-Lagrangian (L-L) approach. A more advanced combustion model —FGM— was used for the turbulence-chemistry interaction. In this study, many different aspects of the modeling, for example, the influence of boundary conditions, different evaporation models, role of the film properties averaging rule, have been tested and compared. Capabilities and limitations of this modeling approach have been carefully investigated.

At the modeling level 3, model developments have all been based on the open source CFD package — OpenFOAM®. The E-L approach along with the LES technique was used. The combustion model was still FGM, but with new development, namely the addition of an extra dimension to account for the enthalpy loss caused by droplets heating and evaporation. A full spray simulation is used at this stage. Analysis of the available experimental information showed that in the hot-diluted coflow cases of DSHC database,

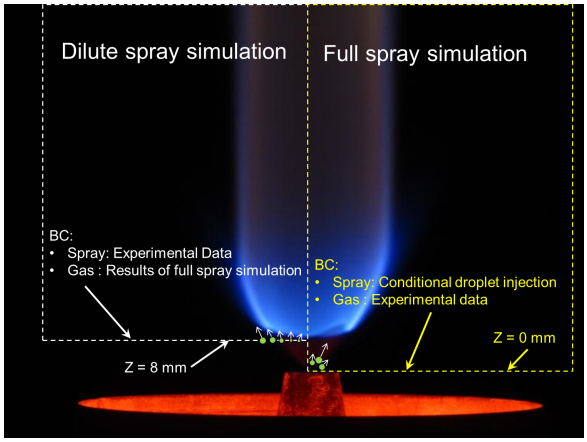

Figure 10.1: Illustration of dilute and full spray simulation.

the flash-boiling atomization occurs. This poses extra difficulties on modeling the atomization process. Instead of modeling the liquid fuel atomization, we proposed a Conditional Injection Model (CIM), which directly injects droplets at the position of the atomizer exit ($\mathcal{Z} = 0\ mm$).

It is worth to mention that in the first two levels of simulation, steady simulations using two dimensional axisymmetric meshes were carried out, while in the third level LES study, an unsteady 3D simulation was conducted, as required to reproduce unsteady 3D nature of turbulence. Therefore the computational cost considerably increases from modeling level 1 to level 3. The transported PDF simulation of modeling level 2 requires consideration of a large amount of Monte Carlo particles, therefore it is computationally more expensive than the approaches of modeling level 1. For the simulation of one single case, modeling level 1 and level 2 respectively take a few hours and two days using a single core on a local computer, while modeling level 3 requires about two days with parallel computing on supercomputer (Cartesius) using 100 cores. These three modeling approaches can be applied in different situations based on the consideration of computational efficiency and accuracy.

Besides the scientific conclusions which will be summarized in section 10.3, contributions of this thesis include also the implementation of FGM model into the open source CFD code OpenFOAM®, and the development of OpenFOAM® FGM solvers for both gaseous and spray combustion simulation. The application of RANS/TPDF/FGM method to modeling spray combustion is also a new extension.

10.2. VALIDATION AND INVESTIGATION STRATEGIES

Modeling of spray combustion involves many different model components, careful validation of the numerical results with available experimental data is crucial for the building of reliable modeling approaches. In this thesis, the following three steps have been taken to develop, validate and apply the modeling approaches.

1. Test performance of different models on a selected test case;
2. Test performance of selected models on a series of test cases;
3. Explore predictions of selected models on other cases.

In Chapters 4, 5 and 7, many different modeling methods, and model components have been tested, compared or developed. The target case for all these studies was the same, namely the DSHC case H_{II}, which has the typical MILD condition, and most importantly has a well defined experimental dataset. This is the first step of model development and validation. Based on the same test case, the performance of different models were compared in a fair way. The studies showed that the modeling approach developed in Chapter 7 produces most satisfactory results for almost all properties when compared with experimental data.

The second step of validation was to apply the best combination of models developed or identified in the first step to a wide range of cases in order to further check its capabilities and limitations. For this purpose, two more hot-diluted coflow cases and the cold coflow case were respectively investigated in Chapters 8 and 9. These results clearly demonstrated that this model approach is not only able to accurately capture important trends such as the change of flame lift-off heights and flame width with varying coflow conditions, but also correctly reproduced the multi-flame structure in the case A_{II}.

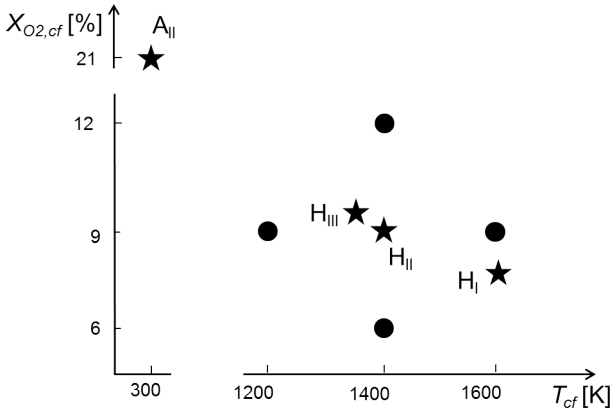

Figure 10.2: Illustration of DSHC cases studied, depicted in $T_{cf} - X_{O_2,cf}$ space, star: experimental case, circle: virtual numerical case.

10

Based on the confidence gained in the previous two steps, some virtual numerical cases have been explored in order to gain deeper insight on the MILD spray combustion. For example, due to the limitation of the DSHC burner configuration, the influence of the coflow temperature and O_2 concentration, which are two important parameters for the establishment of MILD combustion, cannot be studied independently in the experiment. On the contrary, this can be easily done in the numerical simulation. The four virtual numerical cases investigated are shown in Fig. 10.2. With this parametric study, the impacts of these two parameters have been identified, and a suitable combination

of them for the establishment of a MILD spray combustion was suggested (Chapter 8). Another example of the studying of virtual cases is the exploration of the influence of spray polydispersity on the flame structure in Chapter 9.

10.3. MAIN CONCLUSIONS

In general, accurate prediction of spray combustion requires good performance of all sub-models, which are strongly coupled to each other. However, not all model components have equally significant influences on the results.

- For the modeling of spray combustion with low gas phase Reynolds number, the importance of the spray sub-models, e.g. atomization/injection, evaporation, predominates that of the gas phase turbulence models. See Chapter 7 (section 7.6.3 and 7.6.1).

Main conclusions regarding to the spray specific model components and approaches are summarized as following:

- The parabolic temperature profile model was shown to have better performance than the infinity conductivity for modeling evaporation in the hot coflow cases. See Chapter 5 (section 5.5.3).
- The use of "1/3" averaging rule was shown to be not only important for correct prediction of evaporation but also for droplet dispersion. See Chapter 5 (section 5.5.1).
- With carefully specified boundary conditions, the dilute spray simulation method is able to predict correct flow and flame development at downstream. But this method has its own limitations. First, the result is highly sensitive to the boundary conditions, for example the droplet temperature at inlet. And second, the estimation of accurate boundary conditions of the dilute region is very difficult, and sometimes impossible. These factors make this method strongly dependent on the experimental measurements or other simulations. See Chapter 5.
- The models for droplet formation or injection significantly influence the spray and gas phase properties at downstream. Due to the existence of hot coflow, the mechanism that is responsible for the spray atomization is different from that in conventional atomization process, and the flash-boiling atomization occurs in the hot coflow cases. The proposed Conditional Droplet Injection Model, which utilizes the available experimental data measured at downstream, considerably improves the predictions of spray and gas phase properties in a computationally efficient way. This model was demonstrated to perform well also in cold coflow cases. See Chapters 7 to 9.

Two different combustion model have been applied in this thesis study, conclusions about the combustion models are as following:

- The Steady Flamelet Model fails to capture the lifted-off phenomenon of the DSHC flame, while the FGM model can accurately reproduce the proper flame structure of both conventional and MILD spray flames. Chapters 4 and 7 to 10.

- For the modeling of spray combustion, the adiabatic FGM method tends to over-predict the gas phase temperature, especially in the regions where intense evaporation occurs. Inclusion of the enthalpy loss effect considerably improves the predictions. See Chapter 5 (section 5.5.4) and 7 (section 7.6.4).

- The auto-ignition process is highly sensitive to the model constants for the variances of mixture fraction and progress variable if the FGM model is used, and evaluating of model constants using the dynamic procedure in the LES context is preferred. See Chapter 6.

- To correctly capture the flame structure, use of detailed chemical mechanism is indispensable due to the importance of the finite rate reaction under MILD condition. The tabulated chemistry method, more specifically the FGM method, provides a good balance between the accuracy and computational efficiency in this situation. See Chapters 7 to 9.

Using the developed and validated computational tools, further explorations on the spray flame structure and the influences of important factors have been carried out. Important findings are listed below:

- The coflow temperature of the DSHC flames significantly influences the flame lift-off height, and flame topology. The flame changes from having a two-reaction regions (RRs) structure to a triple flame when the temperature of the diluted coflow is reduced. The O_2 concentration in the coflow ($X_{O_2,cf}$) determines the strength of each RR, and the flame peak temperature increases in the case with higher $X_{O_2,cf}$. See Chapter 8 (sections 8.3.3 and 8.3.4).

- The three hot-coflow cases of the DSHC database all fall into the MILD regime according to the definition given by Cavaliere and de Joannon. But when the restriction of flame peak temperature ($T_{peak} < 1800\ K$) is also applied, only the virtual numerical case which has the lowest $X_{O_2,cf}$ and moderate coflow temperature can be strictly called MILD, implying that in a MILD furnace the heat recirculation and flue gas dilution have to be carefully designed to establish an optimal MILD condition. See Chapter 8 (section 8.3.5).

- Multi-flame structure exists in spray combustion. The hot-diluted coflow cases in the DSHC databases typically have two RRs, and the cold-coflow case exhibits four RRs. However, based on experimental visualization, they are respectively referred to as single or double flame structures in literature. These RRs are of different types, premixed or non-premixed, and are formed by different species, major fuel (ethanol) or products of fuel decomposition, for example CO. The rich variety of flame structures in spray combustions is the combined effect of many factors, e.g. gas phase temperature, O_2 concentration, spray polydispersity, etc. And it can be explained by the disparity between the time scales of involved processes. Chapters 8 and 9.

In summary, in this thesis we have focused on the development and validation of predictive modeling approaches for MILD spray combustion, as well as on the use of the

developed numerical tools to gain deeper insight on this new technology. To achieve these goals, many different modeling approaches and model components have been carefully tested and compared. The developed non-adiabatic FGM method has been proven to be able to accurately reproduce main features of the MILD spray flames in a computationally efficient way. Some model components that were originally developed for conventional spray combustion can still be applied in modeling MILD spray combustion, for example the dispersion model. The widely used infinite conductivity model for droplet evaporation works fairly well, but models taking into account the finite conductivity effects can do a better job. MILD conditions also introduce new difficulties in the modeling, for example the occurrence of flash-boiling atomization, for which the conventional atomization model (LISA model) completely failed, and a new model was developed in this study. The spray related model components, e.g. atomization, evaporation, have greater influences on the results than the gas phase turbulence model for the simulation of DSHC flames.

The third modeling level (LES/FGM) developed in Chapter 7 was shown to be the best in terms of prediction power. And this approach has been demonstrated to perform well also in the case of conventional spray flames, which has brought the study of this thesis into a more general context of spray combustion.

The flame structures of conventional and MILD spray flames have been accurately reproduced and the mechanisms that control the transition of flame structures have been revealed for the first time. These results together with the findings from the parametric studies are certainly valuable for the understanding of MILD spray flames, and for the design of MILD spray furnaces.

10.4. RECOMMENDATIONS

Lack of information has always been an issue for model development and validation. For future experimental and numerical study of spray combustion, the following recommendations are made:

- A detailed measurement of key species, for example in case of ethanol fuel, OH, C_2H_5OH, O_2, CO and CH_2O will be very helpful for further understanding of the flame structure and the validation of numerical results.

- In order to develop more predictive models, the atomization process and phenomena happening in the dense region deserves significantly more investigation. For a good spray combustion validation database, a carefully designed and well defined spray formation process is very important. To simplify the numerical study, attention should be paid on the prevention of strong coupling between atomization and other processes, e.g. evaporation, combustion. And information should be provided as close to the dense region as possible. Even qualitative experimental information of the dense region can be very helpful.

- Experimental and numerical studies of flash-boiling atomization are required, because this phenomenon is very common in practical spray combustion systems. In many cases, it is deliberately designed to have flash-boiling atomization, because it greatly improves the atomization efficiency of liquid fuels.

In this thesis and many other studies, the tabulated chemistry method has been shown to be able to provide an nice balance between computational efficiency and accuracy. However, many problems still have to be investigated, especially when the tabulated chemistry method is used in modeling MILD combustion.

- DNS or simple laminar calculation with detailed chemistry under relevant conditions will be very useful to further validate the use of tabulated chemistry methods in MILD combustion condition.
- The definition of progress variable in the FGM method should be further investigated, because this single parameter is used to represent the complicated evolution of the chemical status. Case optimized progress variables are needed due to the change of chemical pathway under different conditions. Different definition of progress variable may be used at different stages of combustion, considering the fact that each species performs differently at different phase of combustion. DNS or sophisticated combustion models, for instance the transported PDF method using detailed chemical mechanism can provide valuable information.

Finally, the progress in modeling spray combustion also depends on progress in understanding fluid mechanics of two-phase flow:

- In the case of spray combustion with low gas phase Reynolds number, the turbulence is mainly generated at small scale by the high speed droplets. This is different from the classic scenario, where the turbulence is generated at large scale and dissipated at small scale due to energy cascade. This phenomenon should be taken into account in the two-way coupling models.

ABOUT THE AUTHOR

Likun MA

05-06-1987	Born in Qingyang, Gansu, China.

EDUCATION

2012.09–now	PhD researcher Delft University of Technology Delft, the Netherlands
2012.01–2012.09	PhD researcher National University of Defense Technology Changsha, China
2009.09–2011.12	Master of Science in Aeronautic and Astronautic Science and Technology National University of Defense Technology Changsha, China Title of thesis: *Investigation of the Dynamic Response of Variable Flow Ducted Rocket Engine*
2005.09–2009.06	Bachelor of Engineering in Aerospace Engineering National University of Defense Technology Changsha, China

AWARDS

2015	First Poster Prize, Combura 2015
2015	Best Poster Prize, JMBC annual meeting
2014	Second Poster Prize, PhD Day of Faculty Mechanics, Maritime and Material Engineering, Delft University of technology

LIST OF PUBLICATIONS

JOURNAL PUBLICATIONS

1. D. Roekaerts, **L. Ma**, “Spray combustion”, Book chapter in: lecture note of International Combustion Institute Winter School, 2016, Eindhoven University of Technology, Editor: J.A. van Oijen, p. 359-383.

2. **L. Ma**, D. Roekaerts, “Modeling of spray jet flame under MILD condition with non-adiabatic FGM and a new conditional droplet injection model”, Combustion and Flame, 165: 402-423, 2016.

3. **L. Ma**, B. Naud, D. Roekaerts, “Transported pdf modeling of ethanol spray in hot-diluted coflow flame”, Flow, Turbulence and Combustion, 96 (2): 469-502, 2016.

4. **L. Ma**, D. Roekaerts, “Structure of spray in hot-diluted coflow flames under different coflow conditions: a numerical study”, Combustion and Flame, under review.

5. **L. Ma**, D. Roekaerts, “Numerical study of the multi-flame structure in spray combustion”, Proceedings of the Combustion Institute, under review (accepted for oral presentation at the 36th International Symposium on Combustion).

CONFERENCE PAPERS AND ABSTRACTS

1. **L. Ma**, D. Roekaerts, “Modeling spray flame under MILD condition with FGM and a new conditional droplet injection model", In: Proceedings of OpenFOAM User Conference, October 2015, Stuttgart, Germany, 18 pages.

2. **L. Ma**, B.Naud, D. Roekaerts,“Lagrangian-Lagrangian modeling of ethanol spray in hot-diluted coflow flame", In: Proceedings of 9th Mediterranean Combustion Symposium, June 2015, Rhodes, Greece, 12 pages.

3. S.H. Jamali, **L. Ma**, D. Roekaerts,“Computational study of ethanol flameless combustion using FGM and steady flamelet", In: Proceedings 9th Mediterranean Combustion Symposium, June 2015, Rhodes, Greece, 12 pages.

4. **L. Ma**, B.Naud, D. Roekaerts,“Modeling ethanol spray jet flame in hot-diluted coflow with transported PDF", In: Proceedings of SPEIC 2014: Towards Sustainable Combustion, November 2014, Lisbon, Portugal, 6 pages.

5. **L. Ma**, S. Zhu, H. Rodrigues, M.J. Tummers, T.H. Van der Meer, D. Roekaerts, “Numerical investigation of Delft Spray-in-Hot-Coflow flame", In: Proceedings of 8th Mediterranean Combustion Symposium, September 2013, Çesme Izmir, Turkey, 12 pages.

6. **L. Ma**, D. Roekaerts, “Large Eddy Simulation of Oxy-Fuel spray flames", 1st International Oxyflame Workshop, February 2016, Montabaur Germany, 1 page.

7. **L. Ma**, D. Roekaerts, “Large Eddy Simulation of MILD spray jet flames", In: Book of Abstracts, Combura Symposium, October 2015, Amersfoort, the Netherlands, 1 page.

8. **L. Ma**, D. Roekaerts, “Numerical study of MILD spray combustion using OpenFOAM", In: Book of Abstracts, Combura Symposium, October 2015, Amersfoort, the Netherlands, 2 pages.

9. **L. Ma**, B. Naud, D. Roekaerts, “Lagrangian-Lagrangian modeling of Spray-in-Hot-Coflow flame", In: Book of Abstracts, 2nd Annual Event of The TU Delft Process Technology Institute, November 2014, Rotterdam, The Netherlands, 1 page.

10. **L. Ma**, B. Naud, D. Roekaerts, “Modeling of an ethanol spray jet flame in hot-diluted coflow with transported PDF methods", In: Book of Abstracts, Combura Symposium, October 2014, Amersfoort, the Netherlands, 2 pages.

11. **L. Ma**, H. Rodrigues, B. Naud, E.H. van Veen, M.J. Tummers, D. Roekaerts, “Transported PDF modeling of ethanol spray in hot-diluted coflow flame", Abstract of Work-in-Progress poster. In: Proceedings of the 35th International Symposium on Combuston (W3P023), August 2014, San Francisco, U.S., 1 page.

12. **L. Ma**, H. Rodrigues, M.J. Tummers, D. Roekaerts, “Transported PDF modelling of spray in hot diluted coflow flame", 23rd Biennial Meeting of the Belgian Section of the Combustion Institute, May 2014, Brussels, Belgium, 2 pages.

13. **L. Ma**, H. Rodrigues, M.J. Tummers, D. Roekaerts, “Numerical study of flameless spray combustion", Physics FOM, January 2014, Veldhoven, The Netherlands, 1 page.

14. **L. Ma**, H. Rodrigues, D. Roekaerts, “Numerical investigation of ethanol Spray-in-Hot-Coflow flame", 1st Annual Event of The TU Delft Process Technology Institute, November 2013, The Haag, The Netherlands, 1 page.

15. **L. Ma**, S. Zhu, H. Rodrigues, M.J. Tummers, T.H. Van der Meer, D. Roekaerts, “Modeling of Delft ethanol Jet-in-Hot-Coflow flame with tabulated chemistry method", In: Book of Abstracts, Combura Symposium, October 2013, Maastricht, the Netherlands, 1 page.

CONFERENCE PRESENTATIONS

(Presenter indicated with underline)

1. **L. Ma**, D. Roekaerts, *Numerical study of turbulent spray combustion and its validation*, Master Course on Combustion in Ghent University, December 2015, Ghent, Belgium, invited by Prof. Bart Merci.

2. **L. Ma**, D. Roekaerts, *Numerical study of turbulent spray combustion using OpenFOAM*, OpenFoam User Conference, October 2015, Stuttgart, Germany.

3. D. Roekaerts, **L. Ma**, *Developments in turbulent spray combustion model validation*, UK Consortium on Turbulent Reacting Flows, September 2015, London, United Kingdom, Keynote lecture.

4. **L. Ma**, D. Roekaerts, *Numerical study of MILD spray combustion using OpenFOAM*, Combura 2015, October 2015, The Netherlands.

5. **L. Ma**, D. Roekaerts, “Numerical study of spray combustion using OpenFOAM", Fluid Mechanics lunchtalk, October 2015, Delft, The Netherlands.

6. **L. Ma**, B. Naud, D. Roekaerts, *Lagrangian-Lagrangian modeling of ethanol spray in hot-diluted coflow flame*, 9th Mediterranean Combustion Symposium, June 2015, Rhodes, Greece.

7. S.H. Jamali, **L. Ma**, D. Roekaerts, *Computational study of ethanol flameless combustion using FGM and steady flamelet*, 9th Mediterranean Combustion Symposium, June 2015, Rhodes, Greece.

8. **L. Ma**, D. Roekaerts, *Implementation and validation of FGM model in OpenFoam*, Burgersdag 2015, January 2015, Delft, The Netherlands.

9. **L. Ma**, B. Naud, D. Roekaerts, *Lagrangian-Lagrangian Modeling of ethanol spray in hot-diluted coflow flame*, SPEIC 2014: Towards Sustainable Combustion, November 2014, Lisbon, Portugal.

10. **L. Ma**, H. Rodrigues, M.J. Tummers, D. Roekaerts, “Transported PDF modelling of spray in hot diluted coflow flame", 23rd Biennial Meeting of the Belgian Section of the Combustion Institute, May 2014, Brussels, Belgium.

11. **L. Ma**, D. Roekaerts, *Simulation of ethanol spray in hot diluted coflow flame*, Fluid Mechanics lunchtalk, May 2014, Delft, The Netherlands.

12. **L. Ma**, H. Rodrigues, M.J. Tummers, D. Roekaerts, *Simulation of ethanol spray jet flames in hot diluted coflow*, Presented at Technical University of Darmstadt, May 2014, Darmstadt, Germany, invited by Prof. Amsini Sadiki.

13. **L. Ma**, X. Huang, *Flameless Combustion Study in TU Delft*, NVV meeting, March 2014, Groningen, The Netherlands.

14. **L. Ma**, H.R.C. Rodrigues, S. Zhu, S.H. Jamali, M.J. Tummers, T.H. Van der Meer, D. Roekaerts, *Simulation of spray jet flames in hot diluted coflow using flamelets and FGM*, Modeling Combustion and Reacting Flows seminar — A joint ANSYS & Dacolt Seminar, March 2014, Delft, The Netherlands.

15. **L. Ma**, D. Roekaerts, *Modelling of spray combustion*, Fluid Mechanics lunchtalk, October 2013, Delft, The Netherlands.

16. **L. Ma**, S. Zhu, H. Rodrigues, M.J. Tummers, T.H. Van der Meer, D. Roekaerts, *Numerical Investigation of Delft Spray-in-Hot-Coflow flame*, Combura 2013, October 2013, Maastricht, The Netherlands.

17. **L. Ma**, S. Zhu, H. Rodrigues, M.J. Tummers, T.H. Van der Meer, D. Roekaerts, *Numerical Investigation of Delft Spray-in-Hot-Coflow flame*, 8th Mediterranean Combustion Symposium, September 2013, Çesme Izmir, Turkey.

18. **L. Ma**, D. Roekaerts, *Numerical study of flameless spray combustion*, NVV meeting, May 2013, Schiedam, The Netherlands.

ACKNOWLEDGEMENTS

I would like to express my deepest gratitude to my promoter and supervisor Prof. Dirk Roekaerts. Thanks to you, the four-year PhD study became a fruitful, memorable and joyful journey. As a promoter, you offered me the opportunity to pursue my PhD in Delft, and made strategic advices on the research; as a supervisor, you participated in daily based discussions and provided many practical supervisions from coding to English grammar correcting. You are very patient in discussions, but can always quickly pinpoint the key issue. You gave me full freedom to proceed the research on my own pace, never push but always ready to give support and advices. You showed respect to my ideas, which greatly helped me in building scientific confidence. You have created many opportunities to help me to grow in the academic society. With your help, I could establish connections with many world-leading experts in this field, and had many opportunities to present our works. I always admire your profound and systematic knowledge in many fields but more importantly your attractive personality. It has been a very nice experience to work with you. Very often I feel you as a friend, with whom I can freely discuss many things — from culture to politics, from history to personal affairs. With these discussions I could see a more colorful world through the eyes of a wise man. Thanks to you, I have learned how to be a good researcher and how to be a respectable person.

Special thanks to my Master supervisor — prof. Zhixun Xia in National University of Defense Technology, China. Under the supervision of you I gained my first experience and knowledge on research. Without the great support and help of you, being studying abroad would not be possible.

I also thank the China Scholarship Council (CSC) for financial support of my PhD study.

I would like to express my acknowledgement to the examination committee members, for reading the thesis and providing valuable feedbacks. I also thank Prof. Amsini Sadiki, Prof. Eve Gutheil, Prof. Luc Vervisch and Prof. Xue-Song Bai for many interesting discussions on spray combustion and other subjects.

It was a nice experience to closely work with Xu Huang, Gerasimos Sarras, Hugo Rodrigues, Seyed Hossein Jamali ,Tariq Ahmed Abul Kalam Azad and Christos Panagopoulos, with whom I had many enlightening scientific discussions. My warmest regards also to Dr. Bertrand Naud. Although I have never met you personally, I appreciate all the help and assistance you provided on the PDFD code and on our first journal paper.

I appreciate the friendly and creative atmosphere created by many colleagues in the Process and Energy department, such as XiangMei Meng, Ming Liu, Jie Lu, Liyuan Fan, Xiaoqian Lu, Zhaochuan Fan, Hongxia Zhou, Meng Wang, Hassan Nemati, Pedro Costa and Manu Goudar Vishwanathappa. Special thanks also to Dr. Mathieu Pourquie for the help he provided at the difficult time when I just started OpenFOAM, and to Gerben Roest for his wonderful support on the computer and softwares.

The accompany of many friends like Qi Wang, Wuyuan Zhang, Tao Zou, Jia Xu, Zongwei Li, Changgong Zhang, Shijie Li, Jialun Liu, Yu Sun, Zilong Wei made my life abroad much easier. Thanks to you guys.

At this moment, the people that I am missing most are my parents, who always love and support me. Thank you for everything you have done for me.

I have always been a lucky man, and the luckiest thing ever happened to me was to marry you — my beloved wife Lin Liu. Being with you makes me peaceful in heart, and full of expectations for the future. You have brought me so many fun and happiness that I have enjoyed so much. Among them, the greatest one is our daughter Zijin. Everyday on the way back home, thinking of her smiling, talking, running, mischievousness or even crying makes me fell so warm and happy, many times I can't help smiling. My little angel, you makes this journey complete and unforgettable.

I thank all the people who have helped me!

Likun Ma
January 2016, Delft